MATT-Q-32

ANNUAL REPORT
1974

PLASMA PHYSICS LABORATORY

PRINCETON UNIVERSITY
PRINCETON, NEW JERSEY

This work was supported by U. S. Energy Research and Development Administration Contract E(11-1)-3073. Reproduction, translation, publication, use and disposal, in whole or in part, by or for the United States Government is permitted.

NOTICE

Printed in the United States of America.

Available from
National Technical Information Service
U. S. Department of Commerce
5285 Port Royal Road
Springfield, Virginia 22151
Price: Printed Copy $ * ; Microfiche $1.45

*Pages	NTIS Selling Price
1-50	$ 4.00
51-150	5.45
151-325	7.60
326-500	10.60
501-1000	13.60

Princeton University
Plasma Physics Laboratory
Princeton, New Jersey

MATT-Q-32

ANNUAL REPORT

covering the period
January 1 - December 31, 1974

Issued
August 1975

Unless otherwise designated, all the work described in this research and development report was supported by the U. S. Energy Research and Development Administration (formerly AEC) Contract E(11-1)-3073.

CONTENTS

SECTION VI
Fusion Reactor Design Division

PREFACE

The program of the Princeton University Plasma Physics Laboratory for 1974 is summarized in this report in reviews of theory, experiment, engineering and conceptual design. The following developments stand out:

(1) Experiments on FM-1 have demonstrated reduction of anomalous electron heat flow in a regime with opposing temperature and density gradients.

(2) The ST device yielded important new insights on gross plasma stability using multiple x-ray detectors. A kink-like mode appears on axis for $q < 1$ and results in an explosive secondary mode while the detailed structure of higher-order kink modes was also studied. These latter results are in accord with resistive MHD theory.

(3) ATC has demonstrated the utility of titanium gettering by permitting hydrogen discharges with effective Z-values near unity.

(4) The PLT fabrication program is well underway as well as construction of a 4-MW, 40-keV neutral beam injection system. First plasmas are still scheduled for the fall of 1975.

(5) Although the PDX fabrication schedule has slipped, the time has been used to provide considerable improvement in the design of the divertor structure. Fabrication of major components is underway.

(6) The conceptual design of the TCT-TFTR, performed in collaboration with the Westinghouse Electric Corporation, is well advanced. The device, approximately twice the size of PLT, is to determine the physics of reactor-level neutral beam-heated plasmas and to achieve reactor level power densities of alphas from two-component D-T reactions.

(7) Major advances in computer codes for MHD stability, transport, and particle simulation have been made in an attempt to explain current tokamak behavior and yield predictions for future devices.

Toroidal research on low-β plasmas continues to be the Laboratory's major effort.

I. TOROIDAL CONFINEMENT EXPERIMENTS

A. Introduction

During 1974, the FM-1 superconducting-ring spherator and the ATC and ST tokamak experiments obtained a number of highly significant new results in the areas of plasma stability, impurity control, and plasma heating. The ST tokamak was dismantled at mid-year to make way for the PLT device, which continues on schedule for completion in the fall of 1975. Detailed design and fabrication of the Poloidal Divertor Experiment (PDX) was begun. A conceptual design was undertaken for the Two-Component Torus (TCT) device, which is to serve as a tokamak fusion test reactor (TFTR).

FM-1 experiments have yielded further detailed information on plasma transport by microscopic instability modes. A particularly important result was the reduction of anomalous electron heat flow in a region of opposing temperature and density gradients. The flow velocity of plasma into the FM-1 poloidal divertor was measured by a sound-wave Doppler-shift method. Impurity ion transport was studied by adding barium ions to noble gas plasmas; both classical and anomalous impurity diffusion effects were found. Lower-hybrid heating was shown to be efficient in raising the plasma electron temperature.

Gross plasma stability on the interior of the tokamak discharge was studied on the ST device by means of multiple x-ray detectors. A discovery of first-rate importance was made: Inside ostensibly stable discharges, a kink-like oscillation appears at the axis as soon as the rotational transform there has risen beyond the Kruskal-Shafranov limit. The oscillation grows to a certain threshold, at which an explosive secondary mode sets in and levels the central temperature profile. This mechanism acts as a kind of "governor" in present-day tokamak discharges to enforce a quasi-steady-state current profile. The x-ray method was also used to measure the detailed structure of higher-order kink modes in the plasma, confirming the validity of the resistive MHD model. The impurity distribution in ST was studied by radial scans of both x-ray and extreme ultraviolet emission; there appears to be no very strong axial concentration of high-Z impurities. Ion-cyclotron heating was applied successfully at the level of several hundred kilowatts, with resultant ion temperature rises in the 100-eV range.

The rf coupling was efficient, but the total energy input was limited by the evolution of wall impurities.

Feedback stabilization experiments on ATC succeeded in demonstrating various forms of MHD mode-locking, including the interesting case of mode-locking into a static helical field perturbation. The neutral-beam injection power was raised to 100 kW, and perpendicular injection into a tokamak was investigated for the first time. The plasma heat outflow pattern was examined in detail by means of bolometers. Impurity transport was studied using laser-produced metal vapor jets for impurity input and a radially scanning ultraviolet spectrometer as diagnostic. Titanium gettering of the vacuum wall was found to permit the generation of exceptionally pure hydrogen discharges, with effective Z-values close to unity.

The PLT fabrication program proceeded approximately as planned. The toroidal field coils were assembled in place and tested to 35 kG. Construction of a 4-MW, 40-keV neutral-beam injection system was undertaken. Considerable improvements were achieved in the design of the PDX divertor structure; fabrication of major device components is under way. A program of PDX-related experimental and computer studies has been initiated. The conceptual design of a twice-PLT-size tokamak device, the TCT, was undertaken in collaboration with the Westinghouse Electric Corporation. The principle objectives are to determine the physics of reactor-like neutral-beam heated plasmas, and subsequently to achieve reactor-like power densities of alpha particle production from two-component D-T reactions.

B. The FM-1 Spherator

1. Introduction

Previous divertor experiments on FM-1 have shown that poloidal field divertors function well on toroidal confinement devices. A simple theoretical model was developed to explain the experimental results, which was used for the design of PDX. This past year, the divertor experiments were extended to test the model further. Plasma flow measurements have shown that the flow velocity into the divertor is consistent with the ion-sound-flow model which has been used. Simple magnetic field considerations suggested that the plasma capture in the divertor could be increased further by optimizing the divertor coil current. Divertor capture experiments verified this prediction.

Impurity transport experiments were undertaken with barium as a test impurity. Indications of both classical and anomalous impurity transport were found.

Experiments on heating near the lower hybrid frequency were carried out to ascertain the mechanisms for, and effects of, this heating on a toroidal device. High electron heating efficiencies (> 50%) were observed along with modest (~ 2%) ion heating efficiencies. Extensive wave measurements were also carried out.

An experimental program was undertaken to determine the effect of magnetic shear on the radial structure of the drift-wave turbulence in FM-1. Computer-correlation techniques were used to determine that the radial structure of the drift modes was relatively insensitive to shear. The radial group velocity, which gives rise to shear stabilization, was much smaller than predicted by contemporary theory. The necessary modifications to this theory are under consideration.

Electron thermal conductivity measurements were made for both positive and negative temperature gradients (relative to the density gradient). The fact that the conductivity was very much larger for positive temperature gradients was a strong indication that the transport in this regime is due to the trapped electron instability.

Ohmic heating was tested to determine its suitability for forming a target plasma for neutral injection.

2. Divertor Studies

a. Flow measurements. The mass flow velocity through the outer divertor throat was measured by propagating ion acoustic waves along the magnetic field lines. Ion acoustic wave pulses were propagated toward and away from the neutralizing plate. The flow velocity was determined by measuring the difference in the two propagation velocities. Ion acoustic waves were ideally suited for this purpose since their phase and group velocity are near the plasma flow speed. These measurements are described in detail elsewhere. (Abstracts 1-3).

A summary of the results of the flow measurements is shown in Fig. 1. High neutral pressures were used in these experiments to cool the ions and eliminate the strong ion Landau damping of the ion acoustic waves. In Fig. 1 the pulse transit time between a fixed and a moveable grid is shown for parallel and antiparallel propagation as a function of the grid separation.

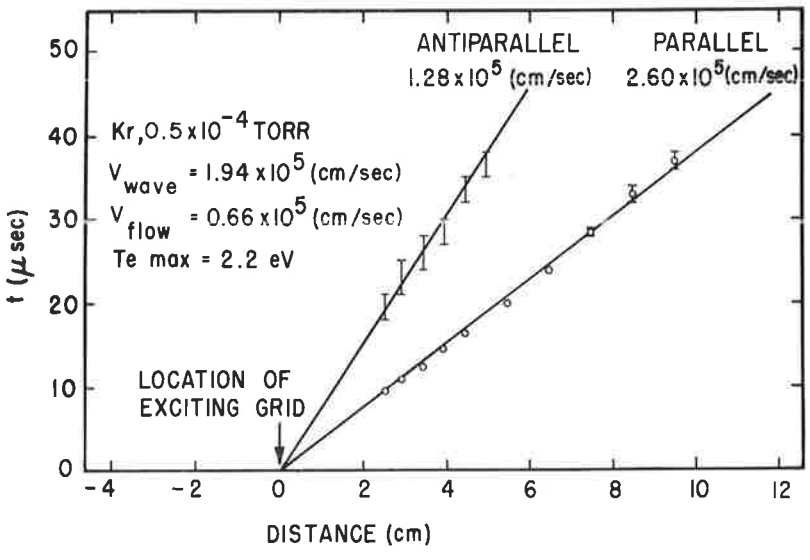

Fig. 1. Receiver signal (upper traces) and exciting signal (lower signal). The distance d is measured from the excitation grid.

From these data, the propagation speed is found to be about 1/3 of the ion sound speed. The data also showed a $(\text{mass})^{-1/2}$ dependence for both the wave speed and the flow speed. These results demonstrate that the flow into the divertor is near (and related to) the ion sound speed, in general agreement

with the simple flow model.

b. Plasma capture. The magnitude of the divertor current was changed relative to other coil currents, to optimize the plasma capture in the divertor. (Abstracts 4 and 5). The optimum plasma capture should occur when the magnetic flux between the separatrix and any obstruction is maximized. This occurs when the magnetic flux through the inner and outer divertor throats is equal.

Plasma collectors were positioned to capture the plasma flow into the divertor, as well as the plasma loss to the toroidal field column and to an external limiter. The ratio of plasma capture by the divertor to the total plasma loss is shown on Fig. 2, as a function of divertor current.

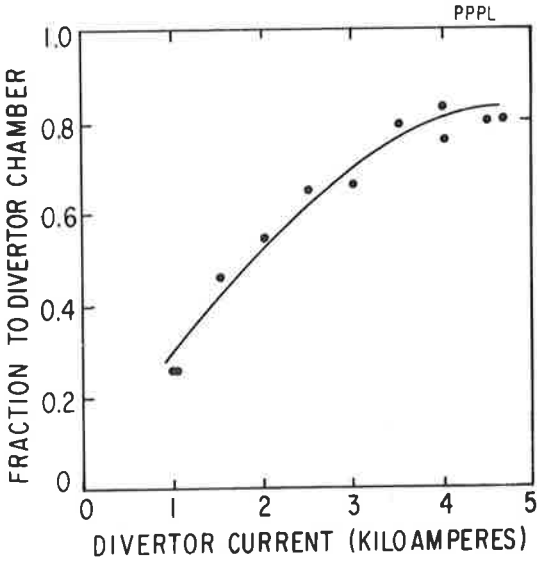

743175

Fig. 2. Fraction of total plasma loss captured in divertor as a function of divertor coil current.

At about 5 kA of divertor current, the magnetic flux between the separatrix and the nearest obstacle is maximum. At higher divertor currents the flux through the outer divertor throat is reduced below the flux through the inner throat.

For the plasma conditions used in these experiments, 80% of the plasma flow across the separatrix could be captured in the divertor. The plasma

capture will likely decrease at higher electron temperatures, due to the increase in the cross-field transport. The plasma flow across the separatrix does not represent the total loss, since some plasma is collected on the internal ring. In general, 10% of the plasma is lost inward.

3. Impurity Transport

The objective of FM-1 impurity transport studies is to determine to what extent the classical or turbulent diffusion of impurities is important. Theory predicts that a strong inward diffusion should exist for impurities with a charge Z which is larger than the background plasma Z. The total transport of impurity ions will be the result of the superposition of this classical inward diffusion and any anomalous transport that exists.

Barium neutrals were injected into the FM-1 plasma and ionized to form a Z = 2 trace impurity in a Z = 1 plasma. (Abstracts 6 and 7). The confinement time of the barium was determined from the measured decay of the barium light. The barium confinement was determined as a function of plasma density and plasma ion mass. The results are shown in Fig. 3.

743574

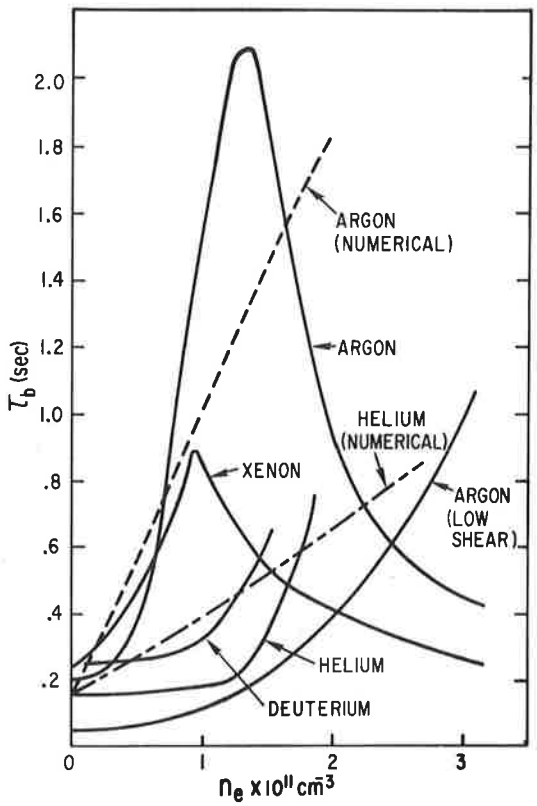

Fig. 3. The observed barium decay times (solid curves) are shown as a function of background plasma peak density for various gases in the FM-1 high shear magnetic field configuration. Also shown is the barium confinement in argon with low shear. The dashed curves are the numerically determined confinement times for a comparable slab geometry using the diffusion coefficients described in the text.

Several characteristics of the barium transport can be observed.

(1) At low density the barium confinement is comparable to, but somewhat larger than, the electron confinement for plasmas of all ion masses.

(2) The confinement time exhibits a slight plateau at low plasma density, and then increases with increasing plasma density.

(3) The rate of increase of confinement of the barium with increasing density is roughly proportional to the square root of the background-ion mass.

(4) At high plasma density, the barium confinement begins to decrease with increasing density for some background-ion masses.

(5) Lowering the magnetic shear reduces the barium confinement time for all plasma densities.

The fact that the barium confinement at low density is comparable to the background plasma confinement, but shows an increase with density, suggests that the total diffusion coefficient is the superposition of an anomalous diffusion coefficient, which dominates at low density, and a classical inward diffusion coefficient, which becomes important at high plasma densities. The diffusion equation resulting from this model was solved numerically for a slab geometry with plasma and magnetic field parameters characteristic of FM-1. The results of this calculation are also plotted in Fig. 3. The numerical results agree with the experimental results in rough magnitude, as well as mass and density scaling. However, there is some detailed disagreement between the numerical and experimental results, which suggests that the model is incomplete. At high density no decrease in confinement should occur. The reduction in barium confinement at high density is likely the result of the known decrease in background plasma confinement at these densities.

4. Plasma Heating Near the Lower Hybrid Frequency

In the past year, we have measured the electron and ion heating efficiency at frequencies near the lower hybrid frequency in the FM-1 Sphera-tor. (Abstract 8). An rf generator operating at 68 MHz was used to drive an antenna structure comprised of two plates out of phase on the exterior of the plasma separated in the direction along the poloidal field. The

generator was capable of delivering a maximum of 4 kW to the plasma.

a. Electron heating efficiency. The electron heating experiments were conducted in the afterglow of a helium ECRH plasma, by applying a short pulse (~ 0.2-0.4 msec). Before and after heating the incident rf power was kept low, so that the final electron temperature was typically ≤ 3 eV. This temperature was not an upper limit for higher rf powers; the electrons could be heated up to 20 eV. The temperature was kept low in order to be able to neglect the energy loss by radiation and ionization. For low densities, the heating was uniform across the plasma, while at high densities the heating was mainly on the exterior of the plasma. When this experiment was performed in an argon plasma, similar results were obtained. The rf frequency in both cases was greater than the lower hybrid frequency. Thus, the heating on the outside does not correspond to absorption at the lower hybrid resonance layer.

The heating efficiency of the plasma was computed from the rf power and the density and temperature profiles and the plasma volume. The plasma volume was evaluated from a calculation of the magnetic field surfaces. The heating efficiency was defined as the energy absorbed by the plasma divided by the rf energy from the antenna structure. As shown on Fig. 4, the electron heating efficiency was very high and comparable for both argon and helium.

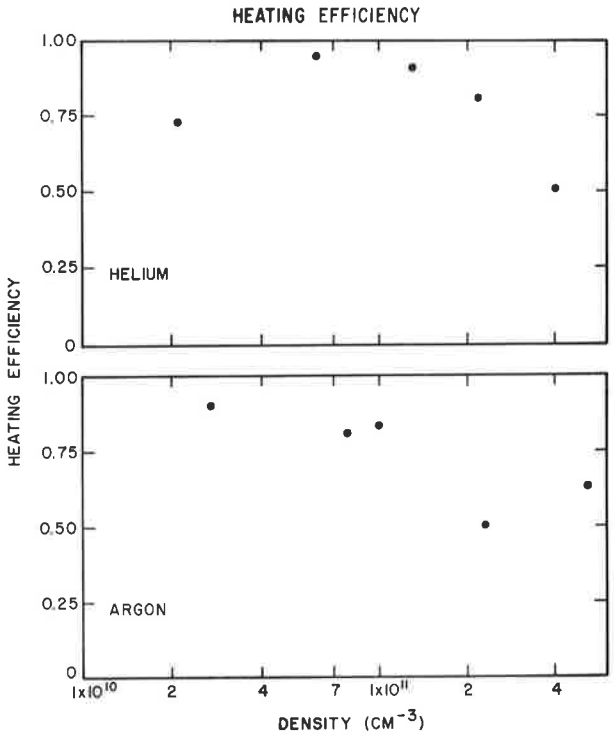

743846

Fig. 4. Electron heating efficiencies as a function of density for a helium and an argon plasma.

b. Ion heating efficiency. The ion temperature was determined before and after the rf heating by measuring the Doppler broadening of a helium and an argon ion line using a Fabry-Perot interferometer. High-power pulsed experiments (1-2 kW) were conducted in an ECRH plasma. Low-efficiency ion heating, between 1-3%, was observed in an argon plasma, while no significant increase in the Doppler broadening of the helium ion line was observed. Because the helium line was weaker in intensity than the argon ion line, a heating efficiency in helium of less than 2-3% was not measureable.

In addition to the heating efficiency experiments described, the onset of parametric instabilities has been observed. This was determined by measuring the frequency spectrum as shown in Fig. 5 for a hydrogen plasma at relatively low rf powers in the vicinity of the plates using a shielded probe.

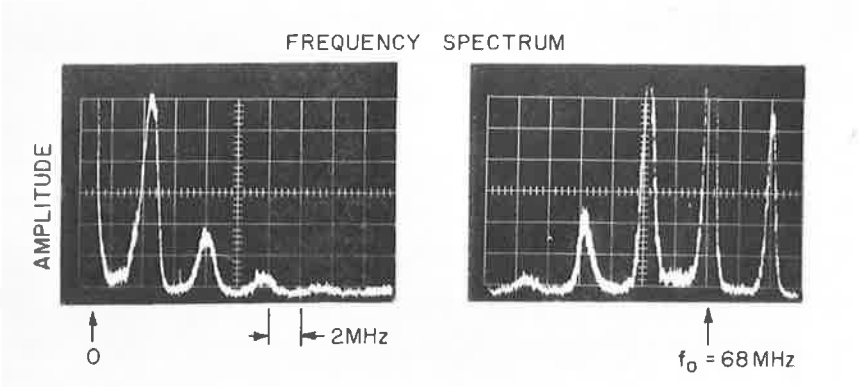

743845

Fig. 5. Spectrum analysis of an rf probe in a hydrogen plasma near the coupling structure.

At somewhat higher powers, the discrete structure of the spectrum vanished and a broad turbulence was observed around the pump frequency and at frequencies near the ion cyclotron frequency. The relationship of the nonlinear decay processes to the observed plasma heating is under investigation.

5. Drift Wave Turbulence

Turbulence measurements in FM-1 during this year have concentrated on three areas: (1) poloidal, (2) toroidal, and (3) radial structure of fluctuations. (Abstracts 9 and 10).

a. Poloidal structure. Due to the complexities inherent in doubly-periodic systems with shear of the magnetic field, two approximations are customarily made in theoretical treatments, a "quasimode" analysis within a magnetic surface, taking into account poloidal dependences and simplifying radial structure, and a radial nonlocal normal mode approach which neglects poloidal asymmetries; with the exception of a few limits, only these two cases have been treated. Previously the poloidal structure in afterglow plasmas has been reported to be localized in the lower-shear region within the surface; recent measurements with continuous upper hybrid resonance heating have found the fluctuation amplitude to be roughly independent of poloidal position. This dichotomy may be due to the dominance of the temperature gradient in the latter case and the reliance on curvature, etc., in the afterglows wherein the temperature profiles have relaxed.

b. Toroidal structure. Due to the turbulent nature of the spectrum, correlations between signals from Langmuir probes biased to collect ion saturation current have been computed, fed into the data acquisition system, processed and displayed. Figure 6 shows the correlation function between two probes displaced toroidally at the same radial and poloidal position.

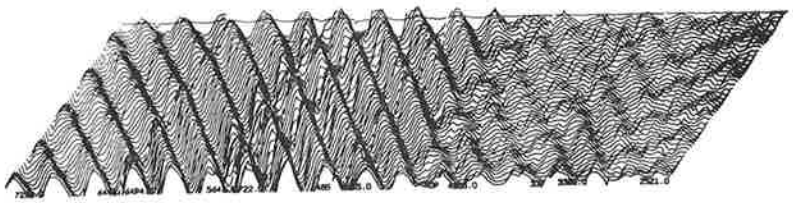

753134

Fig. 6. Correlation between probes displaced toroidally. The horizontal coordinate is probe separation and the vertical the delay

time τ. The probes are adjacent at the maximum of the correlation for $\tau = 0$. The toroidal wavelength is 9.8 cm for this xenon plasma and the correlation length extends roughly one-quarter of the machine circumference.

The toroidal wavelength is well-defined, and is given by the condition $k_{\parallel} =)$ (i.e., $m = \ell q$ where m is the poloidal and ℓ the toroidal mode number) when the toroidal correlation length is less than the circumference of the machine. The correlation length is related to the correlation time by the toroidal group velocity, and is in agreement with theory [$v_{phase}\ \phi \simeq v_{group}\ \phi$ for $B_p >> B_t$ since $k_y = (1/R)\ B/B_p$)]. However, the correlation time is found to be greater than the damping time estimated on the basis of radial energy propagation.

c. Radial structure. Figure 7 displays the correlation between two probes displaced radially at the same toroidal and poloidal position. An inward radial phase velocity is observed, yet no group velocity is apparent.

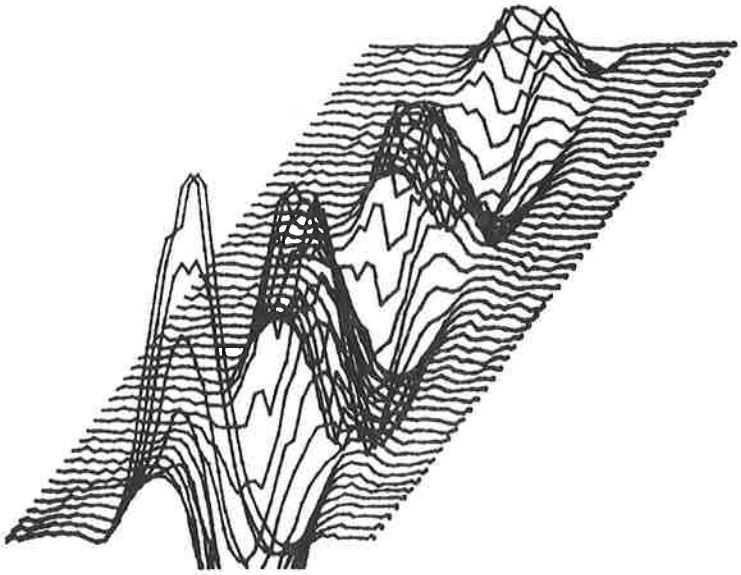

753135

Fig. 7. Correlation between probes displaced radially. Horizontal coordinate is probe separation and vertical τ. For this helium plasma the correlation is 1.8 cm wide and the period 64 msec.

The asymmetry of the phase velocity may be due to dissipation, reflections, of the breakdown of the WKB approximation.

6. Electron Thermal Conductivity

The parametric dependence of the electron thermal conductivity in the trapped electron regime was determined (Abstracts 11-14). The procedure for determining the electron thermal conductivity $K_\perp$ was reported in the last Annual Report. In order to study the cause of the observed anomalous transport as well as its scaling, the parametric dependence of $K_\perp$ was investigated by changing the electron temperature gradient, as well at T_e, L_s, and n_e.

a. The effect of the electron temperature gradient. The previous measurements were carried out for the condition with the electron temperature gradient parallel to the density gradient ($\eta_e = d \ln T_e > 0$) where large anomalous heat conduction was observed. To determine the mechanism responsible for this anomalous thermal conduction, a negative electron temperature gradient ($\eta_e = d \ln T_e / d \ln n_e < 0$) was produced by using two different microwave heating frequencies. The initial localization and sequenced thermal conduction are shown in Fig. 8.

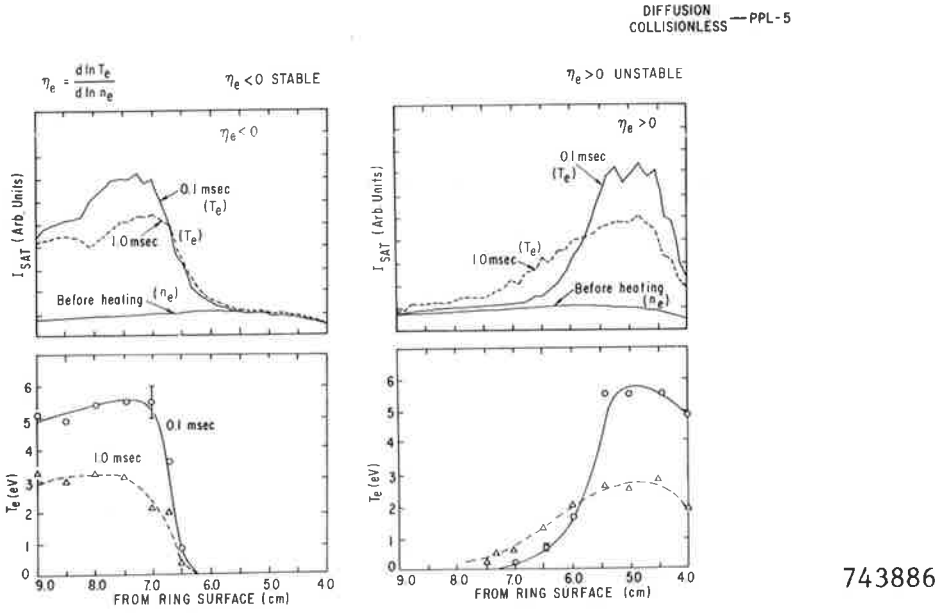

Fig. 8. The ion saturation current and electron temperature are plotted against position 0.1 msec and 1 msec after a heating pulse has produced a sharp positive and negative temperature gradient. The thermal conductivity is much larger for the positive gradient.

The ion saturation current profile before heating represents the density profile because the electron temperature was found to be constant over the plasma volume. When the electron temperature gradient was parallel to the density gradient (c-band heating), the observed thermal diffusion was similar to the previous results. When the electron temperature gradient was produced antiparallel to the density gradient, the electron thermal conduction was small. The $K_\perp$-value obtained for $\eta_e < 0$ is less than 1/20 of the value obtained for $\eta_e > 0$. (Resistive, collisionless, trapped electron, and trapped ion drift modes are possible candidates for the thermal conduction). The observed η_e-dependence is consistent with the trapped electron mode.

b. Scaling of $K_\perp$. Figures 9 and 10 show the dependence of $K_\perp$ on electron temperature and shear.

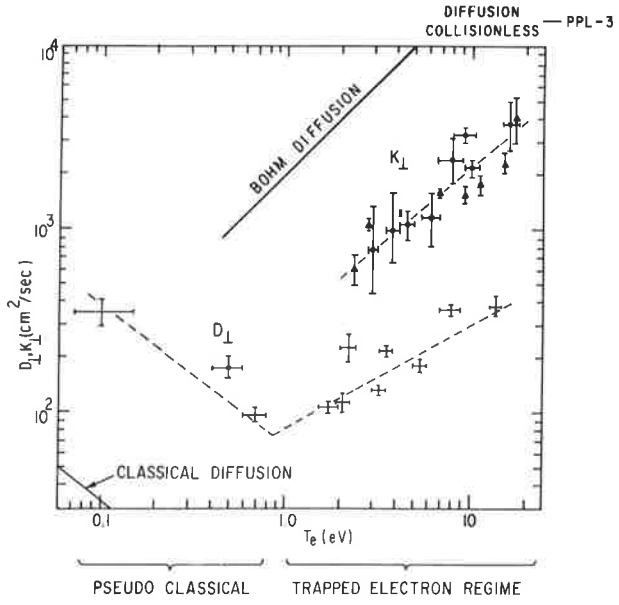

Fig. 9. Diffusion and thermal conductivity coefficients as a function of electron temperature.

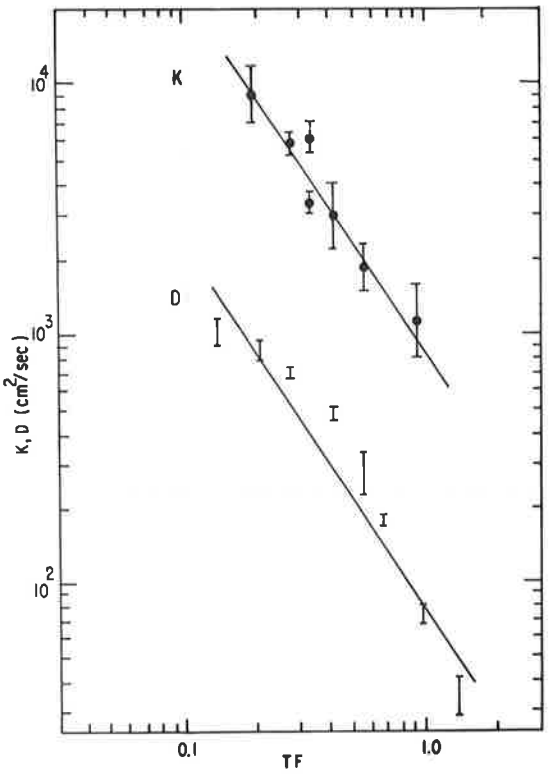

743123

Fig. 10. Diffusion and thermal conductivity coefficients as a function of toroidal field (TF) and magnetic shear length (L_s).

The empirical formula based on these results is

$$K_{\perp} \sim (3\text{-}5)D$$
$$\sim f_o\ (L_s/a)(kT_e/16\ eB)$$

where the B dependence is based on the LSP result, and 1/a is included to adjust the dimension of $K_{\perp}$. By fitting the experimental result, f_o is found to be 1/800. It may be worthwhile mentioning that for a $B_T >> B_P$ tokamak-like configuration L_s/a is given by B_p/B_T, which leads to

$$K_{\perp} \sim f_o\ (kT_e/16\ eB_p)$$

This empirical formula is similar to the poloidal Bohm diffusion of GA and agrees with some tokamak experiments. We can made some predictions about future tokamak experiments by assuming that the observed scaling law may describe the anomalous loss in the trapped electron regime. By balancing the energy loss with the Ohmic heating energy input, we have

$$\tau_e(\text{sec}) \simeq 0.4\ a^2(m)I_p^0\ T_e^0(n_e/2 \times 10^{13})^{1/3}$$

$$T_e(\text{ke}_V) \simeq 1.6\ a^{-1}(m)I_p(\text{MA})(n_e/2 \times 10^{13})^{1/3}.$$

It should be noted that τ_e is independent of I_p and T_e, and T_e increased with an increase in I_p. These predictions are significantly different from those in the pseudo classical regime, where $\tau_e \propto I_p^3$ and $T_e \propto I_p^2$.

7. Ohmically Heated Plasma

Ohmic heating with a 2 msec pulse (500 Hz) at 100 ~ 150 kA was applied to the microwave produced plasma ($n_e \tilde{=} 2 \times 10^{11}$ cm^{-3}, $T_e = 8 \sim 10$ eV and $T_i = 3$ eV) to produce a target plasma for future neutral-beam injection experiments, as well as to study the instabilities of a current-carrying plasma. Different kinds of optical diagnostics were used to study the radial profiles of n_e, T_e, fluctuation amplitude, and T_i. A light probe was designed to have a spatial resolution of 5 mm and to detect drift waves.

A hydrogen plasma with a helium ion trace was used to measure T_e and T_i. Within 2 msec of the initiation of the OH current, the plasma density increased to 2×10^{12} cm^{-3}. The measurement of the light C IV (5801 Å) indicates that the electron temperature reached 30-40 eV. Doppler-broadening measurements at 4686 Å showed that T_i increased from 3 eV to 7-10 eV. Large-scale oscillation were observed on the light signal, around the light-intensity-gradient maximum, where ∇T_e or ∇n_e was maximum. The cause of this instability, and whether it is related to MHD or drift modes is under investigation.

IB 1. MATT-1078 Transport and Divertor Studies in the FM-1 Spherator, by K. Ando, S. Ejima, S. Davis, R. Hawryluk, H. Hsuan, D. Meade, M. Okabayashi, N. Sauthoff, J. Schmidt, and J. Sinnis

Plasma confinement experiments were carried out on FM-1 with dimensionless plasma parameters (ν_c/ω_{be}, ω/ω, etc.) and magnetic field geometries which are similar to parameters and geometries on existing tokamak devices. These studies include the effects of trapped particle and energy transport, and the transport of plasma into a poloidal divertor.

IB 2. MATT-1061 Measurement of Plasma Flow Velocity into the Divertor of the FM-1 Spherator by Using Ion Acoustic Wave Propagation, by H. Hsuan, M. Okabayashi, and S. Ejima

The plasma flow velocity into the divertor chamber of the FM-1 Spherator is determined by measuring the propagation velocity of ion acoustic waves. The observed parametric dependence of plasma flow into the divertor is consistent with the plasma sheath model, which is now frequently used for designing poloidal divertor devices.

IB 3. Measurement of Plasma Flow Velocity into the Divertor of the FM-1 Spherator,* by S. Ejima, H. Hsuan, and M. Okabayashi

The plasma flow velocity into the divertor chamber in the FM-1 Spherator was investigated by exciting ion acoustic waves at the divertor throat. The difference of wave propagation velocity with and against the plasma flow provides the plasma flow velocity. The magnitude and parametric dependence of the observed plasma flow velocity is $\sim 0.3(T_e/M)^{1/2}$. This is consistent with the plasma sheath model, which is now frequently used for designing poloidal divertor devices.

*Presented at the *Sixteenth Annual Meeting of the American Physical Society*, (Albuquerque, N. M., 1974)

IB 4. Poloidal Divertor Experiments on the FM-1 Spherator,* by J. Sinnis, M. Okabayashi, and J. Schmidt.

Recent modifications to the poloidal field divertor on the FM-1 Spherator make it possible to vary the amount of poloidal flux, and therefore the thickness of the scrape-off layer, that reaches the divertor chamber. Initial studies without divertor baffling have been directed towards understanding the processes involved in transporting plasma to the divertor. Langmuir probes and particle collectors in the divertor show that

the plasma flow can be controlled by varying the thickness of the scrape-off layer and that a significant increase in the particle flux to the divertor (factors of 2 or 3) can be achieved by increasing the diverted flux over the "standard" configuration. The plasma profiles in the divertor (which will be used to design the divertor baffling) show significant broadening when fluctuations are present in the main plasma volume.

---

* Presented at the *Washington, D. C., Meeting of the American Physical Society*, (1974)

IB 5. MATT-1078 Transport and Divertor Studies in the FM-1 Spherator, by K. Ando, S. Ejima, S. Davis, R. Hawryluk, H. Hsuan, D. Meade, M. Okabayashi, N. Sauthoff, J. Schmidt and J. Sinnis

Fundamental problems of toroidal fusion devices have been investigated in the FM-1 Spherator. These subjects include the transport due to drift wave turbulence in the trapped electron regime, poloidal divertor and impurities, and lower hybrid heating.

IB 6. MATT-1070 Impurity Transport in FM-1, by J. A. Schmidt, N. R. Sauthoff, and R. J. Hawryluk

The confinement of Z = 2 barium test ions in a Z = 1 plasma was found to be strongly dependent on density and background plasma ion mass. Most of the characteristics of the parametric dependence of the barium confinement could be related to the super-position of an anomalous outward and a classical inward diffusion.

IB 7. Diffusion of "High-Z" Impurity Test Ions in FM-1,* by J. A. Schmidt, N. R. Sauthoff, and R. J. Hawryluk

Z = 2 barium test ions were injected into a Z = 1 background plasma in FM-1 to determine which processes govern "high-Z" impurity transport. Effects related to both classical inward diffusion and anomalous outward diffusion were observed. At low density, where the classical inward diffusion should be small, the barium confinement time was comparable to that of the background plasma. At higher densities, where the classical inward diffusion should become important, the barium confinement time exceeded that of the background plasma by more than an order of magnitude.

The inward component of the diffusion coefficient scaled roughly as the square root of background plasma ion mass, as expected theoretically.

*Presented at the *Sixteenth Annual Meeting of the American Physical Society*, (Albuquerque, N. M., 1974)

IB 8. RF Heating Near the Lower Hybrid Frequency in the FM-1 Spherator,* by R. J. Hawryluk, P. L. Colestock, S. L. Davis, and J. A. Schmidt.

A series of plasma heating experiments have been conducted in the FM-1 spherator by applying up to 4 kW of rf power at 71 MHz which corresponds to a frequency near the lower hybrid frequency for a H or a He plasma. The rf field was excited by two plates driven out of phase on the exterior of the plasma along the poloidal field. The accessibility of the rf field and the location at which plasma heating occurs as a function of density for different gases has been studied. For low plasma densities such that the rf frequency, ω, is much greater than the lower hybrid frequency, ω_{LH}, heating of the bulk of the plasma was measured. The heating efficiency (plasma heating power/rf input power) was found to be between 20-40%. Only a weak dependence on plasma density was noted. For high densities such that $\omega \sim \omega_{LH}$, only heating of the outer surface of the plasma was observed.

*Presented at the *Sixteenth Annual Meeting of the American Physical Society*, (Albuquerque, N. M., 1974)

IB 9. Radial and Toroidal Structure of Drift Instabilities in the FM-1 Spherator,* by N. R. Sauthoff, M. Okabayashi, and J. A. Schmidt

Radially localized drift modes with long toroidal correlation lengths have been observed in a sheared magnetic field configuration. In the case of argon, which gives a relatively coherent spectrum, the wave frequencies are found to be multiples of a dominant frequency which decreases with increasing toroidal field, B_T. The toroidal wave vector is well defined and also decreases with increasing B_T. Measurements of the envelope of the correlation function versus probe position give the toroidal group velocity. The toroidal correlation length increases with B_T until it encircles the machine, introducing a periodicity constraint. The radial correlation length is of order of the ion gyroradius and is smaller than the radial wavelength for most cases.

*Presented at the *Sixteenth Annual Meeting of the American Physical Society*, (Albuquerque, N. M., 1974)

IB 10. MATT-1097 The Defeat of Shear Stabilization by Peaking of the Diamagnetic Frequency Profile, by N. R. Sauthoff, M. Okabayashi, and J. A. Schmidt.

The radial wave equation describing collisionless drift instabilities in plasma is solved including the effects of a peaked diamagnetic frequency profile. Radially localized fluctuations with no radial energy propagation are found in cases with sufficiently low shear and large peaking.

IB 11. MATT-1019 Determination of the Electron Thermal Conductivity Across Magnetic Surfaces in the FM-1 Spherator, by S. Ejima, M. Okabayashi, and J. Schmidt.

A new approach was taken to measure the electron thermal conductivity across magnetic surfaces by utilizing localized upper hybrid resonance heating. The electron thermal conductivity coefficient measured in the FM-1 Spherator was increased with an increase of electron temperature for $T_e > 1$ eV. The absolute value was 10 ~ 20 times smaller than the Bohm coefficient.

IB 12. Numerical Study of Electron Trapped Particle Instability,* by M. Okabayashi and S. Ejima.

Recent experimental results of anomalous electron thermal conductivity and magnetic field configuration dependence in the FM-1 Spherator suggest the turbulent stage of electron trapped particle instability may be responsible for the observed anomalous loss mechanisms. In order to estimate the loss rate, the dispersion of electron trapped particle instability is solved numerically including ion Landau damping and velocity dependence on the electron collision time. The diffusion coefficient estimated from γ_{max}/k^2 is 1/30 ~ 1/200 of Bohm diffusion coefficient depending upon the other parameters. The numerical results for tokamaks and FM-1 Spherator will be presented.

---

*Presented at the *Sixteenth Annual Meeting of the American Physical Society*, (Albuquerque, N. M., 1974)

IB 13. Comments on Toroidal Confinement Devices Based on Electron Thermal Conductivity Measured in FM-1,* by M. Okabayashi and J. Schmidt

Recent investigations of the thermal conductivity in the electron trapped particle regime in the FM-1 revealed that (1) the electron thermal

conductivity $K_\perp$ is larger than particle confinement time by a factor of 3-7, and (2) $K_\perp$ has a dependence on T_e and shear, while it is similar to the particle diffusion coefficient $D_\perp$. The scaling of $K_\perp$ can be written as $K_\perp n_e^o (L_s/a)(T/16B)$ for the electron trapped particle regime. The energy confinement time of tokamaks for the electron trapped regime is estimated for (1) a large circular torus and (2) noncircular cross sections.

*Presented at the *Sixteenth Annual Meeting of the American Physical Society*, (Albuquerque, N. M., 1974)

IB 14. Fluctuations Associated with the Anomalous Electron Thermal Conductivity in the FM-1,* by S. Ejima and M. Okabayashi.

As reported previously electron thermal conductivity experiments were carried out by utilizing localized heating at the upper hybrid resonance. The electron thermal conductivity was found to be anomalous. Suspecting that low frequency fluctuations were responsible for the anomalous electron thermal conductivity, characteristics of the fluctuations were investigated. The experimental conditions and results are the following: (1) the electron temperature gradient parallel to density gradient ($n = d \ln T_e / d \ln a_n > 0$), (2) $\nu_e/\omega_{be} \sim 1 - 10$, $\nu_e/\omega_{bi} \sim 1$, $\nu_e/\omega_{*e} \sim 1 \sim 10$, (3) fluctuations were maximum at $dT_e/dx|_{max}$, (4) the observed frequency was $(0.3 \sim 1)\ \omega_{*e}$ (5)the ratio of K and D was 3-7. These results consistently suggest that the electron trapped particle mode is responsible for the anomalous energy loss.

*Presented at the *Sixteenth Annual Meeting of the American Physical Society*, (Albuquerque, N. M., 1974)

IB 15. MATT-1023 Vertical Stability of Elongated Tokamaks, by M. Okabayashi and G. Sheffield

The vertical stability of an elongated tokamak plasma with infinite conductivity is numerically investigated under simple assumptions, in toroidal co-ordinates. The rectangular configuration is stable for an elongation ratio of less than $3 \sim 4$, depending upon the current profile. It is shown that the stabilization at high elongation ratio is related to the rotational-transform constraint.

C. The Adiabatic Toroidal Compressor (ATC)

1. Introduction

Experiments carried out and reported previously have established that the precompression plasmas produced in ATC are fairly typical of tokamaks and that the adiabatic compression works according to the predicted scaling. Table I, (see pg 48) shows a summary of characteristics of ATC hydrogen and deuterium plasma. Such plasmas are suitable for investigation of heating techniques, and testing of new techniques of measurement and operation.

The principal efforts in 1974 were the extension of the neutral injection heating power to ~ 100 kW and preparation for experiments at the level of ~ 200 kW. In addition to presenting a summary of the experiments involving injection of fast neutral atoms, the following sections are concerned with: 1) observations of soft x-rays similar to the ST results, 2) experiments on stabilization of m = 2 kink-like oscillations, 3) conservation of poloidal flux during compression, 4) bolometric measurement of power lost by charge-exchange and radiation, 5) modification of the vacuum chamber wall by gettering with titanium injection of impurities as a method of determining transport of impurities, and 6) the attempted use of an oscillating rf magnetic field to clamp the energy of fast ions.

2. Neutral Injection Experiments

We have modified our two Lawrence Berkeley Laboratory ion sources by installing curved extraction grids that provide a one-dimensional beam focus at 2 meters. For our rectangular beam ports, this allows considerable improvement in injected power. We have thus extended the earlier 60 kW input power results to 100 kW, producing the ion temperature rise shown in Fig. 1. It is worth noting that, as we have proceeded to higher input beam power, a density increase related to beam energy has been observed, and that the density rise is more pronounced with injection opposite to the plasma current than with injection parallel to the current. This seems reasonable, in view of the fact that antiparallel injection does result in a larger fraction of beam power impinging on the walls, due to somewhat poorer confinement of the injected hot ions. The results of Fig. 1 were obtained under conditions in which the electron density rise during the time of injection is 15%, two-thirds of which is from the beam opposing the current and one-third from the parallel beam. We find the heating efficiency for the beams

injected antiparallel to the plasma current to be only 70-80% of that for parallel injection.

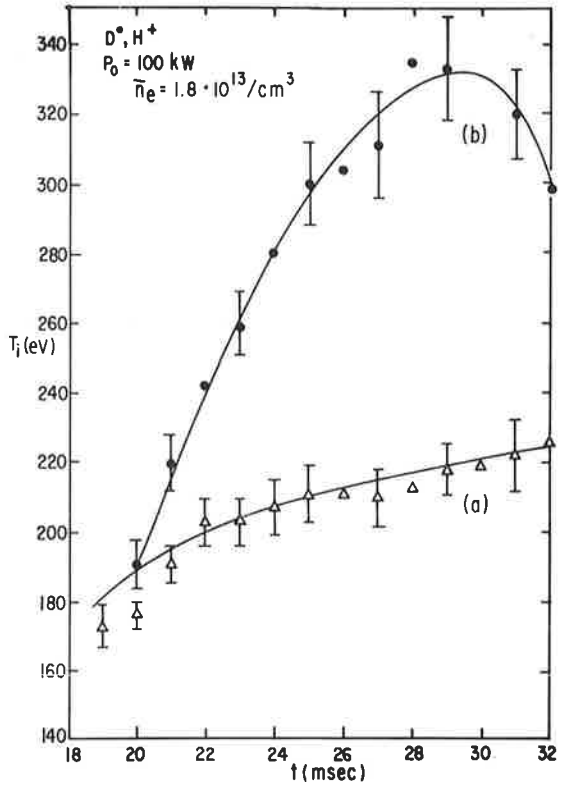

743578

Fig. 1. Ion temperature versus time for (a) no beam, but with source valves open, and (b) two beams at captured power of 100 kW. Beam is on for 20 msec < t < 30 msec.

The ratio of energetic-ion pressure to plasma pressure is typically ≈ 0.25, and the corresponding poloidal field β-values are ≈ 0.06. These numbers are similar to those of a DT-reactor alpha-particle population. The present plasma ion heating rate of ≈ 25 keV/sec would also be appropriate for neutral-beam heating to ignition or subsequent alpha-particle heating in an appropriately larger device with $\tau_{Ei} \sim 1$ sec. It is most encouraging that in spite of the pronounced anisotropy of the injected population (i.e., $v_{\parallel} > v_{\perp}$), the behavior of the fast ions appears to be entirely classical. We find that fast H^+ ions lose energy more rapidly than D^+ ions, as expected; moreover, both H^+ and D^+ lose energy more rapidly when injected against the toroidal electric field than when injected parallel to it. The electric field manifests itself clearly in the decay of neutron production, for D^o injected into D^+ plasma, following beam turn-off. For parallel injection the neutron decay times are 3-4 msec. Both decay times are accounted for by the observed fast-ion energy loss-rate. The most important point of these data on fast-ion deceleration is that no evidence of anomalous energy loss has yet been observed. This result is of particular importance to the feasibility of the "two-component reactor" approach.

With an ion source obtained from Oak Ridge National Laboratory we have extended the measurements of fast-ion slowing-down rates and neutron production, both parallel and antiparallel to the electric field, to 25 keV. Again, the results appear classical.

We have used a single beam source to inject into ATC at 83^{o} and 97^{o} relative to the plasma current, i.e., a fixed beam line 7^{o} off the perpendicular for both directions of the plasma current. In this geometry the fraction of the neutral beam input which is captured by the plasma is reduced relative to tangential injection, as is that portion of the captured beam which is initially on confined orbits. For injection at 83^{o}, taking into account the beam composition at full, one-half and one-third energies, we calculate that 56% of the neutral beam power is captured on initially confined orbits including the effects of initial ionization and of initial drift orbits. This compares with about 80% for tangential injection. As we observe an ion temperature rise in Fig. 1 of ~ 1 eV/kW, we would, on the basis of capture efficiency coupled with the neutral beam power of 70 kW, expect a 40 eV ion temperature rise. In Fig. 2, we see an ion temperature rise of only 20 eV. We take this to imply that the ease scattering into the loss cone halves has the heating effectiveness of the neutral beam.

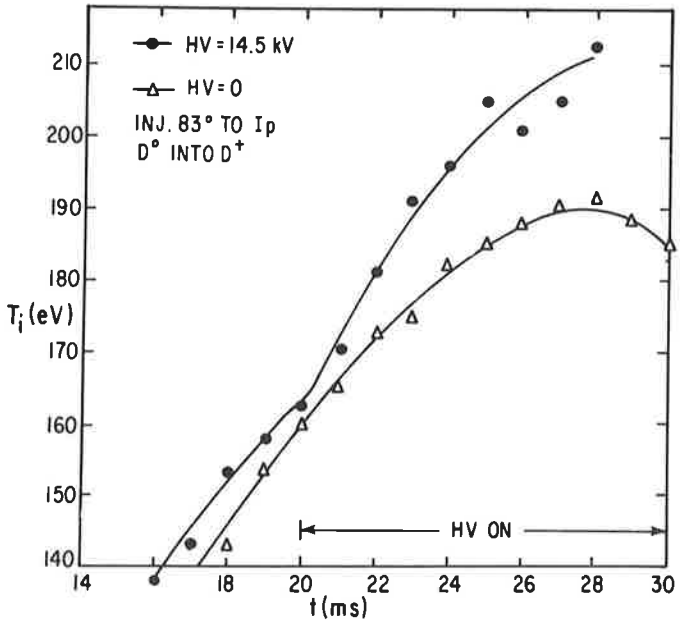

743973

Fig. 2. Ion temperature increase due to beam injection at 83° to the plasma current. The effective beam power input is ~ 20 kW.

For injection at 97% relative to the plasma current, the heating efficiency is considerably reduced due both to bad initial orbits and to the proximity of the "loss-region" at the boundary between trapped and counter-circulating particles. Following the procedure discussed above for 83° injection, we calculate, for 97°, the fraction of neutral beam power on initially confined orbits to be 27%. The neutral beam power of 70 kW and capture efficiency of 27% thus yields 19 kW input to the plasma. Under these conditions we measured a barely detectable change ($\Delta T_i \leq 5$ eV) in T_i as shown in Fig. 3. Thus it would appear that the loss region has removed at least three-quarters of the energy which would, otherwise, have flowed into the ions.

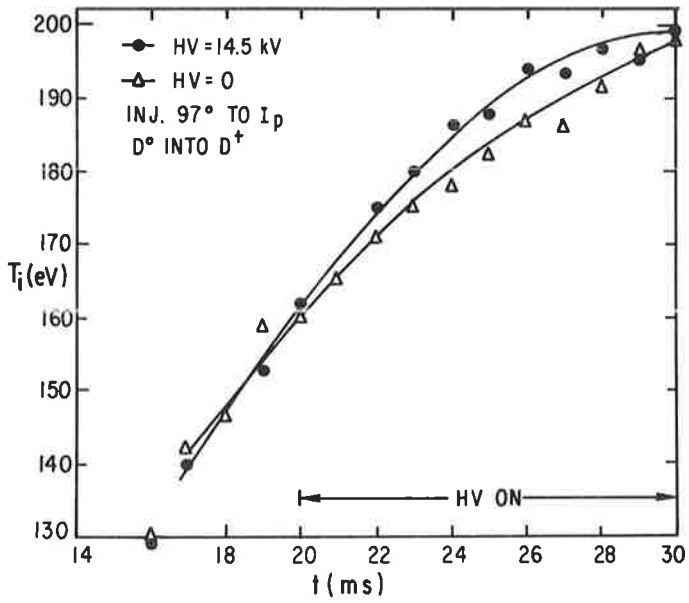

743974

Fig. 3. Ion temperature versus time for injection at 97° to the plasma current. Poor initial orbits and the proximity of the loss region at ~ 120° has reduced ΔT_i to $\leq$ 5 eV.

Even under these conditions of somewhat more unfavorable velocity distribution for the fast ions ($v_\perp / v_\parallel >> 1$) we have not observed any beam-related instabilities. The rather poor heating efficiency is, of course, a direct consequence of our low poloidal field, coupled with the short scattering times for these $Z \simeq 5$ plasmas. Since the hot-ion drift excursions are, for fixed particle momentum, inversely proportional to plasma current, there is good reason to think that near-perpendicular injection will, for larger plasma current, approach the efficiency for heating attainable with parallel injection.

3. Soft X-Ray Measurements

Soft x-ray measurements have been used at ATC to obtain information near the magnetic axis. Either two fixed photo-multiplier and scintillator systems or two movable silicon surface barrier detectors looking through a common horizontal slot were used. The latter system provided spatial resolution better than 2 cm and temporal resolution better than 0.1 msec. As has been observed on ST, during discharges of moderate limiter q without large $m = 2$ "kink" oscillations, the soft x-ray signal has a triangular modulation with an amplitude of about 10% of the total signal and a typical period of 0.5 msec. This triangular or sawtooth oscillation is associated with an $m = 1$ oscillation which grows to a maximum at the time of an abrupt decrease of the detected signal when viewed along a chord through the magnetic axis. The shape of the modulation is very sensitive to the position of the detector and is interpreted to depend upon the relation between the viewed chord and the $q = 1$ surface.

For discharges with sawtooth oscillations, the central electron temperature changes its rate of rise near the time when these oscillations appear. When the limiter q is increased so that sawtooth oscillations are absent, the central temperature rises more smoothly with time. A comparison of the center electron temperature obtained from Thomson scattering and of the x-ray signal is shown in Fig. 4. We speculate that the sawtooth oscillations result in an enhanced energy transport near the magnetic axis which slows the rate of rise of T_e (0).

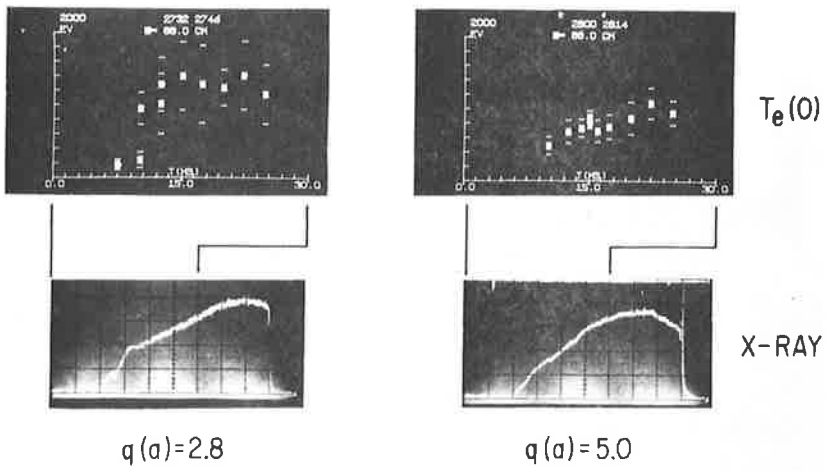

753252

Fig. 4. A sharp change in the slope of the x-ray detector signal at 15 msec occurs at moderate limiter q and is associated with a subsequent saturation of the central electron temperature and with the appearance of relaxation oscillations.

The injection of 65 kW of 15 keV D^o in a direction opposite the plasma current had a pronounced effect on the sawtooth oscillations as shown in Fig. 5. In these eight photographs, two detectors were moved symmetrically up and down from the midplane by the amounts shown in the left and right columns for observations 10 msec after the start of neutral injection and for observations without neutral injection, respectively. Note the clear out-of-phase oscillations of approximately 15 kHz frequency in several pairs of detector signals. The period increased from 500 msec to 800 msec and the amplitude of the modulation increased when a neutral beam was injected. Furthermore, the shape of the modulation as a function of viewed chord changed in a manner which is interpreted as an outward shift of the q = 1 surface, due to neutral injection, by about 1 cm. Such a pronounced shift was not observed for co-injection with similar injection power.

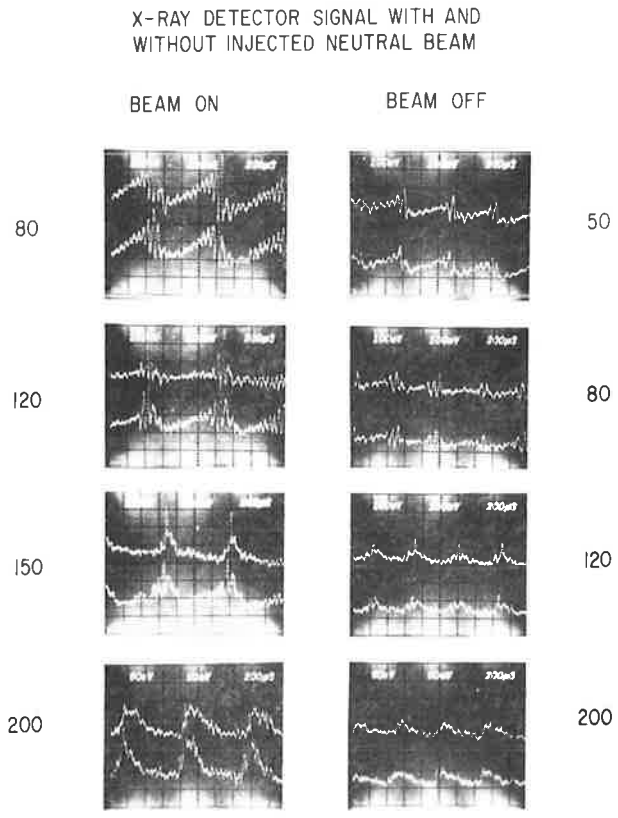

Fig. 5. X-ray detector output filtered to remove the slow increase during a discharge. Different viewed chords are needed to observe similar patterns with and without neutral injection, and this is interpreted as an outward shift of the q = 1 surface caused by neutral injection. The numbers at the right and left of the figure are vertical coordinates such that 100 corresponds to viewing chords 3 cm above and below the center of the discharge.

4. Toroidal Rotation

An indirect way of obtaining the axial velocity of a plasma into which an energetic ion beam has been injected, is to measure the Doppler shift of the low-frequency fluid modes that are easily made to occur in tokamaks (and discussed in detail in Sec. 5). The $m = 2$, $n = 1$ mode can be observed with magnetic loops outside the plasma and also by means of the coherent fluctuations in other quantities, such as the x-ray emission. X-ray signals also allow detection of the $m = 1$, $n = 1$ mode near the axis, a mode which is not readily detectable outside the plasma. X-ray measurements of the $m = 1$, $n = 1$ mode were subject to large scatter, mostly because the frequency before injection was poorly defined. For the $m = 2$, $n = 1$ mode the x-rays and magnetic fluctuations were completely synchronous. The results following below were obtained for a hydrogen plasma of mean density 1.5×10^{13}/cm, into which was injected a deuterium beam of at least 4 A at 15 kV:

Co-injection: Δf ($m = 1$; x-ray) $= - 1.6 \pm 0.7$ kHz

Δf ($m = 2$; B_θ, x-ray) $= - 1.5 \pm 0.6$

Counter-injection: Δf ($m = 1$; x-ray) $= 1.5 \pm 3.8$

Δf ($m = 2$; B_θ) $= + 0.4 \pm 0.6$.

Thus there seems to be a small profile effect which lowers the $m = 2$ frequency by about half a kilohertz, which is somewhat less than 10% of the unperturbed frequency of 6-7 kHz. The effect of injection is a mean frequency shift ($m = 2$ only) of $\langle \Delta f \rangle = 0.95 \pm 0.4$ kHz, which amounts to a toroidal rotation velocity of $\bar{v}_\phi = 5.4 \times 10^5$ cm/sec, or only a few percent of the sound velocity. (The x-ray measurement of the $m = 1$ mode averages to 1.5 ± 1.9 kHz, qualitatively similar, despite the large scatter.)

If the measurement is indeed valid, that is, if the change in poloidal rotation was about the same for both modes of injection, then it cannot be explained either on the basis of charge-exchange or ion trapping in the toroidal field ripple. Defining a momentum confinement time $\tau_M = (NeM\,\bar{v}_\phi)/(I_B M_B v_B)$, where the numerator refers to the plasma and the denominator to the beam, we find $\tau_M \simeq 0.1$ msec, which is more than an order of magnitude less than the charge-exchange time. As to the second mechanism, the field ripple is too small (< 0.3% at edge) and the ion collision frequency too high relative to that permitted by the theory (by a factor of 50) for it to be of any account. Ignoring the collision rate limit, one still

finds a limiting drift velocity in excess of the sound speed, far above that actually observed. Thus the absence of significant toroidal rotation remains an anomalous situation.

5. MHD Behavior and Experiments with m = 2 Mode

a. MHD Behavior. Poloidal magnetic field perturbations have been observed on ATC and are qualitatively similar to those observed on other devices. The slowly changing, oscillating kink-like modes have structures of the form

$$A_{mn} \exp [i(m\theta - n\phi - \omega_{mn}t)]$$

where θ and ϕ are the poloidal and toroidal angles, respectively, m and n are integers, and ω_{mn} is the angular frequency of the m, n mode. Perturbations with m = 2,3,4 and n = 1 have been observed with frequencies in the range 5-25 kHz, the m number being determined with an array of poloidal field pickup coils spaced 30° apart in the poloidal direction on the other 180° of the ATC, and the n number with 4 coils spaced 90° apart in the toroidal direction.

In general, the theoretical prediction is that, as the current is raised, a mode may first appear when the rotational transform near the magnetic axis resonates with the mode; i.e., $2\pi/\iota = m$. When the resonant surface moves out to large enough radius, the mode becomes stable, the precise limit depending on the current profile, although for any profile the m = 2 is unstable out to larger radii than the m = 3. Our findings are that the theory accommodates the m = 2 reasonably well, but that the m = 3 can still occur when the resonant surface is beyond the theoretical limit.

b. Experiments with the m = 2 Mode. It is, in general, possible to pass rapidly through the current range in which modes with m > 2 are unstable, and it is presently unclear that these modes have much effect on plasma transport. The m = 2 mode, on the other hand, even when it does not lead to the disruptive instability, still has a deleterious effect on plasma confinement, and its stabilization or avoidance must be an important goal of tokamak research. Operation at currents above the unstable range may be a possibility, but it has received only brief attention on ATC. Another approach, stabilization of the mode, has been attempted with feedback and pulsed fields.

(1) Feedback Experiments.

Figure 6 shows one arrangement of control loops and magnetic pickup coils. The control loops generated a poloidal magnetic field having m = 2 n = ± 1 symmetry, and unavoidable higher harmonics. However, the results were insensitive to the details of control loop arrangement: essentially the same results were obtained using only the two outermost control loops, and again with two pairs of loops outside the vacuum vessel that subtended approximately 35° each in major azimuth. The pickup coils were located on the midplane and oriented to minimize their mutual inductance to the control loops; opposite coils were connected in pairs, in order to cancel the main (n = 0) poloidal fields, as well as the m = 4, n = 2 harmonic that may accompany the m = 2. The signals from two such pairs, 90° apart in major azimuth, were added in suitable proportion to obtain a signal shifted by an arbitrary amount from a reference phase tied to the mode. After going through a series of phase and amplitude compensation circuits, the signal was fed to a half-megawatt amplifier, transformer-coupled to the control loops.

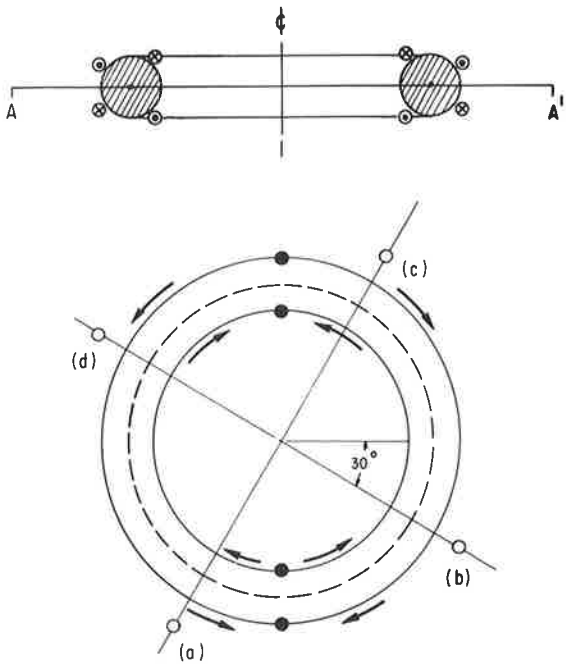

743736

Fig. 6. Diagram of control loops and mode sensors.

For a linear system described by a dispersion equation with well separated zeros, it is easy to see that with weak (low gain) feedback the perturbed zeros execute circular paths about the original ones when the loop phase shift is varied from 0 to 2π. The radius of the circle is proportional to the gain. This is roughly the effect that was observed, as shown in Fig. 7, although the mode was certainly not in the linear regime but, in fact, nearly saturated.

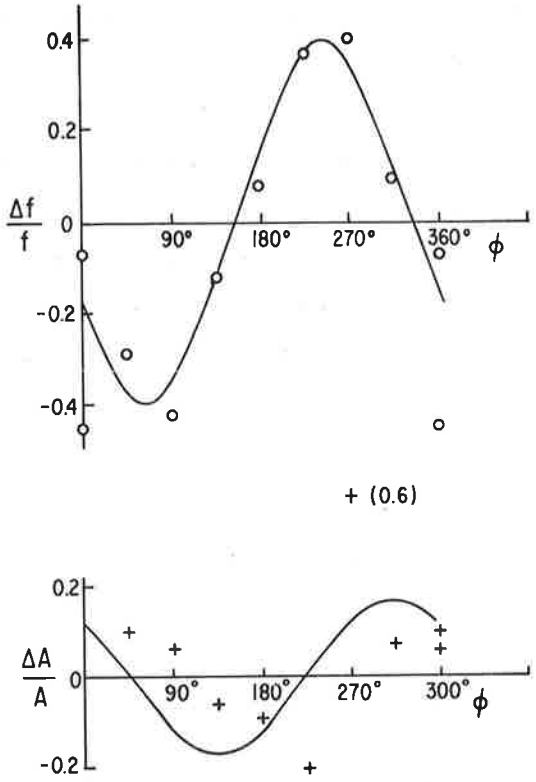

743724

Fig. 7. Mode frequency and amplitude changes as a function of feedback loop phase shift. Curves are least square fit of sinusoids to data.

Apart from the practical difficulty of attaining sufficient isolation between pickup coils and control loops, it is clear that sensing the mode by the magnetic disturbance produced outside the plasma is in any case unsatisfactory. The mode may be harmless to the plasma in its earliest stages, but amplifier economy certainly demands that it be kept to the lowest possible level. It is possible that x-ray measurements may detect the instability at a sufficiently low level so as to be useful as control signal, provided the present feedback results hold at higher loop gain.

(2) Mode-locking.

To obtain the mode-locking results, the feedback loop was opened and the amplifier driven from a signal generator. In general, a control field of about half the mode amplitude at the plasma surface secures locking; however, the threshold is not sharply defined; the mode may jump in and out of synchronism before locking to the control signal, and is locked more easily when saturated than when still growing.

Whereas the threshold shows little frequency dependence, Fig. 8 shows the phase between mode and control signal to vary markedly with frequency. The phases have been corrected for the presence of the vacuum vessel, and, in addition, the phase of the pickup coils located near the control field nodes has been shifted by 90° to make it correspond to the coils near the antinodes. Thus the divergence of the points at low frequencies implies that the locked mode is no longer a single rotating wave; a difference in amplitudes observed at the two locations shows that a standing wave component is generated which becomes dominant at frequencies below ~ 0.2 f_{mode}, the larger amplitude occurring at the control field antinodes. (Note that the pickup coils should not couple to the equilibrium distortions of the magnetic surfaces produced by the control fields.)

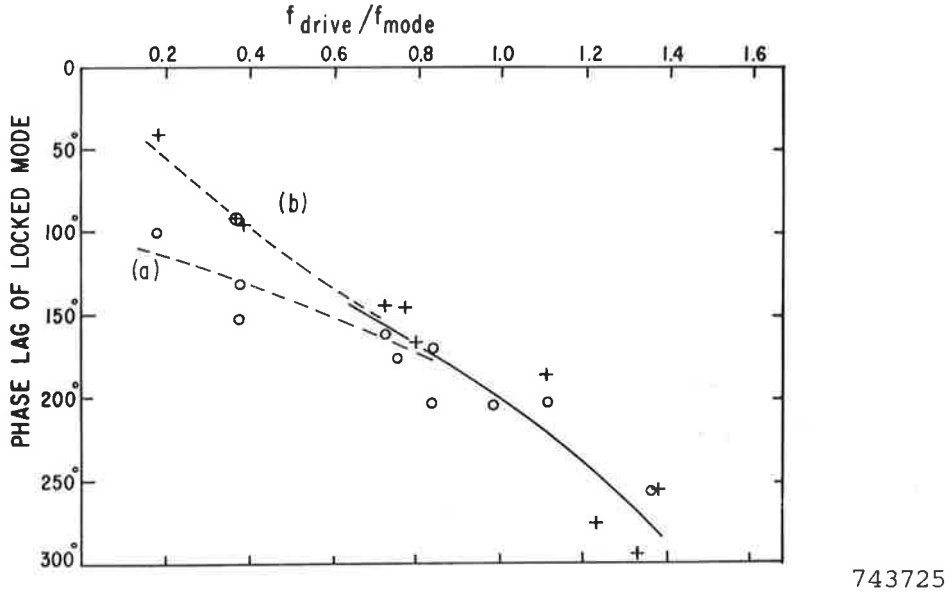

Fig. 8. Phase difference between locked mode and control field versus control frequency. (a) Phase at anti-mode; (b) phase at node +90°.

It is interesting that when mode-locking occurs, it apparently takes place throughout the plasma within a fraction of a cycle, according to the signals obtained from the pickup coils and from x-ray detectors monitoring emission from the plasma core. Presumably, then, the effect propagates through the plasma on the hydromagnetic time scale; skin penetration times would be orders of magnitude longer. The implication of this result would seem to be that the saturated m = 2 oscillations do indeed result from a rotating quasi-stable helical equilibrium, and that the shear-free rotation around the minor axis is due to an appropriately varying radial electric field which compensates for the variation of the electron diamagnetic drift frequency with radius.

(3) Mode-locking and stabilization by pulsed fields.

The most usual result of passing a current pulse of sufficient strength through control loops generating an m = 2, n = 1 magnetic field component is mode-locking at zero frequency. This is shown in Fig. 9, where the mode amplitude is still small when rotation is stopped, but where the mode appears fully saturated when rotation is resumed. The phase of the stationary mode with respect to the applied field is difficult to determine precisely, because transient perturbations accompany and obscure the locking phenomenon. In general, it appears that the field of the locked mode may lag the control field by any phase angle from 180°-360°. It is not clear how this result should be related to the measurements shown in Fig. 6. It may be noted that the pulsed experiments were done with the external loops because the internal ones could not withstand the electromechanical forces.

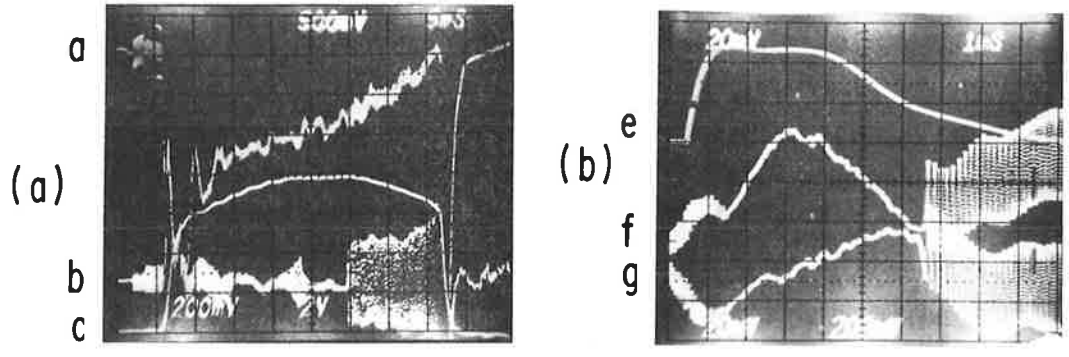

743723

Fig. 9. Suppression of mode rotation by control pulse.

Discharges tend to be unfavorably affected when mode rotation is suppressed: in high-current discharges, which are limited by the disruptive instability, onset of the disruption occurs earlier, on the average, when rotation is suppressed; when the control field is raised above the level needed to stop rotation, small-scale disruptions occur with increasing frequency. Furthermore, plasma density, which ordinarily rises more slowly -- if at all -- when an m = 2 kink is present then when it is not, frequently dropped by ~ 10% during the 5-10 msec that rotation was suppressed in typical cases.

Under certain conditions it appears that the mode can indeed be stabilized by the control field. Thus, Fig. 10 shows a case in which the rotation persists, but the amplitude slowly decreases to the noise level over some tens of cycles. We believe that one of the preconditions for this effect is that the mode is only weakly unstable.

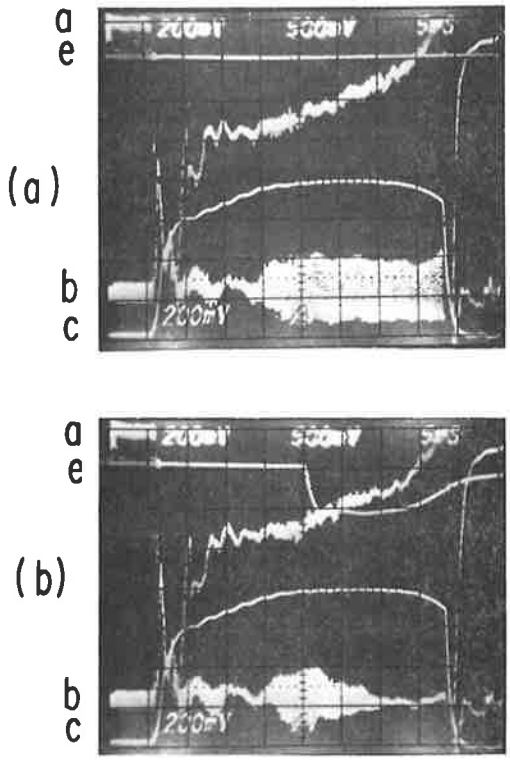

743721

Fig. 10. Mode stabilization by control pulse. 10-a: Zero control field (e). 10-b: With control field, 200 A/cm.

6. Conservation of Poloidal Flux

If the ATC plasma were perfectly conducting, the toroidal and poloidal magnetic fluxes linked by it would be constant during a compression, the one forcing the minor radius a(R) to vary as $R^{1/2}$, and the other plasma current approximately as R^{-1}. More precisely, invariance of the rotational transform inside the plasma would force the toroidal volume current to scale as R^{-1}, and constancy of the poloidal flux outside the plasma ring might require the induction of positive or negative surface currents. Current distributions are not readily measured, of course, and experimental evidence for the existence of surface currents after compression does not go beyond the observation that the actual current may differ by as much as 20% from the ideal volume current. What can be measured, however, is the poloidal flux linked by the plasma, which is, after all, the primary quantity. To be sure, in an actual compression lasting some milliseconds, the poloidal flux cannot be exactly constant since the outer layers of the plasma are resistive on that time-scale, and variations of up to 10% in the flux are indeed observed. Thus the real question is whether the departures from flux conservation are consistent with the normal rate of flux diffusion in a resistive medium, or whether some more radical mechanism is required. From the analysis of a series of poloidal flux measurements it appears that the normal skin effect offers an adequate explanation for the observations.

The model in terms of which the results were interpreted is the following: perfect plasma conductivity out to r = c, resistive plasma for c < r < a, non-conducting medium for r > a. The radius a is the adiabatically varying radius $a = a_o(R/R_o)^{1/2}$, and also corresponds to the radius of the aperture. After an infinitely rapid compression a surface current I_s initially flows at r = a, and then diffuses into r = c. The poloidal flux function ψ_s associated with the surface current is unvarying in the central core, so at $t = \infty$ the drop in the flux at r = a with respect to its initial value is

$$\Delta\psi_s = 4\pi R I_s(c) \ln a/c \quad . \qquad (1)$$

Experimentally I_s is found by comparing the actual current with the calculated volume current: $I_s = I - (R_o/R)\, I_o$, and $\Delta\psi_s$ is the difference in total poloidal flux linked by the uncompressed and compressed plasmas, corrected by the flux loss due to the decay of the total current. The latter is taken to

be the flux change $\Delta\psi$ that is measured when $I_s = 0$. The test consists of seeing whether the values of c given by Eq. (1) are reasonable in that they correspond to the radius of the 100-200 eV isotherm. Plasma conductivity at that temperature is high enough so that within the compression time very little diffusion of flux to smaller radii should take place.

The flux linking the uncompressed plasma was measured with a toroidal loop about 5 cm from the plasma surface, and that linking the compressed plasma by a loop at R ≅ 39 cm and Z ≅ 13 cm. In both cases the correction for the leakage flux between loop and plasma was about 15% of the total. The results of a series of measurements on a 65-70 kA plasma are given in Fig. 11,

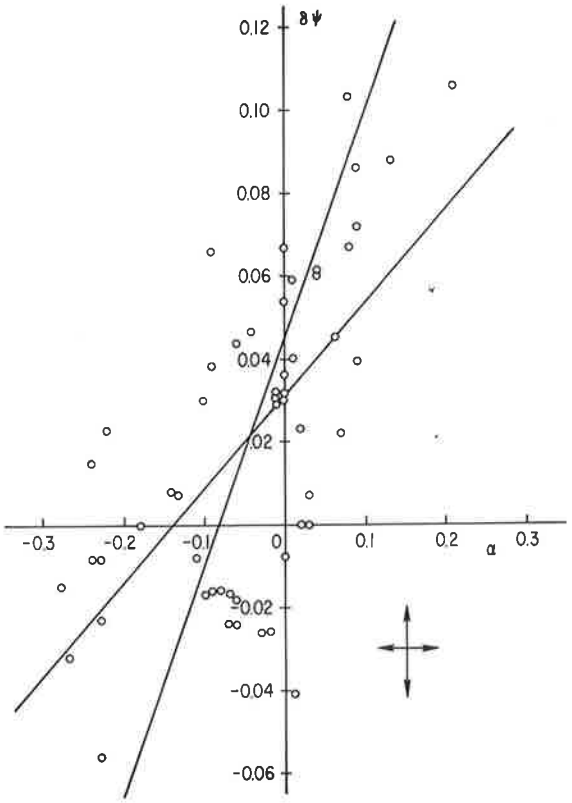

753233

Fig. 11. Normalized differences between pre- and post- compression flux linkages plotted against normalized surface current.

which shows the difference between pre- and post-compression flux-linkages plotted against surface current, both suitable normalized:

$$\delta\psi \equiv \frac{\Delta\psi}{\psi_o} = \frac{\psi(a_o) - \psi(a, t = 2.5 \text{ msec})}{4\pi R_o I_o \left[\ln (8R_o/a_o) - 2\right]}$$

$$\alpha \equiv \frac{I_s}{I_{vol}} = \frac{I_{total} - I_{vol}}{I_{vol}} = \frac{IR}{I_o R_o} - 1 \quad . \qquad (2)$$

The subscript zero refers to precompression values. The variation in α is generated by changing the sign and strength of the OH field at the time of compression (the OH field is not excluded from the space occupied by the compressed plasma).

Most of the data scatter is not random, but we do not know how much comes from systematic errors that are functions of plasma position, and how much from variations in the discharge. No laser measurements were made during this series of measurements. Still, it is clear from inspection of the data (and substantiated by the linear regression lines plotted in Fig. 11) that $\delta\Psi$ increases with α, and that an approximate relation between them can be extracted from the data:

$$\delta\Psi \simeq 0.35 + 0.3\,\alpha \quad . \tag{3}$$

The intercept ($\alpha = 0$) gives a current decay time of $2.5/0.035 = 70$ msec, which agrees qualitatively with a value of 55 msec obtained by extrapolating from the known precompression conditions. Inserting the value of the slope of $\delta\psi(\alpha)$ into Eq. (1) we find $\ln a/x \simeq 0.5$ or $c \simeq 6.5$ cm. Radii of 5-6 cm for the hot core of the compressed plasma in ATC are completely consistent with laser profiles obtained on other occasions, so that we conclude that the flux measurements require no anomalous skin effect for their interpretation.

Proving that no anomalous effects occur is, of course, a different matter, which would require detailed measurements of the flux function of a kind that are not likely to be possible anytime soon. So far as the present data is concerned, it can fit any model of skin-current relaxation which allows the distribution to be somewhat broader after a compression with positive α, and narrower after one with negative α; but there is clearly no need to invoke anomalous effects as long as the normal ones provide a satisfactory and natural explanation of the observation.

7. Bolometric Measurement of Energy Balance

Gross properties of the energy balance in ATC have been investigated in terms of the energy loss to the limiter and through the plasma surface. The energy loss associated with charged-particle diffusion and thermal conduction was monitored by measuring the temperature of the limiters. The radiation and the charge-exchange losses were detected by a bolometer devised out of a thick

film flake thermistor, which had a time resolution of ≈ 1 sec. Peak plasma currents ranged from 40 to 90 kA. Some new findings are that (1) of the 60-80% of the total energy going to the limiters, the greatest part arrives during the steady-state phase of a normal discharge, (2) at the termination of the discharge, the energy loss occurs mainly through the surface via radiation and/or charge-exchange. The amount of surface energy loss at the termination is larger than the stored plasma kinetic energy and includes a large portion of the poloidal magnetic energy for a current larger than 50 kA. In addition to the above findings, our measurement has confirmed the typical results of other tokamaks. These results are as follows:

a. The charged particle loss and the thermal conduction loss are the major mechanisms for the energy loss in our operating region of the discharge current.

b. Radiation loss constitutes less than 20% of the total energy loss before the current decays, with some evidence that the percentage rises with current.

c. Impurity contamination can greatly increase the radiation loss. This was demonstrated by injecting about 10% of neon into the hydrogen working gas, which almost doubled the radiation loss.

d. Disruptive instability also enhances the radiation loss. This was observed as the disruptive instability occurred, but not in a controlled reproducible manner.

8. Gettering Experiments

An interesting method of changing the effect of impurities in present devices was suggested by a recent observation on the ST Tokamak. Extremely unstable discharges which interacted violently with the limiter were often followed by a series of more stable discharges. The improvement seemed to be due to coating part of the torus with a layer of metal removed from the limiter. This was confirmed by flashing molybdenum onto the torus from a rod inserted into the discharge. Immediately following this treatment, discharges were observed to have a reduced level of oxygen impurity and a lower plasma resistance.

We have extended these experiments in the ATC Tokamak using a titanium getter source to deposit a more controllable, renewable metal surface. The plasma resistance is reduced. Figure 12 shows typical discharge current and loop voltage wave forms for both experiments. In each case the plasma resistance falls by 15-30% after deposition of the layer of metal. The external circuit in ST tends to maintain a constant current, while in ATC the loop voltage is relatively insensitive to the discharge parameters for a given setting of the controls. In the following paragraphs we will describe the gettering process and the experimental results in more detail.

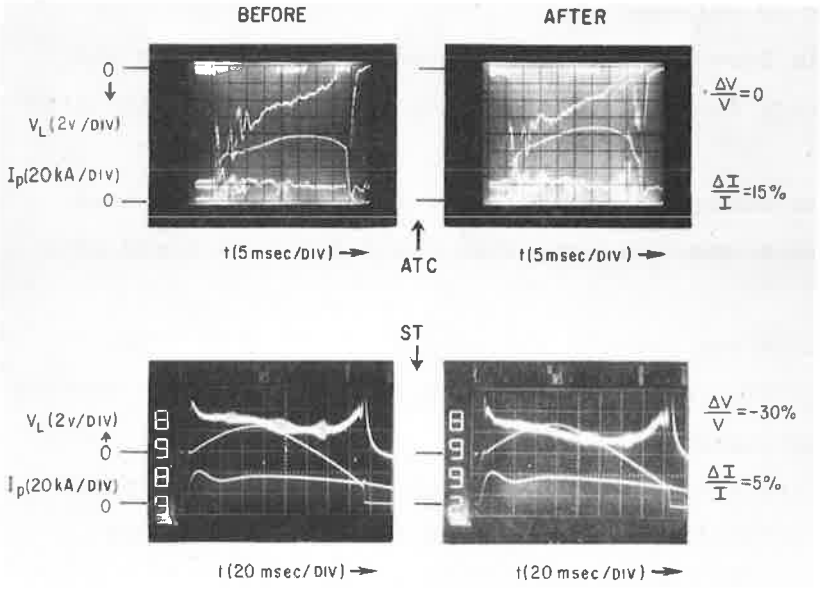

743489

Fig. 12. Typical discharge current and loop voltage wave forms in the ST and ATC Tokamaks showing the effect of depositing an active metal layer on a section of the vacuum wall.

The titanium is evaporated from a Varian Ti-ball source as shown in Fig. 13. This is a nearly spherical, hollow shell of titanium heated by radiation from an internal tungsten filament. The sublimation rate can be varied between 0.01 and 0.5 gm/hr by controlling the filament current. A single getter covers about one-fourth of the surface area of the vacuum vessel.

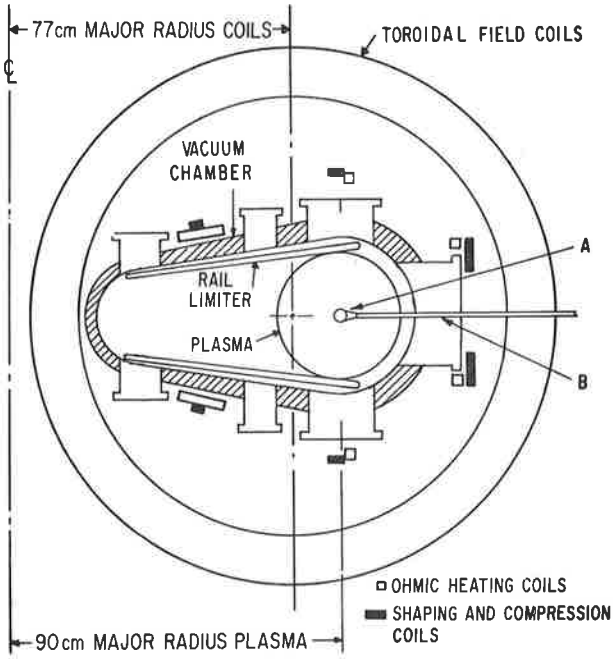

753017

Fig. 13. A cross section of ATC. The position of the getter source is shown, (a) during evaporation, (b) during the discharge.

Titanium freshly deposited on the surface of a vacuum vessel pumps certain gases by chemisorption. The getterable gases include H_2, N_2, O_2, CO_2, CO, and H_2O. In a vacuum system of similar gettering and gas-load conditions, a trapping probability of 0.025 for hydrogen was measured. At a sublimation rate of 0.25 gm/hr the pumping speed measured at ATC for a single source is 10^4 1/sec. Using the above value for the trapping probability, this indicates a gettered surface area of 8×10^3 cm^2. After the source is switched off, the surface will pump 4 Torr l (1.2×10^{20} molecules) before saturating. To avoid saturating the surface before the discharge, the torus is filled via a fast pulsed gas valve some 5-10 msec before the start of the discharge. In some experiments a second, slower pulsed valve is used to inject additional gas into the plasma. Non-gettered discharges with pulsed gas filling are identical to those usually obtained in ATC with steady gas flow. The total quantity of gas admitted to the torus is less than the saturation capacity of the gettered surface.

A large fraction of the plasma particles striking the gettered surface will be neutral atoms or ions with energies ranging from several eV up to several keV. The trapping probabilities for atomic particles on room-temperature gettered surfaces are not accurately known, but are expected to be

larger than for molecular particles. Extrapolating data measured for hydrogen ions on solid titanium surfaces indicates that the trapping probability may be close to unity. Incident particles with large momentum will presumably cause sputtering and desorption of previously trapped gas but quantitive data on these processes for thin titanium films are not available.

Without gettering, the base pressure in the torus is typically $2\text{-}3 \times 10^{-7}$ Torr. With gettering, base pressure as low as 4×10^{-8} Torr have been obtained. There has been no apparent adverse effect resulting from the titanium layers on the vacuum vessel.

Some characteristics of uncompressed ATC discharge without gettering are shown in Fig. 14a, and radial profiles of electron temperature and density, obtained with Thomson scattering, 25 msec after the start of the discharge, when a quasi-steady state has been reached are shown in Fig. 14b. The electron temperature profile is always more peaked than the density profile.

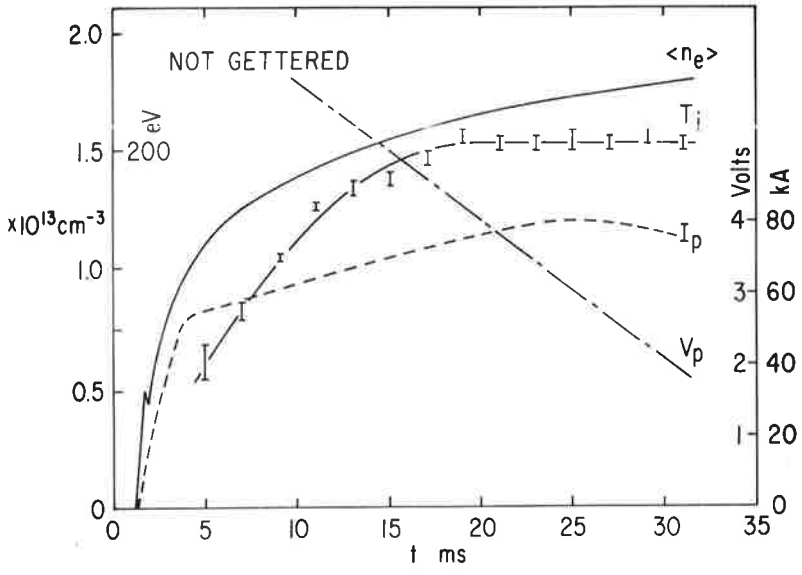

753004

Fig. 14(a). The time dependency of plasma current, I_p, loop voltage, V_p, mean line of sight density, $\langle n_e \rangle$, and central ion temperature, T_i, for a typical non-gettered discharge in hydrogen.

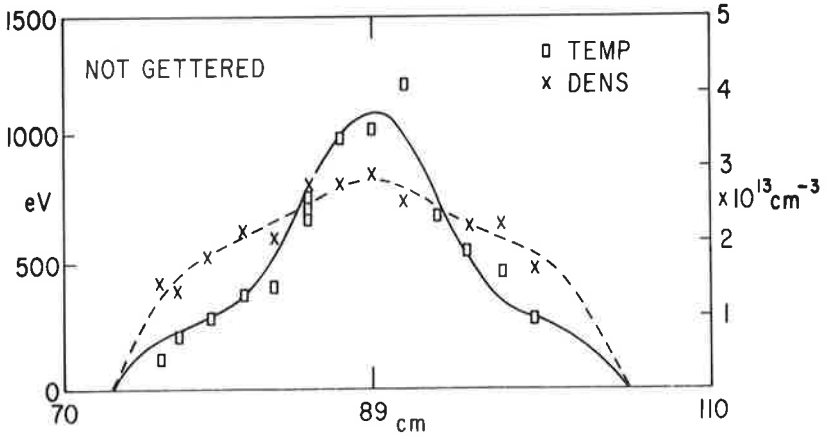

753014

Fig. 14(b). Radial profiles of the electron temperature, T_e, and density, n_e.

The measured resistance of the plasma column is typically 4 to 6 times larger than the value calculated for a Z = 1 plasma, assuming that the current density is proportional to $T_e^{3/2}$. Trapped particle effects are small ($\lesssim$ 20%) if the increased plasma resistance is assumed to be due to an enhanced collision frequency which is independent of radius and affects trapped and untrapped particles alike. With this effect of trapped particles included, the effective collision frequency implies $Z_{eff} \simeq 4\text{-}8$.

The poloidal $\beta_p \equiv 8\pi \langle n_e\ kT_e \rangle / B_\theta^2(a)$, the safety factory $q(r) \equiv rB_\phi / RB_\theta$ (r) and the electron energy confinement time $\tau_E \equiv 3/2 \langle n_e\ kT_e \rangle / V_p I_p$ can be calculated from the Thomson scattering profiles. These parameters are included in Table I, (see pg. 48). Also included, in Table II, (see pg. 49) is the parameter $\beta_p \langle n_e \rangle Z_{eff}^{1/2}$, which, for a fixed plasma current, is observed to be a constant for non-gettered discharges. We note that this parameter remains constant for the gettered discharges. This suggests that the gettering process does not introduce any new heating or loss effects, although it does extend the range of plasma parameters, in particular Z_{eff}.

Within a few minutes of switching on the getter source, there is a dramatic change in the time behavior of the plasma density, as shown in Figs. 15a and 15b.

753009

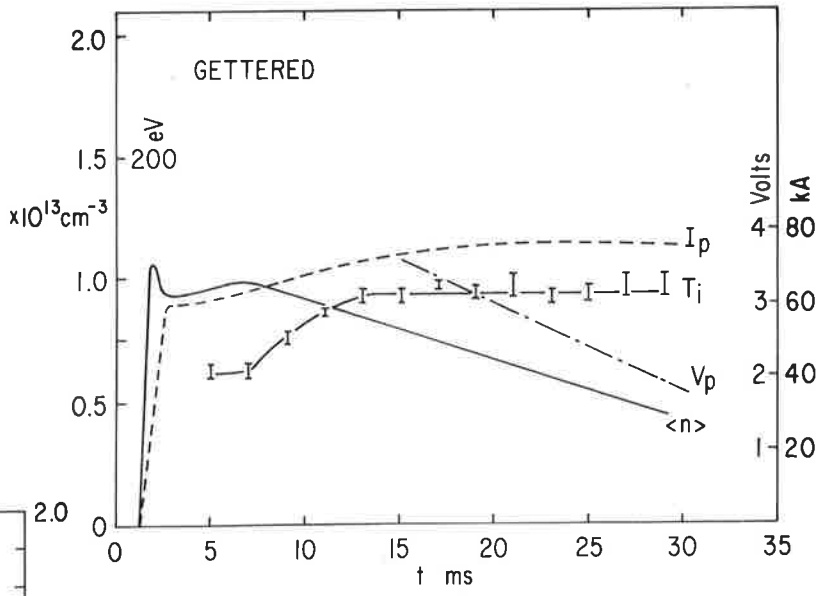

Fig. 15(a). The time dependency of plasma current, I_p, loop voltage, V_p, mean line of sight dnesity $\langle n_e \rangle$, and central ion temperature, T_i, for a typical low-density gettered discharge in hydrogen.

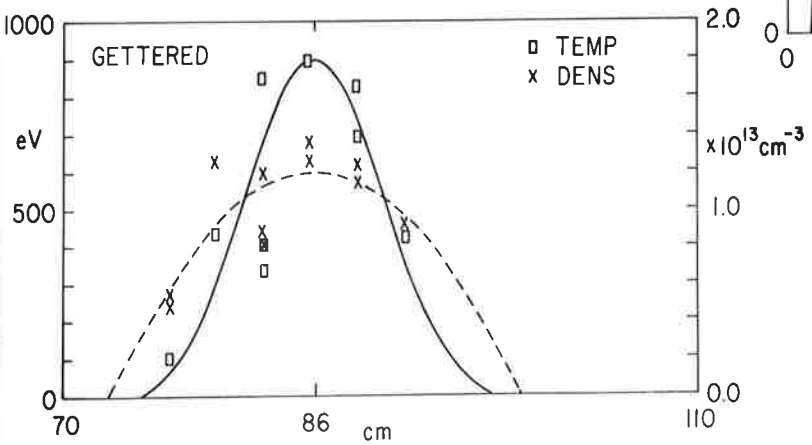

753006

Fig. 15(b). Radial profiles of the electron temperature, T_e, and density, n_e.

After the ionization of the filling gas is completed, the electron density decays with time, indicating a substantially reduced influx of neutral gas. The decay time of the plasma density can be controlled to some extent by varying the titanium evaporation rate. This suggests that a large fraction of the particles diffusing from the plasma is trapped on the gettered surface. There does not seem to be any significant release of previously absorbed gas from the gettered surface when it is exposed to the plasma.

The plasma resistance decreases by 15% and the Ohmic power input decreases by 20% for the gettered discharge. The radial profile of the electron temperature, as shown in Fig. 15b illustrates the narrower profile and lower peak temperature typical of gettered discharges. The ratio of measured plasma resistance to Spitzer resistance (Z = 1) is now 2.0, corresponding to $Z_{eff} = 1.4$. The absence of hard x-ray emission indicates that this low Z_{eff} is not due to a runaway electron current.

The gettering clearly has a dramatic effect upon both the recycling and the average ion charge. The other plasma parameters are in accord with the low density and low Z_{eff} as indicated by the unchanged scaling parameter in the final row of Table II.

To simulate the time dependence of the density associated with non-gettered discharges, we have pulsed hydrogen and other gases from a second valve into the low density gettered discharge after the ionization of the initial filling gas is completed. The time dependences and radial profiles of the usual plasma parameters are shown in Fig. 16a and b for hydrogen. Comparison with Fig. 13 shows that the average density and ion temperature are very similar. The electron temperature profile is slightly narrower, and the peak temperature is lower, for the gettered discharge. Together with lower measured resistance, this gives $Z_{eff} = 1.2$. A summary of the measured and derived parameters is given in Table II which also shows a summary for injection of other gases.

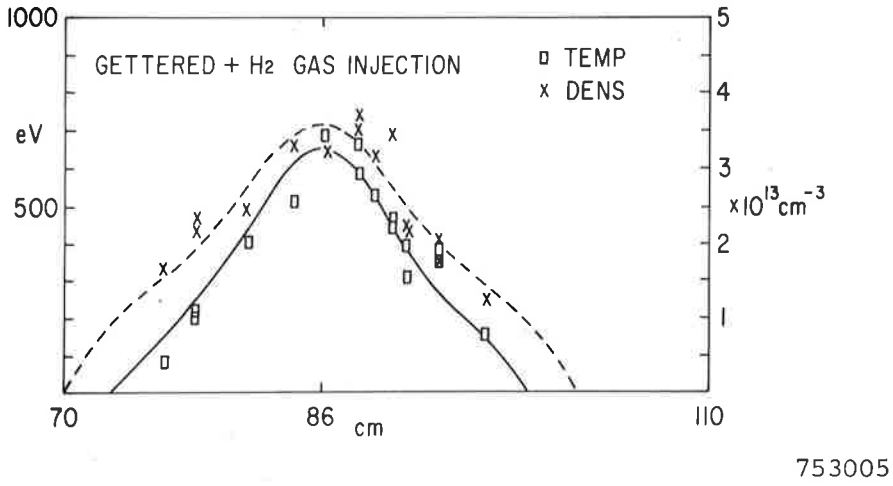

Fig. 16(a). The time dependency of plasma current, I_p, loop voltage, V_p, mean line of sight density, $\langle n_e \rangle$, and central ion temperature, T_i, for a typical gettered discharge with additional injection of hydrogen gas.

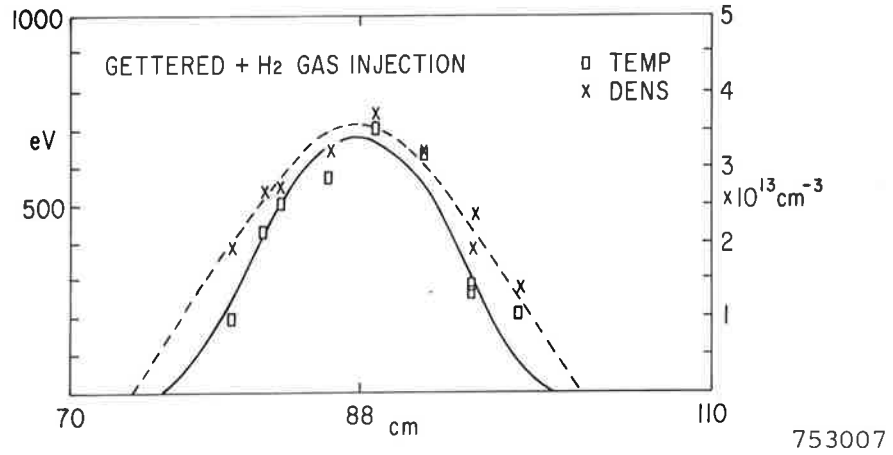

Fig. 16(b). Radial profiles of the electron temperature, T_e, and density, n_e.

For comparison of the relative impurity concentration of gettered and non-gettering discharges, the O VI (172.9 Å) and Fe XV (282.4 Å) lines were monitored. A typical time dependence of these lines for gettered and non-gettered discharges is shown in Fig. 17. The relative impurity concentrations were normalized to the values for a non-gettered discharge and are plotted in Fig. 18 against the value of Z_{eff} calculated from the measured resistance and Thomson scattering profiles. There appears to be a good agreement between

low impurity concentrations and low values of Z_{eff} for gettered discharges. We have observed a number of titanium lines including Ti XX (254.01 Å) in gettered discharges. We do not have an absolute measure of its intensity, but $Z_{eff} \approx 1.2$ places an upper limit of titanium $< 10^{10}$ cm^{-3}.

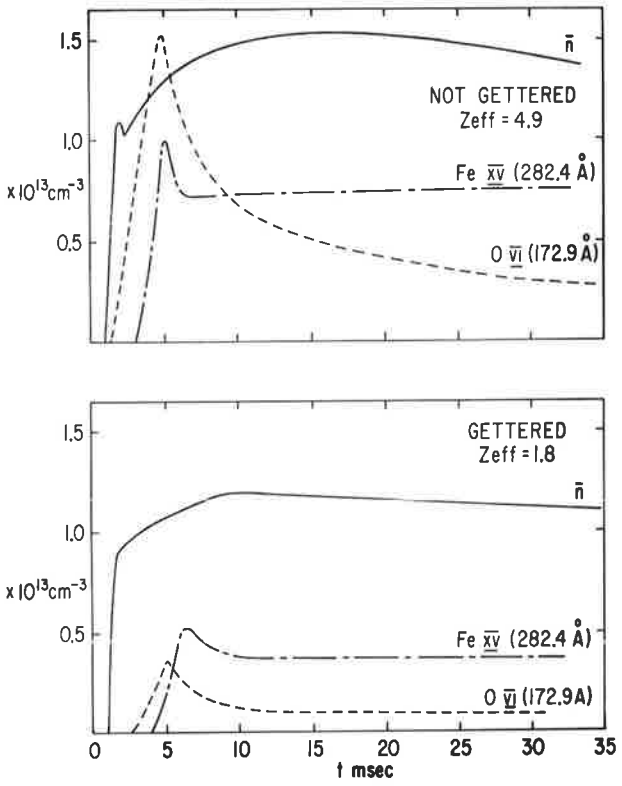

753011

Fig. 17. Time dependence of impurity lines, O VI (172.9Å) and Fe XV (282.4Å) in gettered and non-gettered discharges.

753012

Fig. 18. Relative impurity concentration measured spectroscopically and normalized to the values for a non-gettered discharge plotted against the Z_{eff} calculated from the measured plasma resistance and temperature profile.

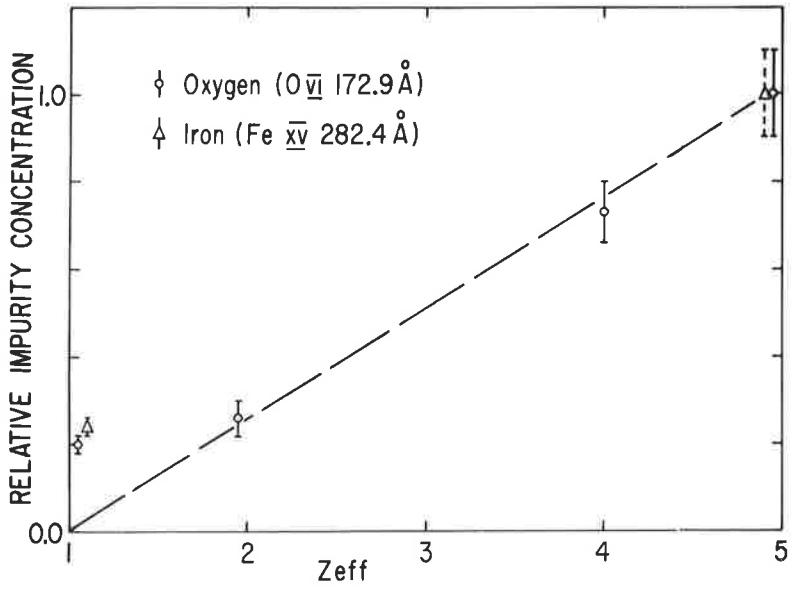

All the results described so far have involved gettering the area of the torus near the limiter. There is no indication that titanium deposition on the limiter itself is an important mechanism. We have gettered a section of torus of similar area 180^{o} away from the limiter and observe essentially the same results and the data from discharges produced in this configuration are summarized in Table II.

By means of gettering we have reduced the measured level of the natural impurities in a hydrogen plasma to give a plasma with Z_{eff} close to unity, and then increased Z_{eff} progressively to the order of 6 by injecting controlled amounts of heavy gases. These experiments help to confirm the widely held assumption that the enhanced resistivity observed in most tokamak discharges is caused by impurities. It is important to note that the low temperatures of the low Z_{eff} discharges are probably due to the lower Ohmic power input. However, in larger devices with better energy confinement, gettering may make it possible to produce high temperature low Z_{eff} discharges.

An interesting result, which is related to the behavior of surface exposed to plasmas, was obtained when discharges were produced in deuterium after long term operation in hydrogen. The relative intensity of H_{β} and D_{β} light was measured at the limiter during many discharges and is shown in Fig. 19 as a function of the number of discharges after the change to deuterium. The date of Fig. 19 are from the "plateau" which occurs after the initial peak corresponding to the ionization of the filling gas. The "plateau" is usually attributed to ionization of gas which has been recycled. The intensity of H_{β} is larger at first than that of D_{β} but after several thousand discharges the situation is reversed. This transition is accompanied by a reduction in the density increase that occurs during the discharge, similar to the reduction which occurs when the vacuum vessel is gettered, as shown in Figs. 14(a) and 15(a). It should be noted that the intensity of D_{β} light was more than an order of magnitude larger than that of H_{β} during the initial ionization peak for all of the discharges from which Fig. 19 was taken.

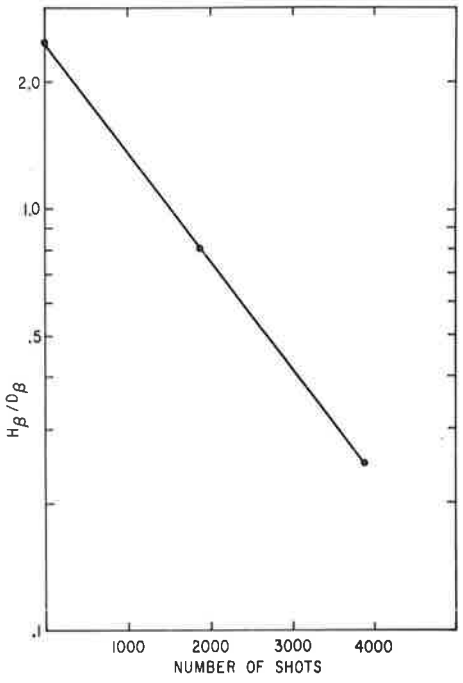

753313

Fig. 19. Ratio of H_β to D_β near limiter in deuterium discharges vs number of shots after changing from hydrogen to deuterium as filling gas.

9. Impurity Injection

In an effort to understand certain aspects of impurity behavior in tokamaks, a new impurity-injection source has been developed. In contrast with the usual pulsed-gas technique, the new injection produces a short-duration (300 μsec) burst of energetic (typically 5 eV) neutral atoms. The method consists of irradiating, with a 150 MW (1-2 J) pulsed ruby laser, a small (~ 1 mm diameter) spot on a 1-2 μm vacuum-evaporated film. The laser beam is directed through the glass onto the film, causing the film to be vaporized and ejected towards the plasma. The mean energy of the ejected atoms is sufficient to penetrate the scrape-off region in ATC.

The source has been installed on ATC using aluminum as the injected impurity. Ultraviolet radiation from the ionization states of Al V to Al XI has been observed. Within 1.5 msec of injection the average electron density increases 5%. In the quiescent ATC discharge (no large MHD oscillations present) Abel inversions of light from Al IX, Al X, and Al XI appear as shells located at successively smaller minor radii. As a function of time, the Al IX

appears first, followed by Al X and then Al XI. The spatial and temporal behavior indicates an inward diffusion of the aluminum at a rate which is roughly consistent with neo-classical diffusion. This estimate of the diffusion time of nearly shipped aluminum is much shorter than the particle containment time in ATC which has been shown to be at least 10 msec.

10. Energy Clamping

The addition to the tokamak configuration of an oscillatory transverse magnetic field, $\vec{B}_R = b\,\vec{e}_R \cos(\phi-\omega t)$, should produce heating of the bulk plasma, according to a magnetic pumping scheme proposed by Koechlin and Samain. We were interested in a somewhat different effect, which should become significant at power levels much lower than those where bulk heating would become noticeable: namely, the trapping of fast injected ions resonant by the traveling perturbation. If the trap were deep enough, so that ions would not readily be scattered out, then this would serve as an energy clamping technique that would be useful in a TCT. This scheme was tried on ATC, using the FM-1 OH Amplifier to drive 375 A at 187 kHz through the pre-ionization loops. The loops are toroidal and located symmetrically above and below the midplane, close to the outer vacuum wall; they were connected so as to provide a field of the proper symmetry. It had been thought that the available power was just enough to get a meaningful result. It was not, and subsequent measurement of both the driving field and of the actual plasma motion showed that the former was reduced a factor of 2 more than anticipated by the presence of the vacuum vessel, and that the latter was only a third (~ 0.02 mm) of what the actual field should have produced. The plasma displacement was measured with an 8 mm reflectometer. Hence it is obvious why no effect was seen on the ion energy distribution, but the reason for the discrepancy between the actual and the anticipated motion of the plasma remains unresolved.

11. Plans for 1975

The extension of neutral beam injection power levels to 500 kW and the initiation of radio frequency heating experiments at 800 and, possibly at 25 MHz are the principal experiments planned for ATC in 1975. The high power neutral injection experiment will take place during the first half of the year and radio frequency heating experiments are planned to follow.

The 800 MHz rf heating frequently referred to as lower hybrid heating, will have a power level of about 200 kW. The 25 MHz experiment, which will have a power level of 400 kW, is planned to extend the ST results to higher poloidal fields, which, in this case, means higher plasma current.

In addition to these major experiments, the investigations described in this report will be brought to completion if possible.

TABLE I. Typical ATC Parameters

	Before Compression	After Compression
Major radius R	90 cm	38 cm
Minor radius a	17 cm	10 cm
Toroidal field B_t	15 kG	46 kG
Plasma current I_p	60 kA	150 kA
Ion temperature T_i	200 eV	600 kA
Electron temperature T_e	1 keV	2 keV
Average electron density $\bar{n}_e$	1-2 x 10^{13} cm^{-3}	10^{14} cm^{-3}

TABLE II

Comparison of plasma parameters for discharges in ATC with and without gettering

	Not Gettered	Gettered near the limiter	Gettered away from limiter	Gettered + hydrogen injection	Gettered + helium injection	Gettered + neon injection
Toroidal magnetic field (kG)	15	15	15	15	15	15
Discharge current (kA)	78	76	67	78	80	78
Loop voltage (V)	3.0	2.5	2.5	2.4	2.4	2.8
Ohmic power (kW)	234	190	167	187	192	218
Plasma resistance (μΩ)	39	33	37	31	30	36
Central electron density ($\times 10^{13}$ cm^{-3})	3.3	1.0	2.5	3.5	2.5	1.8
Average electron density ($\times 10^{13}$ cm^{-3})	1.9	0.6	1.7	2.1	1.8	1.2
Central electron temperature (eV)	1100	950	750	700	830	1400
Central ion temperature (eV)	200	120	167	200	-	-
Safety factor (limiter 16 cm, R = 87 cm)	2.83	2.90	3.3	2.83	2.76	2.83
Safety factor (center)	0.45	0.38	0.45	0.46	0.71	0.50
Z_{eff}	5.4	1.4	1.5	1.2	3.2	6.0
β_p	0.26	0.04	0.13	0.14	0.21	0.19
τ_E (ms)	2.8	0.5	1.4	1.8	2.9	2.2
$\beta_p / \langle n_e \rangle Z_{eff}^{1/2}$ ($\times 10^{-15}$ cm^3)	5.9	5.6	6.2	6.1	6.5	6.5

IC 1. MATT-1092 Experiments on the Adiabatic Toroidal Compressor, by K. Bol, J. L. Cecchi, C. C. Daughney, F. DeMarco, R. A. Ellis, Jr., H. P. Eubank, H. P. Furth, H. Hsuan, E. Mazzucato and R. R. Smith

Magnetic compressional heating of a tokamak discharge has been demonstrated successfully in the Adiabatic Toroidal Compressor (ATC). In addition to these investigations of compressional heating, other basic measurements have been made on ATC recently. These measurements are of interest because the ATC incorporates an air-core transformer and dispenses with the usual copper shell, two features likely to be found on future larger devices with smaller aspect ratios. The following topics will be discussed: (1) characteristics of the uncompressed discharges in ATC, including the dependence of β_p on discharge parameters, bolometric measurements of the energy balance, measurements of the concentration of impurities; (2) MHD behavior and attempts at stabilization of the m = 2 kink-tearing mode.

IC 2. Kink-Tearing Mode Stabilization in the ATC Tokamak,* by K. Bol, H. C. S Hsuan, and R. R. Smith

A partial stabilization of the m = 2, n = 1 kink-tearing mode has been achieved by driving a set of magnetic control loops with a quasi-dc pulse (3-10 msec). The loops generate m = 2, n = ±1 perturbations of the poloidal field (plus higher harmonics), comparable in magnitude to the amplitude of the mode. Large enough control fields abruptly halt the rotation of the mode, as determined by external magnetic probes and confirmed by the simultaneous disappearance of synchronous fluctuations in the emitted x-ray intensity.[1] It appears that the mode amplitude is not reduced, and there may be an actual enhancement of such deleterious concomitants of the mode as the disruptive instability. By contrast, in a plasma only weakly unstable to the m = 2 mode, it is possible under some circumstances to reduce the amplitude to zero while the mode continues to rotate. The effect on the plasma remains under study.

---

*Bull. Am. Phys. Soc. 19, 875, Oct. 1974 - 2A7

IC 3. MATT-1087 Neutral-Beam Heating in the Adiabatic Toroidal Compressor II, by K. Bol, J. L. Cecchi, C. C. Daughney, R. A. Ellis, Jr., H. P. Eubank, H. P. Furth, R. J. Goldston, H. Hsuan, E. Mazzucato, R. R. Smith and P. E. Stott

Results are given for tangential injection into ATC of two 15 keV neutral beams with net power up to 100 kW. Fast-ion drag rates and pitch angle scattering have been measured, the latter to determine Z_{eff}. With a single source we have also injected at 83° and 97° to the plasma current. At 83° some ion heating is observed; at 97° the heating is negligible. The fast-ion energy distributions, observed tangentially, show the severity of the "loss-region" for counter-circulating particles.

IC 4. MATT-1029 Neutral Beam Heating in the Adiabatic Toroidal Compressor,(1) by K. Bol, J. L. Cecchi, C. C. Daughney, R. A. Ellis, Jr., H. P. Eubank, H. P. Furth, R. J. Goldston, H. Hsuan, R. A. Jacobsen, E. Mazzucato, R. R. Smith and T. H. Stix

Experiments have been conducted on ATC with tangential injection of two 14-15 keV, 3-4 A beams of H^0 or D^0. The ion temperature rise for both H^+ and D^+ plasmas is 70-80 eV (i.e., 35-40%), consistent with theoretical expectations for charge-exchange-limited energy transport at neutral atom densities $\sim 10^9$ cm^{-3}. The injected suprathermal ion population simulates the alpha particle population of a DT reactor in respect to partial pressure (~ 10%) and plasma ion heating rate (~20 keV/sec). The injected ions are found to decelerate in agreement with classical theory.

IC 5. Radial Distributions of Impurities in ATC,* by J. L. Cecchi

The impurities in ATC are being investigated spectroscopically using the VUV grazing incidence monochromater capable of scanning the cross section of the ATC plasma. Data from the various lines scanned are Abel inverted to yield the radial distribution of the impurity light. Preliminary results have been obtained for O and Fe. The time evolution of the radial distributions for OVI and Fe XV show the anticipated behavior of a spatially uniform phase coincident with the initial peak of the particular impurity light, followed by a shell-like distribution, which peaks at an electron temperature slightly below the ionization for the particular impurity ion.

---

* Bull. Am. Phys. Soc. 19, 853, Oct. 1974 - 1A7

1C 6. Evolution of Electron Temperature and Density in ATC, by C. C. Daughney

The evolutions of electron density and temperature for two ATC discharges are compared. The filling pressure is 10^{-5} Torr of deuterium, the toroidal field is 14 kG, the discharge current is 70 kA, and the major radius is 89 cm for both cases. The first case is typical of early ATC operation. The temperature and density on axis rise to their final values of 1.0 keV and 1.8×10^{13} cm^{-3} in only 10 msec and the radial profiles grow in a further 20 msec to absorb this central peak. The final profiles have the typical ATC dependence--$T_e = T_{eo}(1 - \rho^2)^2$ and $n_e = n_{eo}(1 - \rho^2)$ where $\rho = r/a$ and $a = 17$ cm. The second case is taken after a series of titanium gettering experiments. The discharge develops in 10 - 15 msec, with no central feature, and then remains relatively constant for the duration of the discharge. In this case the peak temperature and density are 1.0 keV and 2.4×10^{13} cm^{-3}, respectively, and the final profiles have the same radial dependences -- $T_e = T_{eo}(1-\rho^2)^2$ and $n_e = n_{eo}(1-\rho^2)^2$.

---

*Presented at *The Plasma Physics Divisional Meeting of the American Physical Society*, (Albuquerque, N. M.) October 28-31, 1974.

1C 7. Near-Perpendicular Neutral-Beam Injection into ATC,* by H. P. Eubank, R. R. Smith, R. A. Ellis and P. E. Stott

Neutral beam injection has been carried out on ATC at 83° and 97° relative to the direction of the plasma current, using a single beam source. In this geometry, the effects of the "loss-cone" existing near the boundary between trapped and counter-circulating particles[1] are very severe. This is exemplified by the absence of any detectable ion temperature increase, for 97°-injection, and by a marked reduction in energetic neutral flux relative to 83°-injection. At 83° a small ion temperature rise is observed, which is consistant with our earlier results employing tangential injection.

* Bull. Am. Phys. Soc. 19, 897, Oct. 1974 - 4A2

IC 8. Steady State Charge-Exchange Spectra in ATC Near the Injection Energy of Neutral Beam,* by R. J. Goldston and H. P. Eubank

Experimental charge-exchange spectra near injection energy for 6 ms injection of a 6-ampere beam into ATC are presented, and compared to theoretical predictions based on a solution of the linearized Fokker-Planck equation, which takes into account finite beam width, radial dependance of plasma parameters and detector sensitivity as a function of energy and plasma minor radius. Good agreement is found using Z (effective) derived from Thompson scattering and neutral density found from absolute flux measurements.

The use of a collimated neutral beam and a one-dimensional pinhole-camera charge-exchange neutral detector is discussed as a tokamak plasma diagnostic. Possible uses of the beam and detector are for measuring $T_e(r, t)$, $n_o(r, t)$ and Z (effective) (r, t). An injector ramped in time to 70 keV can be used as a poloidal field diagnostic in ATC. Extrapolations to larger machines are discussed.

* Bull. Am. Phys. Soc. 19, 897, Oct. 1974 - 4A3

IC 9. Laser Beam Production of Slow Neutrals for Plasma Diagnostics,* by E. A. Marmar, J. L. Cecchi and S. A. Cohen

A method for producing ~ 100 μsec pulses of neutral atoms in the 1 to 20 eV energy range is developed for the purpose of injecting impurities into the ATC Tokamak. One micron of a metal which has been vacuum evaporated onto a glass slide is irradiated through the glass by a pulsed ruby laser beam of 5 GW per cm^2 peak power density. This produces a pulse with up to 10^{18} neutral atoms of the metal. The energy distribution is adjustable by changing the focus or the power output of the laser or the thickness of the film. Typical energy distributions have a peak at 4 eV and a FWHH of 5 eV. Measurements of the angular distribution show that the beam intensity is very strongly peaked in the direction perpendicular to the glass slide.

This technique will be used in conjection with VUV and x-ray spectroscopy to study impurity diffusion and the effects of impurities on ion temperature, current distribution, plasma resistivity and plasma stability.

* Bull. Am. Phys. Soc. 19, 973, Oct. 1974 - 8F4

1C 10. MATT-1150 Observations of Internal Relaxation Oscillations in The Adiabatic Toroidal Compressor, by Richard R. Smith

Kink oscillations and relaxation oscillations were studied through the time dependence of the x-ray intensity integrated approximately from 1 to 10 keV and emitted along narrow lines of sight from the ATC Tokamak. Both photo multiplier tubes and surface barrier detectors were used. Horizontal slots permitted scanning the central region of the discharge in a vertical plane with a resolution of about 2 cm. Peaked T_e profiles and the temperature dependence of x-ray emission imply that the center of the discharge causes most of the signal. This is confirmed by radial scans and allows investigations of the internal effects of kink mode suppression schemes, which will be discussed in several examples. Discharges without large kink oscillations produced sawtooth or relaxation oscillations with typical periods of 0.5 msec and amplitudes 10% of the total x-ray signal. A gas puff during the discharge caused the period to lengthen before a large kink mode developed.

IC 11. Titanium Gettering Experiments in ATC,* P. E. Stott, C. Daughney, and R. A. Ellis, Jr.

Although the importance of the plasma-wall interaction in tokamaks is well recognized, even if poorly understood, there have been few experiments in which the surface properties of the wall have been varied in a controlled way. Convincing arguments can be made for a clean, degassed wall coated with a chemically inert surface layer (e.g., gold-plated). An interesting alternative is a chemically active surface (e.g., gettered layer) which can trap and retain copious quantities of gas. However, exposure to plasma bombardment may result in high sputtering rates and desorption of previously trapped gas. To test these ideas we have evaporated a titanium getter layer onto a section of the ATC torus. The titanium can be replenished between discharges and the filling gas can be pulsed in just prior to the discharge or fed continuously. Preliminary results show that compared to the non-gettered case, discharges preceded by gettering have higher currents for the same voltage; lowered recyling as indicated by decreasing density with time; and changes in MHD activity.

---

* Presented at *The Plasma Physics Divisional Meeting of the American Physical Society*, Albuquerque, N. M., Oct. 28-31, 1974.

D. The Model ST Tokamak

1. Summary

The high-power wave-heating equipment installed at the end of 1973 has been used to study wave propagation and ion heating near the first and second harmonics of the ion cyclotron frequency. Mode structure and wave generation efficiency (~ 90%) are about as expected from theory. At $\omega/\omega_{ci} = 2$, ion temperatures ($T_{\perp}$) were about doubled from ~ 100 eV to ~ 200 eV. Heating efficiency (increase in ion energy/wave) varied from ~ 45% at lower wave energy to ~ 8% at higher wave energy, reflecting the leveling off of temperature increase at high input energy. Most of the wave energy loss can be attributed to fast loss of high-energy ions through particle orbit loss cones. At the low Ohmic current used for these experiments (required because of the frequency of the available power supply) this loss mechanism is very limiting; at higher currents in larger machines we can expect better efficiency at higher power input. Instabilities that develop after the rf pulse are correlated with impurity influx into the plasma; there is no evidence that the presence of the wave itself produces an inherent instability.

Studies of x-ray oscillations have detected m = 1 and m = 0 (internal disruption) modes near the center of the plasma, which do not affect loop voltage and B_θ-loop signals outside the plasma edge. Rough estimates indicate that the internal disruptions might lead to transport across the q = 1 surface of about half the input power. m = 2 oscillations followed sometimes by large disruptions confirm and add to the results of Hosea, Jobes, and others. The oscillations are probably due to resistive MHD kink modes with magnetic island structure, although there is not yet good quantitative agreement with theory.

The radial distribution of high-Z impurities has been studied by measurements of x-ray intensity in the 2-10 keV range. The radiation intensity is rather sharply peaked, because of the temperature profile, but is consistent with a uniform distribution of Z; the value of $\bar{Z}$ in the central core cannot differ by more than ± 50% from the $\bar{Z}$ averaged over the whole aperture.

Radiation in the extreme ultraviolet has been measured with a silicon diode array (5-20 Å range). Power radiated in this range is estimated to be of the order of 10% of the input power in the central core, probably attributable to line radiation from the L-shell of iron or the M-shell of molybdenum.

The ST machine was shut down at the end of May, so that the room could be prepared for the installation of the PLT tokamak.

2. Wave Heating

Experiments with the new high-power ion cyclotron resonance heating apparatus (ICRH) were conducted from January until May.[1] The earlier (Phase I) apparatus was changed in three ways for the present (Phase II) higher-power system: (i) two half-turn coils, separated along the plasma column by 43 cm, were used in place of the single coil, (ii) the distance between the coils and the vessel wall was increased from ~ 1.3 cm to ~ 4 cm, (iii) the coil feed-through port diameters were enlarged from 3.7 cm to 7.6 cm.

The electrical circuit is shown schematically in Fig. 1(a), and a diagram of the geometry (comparing Phases I and II) is shown in Fig. 1(b). The capacitors are variable, 25-200 pF, with 100 kV rating. The half-turn coils, which run on the inner side (small major radius side) of the plasma torus, are made of copper and encased within ceramic heat shields. The ceramic cases are covered by strips of tungsten that serve as Faraday shields. A photograph of the coil as installed is shown in Fig. 1(c).

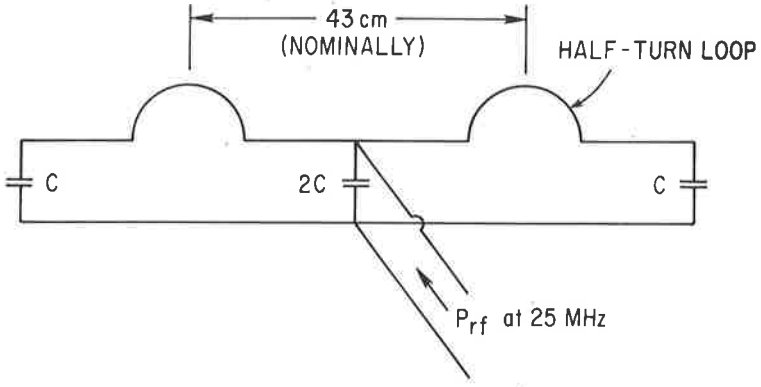

753132

Fig. 1(a) Schematic wave-heating electrical circuit Capacitors, C, are variable, 25-200 pF, 100 kV rating.

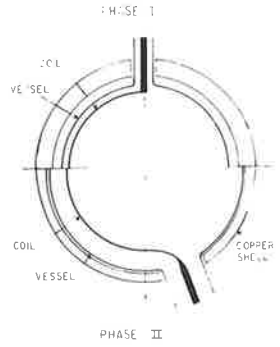

733626

Fig. 1(b) Diagram of the coil configuration. The upper half represents phase I, the lower half phase II experiments.

---

[1] J. Adam, *et al.*, *Fifth Conference on Plasma Physics and Controlled Nuclear Fusion Research, Tokyo, Japan* (Nov. 11-15, 1975), Paper IAEA CN-33/A3-2; also Princeton Plasma Physics Laboratory MATT-1094 (1974).

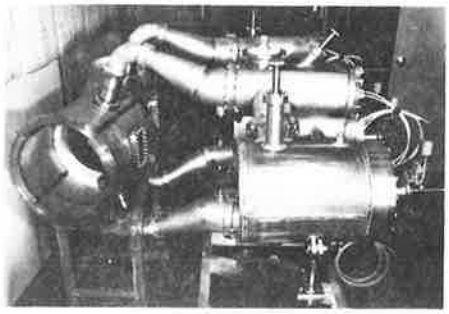

744276

Fig. 1(c) Photographs of the coils installed in place. The two half-turn coils are made of copper, encased in ceramic heat shields. Small strips of tungsten that cover the ceramic casing serve as Faraday shields.

The incident and reflected rf power (25 MHz) was measured by directional couplers and the coil current was monitored by pick-up loops placed behind the coils. The equivalent series resistance (R_S = net rf power/coil current squared) measured in the absence of the plasma, which represents the circuit loss, was 0.06 ohm; in the presence of plasma, R_S was enhanced up to 0.6 ohm, due to wave generation. This represents a wave-generating efficiency of up to 90%.

Figure 2 shows results on loading resistance and mode structure, taken at low power.

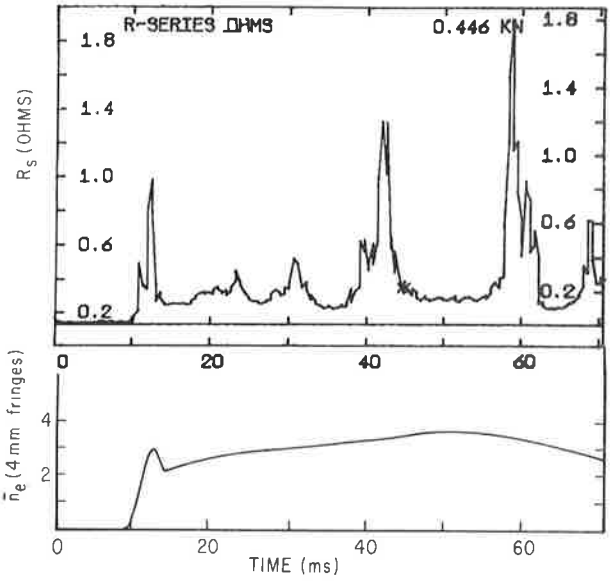

746001

Fig. 2(a) Equivalent series loading of ICRH coils and toroidal eigenmodes. (a) Loading resistance variation with time.

Fig. 2(b) Plasma density variation with time.

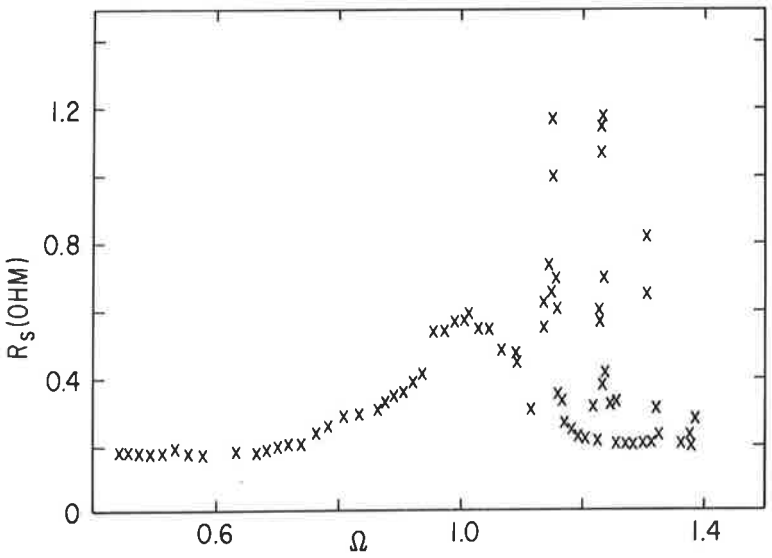

753125

Fig. 2(c) Loading variation with Ω and toroidal eigenmodes (sharp peaks beyond Ω=1).

Figure 2(a) shows the time variation of the loading resistance at $\Omega \equiv \omega/\omega_{ci}$ = 1.18 (ω_{ci} on the magnetic axis) as the plasma density varies with time [Fig. 2(b)]. Sharp peaks in the loading curve are interpreted as the appearance of toroidal eigenmodes[2,3] when the density takes on certain values, the wavelength of the waves propagating around the torus become appropriate for constructive interference and the vacuum vessel acts as a toroidal cavity at a resonance.[4] Similarly Fig. 2(c) shows the occurrence of sharp peaks in the loading resistance as Ω is varied at fixed density. Measurements similar to those in Fig. 2(a) were taken at various values of Ω-time plane [Fig. 2(d)]. The loading resistance is expressed by the degree of darkness of the stripes in this figure. Figure 2(e) shows theoretical predictions of the pattern of eigenmodes (m = -1 modes for $e^{+im\theta}$ minor azimuthal dependence) expected for the conditions of Fig. 2(d). Close similarity of the experimental and theoretical results supports our interpretation.

---

[2] J. Adam, *et al.*, *Bull. Am. Phys. Soc.* 19, 734 (1974).

[3] W. D. Getty and J. C. Hosea, *Bull. Am. Phys. Soc.* 19, 960 (1974).

[4] F. W. Perkins, *et al.*, *Third Int. Sym. on Tor. Plasma Conf.* (Garching, Germany, 1973) Paper B-8; J. Adam and A. Samain, Fontenay-aux-Roses, Report EUR-CEA-FC-579 (1971) 29; F. Perkins, *Symposium on Plasma Heating and Injection*, Varenna, Editrice, Compositori, Bologna (1972) 20.

An array of 22 rf probes was used to monitor the wave fields around the torus. The theoretically predicted minor azimuthal modes ($m = 0, \pm 1$) were observed. Under the conditions in which the fast hydrodynamic waves were above cutoff ($\Omega \gtrsim 1$), the rf probes placed on the side of the torus opposite the generating coils registered strong signals, indicating that the waves propagate around the torus. On the other hand, under the conditions of the slow (ion cyclotron resonance) wave propagation ($\Omega \gtrsim 1$) the probe signals were observed to decay strongly within a distance of 1 m or so, indicating that the slow waves cannot propagate around the torus (at least under the present experimental conditions).

For the heating experiments the device was operated most of the time at a toroidal field of 16 kG and an Ohmic heating current of 25 kA. With this discharge the line average electron density was between 0.6 and 1.2×10^{13} cm^{-3} and the peak electron temperature was about 650 eV. The ion temperature without rf heating was less than 100 eV. These non-optimal operating conditions were necessary in order to utilize the existing 25 MHz generator: a low toroidal field (16 kG) is required for resonance at the second harmonic of the deuteron cyclotron frequency and the Ohmic heating current then needs to be scaled down to maintain a stable discharge. This results in relatively poor confinement of heated ions.

The means of assessing ion heating were two charge-exchange neutral-atom detectors; one of them was located near the rf coil looking perpendicularly at the plasma torus, and the other on the far side looking tangentially. Since the tangential detector is on the side of the torus opposite the rf coils, it is reasonable to assume that the entire plasma is heated to a temperature at least as high as the temperature indicated by this detector. The measurement by this detector is the one used in assessing ion heating.

743614

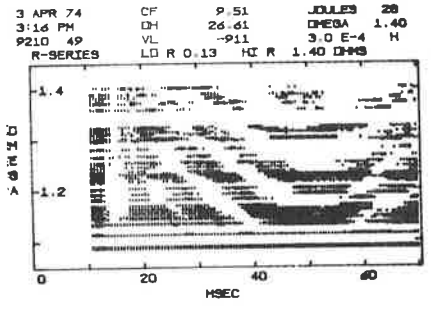

Fig. 2(d) "Tone plot" of the loading resistance in Ω-time plane. Darkness of the stripes expresses the magnitude of the loading.

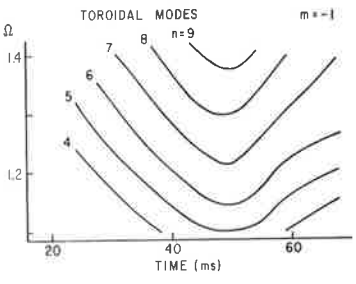

Fig. 2(e) Theoretical prediction of the appearance of toroidal eigenmodes.

Figure 3 shows a typical ion energy distribution measured by the perpendicular charge-exchange neutral detector when an rf pulse is applied.

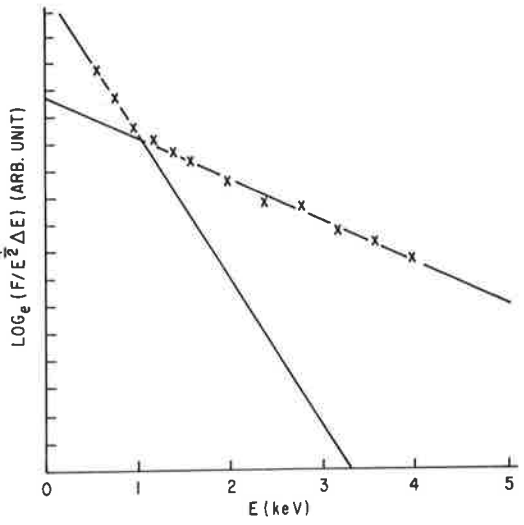

746002

Fig. 3. "Two-Maxwellian" fit to the perpendicular charge-exchange neutral atom analyzer data. F(E) is the detector signal strength at the energy analyzer setting E divided by a known function of E and is proportional to the value of the distribution function at E with the proportionality constant independent of E. The reciprocals of the slopes of the two straight lines give ion temperatures of 180 eV and 650 eV.

The measured distribution is clearly non-Maxwellian. Two straight lines are fitted to the data points as shown in the figure. The effective temperature determined from the low-energy part of the distribution is defined as the "body" temperature, and the one from the high-energy part, the "tail" temperature. All subsequent references to ion temperatures are, unless otherwise specified, the body temperatures. Therefore, we are being conservative in assessing the energy content of the measured part of the distribution function.

Figure 4 shows the time-variation of the perpendicular ion temperature as the $\Omega = 2$ plane comes at different places within the plasma column.

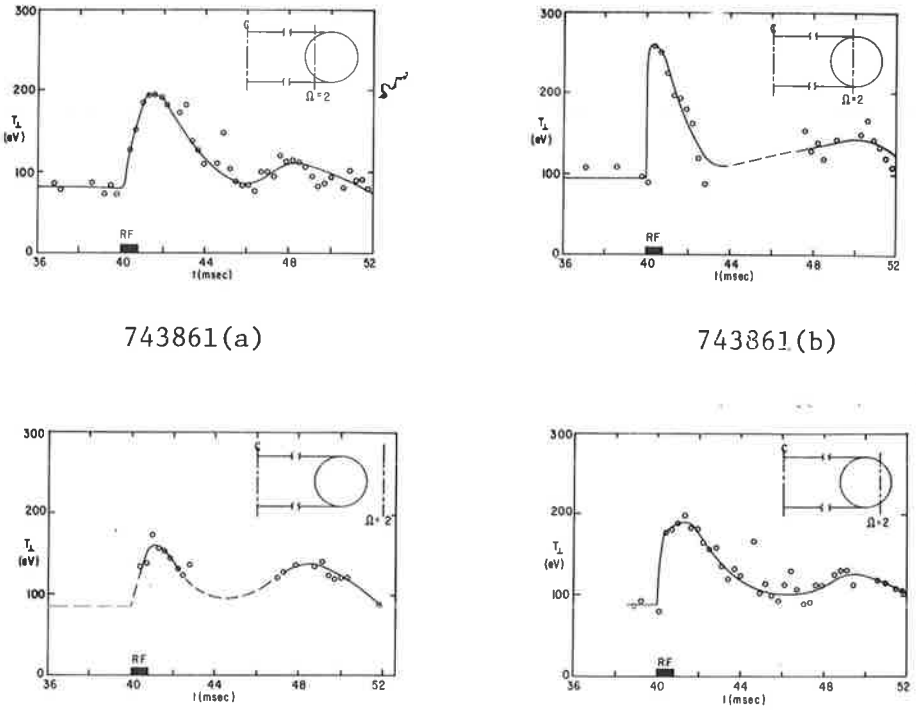

743861(a)

743861(b)

743861(c)

743861(d)

Fig. 4. (a)-(c) Time variation of the perpendicular ion temperature for various positions of the (dueteron) $\Omega=2$ plane within the plasma column. Maximum heating (first peak) occurs with resonant plane at the center (b). (d) Effect of resonant heating of impurities. The late peaks are attributed to impurity influx.

From Fig. 4(a) - (c) it can be seen that the temperature increase is largest when the resonant plane is positioned at the center. Some heating is observed even when the resonant plane is completely outside the plasma [Fig. 4(d)]. This can be attributed to resonant heating of impurity ions; the $\Omega = 2$ resonant planes of O^{7+} and O^{6+} are still inside the plasma. Fast collisional transfer then heats the deuterons (which are measured in the charge-exchange apparatus).

The smaller second peak in the temperature appearing at about 9 msec after the beginning of the rf pulse is caused by the influx of high-Z impurities from the walls and limiters. The high-Z impurities increase the electron-ion coupling and make Ohmic heating more effective. In fact, the electron-ion equipartition time for these cases is about 9 msec. [This impurity heating effect must not be confused with heating due to resonant acceleration of oxygen ions mentioned in connection with the first peak of Fig. 4(d).] For all the ion temperature results presented here, the rf pulse length was only about 1 msec long and the rf and impurity heating effects were well separated from each other. In the subsequent discussions only the temperature increase due to rf heating is considered.

An example of the parallel temperature response is shown in Fig. 5(a).

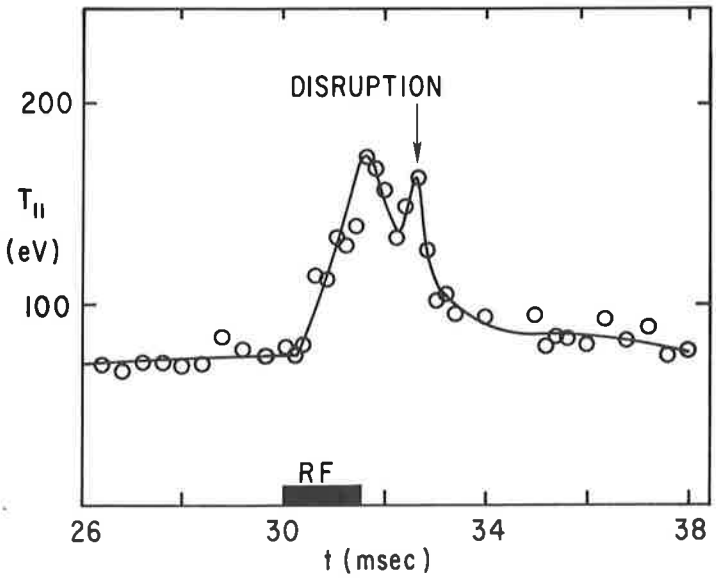

743794

Fig. 5(a) An example of the time variation of parallel temperature at Ω=2. Disruptive instabilities were observed when the energy input into the plasma exceeded several hundred joules.

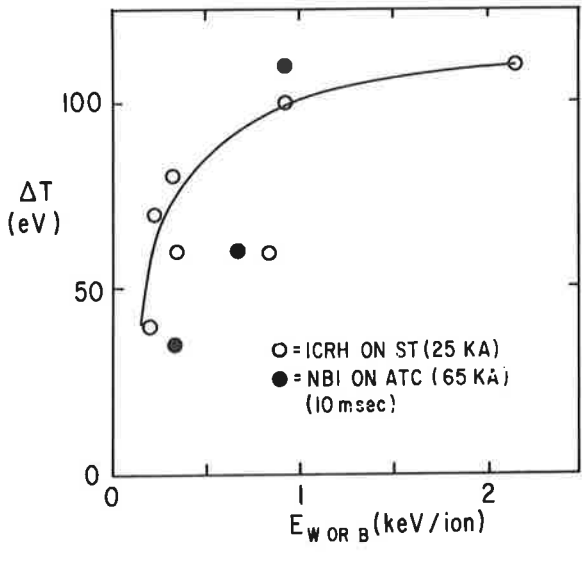

743795

Fig. 5(b) Incremental parallel temperature increase due to the re heating at Ω=2. The abscissae, E_W=(rf power in the wave) × (pulse length)/(total number of ions in the plasma), represent the amounts of energy available for heating (ion density assumed=electron density).

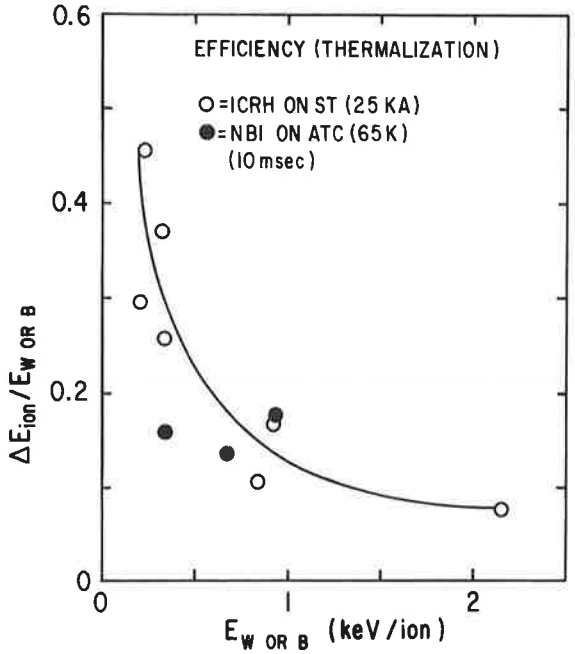

743797

Fig. 5(c) The efficiency, $\Delta E_{ion}/E_W = [(3/2)k\,\Delta T_{ion}/E_W]$, plotted against E_W. The falling efficiency is attributable to loss cone energy loss.

As indicated in the Figure, disruptive instabilities have been observed when the energy input into the plasma exceeded several hundred joules. Since the ion energy confinement time (computed collisional power input and parabolic radial density and temperature profiles) is about 4 msec for these conditions, the optimum rf pulse length would have been greater than 4 msec. However, the disruptive instabilities caused by the impurity influx and subsequent narrowing of the current channel prevented the use of rf pulses longer than 1-2 msec. This was one of the processes that limited the maximum attainable heating.

In the heating experiments at $\Omega = 2$, the net rf power in the wave field was varied from ~ 75 to ~ 350 kW, and the pulse length from 0.6 ~ 1.7 msec. Figure 5(b) shows the increase in $T_{\parallel}$ due to rf heating ranging from 40 eV to 110 eV. The abscissae are values of wave power times the pulse length divided by the total number of ions ($\cong$ electrons)in the machine. This quantity represents the amount of energy available for heating, expressed in units of keV per ion. The curve tends to saturate as the available energy per ion increases, indicating decreasing efficiency. Dividing the energy increase per ion (assuming $\Delta T_{\perp} = \Delta T_{\parallel}$) by the available heating energy, gives an efficiency which is plotted in Fig. 5(c). This ranges from 8% to 45% for the present experiments.

All the previous results refer to $\Omega = 2$ heating. Measurements at $\Omega = 1$ show a smaller increase in $T_{\parallel}$, although the increase in $T_{\perp}$ was comparable to $\Omega = 2$ heating. As noted before, unlike the fast wave ($\Omega = 2$), the ion cyclotron waves ($\Omega = 1$) did not propagate around the torus. It is believed that heating was accordingly localized near the coil, and the parallel temperature detector on the far side of the torus indicated only small temperature changes.

The dominant mechanism of energy loss in the present experiments is believed to be the loss of energetic ions through particle-orbit loss cones. In Fig. 6 the loss cones for the ST Tokamak under the present operating conditions are sketched in the manner originally due to J. Rome.[5] (This particular case was obtained using a computer code written by R. Smith.)

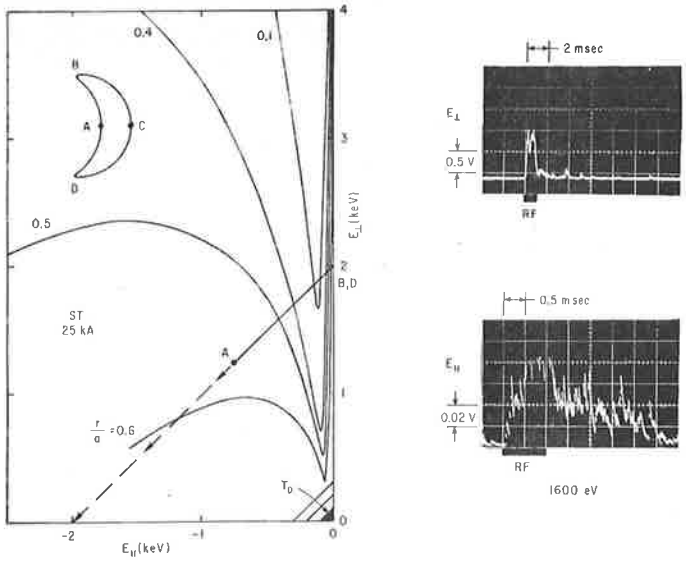

743998

Fig. 6. Loss cones of the ST tokamak at I_{OH}=25 kA, BT=16 kG, presented in the manner due to J. Rome. (These results were computed by R. Smith.) The oscillograms show signals from perpendicular and tangential charge-exchange neutral detectors at E=1600 eV. The much greater $E_{\perp}$ signal during the rf pulse indicates a strongly anisotropic distribution. Because of intervening loss cones, most ions are lost before becoming isotropic by direct deflecting collisions. The $E_{\parallel}$ signal therefore decreases, rather than increasing at the expense of the $E_{\perp}$ signal, after rf pulse ends.

---

[5] J. Rome, et al., Particle Orbit Loss-Cones in Tokamaks Talk delivered at the Meeting on Theoretical Aspect of CTR, Berkeley, April 4, 1974.

Note that the loss cones extend down almost to the thermal energy, indicated by a shaded triangular region near the origin. The wave field accelerates ions in the perpendicular direction and the distribution becomes stretched in the vertical direction. In the absence of the loss cones, the energy of the parallel degree of freedom would increase mainly through deflecting collisions that alter the direction of motion of an ion but keep its energy essentially unaltered. However, because of intervening loss cones, most of the energetic ions escape before the distribution becomes isotropic. The presence of loss cones should then reflect upon the relaxation of the charge-exchange signals after the rf pulse ends; the parallel detector signal should decay, rather than increase at the expense of the perpendicular detector signals. The oscillograms of the perpendicular (top) and the parallel (bottom) detector signals in Fig. 6 confirm these expectations. As the power input and hence the wave amplitude increases, ions are accelerated to higher perpendicular energies, thus increasing the energy loss. This picture is consistent with the observed decrease of heating efficiency as the power input is increased.

Amounts of rf power ranging from several tens of kW to a few hundred kW went into the rf field but did not appear as an increase in $T_{\parallel}$. Now, according to the two-Maxwellian representation of the ion distribution, the tail of the distribution contains between 8% and 40% of the total ion energy. This energy is lost on a time scale comparable to the decay time of the $E_{\perp}$ signal. From this, we estimate that some 20 to 200 kW could be accounted for by this loss-cone mechanism. It must be emphasized at this point, however, that this power loss is related to the unusually low Ohmic heating current at which the device was operated for these experiments.

As mentioned before, when the total energy input from ICRH exceeded several hundred joules, the plasma became unstable due to impurity influx. Thomson-scattering radial profiles of the electron density show that the density increase first appears at the edge of the plasma and then moves inward. The electrons are cooled near the edge while they are heated at the center, leading to an increasingly narrow current channel. (The incremental density increase is strongly dependent on machine conditions; it became progressively smaller as the machine base pressure decreased toward the end of the experimental period.) As the density increased, the one-turn loop voltage rose and finally led to disruptive instabilities, and characteristic negative voltage spikes appeared.

Figure 7 shows how the incremental density increase due to a 2,5 msec rf pulse varied with the toroidal field current.

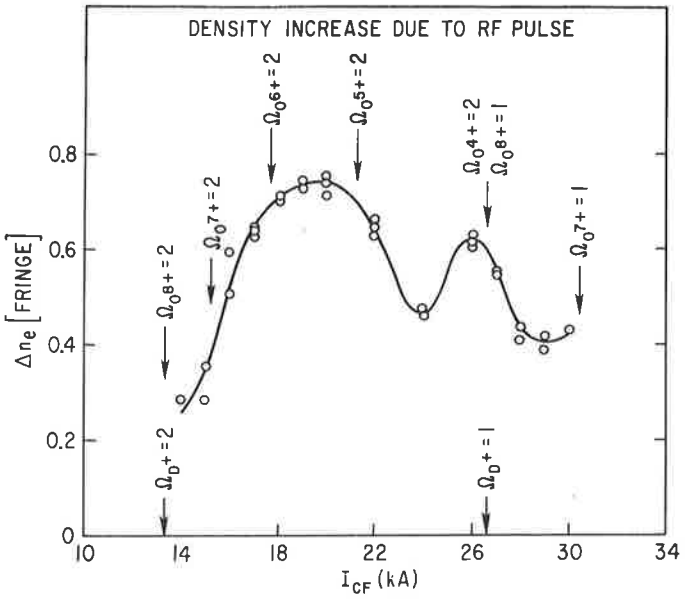

753127

Fig. 7. Density increase due to a 2.5 msec rf pulse as a function of toroidal field current, I_{TF}. Arrows on the horizontal axis show values of I_{TF} for which the Ω=1 or Ω=2 resonant layer for deuterons is located at the center of the plasma. Resonant conditions for various impurity oxygen ions are indicated along the curves.

The arrows at the horizontal axis indicate the values of the current at which the Ω = 2 and Ω = 1 deuteron resonant layers are located at the center of the plasma. A possible explanation for the observed impurity influx is bombardment of the limiters and the wall by energetic deuterons that escape through the loss cones. However, the dependence shown here is inconsistent with the picture of deuteron bombardment alone. The maximum is not at the deuteron resonances but is located between them, the Ω = 2 condition corresponds to a minimum and the increment at Ω = 1 is much greater than that at Ω = 2. The resonance layers of various oxygen ions are also indicated in Fig. 7. Although impurity ion concentrations were at most a few percent (an effective-Z measurement indicated oxygen concentrations of 3% before rf and 5% after rf, while spectroscopic measurements gave increases of the concentration from 2% to 4% due to the rf pulse), the sputtering efficiency of bombarding ions scales as Z^2M and therefore an O^{5+} ion has a sputtering yield 200 times that of a deuteron at the same energy. It appears from the figure that the O^{6+} and O^{5+} ions are probably responsible for the central maximum, while the peak at Ω = 1 is probably caused by O^{4+} as well as by deuterons. These ions with low ionization potentials would be concentrated near the edge of the plasma, where the confinement is poor. On the other hand, O^{7+} and O^{8+} with much

higher ionization potentials would be concentrated near the axis, where T_e is high; they were, therefore, better contained and were probably contributing to heating rather than sputtering. It should be added here that the efficiencies of the resonant acceleration of deuterons and oxygen ions are comparable, and hence the latter would become as energetic as deuterons under the influence of the rf field.

A very important question is whether the rf field itself was the cause of the observed disruptive instabilities. There are strong indications that this was not the case; for example, the instabilities occurred well after the rf pulse had ended, and the processes leading to instabilities could be simulated by injecting cold gas into the vacuum vessel through a pulsed gas valve. This experiment also showed that injection of deuterium gas had no effect on the plasma stability or the ion temperature, while injection of heavier gases such as Ne and N_2 caused the ion temperature to rise and also caused disruptive instabilities to occur. We conclude that heavier impurities, not the recycled deuterium, were primarily responsible for the disruptive instabilities.

3. Plasma Instabilities

Instabilities in the tokamak plasma have been studied by investigating fluctuations in the continuous x-ray emission. This method has detected the existence of n = 0, m = 0 internal disruptions,[6] small n = 1, m = 1 and 2 oscillations, and large m = 2 oscillations preceding a disruptive instability.[7] The m = 2 measurements complement and expand measurements by Hosea and Jobes,[8,9] in which magnetic pickup loops and the thallium-beam probe were used. A survey of conditions under which these various instabilities have been observed is shown in Fig. 8. The internal disruption, preceded by growing

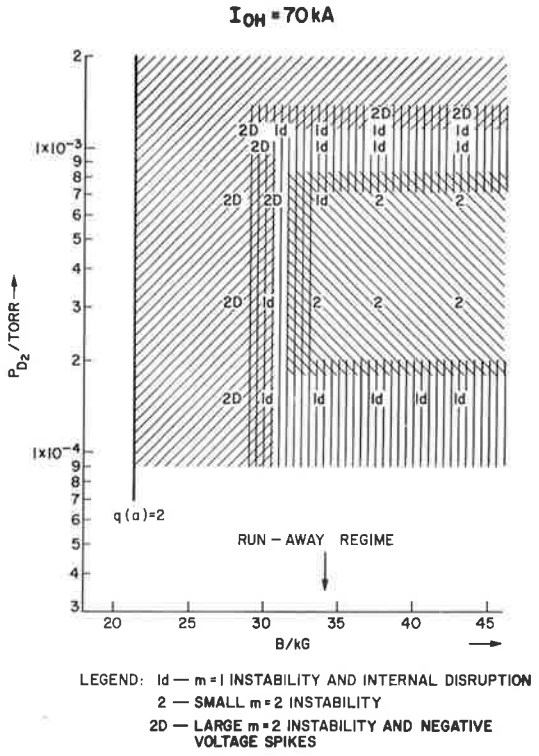

743297

Fig. 8. Instability regimes at constant Ohmic heating current. Ordinates are neutral D_2 filling pressures (Torr) and abscissae are toroidal fields (kG). Approximate regimes at which instabilities occur are shown by shading and lettering:
1d-m=1 instability and internal disruption
2-small m=2 instability
2D-large m=2 instability and negative voltage spikes; The 2D limits are low q and high pressure.

---

[6] S. von Goeler, *et al.*, *Phys. Rev. Lett.* 33, 1201 (1974).

[7] S. von Goeler, *Bull. Am. Phys. Soc.* 19, 883 (1974).

[8] J. C. Hosea, *et al.*, *Phys. Rev. Lett.* 30, 839 (1973).

[9] F. C. Jobes, J. C. Hosea, Princeton Plasma Physics Laboratory MATT-982 (1973).

m = 1 oscillations, is observed at high and low filling pressure. (In general, high filling pressure implies high electron density, but the relation between them is more complex than linear. Filling pressure is used as an operational parameter.) At intermediate pressures, the small m = 2 oscillations are observed for values of toroidal field for which the safety factor at the center, q(0), is greater than one. At the highest values of filling pressure and lowest values of toroidal field, large m = 2 oscillations occur, followed by large disruptions; in these cases the oscillations are observable outside the plasma on B_θ pickup coils, and the disruptions are accompanied by negative spikes in the loop voltage.

The boundary between the different regions depends on the OH current and on the impurity state of the machine; e.g., in a new, not very much outgased machine the high pressure instability limit for the 2D occurs at a much lower pressure than in a well outgased machine which has been run for a few weeks. Figure 8 refers to the instabilities seen at the maximum of x-ray emission. Depending on how the density develops (decrease or increase) a discharge might slide from one regime into another.

Figure 9(a) shows the experimental arrangement.[10]

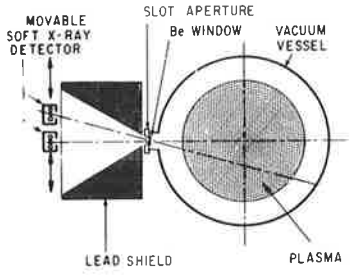

743153(a)

Fig. 9(a) Experimental arrangement of x-ray detectors.

---

[10] S. von Goeler, et al., Princeton Plasma Physics Laboratory MATT-1060 (1974).

An "image" of the plasma column was formed by a slot aperture, and the x-ray emission from different regions of the plasma was measured by silicon-surface-barrier detectors, which were moved in the image plane. The oscillograms of the x-ray emission, shown in Fig. 9(b), are typical for high-density discharges in the ST tokamak.

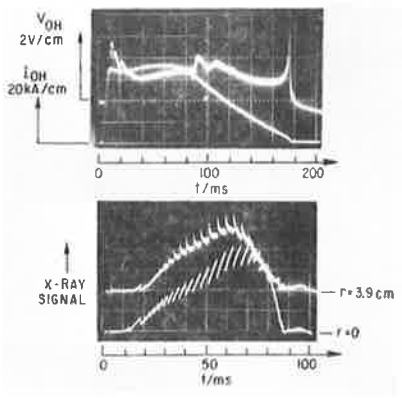

743153(b)

Fig. 9(b) Upper: plasma current and loop voltage. Lower: x-ray signals exhibiting internal disruption sawtooths at different radii (note time scale change).

The traces exhibit plasma current and voltage and a "sawtooth" oscillation on the x-ray signals. The sawtooth is inverted in scans taken a small distance away from the center of the column (e.g., trace marked r = 3.9 cm). Similar sawtooth oscillations seem to be present also in the T-4 Tokamak[11] and have also been seen in the ATC Tokamak.[12] Here it is shown that they have the features of internal disruptions preceded by m = 1 oscillations.

---

[11] V. A. Vershkov, et. al., Kurchatov Institute Report No. IAE-2291, 1973 (unpublished), and Princeton Plasma Physics Laboratory MATT-TRANS-112 (1974).

[12] R. R. Smith, Princeton Plasma Physics Laboratory TM-273 (1974) (unpublished).

In Fig. 10 are plotted radial scans of various quantities for a typical high density discharge in ST.

(a)

(b)

(c)

(d)

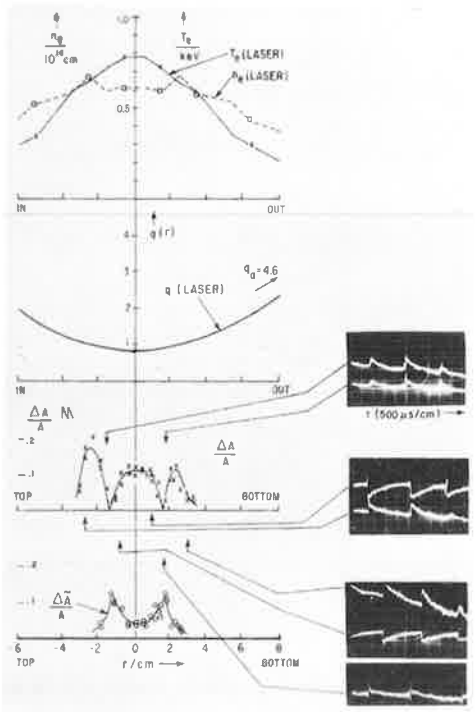

743154

Fig. 10. Radial profiles of (a) electron temperature and density profiles form laser Thomson scattering data (limiter at r = 12 cm), (b) the safety factor q(r) from laser data, (c) amplitude $\Delta A/A$ of the internal disruption (sawtooth), and (d) amplitude $\Delta\tilde{A}/A$ of the sinusoidal m = 1 oscillations preceding the step. Inset oscillograms illustrate the phase relations between various radial positions. X-ray data are intensities integrated over the chord of observation; laser data are for local radii.

In Fig. 10(a) are shown radial profiles of electron temperature and electron density, as derived from Thomson scattering of laser light. If the discharge is nearly stationary (i.e., no skin effects, so that V is independent of r) and if it is assumed that the impurity concentration is uniform across the column, the current density and the safety factor q(r) as a function of radius can be calculated from the profiles of T_e: q is roughly 0.8 in the center of the plasma [Fig. 10(b)] and reaches a value of 1.0 at 4 = 2.6 cm. There is, of course, some uncertainty in the values for q because the abovementioned assumptions may not hold exactly. Figure 10(c) shows the measured relative x-ray sawtooth amplitude $\Delta A/A$. The sawtooth amplitude has a node near the q = 1 point. Outside this node, the sawtooth is inverted. The amplitude is very small for large radii (r > 4 cm). Simultaneous measurement of the sawtooth at different radii and at different locations around the torus shows that the sudden breaks occur at the same times. This indicates that the sawtooth behaves like an m = 0 mode; i.e., an expansion in minor radius of the central region of the plasma column, or "internal disruption."

Internal disruptions have been observed near the q = 1 surface, both in high-density discharges near the high-pressure instability limit and in low-density region, the amplitude of the sawtooth is 3-10% and the frequency is ~ 2 kHz. In the high-density regime, the amplitude is larger, 5-30%, and the frequency smaller, 700-200 Hz.

Each internal disruption is preceded by a growing sinusoidal oscillation. The amplitude ΔA of this sinusoidal oscillation is shown in Fig. 10(d). The amplitude is very small in the center of the column, has a maximum close to the q = 1 surface and vanishes abruptly outside the q = 1 surface. Figure 11 illustrates the method for determining the m-number of the mode.

743286

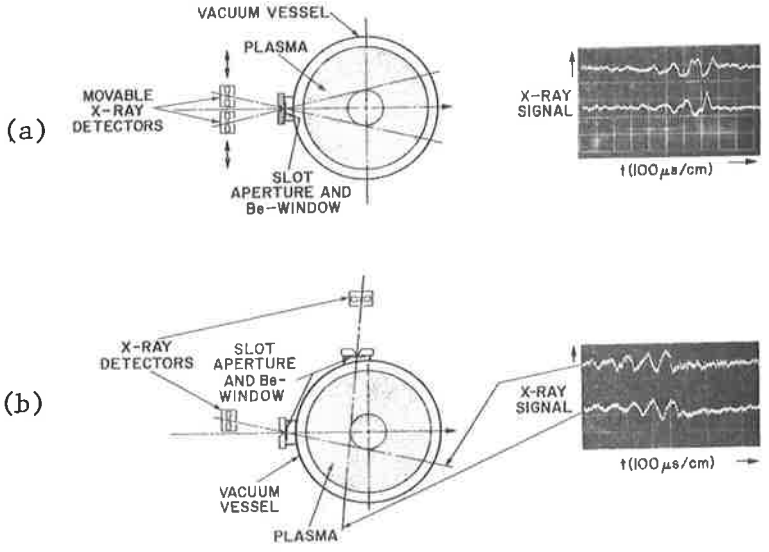

Fig. 11. Determination of m-number of oscillations. Two detectors look (a) slightly above and below, and (b) slightly off-center at right angles through the column. The pictures are for different shots. Case (b) shows that the waves go in the direction of the electron diamagnetic drift (the toroidal field points into the plane of the picture).

Two detectors look (a) slightly below and slightly above the center of the column and (b) slightly off center at right angles. From the phase relations it follows that the oscillation is an m = 1 mode. Similar measurements, placing detectors at different locations around the torus, show that it is also an n = 1 mode. Since in Fig. 11(b) the top trace precedes the bottom trace (and the toroidal field is directed into the plane of the figure), the mode propagates in the direction of the electron diamagnetic drift. The frequency ν of the waves is close to $\nu^* = (1/2\pi r)(kT/eB)(1/p)(dp/dr)$, as determined from the laser temperature and density at the q = 1 surface; it should be pointed out, however, that no correction for E × B drifts has been made, because the plasma potential is not known for these discharges. Measurements by Jobes and Hosea,[13] under somewhat different conditions, have shown negative potentials of the order of T_e, but typically smaller.

Attempts have been made to compare the experimental results with theoretical predictions for the m = 1 internal kink mode.[14] Pictures like Fig. 11 suggest an experimental growth rate $\gamma \approx 5 \cdot 10^3$ sec^{-1}. The theoretical linear growth rate depends on the exact radial dependence of q, n, and T_e. For parabolic temperature profiles (n_e = const, $j \sim T_e^{3/2}$ we derive from Eq. (13) of Ref. 14:

$$\gamma_{theor} = \frac{2}{3}\pi \frac{v_A}{R}\left(\beta_{zo} + \frac{1}{2}\frac{r_s^2}{R^2}\right) \qquad (13)$$

---

[13] F. C. Jobes and J. C. Hosea, *Sixth European Conference on Controlled Fusion and Plasma Physics*, Moscow, 1973, Vol. I, 199.

[14] M. N. Rosenbluth, *et al.*, *Phys. Fluids* 16, 1894 (1973).

where v_A is the Alfvén velocity, R the major radius, β_{zo} the toroidal β in the center of the column, and r_s the radius of the singular surface (q = 1). This formula gives a value of γ_{theor} equal to $2 \cdot 10^4$ sec^{-1}, which is larger than the experimental growth rate by a factor of about 4. The theoretical linear growth rate does not incorporate toroidal effects and resistive effects. Also the oscillation is probably already in a nonlinear phase.

The radial profile of the oscillation amplitude can be compared with the prediction for the internal kink mode; i.e., displacement ξ = const for $r < r_s$ and $\xi = 0$ for $r > r_s$. An analysis of m = 1 oscillation amplitudes is shown in Fig. 12.

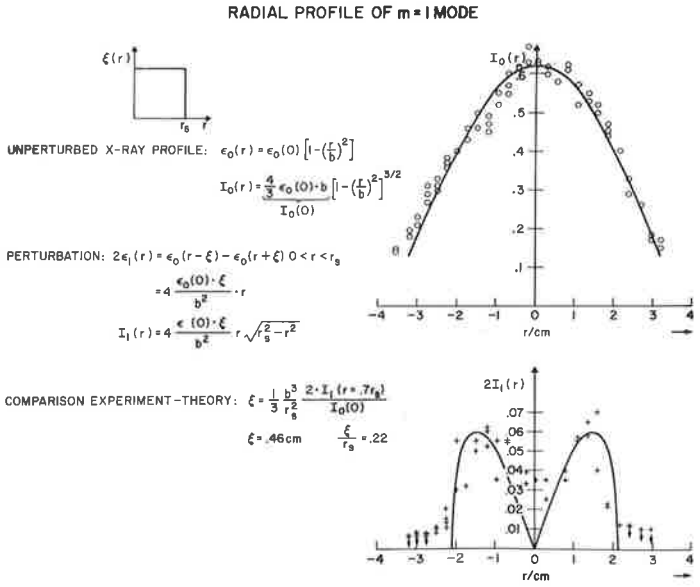

743296

Fig. 12. Comparison of m = 1 mode with MHD theory. (a) Measured average x-ray intensity data; the line is a best fit to the data for an assumed parabolic radial profile of the unperturbed x-ray source. (b) Measured oscillation amplitude versus chord radius. The line is calculated, assuming an m = 1 perturbation of the zero-order profile with a displacement ξ = 0.46 cm out to $r = r_s$ = 2.1 cm, and $\xi = 0$ for $r > r_s$.

We assume uniform displacement within r_s, the radius of the singular surface ($q = 1$), and zero displacement outside. The unperturbed x-ray source profile, $\varepsilon_o(r)$, is assumed parabolic:

$$\varepsilon_o(r) = \varepsilon_o(0)(1 - r^2/b^2) \quad .$$

The parameters $\varepsilon(0)$ and b are determined by a fit to the measured line-integral x-ray intensity:

$$I_o(r) = \frac{4}{3} \varepsilon_o(0) \; b(1 - r^2/b^2)^{3/2} \quad .$$

An $m = 1$ perturbation to $\varepsilon_o(r)$ then yields an intensity oscillation amplitude in terms of displacement, ξ:

$$2\varepsilon_1(r) = \varepsilon_o(r - \xi) - \varepsilon_o(r + \xi) = 4\varepsilon_o(0)\xi \; r/b^2, \quad 0 < r < r_s$$

$$I_1(r) = [(4\varepsilon(0)\, \xi/b^2)]\, r \sqrt{r_s^2 - r^2} \quad .$$

Fitting the expected shape to the measured oscillation amplitude gives a value of displacement ($\xi/r_s = 0.2$) that is an order of magnitude larger than that predicted by a nonlinear theory. It should be pointed out that resistivity is not included in the present theory and that it is likely that a tearing mode version of this instability exists. However, Rutherford has recently calculated even faster growth rates for the tearing mode.

An attempt has been made to construct a model for the effect of the $m = 0$ internal disruption on energy transport near the center of the discharge.[15] In this model, just before the internal disruption the temperature is peaked at the center; during the disruption there is mixing of the plasma of the center core, resulting in a flatter temperature distribution out to a radius somewhat outside the $q = 1$ surface, with a very steep temperature gradient at that radius.

---

[15] W. Stodiek, *Bull. Am. Phys. Soc.* 19, 930 (1974).

After the disruption the outside perturbation decays rapidly away because of the steep temperature gradient, and inside q = 1 the peaked distribution is gradually re-established. This process then repeats to produce the sawtooth x-ray intensity patterns of Figs. 9 and 10. (In Fig. 9 the upper x-ray trace exhibits the fast decay outside the q = 1 surface.) This sawtooth pattern was also observed in the temperature by comparing x-ray transmission of two aluminum filters of different thickness (0.001 and 0.003 inch). Figure 13(a) shows Thomson scattering profiles and Fig. 13(b) representative x-ray signals.

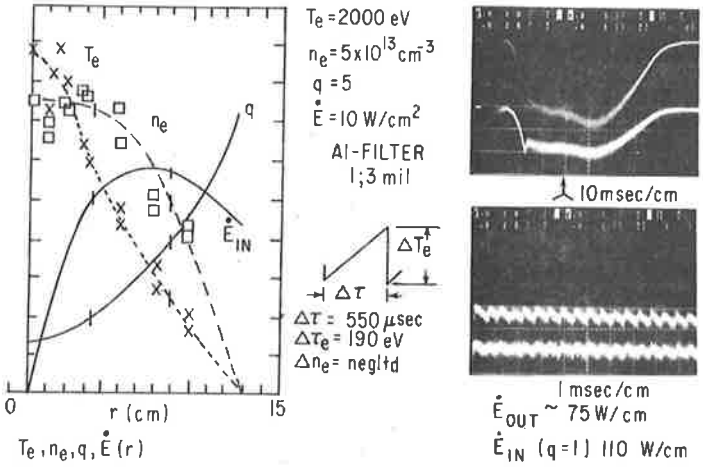

(a) (b)

743285

Fig. 13. Energy transport by internal disruption
(a) Thomson scattering measurements of electron temperature and density profiles and calculation of q(r) and Ohmic heating power input within radius r (per unit surface at r).
(b) X-ray signals through 0.003" and 0.001" Al filters, which imply a temperature sawtooth amplitude of 190 eV with 550 μsec period.

Average power input to the central core can be calculated from the current, voltage, and electron temperature distribution (assuming the E-field and the effective Z not to be functions of r). Rate of energy flow outward across the q = 1 surface can be estimated from the temperature sawtooth amplitude and frequency (the rather flat density profile makes it reasonable to neglect Δn_e here; on the other hand, some preliminary data from the ATC Tokamak indicate fairly large values of Δn_e; this would be expected for a peaked density distribution). In the case shown in Fig. 13, the Ohmic heating power put into the region inside the q = 1 surface is about 75 kW and about half of this could be transported out by the disruption. These numbers are only rough estimates, but they indicate that an appreciable fraction of the energy deposited in the central core of the discharge could be transported out by the m = 0 internal disruption.

The small m = 2 oscillations are observed at intermediate pressures and relatively high values of toroidal field, and with profiles such that generally the value of q at the center is greater than one. Figure 14(a) shows current, voltage, mean electron density, and x-ray traces on a slow time scale, and Fig. 14(b) shows x-ray and B_θ-loop oscillations on a faster time scale.

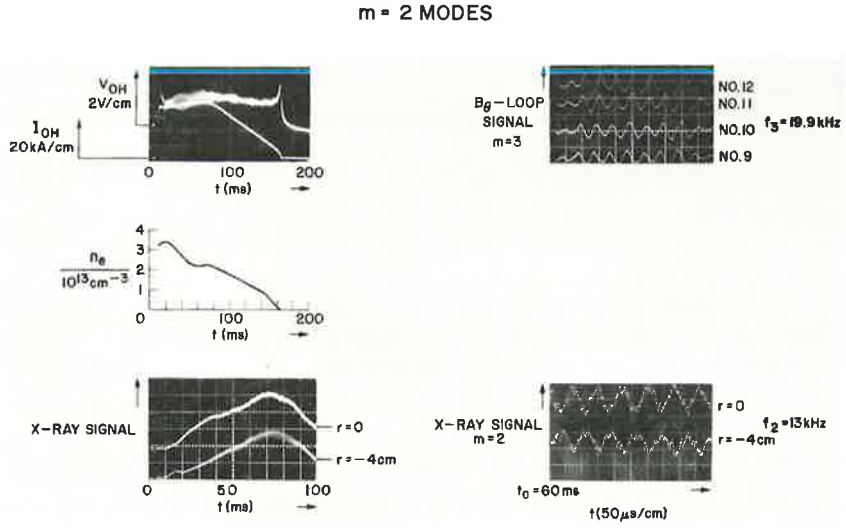

Fig. 14. Small m = 2 oscillations:
(a) current, voltage, mean electron density, and x-ray intensity versus time.
(b) Simultaneous m = 3 B_θ-loop signals outside the limiter, and m = 2 x-ray oscillations inside.

Profiles are shown in Fig. 15.

743295

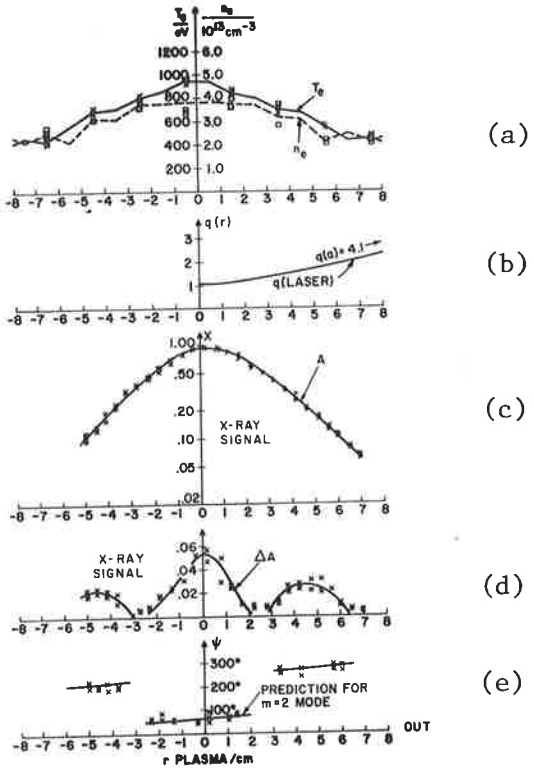

Fig. 15. Radial profiles for conditions of small m = 2 oscillations: I_ℓ = 70 kA, V_ℓ = 3.6 V, a_{lim} = 12 cm, B_ϕ^p = 35 kG, P_o =
(a) Electron density and temperature from laser Thomson scattering;
(b) q(r) calculated from laser temperature profile;
(c) mean x-ray signal intensity versus chord radius;
(d) m=2 x-ray oscillation amplitude versus chord radius;
(e) x-ray oscillation phase with respect to monitor versus radius of point of tangency of line of observation.

Compared with the discharge of Figs. 9 and 10 (m = 1) the central temperature is somewhat higher, the electron density somewhat lower, the temperature profile broader, and q(0) is higher for the same total current. The x-ray oscillations [Fig. 14(b)] were shown to have azimuthal symmetry number m = 2 and toroidal symmetry number n = 1 by relative phase measurements like those described for the m = 1 oscillations. Simultaneous measurements on a set of B_θ pickup loops show that magnetic field fluctuations outside the limiter were not m = 2 but m = 3, presumably originating from the vicinity of the q = 3 surface. The profile of the x-ray oscillations has qualitatively the form expected for the m = 2 mode: an amplitude maximum at the center [Fig. 15(d)] with nodes on either side, at which the phase changes by 180° [Fig. 15(e)]. The phase data in Fig. 15(e) slope slightly because the measurement was made by swinging the angle of observation so that the point of tangency of the line-of-sight moves

in azimuth as the chord radius increases. To compare with theory (Fig. 16), polynominals are fitted to the line intensity data, I_o and I_2, for the "DC" and oscillating parts separately, and inverted to get local source intensities, ε_o and ε_2.

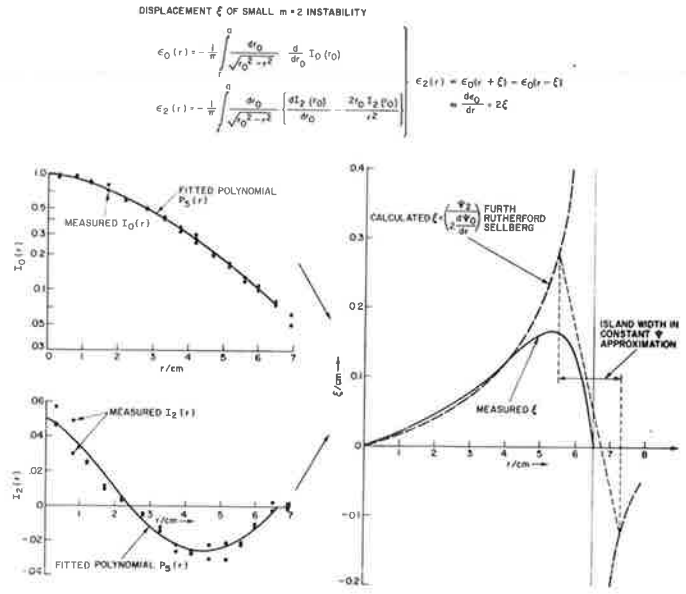

743890

Fig. 16. Comparison of m = 2 x-ray oscillations with theory.

These source intensities are then used to get the displacement profile from the measured oscillation intensity, $\xi = \varepsilon_2/2\ (d\varepsilon_o/dr)$. Also shown is predicted shape derived from the linear analysis of Furth, Rutherford, and Selberg[16] (dashed curves). Linear theory predicts a pole at the singular surface, which, however, at finite amplitudes is smoothed out by island formation. The width of the island is indicated in Fig. 16. At this point the concept of ξ, based on the linear perturbations, breaks down.

The large m = 2 oscillations observed at high pressure and/or low field are accompanied by corresponding oscillations on external B_θ-loops, in the electron density (microwave-interferometer signal), and on the diamagnetic loop. In general, these oscillations precede a large-scale disruption accompanied by sharp changes in average x-ray intensity, negative spikes in the loop voltage, and even perturbations in the plasma current (Figs. 17 and 18).

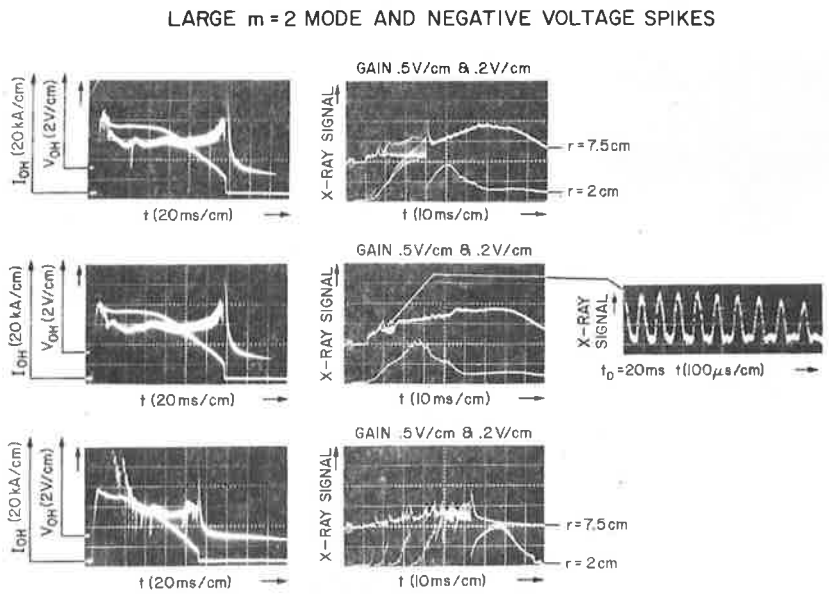

743293

Fig. 17. Large m = 2 oscillations: examples of current voltage, and x-ray intensity. Top, middle, and bottom pictures differ only by slight adjustments in filling pressure.

---

16 H. P. Furth, P. H. Rutherford, and H. Selberg, *Phys. Fluids* 16, 1054 (1973).

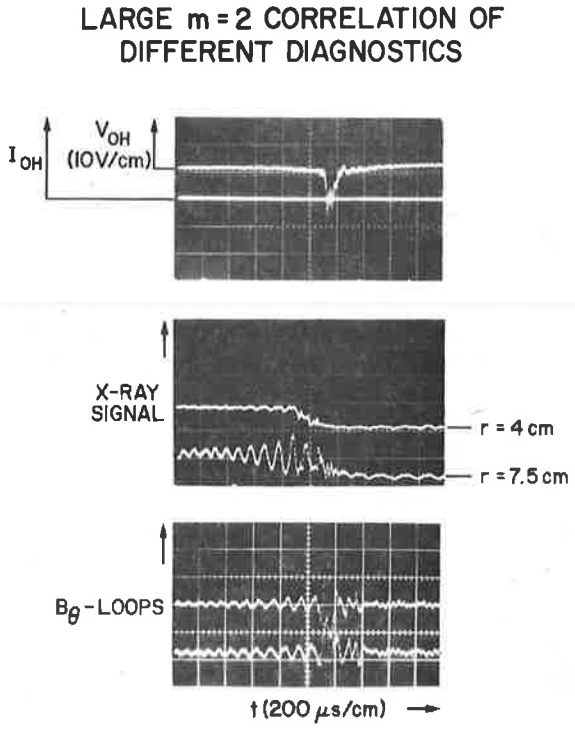

743292

Fig. 18. Large m=2 oscillations, showing correlation of x-ray and B_θ-loop oscillations, and the drop in average x-ray signal preceding the negative voltage spike.

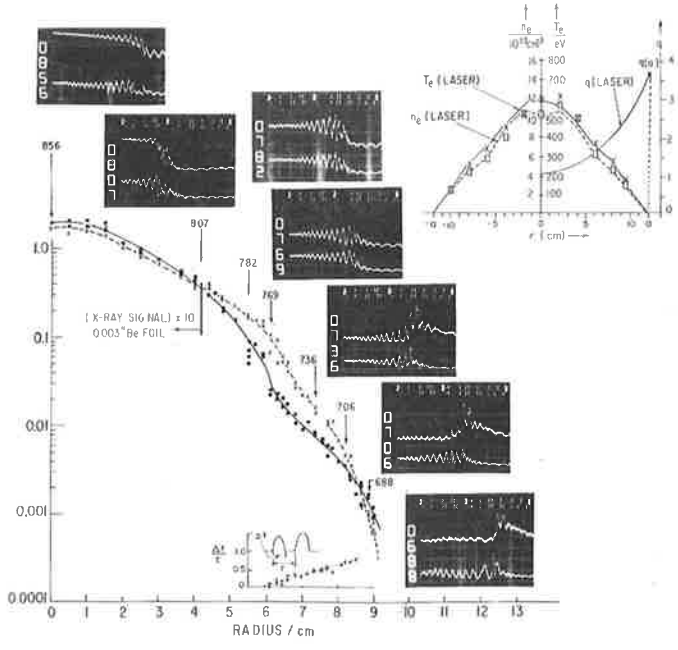

743287

Fig. 19. Profile of x-ray intensity: dots (.) represent peak intensity and crosses (x) valley intensity just before disruption; between the points of phase change (r=4 cm, 8.5 cm) the dots become minima and crosses maxima. The top inset gives profiles of T_e, n_e, and q. The bottom inset illustrates truncated shape expected due to island structure. Bottom trace of each oscilloscope picture is a monitor kept at fixed position (looking through the center).

Figure 19 shows profiles of line intensity of x-ray signal; the upper inset shows corresponding profiles of electron temperature and density and of q. The dots and crosses show the x-ray intensity at the maximum and minimum of the oscillation just before the disruption. The solid and dashed lines are drawn through the epxerimental points. The crossover positions at r = 4 cm, and 8.5 cm represent the points of phase reversal relative to a fixed monitor that looked through the center (the monitor signal is the bottom trace in each of the inset oscilloscope pictures). In the region between r = 6 and r = 8.5 cm, the oscillations are truncated (show #0736 is a good example, or Fig. 17) for a part of the oscillation period, as shown in the small inset, where the fractional period cut off is plotted against radius. This distorted shape can be explained qualitatively as an m = 2 mode with an island structure, as shown schematically in Fig. 20. Figure 20(a) is a plot of flux surfaces (ψ = const) taken from Yoshikawa's[17] calculation of MHD helical equilibrium for a cylindrical current channel with an m = 2 perturbation. To make a comparison with experiment, a source function [(Fig. 20(b)] was assumed, of the form:

$$\varepsilon(\psi) = \begin{cases} b + \psi & \psi > 0,\ r/a < 0.8 \\ b & \psi < 0 \\ b(1 - \psi/0.17404)^2 & \psi > 0,\ r/a > 0.8 \end{cases}$$

[17] S. Yoshikawa, *Phys. Rev. Lett.* 27, 1772 (1971).

where ψ is Yoshikawa's function normalized to zero at the edge of the island. Integrating along chords of observation gives the intensity patterns shown in Fig. 20(c).

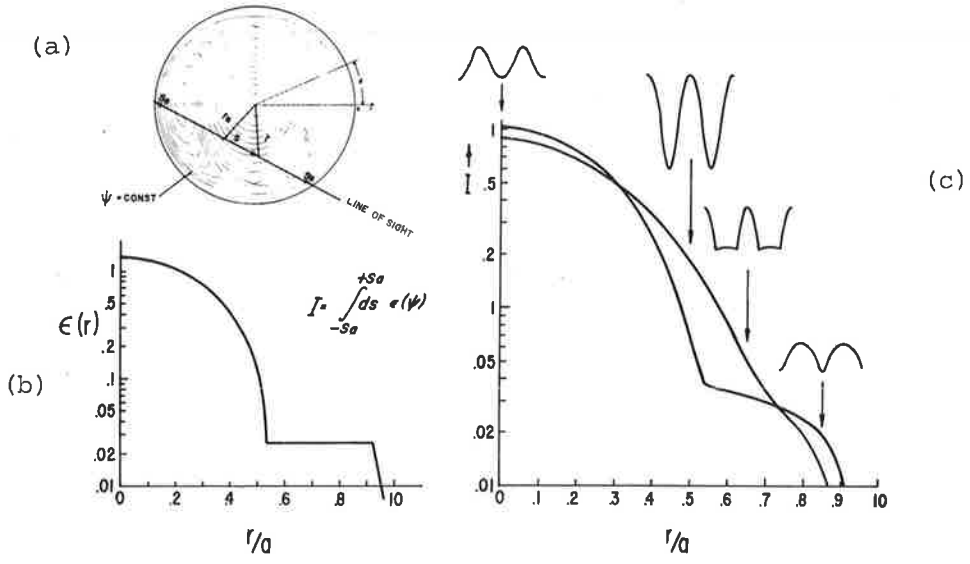

743889

Fig. 20. Theoretical prediction of expected m = 2 x-ray oscillations.

Rotations of the pattern produces oscillations between the maximum and minimum lines, with time shapes at different radii as shown. These calculations qualitatively reproduce some of the features of the observed intensities shown in Fig. 19. Further analysis is being carried out using the tearing mode patterns of Furth, Rutherford, and Selberg.[16,18]

4. Impurities

a. Radial Distribution of Z. Studies of the x-ray intensity in the 3-10 keV region have been used to try to determine the quantity and distribution of impurities in the plasma.[19] This radiation is mostly recombination, and the intensity depends on the elements present, the states of ionization, and the temperature. Attempts have been made both to calculate and to measure the ionization states of iron.

The measurement of ionization state consists of an investigation of the K_α -line shift of iron.[20] The shift results from a reduction in shielding of the nuclear charge as electrons are removed from the L-shell in the process of ionization. Figure 21(a) shows a spectrum in the region 6.4 to 6.7 keV obtained in a discharge with 1200 eV central electron temperature.

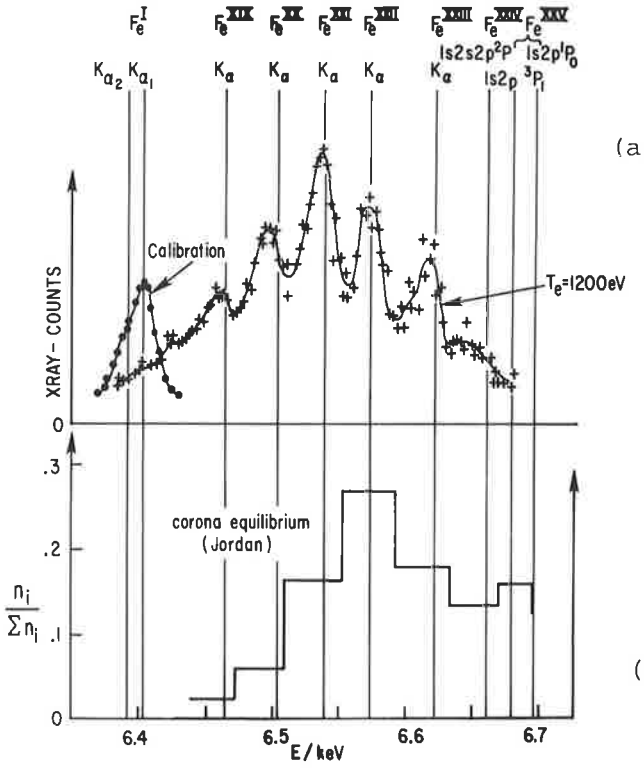

743749

Fig. 21. Spectrum of iron K_α -line structure. (a) Measured spectrum at central electron temperature T_e = 1200 eV(+); neutral K_α -line showing resolution of Bragg spectrometer (.); line identification from Ref. 20. (b) Relative population of ionization states predicted by Jordan (Ref. 21) for corona equilibrium at T_e = 1200 eV.

---

[19] N. Bretz, *et al.*, *Fifth Conference on Plasma Physics and Controlled Nuclear Fusion Research, Tokyo, Japan* (Nov. 11-15, 1974), Paper IAEA CN-33/A3-1; also Princeton Plasma Physics Laboratory MATT-1077 (1974).

The instrument used was a commercially available Bragg Spectrometer with a LiF crystal, looking tangentially to the magnetic axis of the plasma. Its resolution can be deduced from the neutral-iron K_α-line — also plotted in Fig. 21(a) — which was produced by fluorescence from an x-ray tube. The indicated classification of the "satellites" follows that of Lie and Elton.[20] The figure shows that for ST conditions ionization takes place in the L-shell, which contains 2 to 5 electrons at T_e = 1200 eV.

These measurements are compared with calculations balancing ionization and recombination. The computations of Jordan[21] indicate that dielectronic recombination is the dominant recombination process, with $\alpha_{diel} = 10^{-11}$ to $3 \cdot 10^{-11}$ cm^3/sec in the range of interest. The calculations, however, refer to the solar corona; at the higher densities of the tokamak, dielectronic recombination may be somewhat reduced. Recent calculations of Mertz, et al.,[22] confirm this. On the other hand, in the tokamak, the lifetime of the ions is important. Typical values of $1/n_e\tau$, where τ is the appropriate particle confinement time, are in the range 10^{-11} to 10^{-12}. Probably somewhat larger values should be used in a comparison with the recombination rate, because an ion recombines in the outer, cooler plasma regions rather than at the wall. In Fig. 21(b) is plotted the relative population of various ionization states, as calculated by Jordan.[21] These calculations probably overemphasize the population of helium- and lithium-like states, which have smaller dielectronic recombination and are probably determined more by particle loss. The relative intensities of the K_α satellites can be determined from the concentrations, if the excitation functions are known. Calculations by Cowan,[23] based on Gabriel's[24] theoretical considerations, give K_a- spectra qualitatively very similar to the observed ones. Perhaps quantitative agreement might be established in the PLT Tokamak.

Knowing the charge state of the ions, we can calculate the emitted recombination radiation and can compare x-ray and vacuum-UV determinations of the amounts of impurities. The measurements agree within a factor of 2, the x-rays tending towards somewhat higher concentrations than the vacuum UV.

---

[20] T. N. Lie and R. C. Elton, *Phys. Rev. A* 3, 865 (1971).

[21] C. Jordan, *Mon. Not. R. Astr. Soc.* 148, 17 (1970).

[22] A. L. Mertz, et al., private communication.

[23] R. D. Cowan, private communication.

[24] A. H. Gabriel, *Mon. Not. R. Astr. Soc.* 160, 99 (1972).

Representative x-ray intensity data are shown in Fig. 22. Figure 22(a) shows Thomson-scattering measurements of electron temperature and density profiles taken at a time (70 msec) during the steady-state part of the discharge.

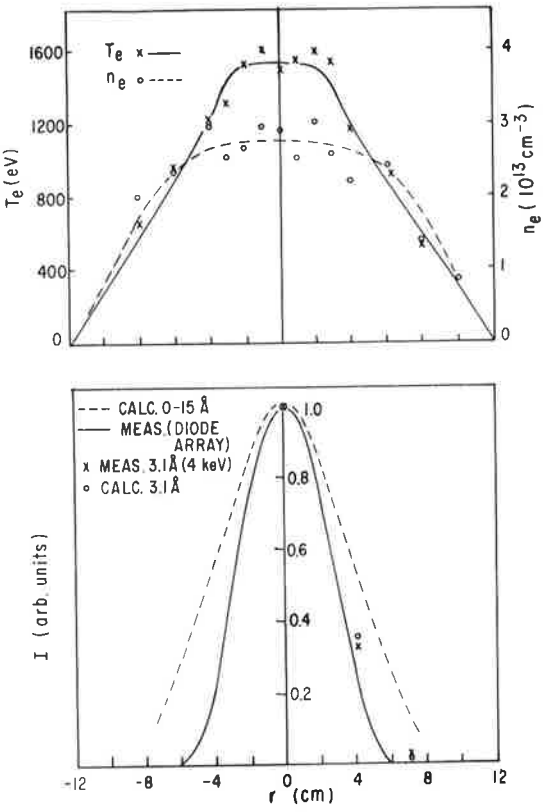

(a)

(b)

743125

Fig. 22. X-ray and extreme UV intensity profiles. (a)Electron temperature and density profiles. (b) Radiation intensity versus chord radius. Crosses (x) are measured x-ray intensity at λ=3.1 Å; circles (o) are corresponding calculated intensities of Z=1 bremsstrahlung normalized to central value by a factor of 50. Solid line is measured extreme UV intensity; dashed line is calculated Z=1 bremsstrahlung (0-15 Å) normalized by a factor of 400.

In Fig. 22(b) the crosses (x) show relative x-ray intensity (at λ = 3.1 Å) observed along chords at three different radii; the circles (o) are the corresponding relative radiation intensities calculated from the temperature and density profiles, assuming a uniform distribution of impurities. The normalizing factor for absolute intensity at the center is 50 times the Z = 1 bremsstrahlung intensity. Interpreted as recombination radiation, these data give $\bar{Z} \cong 7$); therefore we conclude that the concentration of impurity is uniform to within a factor of 2.

Evidence on impurity distribution also comes from the x-ray oscillation measurements discussed above. The m = 1, n = 1 oscillations extend to about r = 3 cm, and according to MHD theory should be bounded by the q = 1 surface. Assuming the loop voltage to be independent of radius and using Spitzer conductivity, we find the value of $\bar{Z}$ within the central 3 cm radius to be equal to that for the whole aperture within an experimental error of ±50%.

Our x-ray intensity profiles are similar to those in the T-4 Tokamak,[25] which are attributed to impurity peaking in the center. This explanation does not apply in the ST plasmas. The difference is that the T-4 temperature profile (determined from x-ray measurements) is apparently much broader than the ST profile (from Thomson scattering).

b. Extreme-UV Radiation. Some data have been taken with a new diagnostic instrument designed to complement the x-ray and vacuum UV data with measurements in the extreme UV range (5-20 Å).[19] This instrument consists of a windowless version of a commercially available self-scanned array[26] of 128 silicon diodes, each measuring ~ 0.0005 × 0.040 cm. This array is placed behind a slit designed for good space resolution; a set of thin metal filters arranged on a wheel gives some crude spectral resolution. Some further description of this instrument is given in Ref. 19.

Typical results are shown in Fig. 22(b) with the x-ray data taken for the same run, after a fairly extensive opening of the ST machine. Vacuum UV measurements for this particular discharge are not available, but past measurements show that such a discharge has oxygen as its dominant impurity, ~ 10%, with smaller amounts of iron, ~ 0.2% and molybdenum, ~ 0.3%. The electrical behavior of the discharge and the electron temperature and density profiles show the character expected for this type of discharge.

In Fig. 22(b) the solid line shows the measured spatial distribution of the emission plotted versus chord radius. The dashed line is calculated as follows: from the electron temperature and density profiles, the Z = 1 bremsstrahlung intensity has been integrated from 0-15 Å, integrated along chord, and plotted against chord radius. This has been normalized to the observed intensity at the center by multiplying by a factor of 400.

The region of emission is extremely narrow, corresponding approximately to the flat-topped region in the temperature profile. As discussed above, the x-ray measurements ($1 < \lambda < 4$ Å) indicate that this strong peaking cannot be attributed to a concentration of high-Z material in the center. The possibility

---

[25] V. A. Vershkov and S. V. Mirnov, Kurchatov Institute Atomic Energy Report IAE-2298, (Moscow, 1973); also Princeton Plasma Physics Laboratory MATT-TRANS-113 (1973).

[26] RL 128A/17 and RS-2C/128A, Reticon Corp., Mountain View, California.

that the signal is due to visible light from a reflection or incandescent spot on the vacuum wall is excluded, because the entire signal was eliminated by inserting a 0.5 mm piece of polished calcium flouride, which cuts out the extreme UV and transmits the visible light over the entire region where the diodes have any sensitivity to visible light.

The emission appears to be stronger and narrower than expected from bremsstrahlung or recombination radiation, and therefore is most probably line emission. If the observed radiation is line emission, the strong intensity peaking can be explained by assuming that the radiation comes from ions that are produced only at temperatures above about 1200 eV. A crude determination of the energy of the emitted photons can be obtained from absorbing filters. A 0.0013 cm Be filter attenuates the signal by a factor of 4, and a 0.0043 cm Al filter by a factor of 8. From Be and Al transmission curves it can be concluded that most of the radiation lies to the long-wavelength side of 12 Å. Of the radiation transmitted by the Be filter, about half must lie in the region of the Al K_α absorption band from 4 to 8 Å. The exact source of the radiation cannot be determined without better spectral resolution, but there are lines from the L-shell of Fe and from the M-shell of Mo in this spectral range.

In Figs. 23(a) and (b) are plotted, respectively, the diameter (full width at half height) and relative peak intensity of the emission versus time.

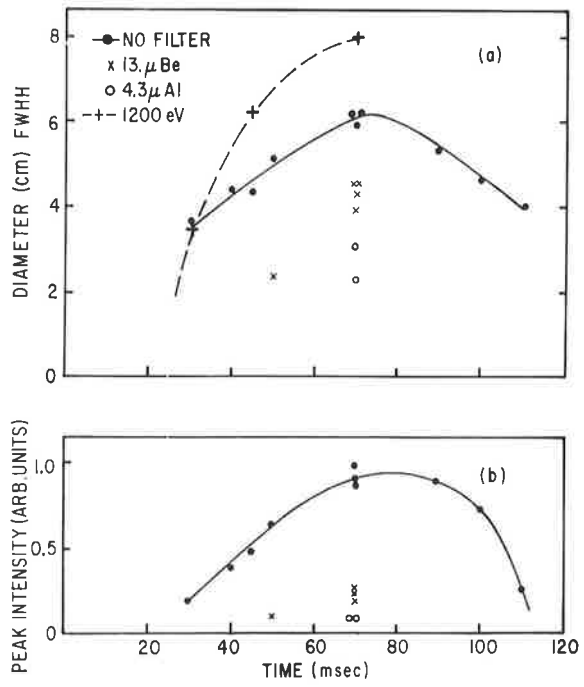

(a)

(b)

743642

Fig. 23. (a)Time variation of full width at half height of extreme UV signal from silicon detector array. no filter; x 13 micron Be; o 4.3μAl; + 1200 eV contour. (b) Relative peak intensities for same conditions as for (a).

It can be seen that at 30 msec the width is even less than that shown in Fig. 22(b) (t = 70 msec) and increases in time. The radiation first appears at about the time when the center of the plasma reaches 1200 eV . At first, the profile width is about that of the 1200 eV contour; later it broadens with time, but not as much as the 1200 eV contour; this might be expected if the center intensity increases disproportionately because the increased temperature in the center brings in more lines at shorter wavelength. The increase in intensity with time is expected if the effective diameter of the radiating source increases as the temperature increases. It is not consistent with a concentrating of high-Z impurities into the center.

A crude estimate of the power radiated in the 0-15 Å region and of the number density of the emitting species can be obtained as follows. From the known solid angle of the slit, the peak observed emission intensity is approximately 0.45 W/cm^2, i.e., 0.075 W/cm^3, using 6 cm as the diameter of the emitting column. When absorption of the diode silica coating in the 12 Å region is taken into account, and a correction is applied for the effect of scattering and x-ray fluorescence, it is concluded that 0.2 W/cm^3 is a reasonable estimate for the emission in the spectral region from 0 to 15 Å.

Using this value of radiated power ($\sim$ 0.2 W/cm^3) and assuming a highly allowed $\Delta n = 1$ transition (the 11.9 Å line of Fe XXII, for example), the number density of the emitting species is calculated to be $\sim 2 \times 10^{11}$ cm^{-3} ($\sim$ 1% of electron density). In view of the crudeness of the estimate, this is in reasonable agreement with the vacuum-UV and x-ray measurements.

Further development of the silicon diode technique, coupled with crystal-spectrometer measurements, can be expected to be very useful in analyzing the radiation in this important extreme UV region.

lD 1. MATT-1022 The Role of Atomic Physics in the Quest for CTR by E. Hinnov

The interpretation of the plasma behavior in the various devices of controlled-thermonuclear-reactions research, of which the tokamak is a particularly interesting example, has been vitally dependent on quantitative atomic-physics data. Determination of plasma composition, electrical resistivity, radiative-energy losses, recycling rates (and hence the confinement times) would be impossible without the knowledge of the energy levels and transition rates of various atoms. In the past, the light elements, primarily H, He, O and C, about which reasonably adequate data exist, have been of substantial importance. However, with increasing plasma temperatures and confinement times, metallic elements such as Fe, Cr, Mo, W, and others are becoming increasingly prominent; in many cases the necessary basic data are inadequate or completely absent. In this paper, we review the type of data and measurements that have been useful in the past CTR research, and point out some of the areas of *terra incognita* that will be of acute interest in the future.

ID 2. Plasma Loading and Wave Generation for ICRH in the ST Tokamak,* by J. Adam, W. Getty, W. Hooke, J. Hosea, F. Jobes, R. Sinclair, and H. Takahashi

Plasma loading and wave generation for two out of phase half-turn loops operating at 25 MHz are being investigated on the ST Tokamak at power levels up to 1 MW. The equivalent series resistance $R_S = P_{rf}/I_{rf}^2$, measured as a function of $\Omega = \omega/\omega_{ci}(r=0)$ and plasma density, is found to be in good agreement with the predictions of the cylindrical theory. R_S values as high as several ohms are obtained at high densities giving wave generation efficiencies well above 90%. Loading near $\Omega = 1$ and 2 is apparently independent of power level. Measurements of B_{Zrf} at 20 locations about the torus reveal the predicted wave generation: M = 0, +1 slow waves in the vicinity of $\Omega = 1$, m = -1 fast waves after the expected onset (usually $\Omega \gtrsim 1$), and m = 0, +1 fast waves for higher Ω. Toroidal eigenmodes accompanied by large loading are detected for the fast waves when the damping lengths are long.

---

*Presented at the *Second Topical Conference on RF Plasma Heating*, (Lubbock, Texas, June 22-24, 1974)

ID 3. MATT-1107 Mode Conversion and Harmonic Generation at the Upper Hybrid Layer, by J. J. Schuss and J. C. Hosea

A theoretical understanding of harmonic generation at the upper hybrid layer is important to the employment of this mechanism for poloidal field measurements in tokamak plasmas.[1] We have formulated and numerically

---

[1] R. Cano, et al., *Sixth European Conference on Controlled Fusion and Plasma Physics* (Moscow, 1973), Vol. 1, p. 195.

solved equations that predict the complete conversion of an extraordinary wave into a Bernstein wave at this layer; the backward Bernstein mode is absorbed in the vicinity of the cyclotron layer. [This absorption offers a method of electron heating in toroidal plasma.] This solution predicts the backward harmonics and power level found experimentally, which were not predicted by previous theory.[2] This solution also possibly explains the local harmonic signal observations of the French experiment.[3]

---

[2] I. Fidone, et al., *Phys. Fluids* 14, 737 (1971).

[3] R. Cano, et al., EUR-CEA-FC-613 (France, Sept., 1971).

II. TOROIDAL DEVICE FABRICATION AND DESIGN STUDIES

A. Princeton Large Torus (PLT) Fabrication

A detailed consideration of the PLT fabrication program is to be found in the section of this report concerned with engineering. Here we report only on some highlights.

As the year began, we had arrived at a stage of fabrication where, for the first time, some preassembly of components was underway. A major accomplishment, early in the year, was the completion of all toroidal field coils, on time and on cost. A second important event was that the OH Rectifier/Switch system met all specifications during full power tests at the factory.

The initial assembly of the substructure and structure at C-site was begun three weeks later than the schedule date, which had been set almost two years earlier. Of the three weeks, two were due to fabrication delays and one was to allow for some last-minute experiments on the ST Tokamak. The disassembly of the ST and initial PLT site preparation went smoothly, but an additional two weeks' delay developed when some problems developed at final assembly of the structure.

An intensive program directed toward recovering schedule resulted in the beginning of TF coil power tests (in final toroidal configuration) only one week behind the original schedule. These tests showed the coils to be thermally satisfactory, but also showed deflections under load to be several times the calculated values. It was not clear whether these increased deflections could have serious consequences, but it seemed prudent to make extensive further measurements before concluding power tests at year end.

The year also saw the successful completion of a one-meter diameter, hard-vacuum sealed, high-alumina ceramic break for use in the PLT vacuum vessel. Nothing even approaching this size has ever been done before anywhere in the world. The vacuum vessel itself was completed, assembled into a torus, and demonstrated to be mass-spectrometer leak-detector tight. This complete system was delivered to the assembly site just before the end of the year.

During the year both the OH and SF power supply systems were delivered by their manufacturers and installed at PPPL by the installation contractor. At year end, final acceptance tests were underway on both systems.

A major disappointment was the failure to obtain a satisfactory casting for the PLT center column. Repeated efforts to salvage the casting were unsuccessful, leading finally to abandoning this approach. It was consequently necessary to design and construct, on a crash basis, a temporary column which was used during rf coil power tests and which will be used to provide the required pre-load on the OH and SF windings at assembly and for first operation of the machine. A new demountable permanent center column is now in the design stages. It will be installed upon completion late in 1975.

During the year (October) approval was received to begin work on the power supplies for neutral beam injection in PLT. These are to permit injection of up to one megawatt of 40-keV neutrals from each of four guns operating simultaneously. The system is scheduled for final operation in October of 1976, but may be accelerated.

Finally, considerable effort has gone into the planning and initial fabrication of a great variety of diagnostic instrumentation. The goal is to have virtually all standard diagnostics ready to go at the time the machine assembly is complete. Some of these are relatively simple, but others, such as a Thomson-scattering laser system that gives a temperature profile in one shot, are sophisticated advances in the state of the art.

Our current expectations are that first plasmas will be available in the fall of 1975.

B. Poloidal Divertor Experiment (PDX) Fabrication

The PDX proposal, Special Report 74/2, was approved in June 1974. Presently the device is scheduled for operation in October 1977 with a total fabrication cost including escalation and contingency of 17.3 million dollars. The status of PDX engineering is given under major projects in the Engineering and Development section of this report.

The fundamental objective of the PDX device is to evaluate the effectiveness of poloidal divertors, magnetic limiters and other techniques for controlling impurities in large high-temperature collisionless tokamaks. PDX has been designed with a large degree of experimental flexibility that will allow several poloidal divertor configurations, plasma startup sequences and plasma cross-sections to be easily investigated.

Assuming that the PDX divertor experiments are successful, PDX will provide a unique toroidal plasma which can be used to:

(1) Determine confinement scaling versus collisionality using divertor control of the effective Z and neutral beam control of plasma temperature.
(2) Optimize the plasma cross-section under conditions of relatively "flat" current distributions which are produced using magnetic limiter control of the skin effect and divertor control of neutrals and impurities.
(3) Study the effects of two-component plasmas in a neutral-free environment.

A key feature of the PDX device (Fig. 1) is the demountable toroidal coil system, which allow the internal divertor coils and vacuum vessel to be assembled as a sub-unit, and then allows the toroidal field (TF) coil system to be assembled around this sub-unit, using the TF coil-joint clamp.

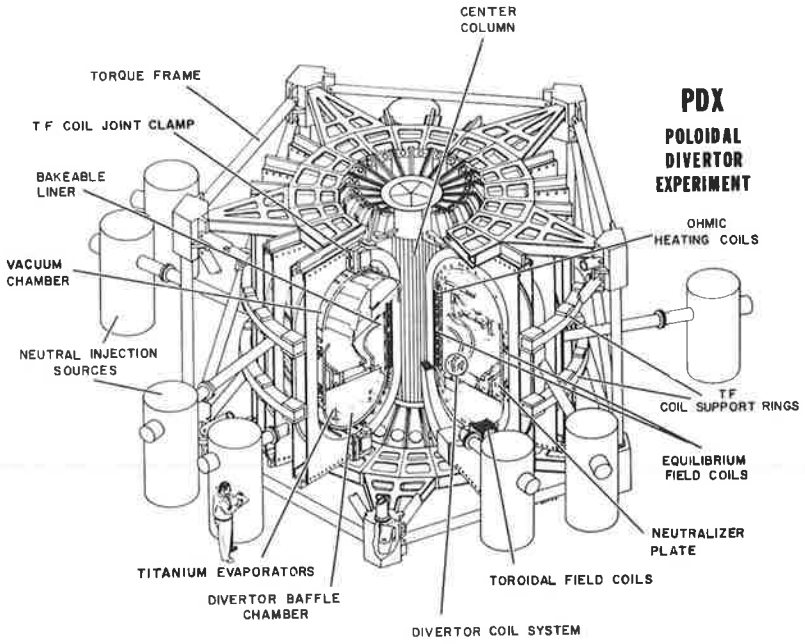

753247

Fig. 1. Isometric View of the PDX device.

This assembly technique allows simultaneous fabrication of the toroidal and poloidal coil systems, resulting in a shorter total fabrication time than that achieved using the PLT poloidal coil fabrication technique. Other features of PDX are an air-core ohmic heating transformer, internal divertor coils, and a bakable vacuum liner with titanium gettering in the divertor burial chamber. The torque frame structure is 15 feet high and 26 feet in diameter. The vacuum vessel volume is 3.7×10^7 cm^3, which is five times the volume of the PLT vacuum vessel.

The overall size of PDX was chosen to make maximal use of the existing power supplies at PPPL. All of the large motor generator sets will be required for the TF and DF systems. Also, the PLT OH and vertical field power supplies will be used for the corresponding fields on PDX. PDX will be located in the high-bay area now occupied by ATC and FM-1.

The basic parameters of PDX are summarized in Table I. Neutral beam heating (2-4 MW) will be provided, using the PLT high-voltage

power supplies, thereby allowing the plasma temperature to increase into the 2-4 keV range, according to estimates using the "6-regime" tokamak transport computer code.

TABLE I

PDX Parameters

	Diverted	Undiverted
Plasma		
minor radius a	47 cm	57 cm
major radius R	145 cm	145 cm
toroidal field $B_T(R)$	24 kG	24 kG
plasma current $I_p (q = 3.6)$	500 kA	700 kA
plasma temperature* $(T_i \simeq T_e)$		
ohmic heating	1-2 keV	
1 MW auxiliary heating	2-4 keV	
plasma density, n_e	4-8 x 10^{13} cm^{-3}	
confinement time* $(\tau_p \simeq \tau_E)$	0.3 sec	
Heating		
Ohmic heating	0.3 MW	
neutral beam	4.0 MW @ 0.3 sec	

* estimated from transport code (6-regime model).

The present poloidal-coil system is shown in Figure 2, for the standard 500 kA plasma current.

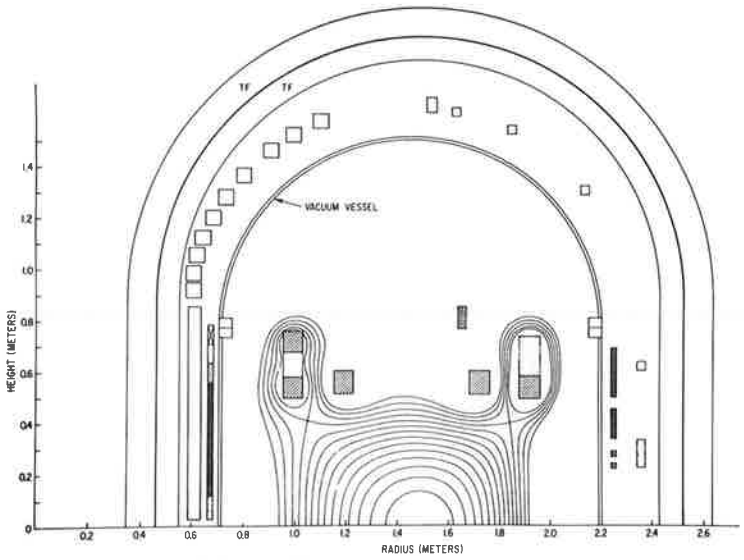

Fig. 2. The PDX poloidal coil system.

This design is substantially improved over the initially proposed PDX design, with regard to both physics and engineering requirements. The divertor field (DF) coils are driven by two of the large generators and provide the basic four-lobe divertor field structure. The equilibrium field (EF) is driven by a programmed power supply and provides the vertical field required for plasma equilibrium. A double-inside divertor, with a "D" shaped plasma, can be produced by simply increasing the EF current above the value used in Fig. 2, while a double-outside divertor, with an "inverse D" shaped plasma, is produced by decreasing the EF coil current. The plasma discharge is initiated at a major radius of 1.15 meters by causing a hexapole null in the poloidal field to form transiently at this point, away from material walls or limiters, using the pulsed null-field (NF) coil system. As the plasma current increases, the compression field (CF) coil current is increased, to provide the proper shape for the vertical field and hence the plasma, as the plasma moves from R + 1.15 meters to 1.45 meters. This start-up sequence maintains a very nearly linear relationship between the plasma current and plasma cross-sectional area inside the divertor separatrix, thereby providing a linear expanding magnetic limiter suitable to suppress the skin effect. During this start-up phase the

plasma has a "D" shaped cross-section, and the divertor separatrices of the double-inside divertor pass comfortably through the divertor throats. Standard round plasmas with currents up to 700 kA can be generated simply by not energizing the DF, CF and NF coil systems. The present ohmic heating system is capable of inducing 900 kA plasmas (Z = 1), lasting for longer than 0.5 sec with a risetime of 30 msec.

The present divertor field design has a 10-15 cm wide divertor scrape-off entering the divertor burial chamber. This will allow the formation of a shielding divertor, on the basis of either the usual plasma particle loss or by means of external plasma sources.

The divertor baffle structures are still being designed but will probably be made from titanium sheets, since tests at PPPL indicated no flaking of titanium films that were evaporated onto titanium plates. Also, measurements of the sticking probabilities of room-temperature molecular and atomic hydrogen on titanium films indicated sticking probabilities for molecular hydrogen of 5%, while atomic hydrogen had a sticking probability of at least 20%. An experiment is being designed to investigate the pumping speed of a model divertor chamber that is fed with warm (20 eV) hydrogen plasma. This test should give us a reliable estimate for the pumping speeds of the PDX divertor.

Studies of vacuum surfaces are an important part of PDX operations. Presently we are studying the sputtering of various wall materials. Theoretical studies of plasma behavior in a divertor tokamak using the computer code are described in the theory section, along with studies of the MHD equilibrium and stability of PDX plasmas.

C. Two-Component Torus (TCT) Conceptual Design

At the beginning of 1974, PPPL and Westinghouse Electric Corporation undertook a joint conceptual design study for a tokamak fusion test reactor (TFTR), based on the two-component-torus (TCT) principle. By July 1974, a preliminary conceptual design of the TCT device was in hand[1] (Fig. 1). This design was selected by the Atomic Energy Commission for submission as a proposal for a TFTR device, to be constructed at PPPL.

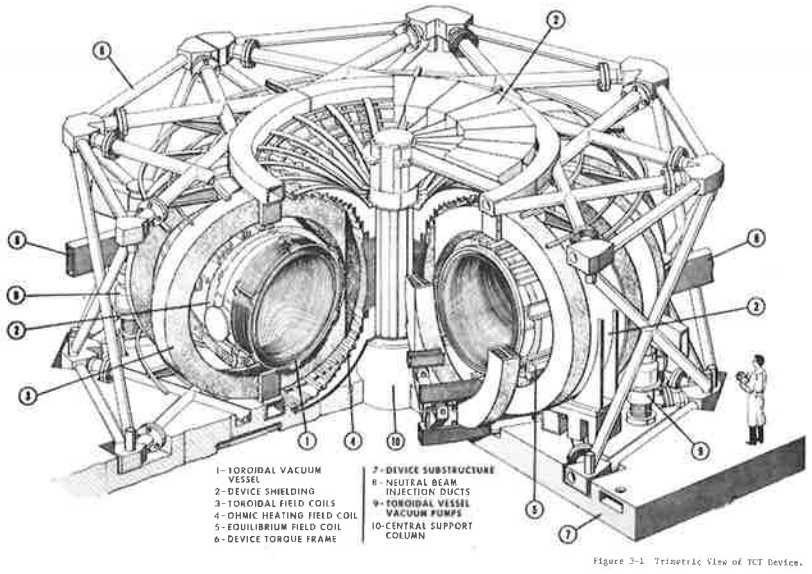

Figure 3-1 Trimetric View of TCT Device.

743494

Fig. 1. Preliminary conceptual design of TFTR.

The device parameters of the July 1974 conceptual design are given in Table I. Some typical operating scenarios are illustrated in Fig. 2.

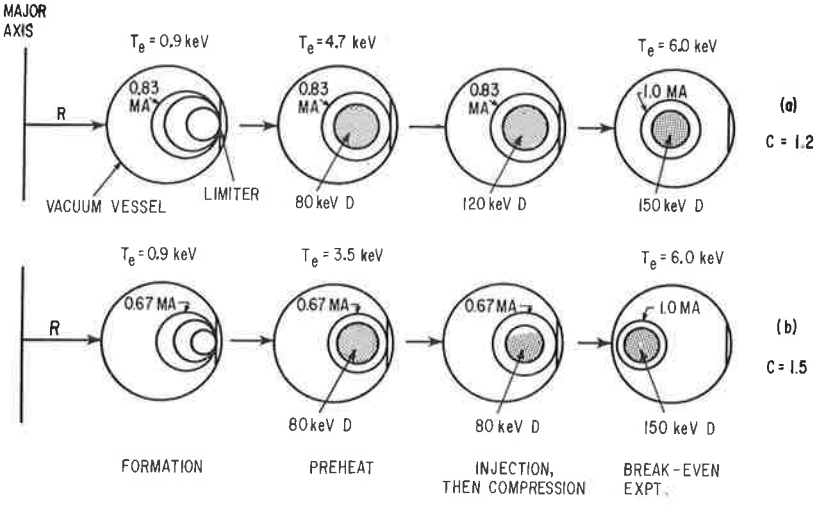

753030

Fig. 2. Typical operating scenarios of TFTR.

---

[1] Two Component Torus Joint Conceptual Design Study, Plasma Physics Laboratory and Westinghouse Electric Company, July 1974.

In initial operation, the TCT is envisaged as a device for investigating the physics of large "hydrogen" plasmas. After attainment of the desired plasma objectives ($T_e \gtrsim 5$ keV, $n_{\tau E} \gtrsim 10^{13} cm^{-3} sec$) the TCT is to be operated with tritium plasmas and injected deuteron beams, giving approximate energy break-even (in terms of fusion power relative to injected power), and generating alpha-particle densities comparable to those in standard tokamak fusion reactor designs (i.e., a few tenths of a watt per cm^3). The relatively high fusion power density and low $n\tau_E$-requirement for break-even are obtained by virtue of the two-component principle.[2] Extensive recent work on the theory of the TCT is reviewed in Section IIIB of the present report.

During the second half of 1974, the TCT conceptual design was refined.[3] While the basic parameter objectives and design features of the July study were maintained, a number of improvements and simplifications were introduced, and more detailed designs and cost estimates were prepared. In particular, the generator facility was redesigned to increase its versatility. The December study concludes that the physical size of the device should be reduced somewhat in order to effect necessary economies, and that this could be done by a rearrangement of the TCT coil systems. Further design refinements, incorporating this idea are currently in progress.

---

[2] J. M. Dawson, H. P. Furth and F. H. Tenney, *Phys. Rev. Lett.* 26, 1156 (1971)

[3] Two Component Torus Joint Conceptual Design Study, Plasma Physics Laboratory and Westinghouse Electric Company, Addendum 1, December 1974

TABLE 1.

SUMMARY DESCRIPTION
TCT REFERENCE DESIGN

VACUUM VESSEL	
Inner Minor Radius	1.2 m
Major Radius	2.8 m
Material	AISI 305 SS
Construction	Bellows, Ring-stiffened shells
TOROIDAL FIELD COILS	
Number	20
Construction and type	Inconel-stiffened, water cooled copper
Inner Bore	3.2 m
Maximum Field (at inner bore)	10 T
Coil Current	71 kA
Flattop Time at Maximum Field	1 sec
Stored Energy	1548 MJ
OHMIC HEATING COILS	
Type	Water-cooled copper, air core
OH System Flux Swing Capacity	13.8 volt-seconds
Plasma Current Capability	2.5 MA
Plasma Current Rise	50 msec
Plasma Current Duration	0.5 sec
Primary Current: for 1.0 MA Plasma	14.2 kA
for 2.5 MA Plasma	27.5 kA
Primary Induced Voltage Capability	115.7 kV
Stored Energy	39.8 MJ
EQUILIBRIUM FIELD COILS	
Type	Water-cooled copper
Flattop Capability	0.5 sec
Coil Current: for 1.0 MA Plasma	15.0 kA
for 2.5 MA Plasma	21.2 kA
NEUTRAL BEAM INJECTION SYSTEMS	
Number	8
Plasma Heating Injectors	6-80 kV Systems
Total Plasma Heating Beam Current	510 A, D°
Fusion Reaction Injectors	2-150 kV Systems
Total Fusion Reaction Beam Current	72 A, D°
POWER SUPPLIES	
Capability of Stored Energy Source	540 MW
Total Energy Storage Capability	3.40 MJ
Peak Utility Power Demand	30 MW

III. THEORY

A. Introduction

The past year was characterized by the unusually large fraction of the theoretical division's effort that was devoted to the interpretation of results from the major experiments, and to problems arising in the conceptual design of future devices. Thus, most of the MHD group were involved in detailed equilibrium and stability computations in connection with the PDX device, and our code development program in this area progressed well. The low-frequency microinstability work had many points of contact with results from FM-1. In addition, a substantial analysis of possible high-frequency velocity-space microinstabilities in the TCT was completed. In rf heating theory, attention was focused on the interpretation of the results from the ICRH experiment on ST, and on a calculation of parametric thresholds for lower-hybrid heating, as is proposed for ATC. In particle-code simulation, initial results were obtained for cross-field transport in a toroidal geometry, and for transport from low-frequency microinstabilities.

This report has been divided into four sections: Equilibrium, tability, and Transport; Plasma Heating; Computer Simulation - Particle and Fluids; and Theoretical Research under the Air Force Contract.

B. Equilibrium, Stability, and Transport

1. MHD Analytic Theory

Several analytical studies have considered the effects of noncircular cross-sections on the magnetohydrodynamic stability of a toroidal plasma. In connection with a large, ongoing computational program, these calculations should be useful in understanding the stability of complex configurations like the PDX experiment, and in prescribing the most favorable cross-section for plasma confinement. The Mercier criterion for ideal MHD interchanges was evaluated for a large-aspect-ratio, uniform-current tokamak with arbitrary ellipticity and small triangular distortion, taking account of the geometry of the vacuum region (Abstract III B 1). This work supported the conclusion that small triangular distortions can stabilize such a configuration. The ideal m - 1 internal kink mode was found to be stable only for $q > 1$ on the axis in a tokamak with small ellipticity (Abstract III B 2), and the growth

rate in the elliptical case was found to greatly exceed that for a circular cross section. The stabilizing influence of favorable toroidal curvature on this mode in a circular tokamak would thus be negligible in an elliptic tokamak. A straight plasma column with a rectangular free boundary was found to be stable to infinitely long (k = 0) rigid displacements (Abstract III B 3). However, a displacement with a small m = 3 perturbation led to instability. An extensive study of resistive MHD modes in an arbitrary shaped torus led to a better understanding of the relations among the ideal interchange, the resistive intercharge, the tearing mode, and a new modified tearing mode (Abstract III B 4). Sufficiently favorable average curvature was found to stabilize all of these modes. The criteria obtained in this work were incorporated into the computational program (Abstract III D 13). Another analytical work closely related to the computational program (Abstract III B 5) used a Lagrangian technique, and a natural coordinate system, to study the ideal MHD stability of a straight, elliptical plasma column with uniform current and mass densities. Coupling between kink modes and Alfvén waves was found to be destabilizing.

2. Microinstability

The work on low-frequency microinstabilities was primarily focused on the linear theory of the dissipative trapped-electron modes and on the nonlinear evolution of the dissipative trapped-ion instability. For the dissipative trapped-electron modes a detailed analysis of the mode structure along the field lines indicated the existence of a class of "ballooning" modes in the case of weak shear (Abstract III B 6). The effects of finite-β on the trapped-electron instabilities was also determined (Abstract III B 7), and it was found that the coupling to Alfvén waves leads to significant stabilizing effects at sufficiently short perpendicular wavelengths. For the dissipative trapped-ion mode the nonlinear evolution of the instability was investigated both analytically (Abstract III B 8) and numerically (Abstract III B 9). The basic saturation process studied here was the nonlinear transfer of energy from the long-wavelength instabilities to short wavelengths, where ion bounce resonance damping dominates. A different nonlinear mechanism arising from anomalous velocity-space scattering was also considered (Abstract III B 10) and found to aid in stabilizing the

longer wavelength modes. Except for the finite-β analysis, conclusions of much of the above work, together with a discussion of the effects of shear on the dissipative trapped-electron mode, were summarized in an IAEA Tokyo paper (Abstract III B 11).

3. Two-Component Tokamak

The stability of two-energy-component plasmas to velocity-space modes and finite-medium modes has been examined in detail (Abstract III B 12-15). For tangential or isotropic injection and for injection speeds less than the Alfvén speed, all velocity-space modes are stable, with the possible exception of weak loss-cone modes in the case of a plasma with $Z_{eff} >> 1$ (Abstract III-B 12-14). The only beam-driven finite-medium instability occurs in the ion branch of the shear-Alfvén wave. This mode arises because of resonances of the Alfvén frequency with harmonics of the beam-ion ∇B drift frequency (Abstract III B 12, 14, 15), and would result in a flattening of the beam profile near the magnetic axis.

Finite ion temperature can significantly increase the fusion gain of two-component plasmas, because of energy dispersion and changes in fast-ion drag and beam-plasma reactivity (Abstract III B 16). A Fokker-Planck code has been used to follow the energy dispersion and pitch-angle scattering of beam-injected ions during a slow-radius compression of the tokamak plasma, and the resultant fusion energy gains have been compared with analytic calculations (see Abstract III D 21). The operation of a two-component plasma in which the suprathermal component is produced by harmonic ion-cyclotron resonant heating was investigated, and the performance found to be less favorable than that of the beam-injected scheme (Abstract III B 17).

A pulsed tokamak reactor was considered in which a fractional-sized plasma core is heated to ignition by means of injected beams and major-radius compression, while the bulk of the cold plasma is ignited by means of a propagating thermonuclear burn. For large plasmas, fusion energy gains much greater than 10 can be achieved with pulse times ~5 seconds (Abstract III B 18).

4. Transport

Certain aspects of neoclassical transport theory were further extended. For an axisymmetric tokamak it is well known that poloidal rotation decays

rather rapidly, especially in the more collisionless regimes, but that toroidal rotation decays much more slowly. With a small non axisymmetry, such as a field ripple, it was shown that toroidal rotation also decays rapidly. (Abstract III B 19). Small non axisymmetries of the kink-mode type, with amplitudes similar to those commonly observed, were shown to lead to significant superbanana-type diffusion in the collisionless regimes typical of future experiments (Abstract III B 20). In connection with impurity diffusion in tokamaks, the neoclassical theory was completed with a detailed treatment for the Pfirsch-Schluter regime (Abstract III B 21).

The anomalous transport observed in the computer experiments of Okuda and Dawson (particle simulation) has motivated a re-examination of the basic theory of fluctuations and transport in magnetized plasma (Abstract III B 22, 23). Thus far this investigation has been confined to the regime of very strong fields where the low-frequency ($\omega < \nu$) long wavelengths ($k_\perp \rho_i < 1$) hydrodynamic fluctuations dominate the transport because of their long autocorrelation time. It is found that the usual hydrodynamic description (where the transport coefficients are local in space and time) must give way to a general non-Markovian one (where the transport coefficients are nonlocal in space and time). In this non-Markovian description the hydrodynamic fluctuations themselves contribute to the transport coefficients determining their regression.

For example, the anomalous ion-shear viscosity μ has been studied from the point of view of the Generalized Langevin Equation. In the renormalized bilinear mode-coupling approximation of this theory, the result is

$$\mu\ (k,\ s) = (v_{Ti}^2/2\ \pi n)^{1/2}\ (1+\Omega^2{}_i/\omega_{Pc}^2)^{-1/2} \left(\frac{1}{2}\ \ell n\ \frac{(s\ +\ 2\mu\ k_c^2)}{(s\ +\ 2\mu\ k^2)} \right)^{1/2} .$$

The result is essentially the same as those obtained from the simpler Landau-Placzek method and is in excellent quantitative agreement with the particle diffusion coefficient and mode autocorrelation function as given by Okuda and Dawson. Because of the long lifetime of the hydrodynamic modes, it is predicted that the momentum flux autocorrelation function decays as t^{-1}. These long-time tails have been observed in the computer experiments. The

heat conduction mode has been treated in a similar fashion. We are now able to extend the theory to weaker magnetic fields and hence to regimes where other classes of fluctuations (hybrid waves, drift waves, etc.) may dominate the transport.

IIIB 1. MATT-1063 Localized Magnetohydrodynamic Instabilities in Tokamaks with Noncircular Cross Sections, by J. L. Johnson, K. E. Weimer, E. A. Frieman

Evaluation of the Mercier stability criterion indicates that localized modes should impose few constraints on the possibility of using tokamaks with noncircular cross sections. The importance of the details of the geometry in the vacuum region is noted.

IIIB 2. MATT-1059 Internal Kink Mode in a Diffuse Pinch with a Noncircular Cross Section, by Guy Laval

It is shown that the internal kink mode is no longer marginally stable within the kink mode order in a plasma with non-circular cross section. For a step current density with a small ellip-ticity, the internal kink mode becomes unstable as soon as the rotational transform exceeds 2π close to the magnetic axis.

IIIB 3. MATT-1063 Infinite Wavelength Kink Instabilities in Uniform Current Cylindrical Plasmas with Rectangular Cross Section,* by M. D. Rosen

The magnetohydrodynamic stability of a free-boundary straight plasma column with a slightly elongated rectangular cross section, carrying a uniform axial current, is investigated analytically. Axisymmetric modes ($n = 0$), for which the circular cross section case is marginally stable ($m = 1$) are considered. Stability is found for a rigid vertical displacement, in good agreement with numerical results. However, a vertical displacement with a small additional $m = 3$ like perturbation, localized near the plasma surface, leads to instability.

---

* Also presented at the *Sixteenth Annual Meeting of the American Physical Society*, 1974.

IIIB 4. MATT-1068 Resistive Instabilities in General Toroidal Plasma Configurations, by A. H. Glasser, J. M. Greene, and J. L. Johnson

Previous work on resistive instabilities is extended to

N.B. *The Sixteenth Annual Plasma Physics Meeting of the American Physical Society* was held in Albuquerque, N. M., from October 28-31, 1974.

finite-β systems. Let

$$D \equiv \frac{\langle B^2/|\vec{\nabla}V|^2\rangle}{\Lambda^2}\left[J'\psi'' - I'\chi'' + \Lambda\frac{\langle\sigma B^2\rangle}{\langle B^2\rangle} + p'^2\langle 1/B^2\rangle + \langle\sigma^2B^2/|\vec{\nabla}V^2\rangle - \frac{\langle\sigma B^2/|\vec{\nabla}V|^2\rangle^2}{\langle B^2/|\vec{\nabla}V|^2\rangle}\right],$$

$$H \equiv \frac{\langle B^2/|\nabla V|^2\rangle}{\Lambda}\left[\frac{\langle\sigma B^2/|\vec{\nabla}V|^2\rangle}{\langle B^2/|\vec{\nabla}V|^2\rangle} - \frac{\langle\sigma B^2\rangle}{\langle B^2\rangle}\right],$$

$\Lambda \equiv \psi'\chi''-\chi'\Psi''$, $\sigma \equiv \vec{J}.\vec{B}/B^2$; ψ, χ, I, and J are the toroidal and poloidal magnetic field and current fluxes, primes denote derivatives with respect to the volume V, and brackets denote field line averages. The ideal MHD interchange is stable if $D+H-1/4<0$. The resistive interchange is stable if $D+H^2<0$. Relations to the tearing mode and a new overstable mode are established.

IIIB 5. Long-wavelength Kink Instabilities in Low Pressure, Uniform Axial Current, Cylindrical Plasmas with Elliptic Cross Sections,* by R. L. Dewar, R. C. Grimm and J. L. Johnson

The desire for axisymmetric tokamak configurations with higher β and stronger ohmic heating currents at a fixed rotational transform, together with the observation that non-circular plasma cross sections may alleviate trapped particle instabilities, has motivated interest in configurations with non-circular cross sections. Detailed study of the magnetohydrodynamic stability of systems with realistic current and density profiles is not analytically tractable. For this reason we are developing a computational program to study the nature of the most unstable modes in such devices. It is essential that the development of the program be coordinated with analytic work on tractable special cases, where the analytic work can provide an indication of the accuracy of the numerical program. Analytic studies of such special cases are also useful because they produce insight into the physical mechanisms at work in the system. In the spirit of the above remarks we have investigated the magnetohydrodynamic stability of a straight plasma column with elliptic cross section, carrying a uniform axial current, by extremizing the Lagrangian of the system using a natural coordinate system based on the magnetic field lines. Stability criteria and eigenfrequencies are derived analytically for systems with uniform mass density inside the plasma. It is shown that coupling between kink modes and Alfven waves, produced by noncircularity, is a destabilizing

effect. A technique for solving the problem numerically is also discussed and used to demonstrate the effect of a spatially varying plasma density on the growth rate.

---

* *Supplement to the Australian Physicist*, 16 (1974)

IIIB 6. Mode Structure of the Trapped-Electron Instability,* by W. M. Tang, P. H. Rutherford, E. A. Frieman, and C. S. Liu

The mode structure of the dissipative trapped electron instability along the magnetic field lines is analyzed, and the effectiveness of shear stabilization is examined within this new framework. In the weak shear limit the eigenmode equation to lowest order has the same form as the integral equation encountered in the trapped-ion mode problem. A variational procedure yields the solution for the orbit averaged potential which maximizes the growth rate of the instability. To satisfy the requirement that the potential and its derivative be continuous, we include the ion sound term and solve the resultant differential equation as a boundary layer problem in the region of the field maximum, where the lowest order solution breaks down. For a step magnetic field this weak shear problem can be solved exactly without recourse to the above perturbation formalism. Modifications of these results when the shear increases are determined.

---

* *Bull. Am. Phys. Soc.* 19, 866 (1974); also presented at the *Sixteenth Annual Meeting of the American Physical Society*, (1974).

IIIB 7. Trapped-Particle Instabilities in Finite-β Tokamaks,* by P. H. Rutherford, C. S. Liu, W. M. Tang, and M. N. Rosenbluth

Since β, the ratio of plasma pressure to magnetic field pressure, generally exceeds the electron-ion mass ratio, m/M, in tokamaks, the coupling between the Alfvén and low frequency electrostatic modes can lead to significant effects. These electromagnetic modifications, which are usually ignored in dealing with trapped-particle instabilities, are taken into account in our analysis. In the trapped-electron regime, it is found that such effects are stabilizing for both the well-known temperature gradient driven collisional instability as well as for a universal (finite ion Larmor radius) type dissipative mode. The effect of shear is also treated within this context and stability criteria obtained. In addition, a new poloidal Alfvén mode associated with the presence of trapped ions is found and its properties analyzed. Nonlinear effects of these modes on plasma diffusion are calculated using energy-momentum conservation and the maximum bound on the available free energy.

---

* *Bull. Am. Phys. Soc.* 19, 866 (1974); also presented at the *Sixteenth Annual Meeting of the American Physical Society*, (1974)

IIIB 8. MATT-1096 Nonlinear Saturation of the Trapped-Ion Mode, by P. H. Rutherford, R. E. LaQuey, S. M. Mahajan, and W. M. Tang

A nonlinear model of the collisional trapped-ion mode in tokamak geometry is presented, in which the energy in long wavelength instabilities is transferred to short wavelength modes which are then damped by ion bounce resonances. Near marginal stability, the saturation of a single unstable Fourier mode is computed. Far from marginal stability, steady-state nonlinear solitary waves containing many Fourier modes are found. Particle transport is computed in both cases.

IIIB 9. Nonlinear Evolution of the Turbulence Arising from the Trapped-Ion Instability,* by R. V. Lovelace and W. M. Tang

The nonlinear evolution of plasma density fluctuations arising from the trapped-ion instability is analyzed with a model based on continuity equations for trapped ions and electrons and a quasi-neutrality condition (a similar model was first proposed by Kadomtsev and Pogutse). For typical frequencies, Re $(\omega) = k_y v^*$, much less than the electron trapping rate we find,

$$\frac{\partial N}{\partial t} - \gamma N = \alpha \left[\frac{\partial^2 N}{\partial y^2} \frac{\partial N}{\partial x} - \frac{\partial^2 N}{\partial x \partial y} \frac{\partial N}{\partial y} \right] - \beta N \frac{\partial N}{\partial y} \qquad (1)$$

where N is the fractional ion density fluctuation in a reference frame moving in the y direction with speed v^*; $\gamma = \gamma(k_y)$ is the linear growth/damping rate including Landau damping; α and β are constants; and the coordinates (x, y), $(r, r\theta)$. The time evolution of N has been followed over long periods $(>\gamma^{-1})$ by numerical integration of (1). A valuable check on the numerical solutions is provided by an "energy equation" for $\langle N^2 \rangle$ which is derived from (1). For cases where the β term is negligible a class of analytic 2D solutions of (1) have been found and these are compared with the appropriate numerical solutions.

---

*Bull. Am. Phys. Soc. 19, 867 (1974)

IIIB 10. Ion Cyclotron Instability Resulting From Ion-Trapped Particle Mode,* by M. N. Rosenbluth and H. L. Berk

The trapped-ion mode results essentially in an interchange of trapped ions, while untrapped ions and electrons remain Maxwellian. The deviation of the trapped-ion distribution from Maxwellian will give rise to an anisotropic velocity space distribution that can cause instability

at the ion cyclotron frequency and its harmonics. These oscillations in turn can limit the amplitude of the low-frequency trapped-ion instability by causing an enhanced rate of scattering of the trapped ions to passing orbits. As a result, in some circumstances, the nonlinear radial diffusion due to the trapped-ion mode can be lowered from that predicted by assuming that the local density gradient needs to be destroyed.

* Presented at the Annual Meeting on Theoretical Aspects of CTR, (Sherwood Meeting) Berkeley, Calif., April 3-5, 1974.

IIIB 11. MATT-1075 Stability Theory of Dissipative Trapped-Electron and Trapped-Ion Modes, by P. H. Rutherford, W. Horton, Jr., D. W. Ross, W. M. Tang, H. L. Berk, E. A. Frieman, R. E. LaQuey, R. V. Lovelace, S. M. Mahajan, and M. N. Rosenbluth

This paper treats topics in the linear theory of dissipative trapped-electron instabilities, and in the nonlinear theory of the dissipative trapped-ion instabilities. Stability criteria are obtained for dissipative trapped-electron modes in a tokamak-type magnetic field with shear. In the important case where the mode is driven by the electron temperature gradient, and neglecting "ballooning" effects, shear is found to stabilize the mode if typically $r_n/L_s > 0.1\,(r/2R)^{1/2}\, d\ell nT_e/d\ell nn$, a condition that can be attained. With weak shear, it is shown, however, that the mode-structure along the field can exhibit substantial "ballooning." The dissipative trapped-ion mode, which is not shear-stabilized, is considered in its non-linear regime. Including nonlinear $\underline{E} \times \underline{B}$ motions, exact stationary trapped-ion-mode solitary-wave solutions are found, in which the wave energy in longer azimuthal wavelengths passes to shorter-wavelength components that are strongly damped by ion bounce resonances; the amplitudes are sufficiently reduced that a diffusion lower than Kadomtsev's is indicated. As a second nonlinear mechanism, anomalous velocity-space scattering due to the development of an unstable loss-cone type ion distribution function is considered; this mechanism raises the effective ion collision frequency and increases the stability of the longer azimuthal-wavelength modes.

IIIB 12. MATT-1088 Two-Energy-Component Toroidal Fusion Devices, by R. M. Kulsrud, H. L. Berk, H. P. Furth, D. L. Jassby, C. S. Liu, M. N. Rosenbluth, P. H. Rutherford, F. H. Tenney, T. Johnson, J. Killeen, A. A. Mirin, M. E. Rensink, and C. W. Horton, Jr.

Injection of a superthermal ion component into a toroidal plasma can raise the fusion power density to levels considerably higher than those attainable in ordinary one-component plasmas. As a result, energy break-even

in D-T can be attained in bulk plasmas with $n\tau$-values as low as $10^{13} cm^{-3} sec$, at temperatures of ~5 keV. The optimal energy of the superthermal ion component is in the range 100 - 200 keV; injection-energy requirements can be reduced by adiabatic compression prior to or during the reaction phase. The appropriate ratio $\bar{\Gamma}$ of fast-ion pressure to bulk-plasma pressure is about 0.5. The stability of two-component tokamak plasmas has been examined, and is found to be favorable for parameters of practical interest.

IIIB 13. Stability of an Ion Beam to Velocity Space Instabilities,* by P. H. Rutherford, M. N. Rosenbluth, H. L. Berk, N. R. Sauthoff and C. S. Liu

The steady state distribution of an ion beam injected nearly parallel to the magnetic field and slowing down in a background plasma has been investigated for possible velocity space instabilities. The beam is a small fraction of the overall plasma density, and hence, stability can only be produced from inverse dissipation arising from the resonances at $V_{||} = (\omega - n\omega_{ci}) / k_{||}$. For long wavelengths, the dominant instability term comes from the n = -1 resonance, but it is difficult to find particles that resonate at this velocity. For example, waves corresponding to the fast Alfven-Whistler branch would resonate a minimum particle velocity $V_{||} = 1.5\ (3)^{1/2} V_A$, where V_A is the Alfvén speed), which corresponds to an injection energy far higher than has been contemplated. The n = 0 resonance can cause instability for the low-frequency fast Alfvén wave, if $V_A < V_{||}$, a condition that may at times be satisified in two component systems. This is a weak instability, and the quasi-linear theory predicts the relaxation of the distribution to one that damps this mode. The shear Alfvén wave will not be destabilized by the n = 0 resonance because the wave polarization produces an extremely small matrix element that is dominated by electron Landau damping. Similarly, any destabilizing tendency of loss-cone-like resonances tend to be stabilized by electron Landau damping.

* Presented at the *Annual Meeting on Theoretical Aspects of CTR* (Sherwood Meeting) Berkeley, Calif., April 3-5, 1974.

IIIB 14. Microinstability Theory for Toroidal Plasma Heated by Intense Energetic Ion Beams,* by H. L. Berk, W. Horton, Jr., M. N. Rosenbluth, and P. H. Rutherford.

A survey is given of possible microinstabilities in two-component neutral-injection-heated tokamaks. It is concluded that infinite-medium velocity-space modes should be quite strongly stable, and possible instabil-

ities of the shear-Alfvén finite-medium modes should be localized to near the axis.

Symposium on Plasma Heating in Toroidal Devices, Varenna, Italy, (1974)

IIIB 15. Drift-Alfvén Instability in a Two-Component Tokamak,* by P. H. Rutherford and M. N. Rosenbluth

Typical parameters of proposed two-component tokamaks have beam energies T_b such that $T_b/T_{ei} \sim 10\text{-}20$, and beam velocities v_b such that $v_b < v_A$. In this case, the drift-Alfvén wave that rotates in the sense of the ion diamagnetic drift can be destabilized by resonances $\omega = \omega_{Db}$, where ω_{Db} is the local ∇B drift of the beam ions, if the latter is in the unfavorable sense. With uniformly unfavorable curvature of order R^{-1}, neglecting shear, and assuming that electron Landau damping is the dominant stabilizing mechanism, the stability condition is $\Gamma \equiv n_b T_b / nT_e < (r/R)\,(k_\perp \rho_b)^4 (m_e/m_i \beta)^{1/2}$, where $\rho b = (m_i T_b)^{1/2}/eB$, the beam Larmor radius. With the same curvature assumption, but including shear, the most unstable modes have low m and become localized to a width r_o around the magnetic axis, with stability condition $\Gamma < (r_o^2\, r_b \rho_b m^{5/2}/3R)\,\beta^{-5/4}\,(d\ln q/dr)^{3/2} (T_b T_e)^{3/4} (m_e/m_i)^{1/2}$ where r_b is the beam radius. This stability condition is quite severe, although a proper treatment of the beam resonance in a variable-curvature torus gives substantial improvement.

*Presented at the *Sixteenth Annual Meeting of the American Physical Society* (1974)

IIIB 16. Enhanced F. Values for the TCT,* by E. A. Frieman and F. H. Tenney

Previous calculations of the ratio F of fusion energy produced to the injected beam energy in a TCT were based on the slowing down test particle calculation of Sivukhin. We here report on a more detailed numerical calculation of F based on an analytic solution of the Fokker-Planck equation for an isotropic source of beam particles. The assumption is also made that beam-beam interactions are negligible. The major new effects in the present calculations are (1) electron and ion velocity space scattering effects, (2) corrections to the drag coefficients and (3) corrections to the reaction rates resulting from the relative velocity between beam and background ions.

The results indicate that a significant enhancement of F over the previously reported values exists over a wide range of injected beam energy W_0 and background plasma temperature.

* Presented at the *Sixteenth Annual Plasma Physics Meeting of the American Physical Society* (1974)

IIIB 17. Maximum Power Gains of Radio-Frequency-Driven Two-Energy-Component Tokamak Reactors,* by D. L. Jassby

Two-energy-component fusion reactors in which the suprathermal component (D) is produced by harmonic cyclotron "runaway" of resonant ions are considered. In one ideal case, the fast hydromagnetic wave at $\omega = 2\omega_{cD}$ produces an energy distribution $f(\omega)$ constant (up to W_{max}) that includes all deuterons which then thermalize and react with the cold tritons. In another ideal case, $f(\omega) \approx$ constant is maintained by the fast wave at $\omega = \omega_{cD}$. If one neglects (1) direct rf input to the bulk-plasma electrons and tritons, and (2) the fact that many deuterons are not resonantly accelerated, then the maximum ideal power gain is about $0.85\ Q_m$ in the first case and $1.05\ Q_m$ in the second case, where Q_m is the maximum gain in the beam-injection scheme (e.g., $Q_m = 1.9$ at $T_e^m = 10$ keV). When unavoidable rf interactions with the bulk plasma are taken into account, it seems that the cyclotron runaway phenomenon may find its most practical use in the heating of 50:50 D-T plasmas to ignition.

*Presented at the *Sixteenth Annual Plasma Physics Meeting of the American Physical Society* (1974)

IIIB 18. Maximization of Energy Multiplication in a Pulsed Tokamak Reactor,* by P. H. Rutherford, H. P. Furth, D. L. Jassby

We consider a D-T pulsed-ignition tokamak discharge that is terminated prior to appreciable plasma energy deposition on surrounding walls. The total fusion yield is limited to ~5 times the α-energy that can be retained in the plasma for $\beta_p < R/a$. To reach high energy multiplication Q, we ignite a fractional-sized tokamak core and allow the thermonuclear burn to propagate outward into a plasma mantle of radially increasing density. To meet the core ignition condition ($n^{\tau}_E \gtrsim 2 \cdot 10^{14}\text{cm}^{-3}$sec at 13 keV) in minimum size, our model specifies that β_p should start at the MHD limit and follow it during the burn, with $T_e \approx T_i \approx$ constant. The current I is programmed to maintain q = constant. If the initial and final radii are a_o and a_m, then $Q \sim 5\ [(a_m/a_o)^3 - 1]$. Large gains can be made over pulsed ignition with fixed a, $\bar{n}$ and variable T. For illustrative parameters: R = 12 m, B_t = 60 kG; a_o = 2m, $\bar{n}_o = 10^{14}\text{cm}^{-3}$, I_m = 13 MA, we obtain Q = 35 with a 3.5 sec burn time and a 24-GJ yield.

*Presented at the *Sixteenth Annual Plasma Physics Meeting of the American Physical Society* (1974)

IIIB 19. Effect of Magnetic Field Ripples on Toroidal Plasma Rotation,* by E. A. Frieman and K. T. Tsang.

We have extended the work of Rosenbluth, et al., for an axisymmetric toroidal system in the banana regime to include (a) intermediate and collision-dominated regimes, and (b) the effect of small magnetic field ripples in all three regimes. The results for the collision-dominated regime reduce to those found by Hazeltine with the addition of a new term resembling the classical perpendicular viscosity modified by a Pfirsch-Schluter factor. In the intermediate regime, results for the case with zero temperature gradient have been obtained. In (b) our result for the banana regime is $\partial U/\partial t = -16.5\delta^{3/2} G(\alpha),(r/R) \times (B_p V_{Ti})/(B_T r)^2 \nu_{ii}^{-1} (U-U_b)$ where $U_b = 3.57 \times (CT')/(CB_p)$, δ is the ripple size; α and $G(\alpha)$ are the same as that which appeared in Connor and Hastie. This result is qualitatively in agreement with that of Rosenbluth but appears to be a more detailed calculation.

*Presented at the *Sixteenth Annual Meeting of the American Physical Society*, (1974)

IIIB 20. MATT-1026 Neoclassical Diffusion in a Helically Perturbed Magnetic Field, by J. A. Krommes and P. H. Rutherford

Neoclassical particle diffusion and heat transport are discussed for tokamak-like devices in the "banana" regime ($\nu_{eff} < \omega_b$) with helically perturbed magnetic fields, such as might be produced by kink-like instabilities.

IIIB 21. MATT-1039 Impurity Transport in the Pfirsch-Schlüter Regime, by P. H. Rutherford

It is shown that the classical inward diffusion of high-Z impurities in toroidal plasmas is enhanced by the Pfirsch-Schlüter effect. Numerical transport coefficients are evaluated. Typically, both density and temperature gradients are found to produce inward impurity diffusion.

IIIB 22. Hydrodynamic Correlation Functions and Transport in a Strong Magnetic Field*, by C. Oberman and J. Krommes

The generalized Langevin equation of Mori is used to derive a closed set of equations for the time-dependent correlations functions

of the hydrodynamic modes of plasma in a strong magnetic field. From these correlation functions, transport coefficients are deduced. The linear theory is augmented by mode-coupling terms in order to extract the collective contributions to the transport.

---

* Presented at the *Sixteenth Annual Meeting of the American Physical Society*, (1974)

IIIB 23 Fluctuations and Cross-Field Transport in Guiding Center Plasma *
by C. R. Oberman and J. A. Krommes

A generalization of the Rostoker theory of fluctuations, developed by Williams and Oberman, is applied to the two-dimensional guiding center plasma. Formal expansion in the plasma parameter recovers to lowest order the results of the random phase approximation. This predicts a convergent diffusion coefficient, thus correcting a result of Taylor and Thompson. However, strong wave-wave interactions invalidate the expansion; the random phase approximation is believed to be inadequate for the guiding center model. The electric field autocorrelation is computed. Landau and cyclotron-like damping due to like-unlike and like-like particle pairs compete with diffusive processes as temporal damping mechanisms. The fluctuation spectrum is used to compute the test particle diffusion coefficient.

---

* Presented at the *Annual Meeting on Theoretical Aspects of CTR* (Sherwood Meeting), Berkeley, Calif., April 3-5, 1974.

C. Plasma Heating and Parametric Instabilities

Both fundamental and applied research on plasma heating via absorption of waves has been pursued during the past year. These studies impact on a wide range of experiments: tokamaks, laser-fusion, and basic laboratory research devices.

Abstracts III C 1-3 describe theoretical calculations of the rather wide variety of damping processes germane to wave heating of tokamaks near the ion-cyclotron frequency. The theory presented in Abstract III C 4, sets forth the equations which govern the evolution of the ion velocity distribution under rf heating. These equations have been incorporated into Fokker-Planck codes of ion-velocity space diffusion which show good agreement with the ST ion-cyclotron heating experiment.

Heating of large tokamaks by waves near the lower-hybrid frequency has been found to be quite sensitive to the wave launcher geometry; Abstract III C 5 details the reasons.

Abstracts III C 6-8 deal with the heating of a Tormac (toroidal cusp) device in which magnetosonic waves steepen into shocks. The final electron and ion temperatures are comparable.

Parametric instabilities continue to be of importance in plasma heating schemes. Abstracts III C 9-10 deal with parametric instabilities near the ion-cyclotron frequency. These are of importance in ion heating of laboratory multipole devices.

In Abstract III C 11 and 12, there is given a simple but quite general method for computing the contribution of induced emission to the wave-kinetic equations describing parametric interactions. The induced emission often far outweighs the Cerenkov (Abstract III C 11) or longitudinal bremsstrahlung emission (Abstract III C 12).

The influence of density gradient, and in the case of expanding (laser-pellet) plasma, velocity gradient, on the threshold condition and growth rate of back- and side-scatter instabilities is considered in Abstract III C 13, for both slab and spherical geometry. Inhomogeneity limits the spatial extent of the resonance zone where the three-wave is satisfied. It is concluded that for presently available laser powers decay of the incident electromagnetic wave into two plasmons at quarter-critical density and the decay into a plasmon

and phonon at the critical density are dominant absorptive processes whereas the Brillouin scattering (decay into another photon and a plasmon) is important in the underdense region.

Electromagnetic radiation obliquely incident on a density gradient is resonantly transformed into an electrostatic wave at the singular point where $\omega_p(x) = \omega_o$. This converted wave is much enhanced in amplitude over the incident wave and can serve as a pump for parametric instabilities. In Abstract III C 12, the oscillating two-stream instability is examined near this singular point taking into account the pump shape as well as the plasma inhomogeneity. The structure of the unstable modes (incipient caviton formation) is given as well as threshold and growth rates.

Abstract III C 15 represents a beginning to the study of tokamak-type plasmas consisting primarily of ion beams: the "Colliding Beam Torus". The concept has certain advantages, but the plasmas tend to have velocity-space instabilities.

Three further abstracts (Abstract III C 16-18) are concerned with partially neutralized E-layers. Abstract III C 16 is concerned with the Vlasov stability of a magnetically confined nonrelativistic layer. An $\ell = 1$ diochotron instability is found which is not revealed by the cold fluid analysis. The equilibrium of a thin relativistic E-layer with a narrow spread in canonical angular momentum is studied in Abstract III C 17. It is found that even when ν/γ_o is small the influence of self-field can be large in determining the radial thickness whereas their influence on the mean radius is small. The work of Abstract III C 18 shows that it is possible to determine the electron distribution function for the aforementioned situation when the synchrotron radiation spectrum is known (or measured).

IIIC 1. Ion-Cyclotron Heating of Tokamaks: Theoretical Considerations,* by F. W. Perkins and M. S. Chance

This paper deals with the linear and nonlinear interaction of waves in the ion-cyclotron frequency range with a tokamak plasma. The propagation and absorption of both the torsional ion-cyclotron wave and the compressional magnetosonic wave are discussed. The ion-cyclotron wave is absorbed by a mode-conversion processes near the surface of the plasma in the vicinity of the launching coil, while the magnetosonic wave fills the entire toroidal chamber and is absorbed by hot plasma effects. Nonlinear calculations show that ample heating can be obtained by the magnetosonic wave with wave energy densities three orders of magnitude below the thermal energy density of the plasma. The spatial diffusion resulting from these waves is negligible.

*Presented at the *Topical Conference on RF Plasma Heating, American Physical Society*, (Lubbock, Texas, 1974)

IIIC 2. Ion-Cyclotron Heating of Tokamaks: Wave Intensities and Loading,* by F. W. Perkins

Collisionless absorption of magnetosonic waves in tokamak plasmas yields ion heating when the frequency coincides with either the fundamental or second harmonic of the ion cyclotron frequency and electron heating by transit-time magnetic pumping throughout this frequency range. We show that the collisionless wave damping decrements are very large compared to the expected energy loss rates in tokamaks so plasma heating can be carried out with $\tilde{B}^2/8\pi nT \lesssim 10^{-3}$. Such small wave intensities do not produce important nonlinear effects but can produce two-component tails as computer simulations show. We also show theoretically that the loading of the slow electromagnetic ion-cyclotron wave is much less than the fast wave and agrees qualitatively with experiment.

*Presented at the *Sixteenth Annual Meeting of the American Physical Society*, (Albuquerque, N. M., 1974)

IIIC 3. On Radio Frequency Heating of Tokamaks,* by F. W. Perkins, F. Troyon and J. L. Sperling

Two results are presented: (1) calculations of the nonlinear effects of heating by magnetosonic waves in tokamaks and other devices, and (2) the damping of lower-hybrid waves in tokamak geometries. Three types of non-linear processes are induced by magnetosonic waves: (1) velocity space diffusion, (2) real space diffusion, and (3) parametric instabilities. We will present quasilinear equations giving the velocity space diffusion, argue that real space diffusion is negligible, and identify a parametric

instability which occurs for pump frequencies in the ion-cyclotron frequency range. The damping of lower-hybrid waves in a plasma with varying magnetic field intensity (so that there are many regions where $\omega_{pi} - \omega = k_{||} v_{||} + n\omega_{ci}$) is shown to be the same as the Landau damping by unmagnetized ions.

---

* Presented at the *Annual Meeting on Theoretical Aspects of CTR* (Sherwood Meeting), Berkeley, Calif, April 3-5, 1974.

IIIC 4. MATT-1094 Wave Generation and Heating in the ST Tokamak at the Fundamental and Harmonic Ion Cyclotron Frequencies,* by M. Chance, J. Adam, H. Eubank, W. Getty, E. Hinnov, W. Hooke, J. Hosea, F. Jobes, F. Perkins, R. Sinclair, J. Sperling, and H. Takahashi

The feasibility of employing wave heating at frequencies in the vicinity of the ion cyclotron frequency and its harmonics to supplement ohmic heating in future toroidal reactors is being investigated theoretically and with experiments on the ST Tokamak. This work demonstrates that heating by cyclotron absorption of fast magnetosonic waves is an efficient and attractive supplementary method from the viewpoint of both physics and the availability of high power rf generators.

---

*also presented at the *Fifth Conference on Plasma Physics and Controlled Nuclear Fusion Research* (Tokyo, Japan, 1974)

IIIC 5. Heating of Large Tokamaks to Thermonuclear Temperatures by Electromagnetic Waves in the Vicinity of the Lower-Hybrid Frequency,* by F. Troyon and F. W. Perkins

We derive the accessibility conditions for waves launched at the plasma boundary to reach the center for frequencies above the lower-hybrid frequency, taking into account both propagation and linear damping. For typical tokamak parameters, the operating range of $n_{\parallel} = k_{\parallel} c/\omega$ is at best very narrow when the slow, electrostatic wave is launched, shrinking rapidly as the temperature increases above 5-10 keV. The fast Whistler wave leads to a less stringent condition, but requires a high density at the wall. It is shown that a non-selective launching structure leads to peripherial heating.

---

* Presented at the *Sixteenth Annual Meeting of the American Physical Society*, Albuquerque, N. M., 1974)

IIIC 6. MATT-1071 Ion Heating in a Train of Orthogonal Magnetoacoustic Shocks, by Allen H. Boozer

The deposition of energy from a train of magnetoacoustic waves, which have steepened to form shocks, is considered in a collisionless plasma.

It is shown that an initially lower ion temperature tends to rise to a value comparable to the electron temperature.

IIIC 7. Magnetoacoustic Wave Heating of Cusps,* by A. H. Boozer

Magnetoacoustic wave heating is the primary heating method under consideration for the toroidal line cusp, Tormac. Results are presented on the interaction of the plasma and the heater circuit and on the theory of wave absorption. The plasma-heater circuit interaction is given in a model which assumes complete absorption of waves during their first transit of the plasma. Under wave absorption theory, it is shown that if a train of low-frequency orthogonal magnetoacoustic waves damp by steepening into collisionless shocks, then the ions are heated at least comparably to the electrons.

*Presented at the *Sixteenth Annual Meeting of the American Physical Society*, (Albuquerque, N. M., 1974)

IIIC 8. Wave Heating of Plasma in a Toroidal Cusp (Tormac),* by Morton A. Levine, Lawrence Berkeley Laboratory, Charles C. Gallagher, Air Force Cambridge Research Laboratories and Allen H. Boozer, Princeton University.

A two pole toroidal line cusp is formed and filled with a 7 eV plasma with 10^{15}ptcls/cc by preionizing and compressing a gas in situ. A toroidal magnetic field is trapped within the plasma. Previous Tormac experiments have indicated the plasma density is near uniform across with a sharp pressure drop in the sheath. The plasma is estimated to have an 8 cm minor diameter and a 32 cm major diameter. A hydrogen-helium gas mixture is used. Waves are launched into the plasma using a 700 kHz time varying poloidal magnetic field. Spectral line intensity measurements indicate the electrons are heated to 40 eV and line broadening measurements of He 4686 indicate an ion temperature near 40 eV The temperature measurements correlate with primary circuit measurements and show that better than 50% of the electrical energy is absorbed by the plasma.

*Bull. Am. Phys. Soc. 19, 928, (1974).

IIIC 9. Parametric Excitation by Magnetosonic Waves in a Multispecies Plasma,* by F. W. Perkins, J. L. Sperling

Magnetosonic waves propagating near the sum of two of the ion-gyrofrequencies in a multi-species plasma can excite the decay instability into two electrostatic ion-cyclotron with $k_\perp \rho_i \gg 1$, where ρ_i is the ion-

gyroradius. Excitation of this instability may be an important mechanism in heating the ions of multispecies plasmas in which normally $T_e >> T_i$. The presence of density and magnetic field gradients are shown to affect the dispersion of electrostatic ion-cyclotron waves and their excitation by the decay instability. Nonlinear aspects of the instability are discussed.

---

*Presented at the *Sixteenth Annual Meeting of the American Physical Society*, (Albuquerque, N. M., 1974)

IIIC 10. MATT-1027 Parametric Excitation by Magnetosonic Waves in a Multispecies Plasma, by F. W. Perkins and J. L. Sperling

A magnetosonic pump wave propagating in a plasma with two ion species decays into two electrostatic ion-cyclotron modes at a threshold significantly less than those needed to excite parametric or modified two-stream instabilities in a single-species plasma when $T_e/T_i > 1$. The pump wave frequency must somewhat exceed the sum of the ion gyrofrequencies.

IIIC 11. MATT-1041 General Theory of Enhanced Induced Emission in Plasmas, by C. Oberman and G. Auer

A simple formalism yields a general expression for the enhanced induced emission in plasma influenced by a strong electromagnetic or electrostatic pump. Applications to subcritical Brillouin, Raman, and other resonant and nonresonant interactions are given.

IIIC 12. MATT-1073 Enhanced Induced Emission for Stimulated Raman Scattering in Plasmas, by Gerhard Auer and Carl Oberman

It is shown how longitudinal bremsstrahlung can be included in the formalism for calculating the enhanced induced emission of high-frequency waves in a plasma influenced by a pump field.

IIIC 13. Raman and Brillouin Scattering of Electromagnetic Waves in Inhomogeneous Plasmas*, by C. S. Liu, Marshall N. Rosenbluth, and R. B. White

Raman and Brillouin scattering of an electromagnetic wave in an inhomogeneous, expanding plasma are studied. Application to laser-pellet irradiation is considered.

* Phys. Fluids 17, 1211 (1974).

IIIC 14. Oscillating Two-Stream Instabilities at the Singular Point of Obliquely Incident Radiation,* by F. Troyon, C. S. Liu, and C. Oberman

For radiation obliquely incident onto a plasma slab with increasing density, it is resonantly transformed into electrostatic plasma wave at the singular point where $\omega_p(x) = \omega_o$. This converted plasma wave is generally much enhanced over the incident wave and can serve as a pump to the parametric instabilities. Here we examine the oscillating two-stream instability near this singular point, taking into account the electrostatic pump shape as well as the plasma inhomogeneity. The structure of the unstable modes are Airy-function-like with modified envelope, propagating mainly along the density gradient. The threshold and growth are derived. The comparison with the oscillating two-stream instability at the cutoff for normal incidence is made.

*Presented at the *Sixteenth Annual Meeting of the American Physical Society*, (Albuquerque, N. M., 1974)

IIIC 15. Current Driven Instabilities,* by R. W. Landau

We have included counterstreaming currents along the magnetic field in our previously derived dispersion relations for the various $k_\perp$, almost electrostatic, $T_\perp = 0$ instabilities. We find that for a $T = T_+ = T_-$ plasma that there is instability for arbitrarily low-β, if, for the electron stream $V_- > .9\ (2T/m_-)^{1/2}$. This criterion becomes weaker as β increases and for large-β increases and for large-β the limit of Bornatici and Lee is recovered. When only the ions stream, there is instability in the low-β limit, if $V_+ > .9(2T/m_+)^{1/2}$, which gives Weibel's result for the "ion cyclotron instability." In general, when the full (not electrostatic) dispersion relation is considered, much larger growth is obtained for lower values of streaming.

*Presented at the *Sixteenth Annual Meeting of the American Physical Society*. (Albuquerque, N. M., 1974)

IIIC 16. Kinetic Theory of the Diocotron Instability,* by S. M. Mahajan and R. C. Davidson.

Stability properties of a magnetically confined nonrelativistic partially neutralised E-layer to electrostatic perturbations of the form $\phi(\vec{x}, t) = \phi(r)\exp(i\ell\theta - i\omega t)$ are discussed. The analysis is carried out for a thin E-layer, i.e., $a/R_o \gg 1$. The dispersion relation is evaluated for $f_e^o(H, P_\theta) = \text{const}\ \sigma(H-H_o)\ \sigma(P_\theta - P_o)$ where H and P are the total energy and canonical angular momentum of the electron respectively. The E-layer is found to be unstable, a result which contradicts the earlier theory of Nocentini, et al. It is found that unlike the cold fluid description of the diochotron instability, the Vlasov stability analysis predicts instability for $\ell = 1$ mode. The mechanism for instability is similar to that of the negative mass instability. The analysis is valid for $0<\omega_p^2/\omega_c^2<(1-f)^{-1}$, where $f = n_i^o/n_e^o$ is the fractional neutralization.

*Presented at the *Sixteenth Annual Meeting of the American Physical Society*, (Albuquerque, N. M., 1974)

IIIC 17. MATT-1086 Intense Relativistic Nonneutral E-Layers I-Equilibrium Theory, by R. C. Davidson and S. M. Mahajan

Equilibrium properties of intense relativistic nonneutral E-layers are studied within the framework of the steady-state Vlasov-Maxwell equations. The analysis is carried out for an infinitely long E-layer aligned parallel to a uniform magnetic field $B_0^{ext}\hat{e}_z$, assuming that the E-layer is thin (radial thickness is small in comparison with the mean radius R_0) and $\nu/\gamma_0 \ll 1$ (ν = Budker's parameter, and $\gamma_0 mc^2$ = electron energy). Equilibrium properties are calculated for the class of thin E-layer equilibria in which all electrons have the same canonical angular momentum P_θ but an arbitrary distribution in energy H, i.e., $f_e^0(H,P_\theta) = R_0 F(H + e\phi_0)\ \delta(P_\theta - P_0)$ where R_0, θ_0 and P_0 are constants. One of the most important features of the analysis is that the influence of equilibrium self fields on the radial thickness of the E-layer can be large, even though $\nu/\gamma_0 \ll 1$ is assumed and the self-field corrections to the mean radius of the E-layer are small.

IIIC 18. Determination of Relativistic Electron Ring Microstate from the Synchrotron Radiation Spectrum,* by S. M. Mahajan and C. R. Oberman

It is shown that a knowledge of the synchotron emission spectrum for a thin ring of relativistic electrons is sufficient information to reconstruct the microscopic distribution function that self-consistently generates the ring equilibrium.

*Plasma Physics, 16, 1147-1153 (1974)

D. Computer Simulation

1. Particle Codes

Most of the particle code effort was devoted to the study of plasma transport across magnetic fields for both quiescent and turbulent states. Initial work on the transport in toroidal systems was carried out. Some work on the theory of simulation models was also carried out.

Code Development: A particle code in a toroidal magnetic field was developed which makes use of a Monte Carlo collision operator to simulate collisional processes. A 2 1/2 dimensional electrostatic simulation code in a toroidal geometry was developed to follow the tokamak discharge for a short time. A 2 1/2 dimensional bounded, inhomogeneous plasma model was developed to study drift waves in both uniform and sheared fields. A slab model was developed to study the trapped electron instability in a mirror field.

Problems investigated: Several topics in the theory of heat and particle transport in a quiescent plasma were studied. Energy transport due to plasma oscillations was studied numerically and theoretically (Abstracts III D 1,2) confirming the importance of this process. Some preliminary results of numerical simulation on drift waves and trapped-electron modes were reported (Abstract III D 3). The work on toroidal transport confirmed the neoclassical diffusion picture, and indicated the importance of modifications due to convective transport (Abstract III D 4). The effects of density and temperature gradients on thermal convective cells were studied, showing that viscosity destabilized the flute mode (Abstracts III D 5,6).

A detailed computer measurement on the damping of convective cells and lower-hybrid modes to turbulent diffusion was carried out, indicating necessary modifications of turbulence theory (Abstract III D 7). Several review talks were given on the computer study of plasma transport in magnetic fields: at the IAEA Conference in Tokyo (Abstract III D 8); Albuquerque APS Conference (Abstract III D 9); and Third U.S.-Japan Seminar, Kyoto, Japan (Abstract III D 10).

Considerable effort was made on the theory of particle-code plasma simulation (Abstract III D 11), and on treating collisions in multi-dimensional simulation (Abstract III D 12).

2. MHD and Fluid Codes

Continued progress was made in the development and application of our equilibrium and stability codes. The toroidal axisymmetric equilibrium

code was modified to include parameters for localized instability criteria for systems with finite pressure. This was used to investigate the MHD properties of various plasma configurations, particularly those of the PDX device to be built at Princeton (Abstracts III D 13, 14).

A major thrust of our work was the development of stability codes for axisymmetric toroidal configuration via the δW method. For maximum efficiency in our numerical schemes, we carefully chose a natural coordinate system based on the magnetic field lines and decomposed the perturbations into components selected to match the polarizations of the different modes as closely as possible (Abstracts III D 13, 15). Because of the considerable amount of algebra involved, we made use of symbolic programming to check the analytic form of the potential and kinetic energies (Abstract III D 16). We adopted Galerkin's method for extremization of the Lagrangian, and chose a finite element expansion scheme to describe the radial variation of the modes; the choice was shown to be more useful and accurate than a corresponding global expansion scheme when localized modes are encountered (Abstract III D 17). We have generalized our computational code for the straight, elliptical pressureless case to include the effects of finite pressure and finite wavelength, while preserving our analytical equilibrium by retaining the constant axial current and similar elliptical magnetic surfaces (Abstract III D 18). We used this code to study the effects of field line curvature, pressure, and finite axial wavelength on the stability of kink modes (Abstract III D 19), and we also determined the limits of the continua expected in the sound and Alfvén wave spectra (Abstract III D 20).

3. Fokker-Planck Code

Improvements and modifications of the Fokker-Planck code in spherical coordinates were continued. Impurity ions, compression terms, $\ell n\Lambda$ corrections, D-T collision cross-sections, and nuclear reaction rate routines were included. Following this, the code was used to simulate the TCT device at various temperatures, beam energies, and Z_{eff} (Abstract III D 21). A major improvement of the program was accomplished by using Legendre polynomial expansion methods, instead of straightforward numerical integrations, to compute the Rosenbluth potentials. The new version was further generalized into a multiple species code, which follows the time evolution of distribution function of two or more species simultaneously. The code is currently being used to investigate the properties of neutralized colliding-beam toroidal fusion reactors.

Another Fokker-Planck code in cylindrical coordinates was also developed. In addition to the usual Coulomb collision terms, it includes a loss cone and rf heating terms. The code was employed to study the ICRH heating experiment in the ST Tokamak. The results agreed qualitatively with experimental observations.

4. Transport Code

The tokamak transport code was extensively developed during 1974 with PDX and TCT design problems especially in mind. Major developments were: inclusion of diffusing impurity ions with rate equations and radiation losses for high-Z metallic impurities; development of "divertor boundary conditions"; self-consistent inclusion of heating by the slowing down of high-energy beam ions created by neutral injection; inclusion of adiabatic compression of the beam ions. The impurity and divertor studies were applied to PDX (Abstract III D 22), and the beam injection computations were carried out in connection with TCT design (Abstract III B 12, and Special Report 74/3).

IIID 1. Energy Transport Across a Magnetic Field by Plasma Waves,* by J. Canosa and H. Okuda

Rosenbluth and Liu's recent asymptotic treatment of cross-field energy transport by plasma waves has been extended to include explicitly and in some detail the influence of the magnetic field magnitude and of the plasma size on the energy transport. In the limits of infinitely large magnetic field and plasma size our results approach asymptotically the first-order results. A 2 1/2-dimensional (two positions and three velocities) particle code has been used to simulate wave energy transport. For strong magnetic fields, the computations verify the theoretical prediction that energy transport by plasma waves increases slowly with the magnetic field, and that in the limit of large field amplitudes wave transport dominates classical collisional transport. For weak fields, the simulation shows that collisional transport is more important than wave transport, also in agreement with the theory.

---

*Presented at the Sixteenth Annual Meeting of the American Physical Society (1974). Albuquerque, N. M.

IIID 2. MATT-1084 Energy Transport Across a Magnetic Field by Plasma Waves, by J. Canosa and H. Okuda

Cross-field energy transport by electrostatic plasma waves has been studied theoretically and numerically for a plasma near thermal equilibrium. Energy transfer by plasma waves is significant in a high temperature plasma where collisional transport is quite small. For strong magnetic fields ($\omega_c \gtrsim \omega_p$), the simulations verify the theoretical prediction that energy transport by plasma waves increases slowly with the magnetic field, and that in the limit of large field magnitudes wave transport dominates classical collisional transport. Furthermore, in a strong magnetic field the relaxation of the temperature by wave transport may result in an anisotropic velocity distribution. For weak fields ($\omega_p > \omega_c$), the simulation shows that collisional transport is more important than wave transport, also in agreement with the theory.

IIID 3. Numerical Simulation on Drift Waves and Trapped Electron Instability,* by Y. Matsuda and H. Okuda

A 2 1/2-D particle simulation model for simulating low-frequency drift waves and trapped electron instability has been developed to study the associated turbulent transport processes. For the collisionless drift waves, both quiet and non-quiet starts were used in a uniform magnetic field. For a strongly unstable case, turbulent diffusion continues until it wipes out the initial gradient. A square mirror magnetic field and a Monte-Carlo collision operator are introduced to simulate the trapped electron mode. It is found that the azimuthal potential due to trapping tends to rotate the plasma radially which tends to mask the turbulent transport associated with the

instability. Various methods to stop plasma rotation will be shown with the results of simulation.

---

* *Presented at the Sixteenth Annual Meeting of the American Physical Society* (1974). Albuquerque, N. M.

IIID 4. Numerical Simulation of Neoclassical Diffusion and Convective Cells in Tokamaks,* by K. T. Tsang, H. Okuda and Y. Matsuda

We report here the result of a set of numerical experiments devised to observe the neoclassical diffusion across a tokamak field. A straight field with tokamak-type spatial variation plus a small poloidal field that generates the rotational transform is installed in a Monte Carlo scattering particle simulation code. Our result shows a clear distinction of banana, plateau and Pfirsch-Schlüter regimes for an axisymmetric tokamak. Enhancement of the neoclassical diffusion over the classical value is roughly in agreement with theory. For nonaxisymmetric tokamak with small ripples, additional enhancement of diffusion due to superbanana in very low collision frequency regime is observed with the desired ν^{-1} dependence. After reproducing neoclassical diffusion using Fokker-Planck collision operator effects of long wavelength collective fluctuation (convective cells) are now being investigated and will be reported.

Presented at the Sixteenth Annual Meeting of the American Physical Society (1974). Albuquerque, N. M.

IIID 5. Effects of Gradients on Convective Plasma Diffusion,* by M. True and H. Okuda

The effects of density and temperature gradients of the 2-dimensional diffusion due to convective cells $[\omega=ik_r^2 D_\perp/(1+\Omega_i^2/\omega_{pi}^2)]$ have been studied analytically and by numerical simulations. The linear analysis shows that, in the presence of ∇N, the ion flute modes become unstable due to viscosity $[\omega=\omega_{ion}^* + ik_r^2 D_\perp/(1+\Omega_i^2/\omega_{pi}^2)]^2$, while the convective modes are unchanged. When ∇T is present, the convective modes grow ($\omega = +ik_r^2 D_\perp$) while ion flute modes are stable ($\omega=\omega_{ion}^*-ik_r^2 D_\perp$). Numerical simulations in 2-dimensions ($\underset{\sim}{k}\cdot\underset{\sim}{B}=0$) verify these instabilities showing the enhanced diffusion. These instabilities provide two counter examples for the usual estimate of diffusion coefficient in strong turbulence theory $D_\perp = \gamma/k_r^2$, since the instability is driven by diffusion.

Presented at the Sixteenth Annual Meeting of the American Physical Society (1974). Albuquerque, N. M.

IIID 6. Large Amplitude Convective Cells and the Low-Frequency Electrostatic Instabilities,* by H. Okuda

Convective plasma diffusion due to thermal vortices ($\omega=-ik_\perp^2\mu_\perp$) in a uniform plasma is considerably reduced in an inhomogeneous plasma because the fluctuation energy at $\omega=-ik_\perp^2\mu_i$ shifts to ion flute mode at $\omega=\omega^*$ from convective cells ($\omega^*/k_\perp^2\mu_i \gtrsim 10^5$ for $n = 10^{14}cm^{-3}$, T = 1 keV, B=50 kG, $k_\perp\rho_i \lesssim 1$). However, since the net charge or the electric field associated with the stable drift oscillation is quite small [$(E^2)k/8\pi = T/2(1+\omega_{pi}^2/\Omega_i^2)$], it appears that quite a modest amount of superthermal charge imbalance across density gradient and magnetic field will dominate drift oscillation, thereby causing a large diffusion. One sufficient condition for this to occur will be $k^2D_\perp \gtrsim \omega^*$ where $D_\perp$ is the particle diffusion due to superthermal cells. It is possible that a superthermal cell does not see the gradient, then the condition will be much weaker. Results of 2D simulation with superthermal convective cells excited across B and the gradient show an enhanced diffusion regardless of the gradients, indicating weak dependence on $(E^2)k$ and B of $D_\perp$.

Superthermal convective cells and enhanced transports appear inherent to magnetically confined plasmas due to various causes such as plasma formation and low-frequency electrostatic instabilities (drift, flute, trapped-particle) which build up charge imbalance across B and ∇n. In order to study the formation of convective cells, saturation amplitude and particle diffusion associated with the low-frequency instabilities, we have simulated a current-driven, low-frequency drift instability. The most unstable mode saturates at $(E^2)k/4\pi T \sim 50$ with $D_\perp \sim D_\perp^{classical}$. Saturation level seems to be low ($E^2/4\pi nT \lesssim 10^{-3}$) and the dominant saturation mechanism appears the disappearance of gradient (change of distribution) rather than orbit diffusion for strongly unstable case ($\gamma_k \lesssim \omega_k$).

---

* Presented at the *Annual Meeting on Theoretical Aspects of CTR* (Sherwood Meeting), Berkeley, Calif., April 3-5, 1974.

IIID 7. MATT-1051 Turbulent Damping of the Convective Cells and the Lower Hybrid Waves, by H. Okuda, C. Chu, and J. M. Dawson

A detailed numerical study has been made for the turbulent damping of the convective cells and of lower-hybrid waves for a plasma near thermal equilibrium. It is found that some of the theories of strong turbulence, taking into account the diffusing orbits of particles, are inadequate for describing the observations; observations are, however, in good agreement with the linear dispersion relation with a turbulent diffusion coefficient.

IIID 8. MATT-1076 Theory and Numerical Simulation of Collective Transport of Plasma in Magnetic Fields, by J. Canosa, J. Krommes, C. Oberman, H. Okuda, K. Tsang, J. M. Dawson and T. Kamimura.

Numerical and theoretical studies have been made on the transport of particles and heat in collisionless plasmas in magnetic fields for both quiescent and turbulent states. The following problems have been investigated: (1) A systematic kinetic theory of hydrodynamic fluctuations in a strong magnetic field has been developed to study the particle diffusion due to thermal convective cells. (2) Effects of density and temperature gradients on thermal convective cells; they are found to destabilize both the ion flute and the convective cells. (3) Effects of mirroring magnetic field on convective diffusion; they are found to increase the diffusion significantly even for open field lines of force. (4) Turbulent electron heat transfer due to short wavelength ion fluctuations near the lower-hybrid frequency; this may be important in a collisionless plasma. (5) Heat transfer due to emission and absorption of electrostatic plasma waves are studied theoretically and by simulation; agreement has been found for a strong magnetic field case. (6) Particle diffusion in a toroidal magnetic field due to collisions (neo-classical diffusion) and due to collective effects is studied by numerical simulations. Neoclassical theory agrees well with the numerical results when the long wavelength collective modes are suppressed.

IIID 9. Numerical Studies on the Transport of Plasmas in Magnetic Fields,* by H. Okuda.

Numerical and theoretical studies have been made on the transport of particles and heat in collisionless plasmas in magnetic fields for both quiescent and turbulent states. The problems being investigated are: (1) Particle diffusion due to thermally excited convective cells for both homogenous and inmomogenous plasmas in which density and temperature gradients drive the plasma unstable. (2) Cross-field heat transfer due to the turbulent electron motion associated with the short wave length ion fluctuation at the lower-hybrid frequency. (3) Heat transfer due to electrostatic waves in both thermal and turbulent plasmas. (4) Particle diffusion in a toroidal magnetic field due to collisions (neoclassical diffusion) for both axisymmetric and nonaxisymmetric systems and due to thermal convective cells which are enhanced by the presence of trapped particles. (5) Turbulent transport due to low frequency electrostatic instabilities, specifically the drift instability, in a uniform magnetic field, and the collisional trapped electron instability associated with the mirroring field in toroidal systems.

---

* Presented at the *Sixteenth Annual Meeting of the Division of Plasma Physics of the American Physical Society*, (Albuquerque, N. M., 1974).

IIID 10. Numerical Studies of Plasma Transport in Magnetic Fields,* by H. Okuda

Several topics of the numerical and theoretical studies on plasma transport in magnetic fields will be discussed. (1) Convective cells in a non-uniform two-dimensional plasma; it is shown that the convective cells ($\omega \sim -ik_{\perp}^2 D_{\perp}$) couple to the ion-flute modes ($\omega = \omega_{ion}^*$) which destabilized the low-frequency oscillations due to viscosity ($\omega \sim +k_{\perp}^2 D_{\perp}$). (2) Turbulent electron heat transfer due to ion-fluctuations; it is shown that the short wavelength ion lower-hybrid fluctuations may cause anomalous electron heat conduction if the level of fluctuations is high enough. Series of simulations verify this process. (3) Heat transfer due to emission and absorption of electrostatic plasma oscillations is studied numerically and theoretically; it is found that this process produces an anisotropic velocity distribution in a collisionless plasma. Agreement between theory and simulation is found to be very good. (4) Neoclassical diffusion and convective in a toroidal geometry; a model is developed to study the neoclassical diffusion and the convections is a tokamak using a mode Fokker-Planck operator in addition to the self-consistent fields. Neoclassical theory of diffusion gives good agreement with the simulation results only when the long wavelength collective modes are deliberately suppressed. Enhancement over the neoclassical transport appears due to the convective motion associated with the low-frequency, long wavelength convective cells. (5) Some preliminary results on low-frequency, micro-instabilities (drift-wave and drift-wave type mode) will be discussed.

---

* *Presented at the 3rd U.S.-Japan Plasma Physics Seminar, Kyoto, Japan,* (1974)

IIID 11. MATT-1093 Theory of Plasma Simulation Using Multipole-Expansion Scheme, by Liu Chen and Hideo Okuda

Nonphysical grid effects in plasma simulation using the Multipole-Expansion scheme and Gaussian-shape charge particles are studied analytically in one dimension. General expressions for the linear dispersion relation, fluctuation spectra, energy, and momentum conservations are derived and then compared with those of the Cloud-in-Cell (CIC) scheme. The results indicate that generally the Multipole-Expansion scheme and its subtracted version have less grid effects and, hence, are considered to be better than CIC.

IIID 12. Collisions in Multidimensional Plasma Simulations,* by Y. Matsuda and H. Okuda

Collisions in multidimensional plasma simulation models using finite size particles are studied numerically and analytically. Drag and diffusion of particles in velocity space are measured and are compared with the theoretical predictions for two-, two-and-a-half-, and three-dimensional models. For two- and three-dimensional models, the measurement agrees reasonably well with the theory. For two-and-a-half-dimensional model, it is shown that the collisions strongly depend on the choice of the angle between magnetic field and wave vector due to the limited phase space available for scattering the particles in the model. For a strongly magnetized plasma with

$\omega_{ce} > \omega_{pe}$, the effective collisions are significantly reduced for a simulation plasma when $a \gtrsim \rho_e$ (a = particle size, ρ_e = gyroradius) in contrast to a real plasma where the effective collisions increase slowly with the magnetic field.

---

* *Presented at the Meeting on Particle Codes*, Berkeley, Calif., Dec. 4, 1974.

IIID 13. MATT-1095 Study of Magnetohydrodynamic Modes in Tokamak Configurations with Noncircular Cross Sections, by M. S. Chance, R. L. Dewar, A. H. Glasser, J. M. Greene, R. C. Grimm, S. C. Jardin, J. L. Johnson, B. Rosen, G. V. Sheffield and K. E. Weimer

Stability criteria for localized instabilities for both ideal and resistive models are derived and evaluated for general axisymmetric configurations. A numerical scheme for determining the spectrum in these configurations is developed. Application is made to the special case of an elliptical cylindrical plasma column, with finite pressure and length, carrying a uniform axial current.

IIID 14. Numerical Study of Equilibrium and Localized Stability Properties of Axisymmetric Toroidal Configurations,* by K. E. Weimer, R. C. Grimm, S. C. Jardin, and G. V. Sheffield

In design studies for the PDX device being built at Princeton University, it is useful to investigate the MHD properties of specific configurations. We solve numerically the usual (x) = RJϕ equation for a reasonable prescription of the pressure and poloidal current distributions, given the total toroidal current. The boundary conditions are fixed by specifying currents in external coils so that no conducting boundary is required. We evaluate the criteria for localized instabilities for both ideal and resistive models.

**Presented at the Sixteenth Annual Meeting of the American Physical Society* (1974). Albuquerque, N. M.

IIID 15. Techniques for Study of MHD Modes in General Axially Symmetric Toroidal Configurations,* by R. C. Grimm, M. S. Chance, J. M. Greene, J. L. Johnson, B. Rosen, and K. E. Weimer

Earlier programs for study of tokamak stability have been extended to include toroidal effects. We adopt a natural coordinate system based on the magnetic field lines and decompose the perturbations into components selected to match the polarizations of the different modes as

nearly as possible. This enables us to study the spectrum and shape of the perturbations for frequencies extending over many orders of magnitude.

---

* *Presented at the Sixteenth Annual Meeting of the American Physical Society* (1974). Albuquerque, N. M.

IIID 16. Use of Symbolic Programming in Code Construction for Studying MHD Modes in Toroidal Systems,* by B. Rosen, J. M. Greene, R. C. Grimm, and J. L. Johnson

Use is made of the MACSYMA system to calculate the analytic form of the potential and kinetic energies, δW and K, in toroidal geometry. The Lagrangian displacements are decomposed in a non-orthogonal coordinate system chosen to make the secular matrix have a band structure. The calculation is carried out in terms of vectors; components appear only when the vectors are explicitly expressed in terms of the basis vectors. Extensive use is made of the patterm-matching facilities of MACSYMA for this purpose. Pattern matching is also used to evaluate the Fourier integrals arising from the insertion of Fourier series for the displacements together with the specification of the equilibrium.

---

* *Presented at the Sixteenth Annual Meeting of the American Physical Society* (1974). Albuquerque, N. M.

IIID 17. MATT-1099 Numerical Study of the Magnetohydrodynamic Spectra in Tokamaks Using Galerkin's Method, by R. L. Dewar, J. M. Greene, R. C. Grimm and J. L. Johnson

A computational technique is described for determining the ideal magnetohydrodynamic spectrum and its associated eigenfunctions. The method is suitable for axisymmetric toroidally confined plasmas with arbitrary cross sections. Using the special case of a long, straight, elliptical plasma column with low pressure and uniform axial current where analytic results are available, a study is made of the efficacy of two different choices of expansion functions. The use of a finite-element representation, keeping only a small number of terms, is shown to provide a good description of the system.

IIID 18. Numerical Determination of Mode Spectra in a Finite Straight Tokamak with Uniform Axial Current and Elliptic Cross Section,* by M. S. Chance, R. C. Grimm, J. M. Greene, J. L. Johnson, and K. E. Weimer

We have generalized a previously reported computational program which gives the mode spectrum for small perturbations from special low-pressure equilibria. The present generalization incorporates the effect of finite pressure and finite wave length but retains the constant axial current and similar elliptic magnetic surfaces of the previous calculation. This model is appropriate for studying ballooning effects associated with variations of field line curvature along a magnetic line. For this model we can determine the limits of the continua expected in the wave spectrum. We give a comparison of the numerical results with these predictions, as well as typical eigenmodes associated with instabilities.

---

*Presented at the *Meeting on Theoretical Aspects of CTR* (Sherwood Meeting), Berkley, Calif. April 3-5, 1974.

IIID 19. MHD Modes in Straight Tokamaks with Elliptic Cross Sections,* by M. S. Chance, J. M. Greene, R. C. Grimm, and J. L. Johnson

A numerical procedure for investigating MHD stability by extremizing the Lagrangian is applied to the case of a straight plasma column with elliptic cross section, carrying a uniform axial current, and embedded in a vacuum with an arbitrarily placed conducting wall. The plasma pressure is taken sufficiently large, and the periodicity length small, that all the modes of the spectrum must be treated together. By examining the structure of an unstable kink mode as the ellipticity of the column is increased, we investigate the importance of ballooning effects associated with variations of line curvature along the magnetic field.

---

* *Presented at the Sixteenth Annual Meeting of the American Physical Society* (1974). Albuquerque, N. M.

IIID 20. MATT-1054 Fluid Simulation of a Low Pressure Toroidal Plasma Using Axisymmetric Field-Line Coordinates, by R. C. Grimm and J. L. Johnson

A numerical model is developed to study the confinement of low-pressure plasmas in axially symmetric configurations with arbitrary shaped magnetic surfaces. The equations contain the effects of resistivity, plasma inertia, and pressure gradients in that the magnetic fields, although assumed static, can be self consistent. The Lax-Wendroff scheme is used to advance the plasma density and velocities in time. Applications include demonstration that classical expressions for diffusion are valid when there are small plasma flows, and study of the propagation of acoustic and geodesic waves in levitrons.

IIID 21. Fokker-Planck Simulation of Compressional Energy-Clamping of Beam-Injected Ions in a Tokamak,* by R. M. Kulsrud, D. L. Jassby, and Y. C. Sun

A multi-species, 2-D code that numerically solves the Fokker-Planck equation over a mesh in velocity space is used to follow the velocity distribution of ions injected at energy W_o parallel to the toroidal magnetic field of a tokamak, and subjected to slow major-radius compression. The compression rate is optimized to "clamp" the energy of the injected ions. In simulation of the proposed TCT device (C = 1.5), slow compression is followed by thermalization of the fast ions. The Fokker-Planck calculations for W_o = 115 keV, $n_{eo} = 4 \times 10^{13} cm^{-3}$, T_{eo} = 3.5 keV (precompression), compression period = 76 msec, give Q = 1.38 for Z = 1 and Q = 1.24 for Z = 3, with Fe impurity (D beams on T target). Analytic expressions for a nonscattered beam give Q = 1.46; the smaller values in the 2-D simulation are due to the smaller energization experienced by the perpendicular energy components. The observed energy dispersion, up to 35 keV, has insignificant effect on Q.

*Presented at the *Sixteenth Annual Meeting of the American Physical Society* (1974), Albuquerque, N. M.

IIID 22. MATT-1079 The Effects of Impurities and Magnetic Divertors on High-Temperature Tokamaks, by D. M. Meade, H. P. Furth, P. H. Rutherford, F. G. P. Seidl, and D. F. Düchs

A one-dimensional tokamak plasma transport code has been adapted to include impurity influx, stripping, radiation, and diffusion, as well as the usual processes of hydrogen plasma and heat transport, recycling at the boundary, and multi-generation charge-exchange. Neutral-beam heating, adiabetic compression, and divertor boundary conditions are included as optional features. Illustrative computations are given for present-day and next-generation tokamaks. The problems of impurity control are discussed, and two technical approaches are examined in greater detail: the transient cold-plasma shield, and the poloidal divertor.

E. Theoretical Research Under the Air Force Contract

Research has been carried out in a number of areas which are supported either partially or fully by the Air Force Contracts. Research on numerical simulation, plasma heating, or parametric instabilities is described in other sections. The remainder is summarized here.

1. Laboratory Plasmas

Ono and Kulsrud have used the Fokker-Planck code to numerically derive the damping rate and frequency of ion-acoustic waves in the presence of collisions. They have derived the entire curve for collisional rates ranging from strong collisions to weak collisions for $T_e = 4T_i$, $2\ T_i$, T_i, $T_i/2$. These results agree well with known theory in the limit of strong and weak collisions.

Johnston (Abstract III E 1) has developed an oscillating center formalism for studying two-wave particle processes such as nonlinear Landau damping and Chen-Porkolab coupling. This formalism treats these phenomena as modified induced scattering processes and obtains the rates for these processes in compact form. Perkins has reviewed the variety of parametric instabilities in their various applications and isolated the remaining problems (Abstract III E 2). Williams and Liu have discovered a new nonlinear mode conversion process in inhomogeneous plasmas (Abstract III E 3).

2. Space Physics and Astrophysics

Perkins has derived the basic equation for the study of plasma density striation in the ionosphere (Abstract III E 4). These density striations have important applications for space communications.

Cohen, Dewar, and Kulsrud have been studying the hydromagnetic turbulent spectrum in the solar wind. Dewar and Cohen have shown that the decay instability can modify the spectrum in an important way (Abstract III E 5) causing the spectral index to spectrum to steepen with distance from the sun (Abstract III E 6). Cohen and Kulsrud have completed their theoretical study of the long term evolution of non-circularly polarized Alfvén waves. They have determined the constants which determine the final circularly polarized state (Abstract III E 7).

IIIE 1. PPL-AP-80 Oscillation-Center Formulation of the Classical Theory of Induced Scattering in Plasma, by Shayne Johnston

Particle trapping in the beat potential produced by the mixing of two coherent waves lies outside the domain of the conventional weak-turbulence theory of induced scattering in plasma. In this paper a reformulation of the theory is presented which is applicable to this extended domain. The formulation is based upon a canonical transformation to "oscillation-center variables" due to Dewar,[1] and affords in particular a simpler method for deriving the "linear" matrix elements of weak-turbulence theory. This method is first illustrated in the problem of the induced scattering of longitudinal plasma modes. The power of the method is then usefully exploited in two more difficult situations, namely the cases of electrostatic waves in the presence of a uniform magnetic field, and electromagnetic waves in an arbitrarily relativistic plasma. The application of the transformation to the extended strong-interaction regime is demonstrated.

IIIE 2. Parametric Instabilities: Nonlinear Optics in Plasmas,* by F. W. Perkins

Intense monochromatic (pump) radiation propagation in a plasma is subject to a wide variety of instabilities, depending on the nature of the pump wave, the geometry of the plasma, and the details of the nonlinear coupling. Nonlinear wave phenomena have been invoked in many areas of plasma physics: magnetically confined laboratory plasmas, laser-plasma interactions, ionospheric modification, and pulsars. This talk will attempt to survey the recent results and point out unresolved problems.

---

*Washington Meeting of the American Physical Society, April 22-25, 1975

IIIE 3. Harmonic Generation of Obliquely Incident Radiation on a Nonuniform Plasma,* by E. A. Williams and C. S. Liu

At the point where the frequency of an electromagnetic wave, obliquely incident onto a plasma of increasing density, equals the local plasma frequency, the electromagnetic wave is resonantly transformed into an electrostatic plasma wave. This plasma wave can beat with itself to generate an electromagnetic wave at twice the incident frequency, corresponding to a two plasma → one photon process. The generated harmonic peaks at 90° to the incident wave, consistent with experimental observation. The electric field $E^{(2)}$ of the second harmonic is given approximately by $[E^{(2)}]^2/8\pi nT \sim 3 \times 10^{-4}(v_{Te}/c)^2(L/\lambda_D)^{4/3}(E_{in}^2/8\pi nT)^2$, where L is gradient scale length, giving about 1% harmonic generation for the experimental parameters of Lee, et al., again consistent with their observations.

*16th Annual Plasma Physics Meeting of the American Physical Society, October 28-31, 1974, Albuquerque, N. M.

IIIE 4. PPL-AP-78 A Theoretical Model for Short-Scale Field-Aligned Plasma Density Striations, by Francis W. Perkins

The short-scale (~ 3 m), field-aligned plasma density striations found in ionospheric modification experiments are generated by the plasma turbulence resulting from ion acoustic-plasma wave parametric decay instabilities. The field-aligned geometry results from the fact that nonlinear wave coupling arises from thermal, Ohmic heating terms rather than pondermotive force (radiation pressure). The theory shows that field-aligned striations increase rapidly in intensity as the wavelength increases--in agreement with experiment.

IIIE 5. PPL-AP-72 On the Backscatter Instability of Solar Wind Alfvén Waves, by R. H. Cohen and R. L. Dewar

A coherent Alfvén wave propagating along the equilibrium magnetic field is unstable against decay into an Alfvén wave traveling in the opposite direction and a sound wave [Sagdeev and Galeev, 1967]. The stability of incoherent Alfvén waves against this mode decay is considered, assuming that the sound waves are damped. The criterion for stabilizing waves with power spectral density $I_k \propto k^{-N}$ is $N > 1$. The results indicate that solar wind Alfvén waves are stable in the wavelength range considered in Mariner V observations, although a mild instability is predicted for longer wavelengths.

IIIE 6. PPL-AP-73 Mode Decay and Gradients in the Interplanetary Magnetic Field Fluctuation Spectrum, by Ronald H. Cohen

Resonant mode decay can lead to selective degradation of portions of a broadband spectrum of Alfvén waves [Cohen and Dewar, 1974]. This effect may be responsible for the observation [Smith, 1974] that, in Pioneer 10 data, 24-hour variances in the magnetic field component fluctuations decrease with distance from the sun faster than 1-hour variances.

IIIE 7. PPL-AP-74 Nonlinear Evolution of Parallel-Propagating Hydromagnetic Waves, by Ronald H. Cohen and Russell M. Kulsrud

The nonlinear evolution of plane hydromagnetic fluctuations propagating along the unperturbed magnetic field direction is considered. From an expansion of the ideal magnetohydrodynamics (MHD) equations and the hydromagnetic shock jump conditions, it is shown that a wave in which the magnitude of the magnetic field is non-constant steepens into a shock and subsequently evolves toward a purely Alfvénic fluctuation of lower mean energy density. Explicit expressions are derived for the asymptotic state and for the characteristic lines which describe the evolution toward that state. A class of fluctuations which includes linearly polarized waves is shown to evolve into rotational discontinuities. The results are applied to observations of hydromagnetic fluctuations in the solar wind.

IIIE 8. PPL-AP-79 The Stabilizing Effects of Cloud Reacceleration: Microturbulence, and Rotation on Parker's Instability, by Ellen G. Zweibel and Russell M. Kulsrud

We reconsider Parker's instability including a model equation of state for the gas of interstellar clouds, a tangled interstellar field, and galactic rotation. We find that for most choices of interstellar parameters consistent with observation the instability is stabilized. For the remaining choices which can lead to instability the growth time is longer than 10^8 years. Thus, we conclude the instability can have little to do with cosmic ray escape and probably cannot destroy a primordial galactic field.

IIIE 9. PPL-AP-76 A Multiple Pulsar Model for Quasi-Stellar Objects and Active Galactic Nuclei, by J. Arons, J. Ostriker and R. Kulsrud

We assume that there have existed small (~10° pc) central regions in galaxies where the rate of pulsar-forming supernova events is high (10° - 10^2 yr^{-1}). The supernova remnants in these regions largely overlap and constitute ideal environments for the production of and radiation from high energy particles. We calculate in the context of the specific magnetic dipole model of pulsars, expected distributions of EM fields, particle energies, and emitted radiation and find that, within the accuracy of the calculations there is rough agreement between computed quantities and observed properties of active galactic nuclei and QSOs.

One new physical process is investigated in detail. In a collection of emitters radiating strong waves, there will exist regions in which waves from pairs of emitters are in resonance along particular particle orbits. In these regions the particles experience both scattering and a strong secular acceleration. The latter is the dominant means by which relativistic particles gain energy.

IV. SMALL MACHINE EXPERIMENTS

A. Introduction

Research on the major toroidal-confinement devices at PPL is supplemented by a program of investigation carried out on a group of small linear-geometry plasma devices. Studies of plasma produced by a CO_2 laser and confined in a strong solenoidal magnetic field comprise the COOL experiment which examines the plasma physics concepts underlying the CTR reactor proposed by Dawson, Kidder and Hertzberg. Plasma heating in the range of the lower-hybrid frequency (i.e., a few gigahertz for a fusion reactor -- a frequency range where megawatt electron tubes are commercially available) is under investigation in the H-1 device, while nonlinear and inhomogeneous-plasma wave phenomena are the subjects of current research on the hot-electron L-3 and L-4 machines. On the alkali-metal quiet plasma device, Q-1, the past year has seen the completion of a series of experiments on parametric decay instabilities in isothermal plasmas, and on the evolution of current-driven (parallel to B) instabilities tying together phenomena in four different regimes. In the surface science laboratory, work on sputtering of ions from stainless steel has been completed, and preparations have been made to study sputtering of neutrals from graphite and stainless steel.

B. CO_2-Laser-Heated-Plasma Experiment (COOL Experiment)

The COOL experiment, initiated in November 1972, is directed at answering several fundamental questions governing the Dawson-Kidder-Hertzberg CTR scheme utilizing CO_2 -laser heating of magnetically confined, weakly-underdense plasmas: (1) formation of an on-axis density minimum, by the action of the laser itself, for laser-beam guiding, (2) laser-beam self-focusing (Abstracts IV B1 and IV B2), (3) elimination of beam shielding, an effect in which a backward-propagating laser-driven shock wave shields the plasma core from the incident radiation (Abstracts IV B3 and IV B4), (4) plasma transport and its inhibition by a strong magnetic field, and (5) preservation of beam self-focusing in the presence of a strong magnetic field (Abstract IV B5).

Experimental results on items (1) and (2) in zero magnetic field were reported a year ago, in MATT Q-31. In particular, the observation of a laser-driven, backward-propagating detonation wave led to the conclusions first that this wave produces the undesirable beam-shielding effect because of the high plasma density and low plasma temperature in the wave, and second, that methods must be found to minimize or to eliminate this effect. Since a shock wave cannot propagate into a vacuum, it was found possible to eliminate the backward-propagating shock wave and its accompanying beam-shielding effect by initiating the laser-plasma interaction at a plasma-vacuum interface produced with a free expansion jet, Figs. 1 and 2.

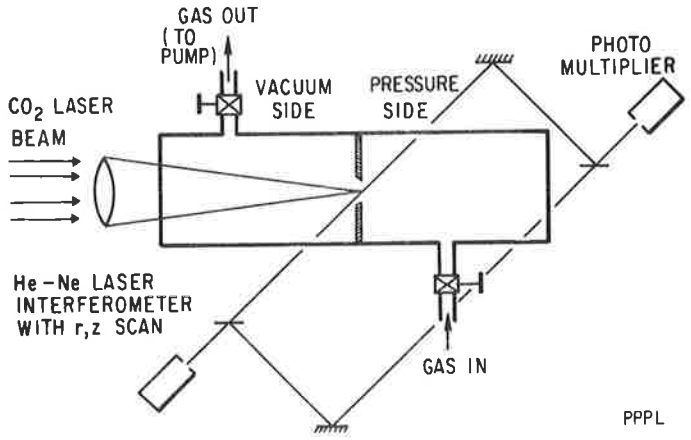

Fig. 1. Schematic of COOL test section. A steep gas pressure gradient is established at the exit of the orifice when the pressure side is pulse-filled just prior to laser pulse. In experiments without the steep-gradient interface, the entire chamber is filled to desired pressure and the orifice may be removed.

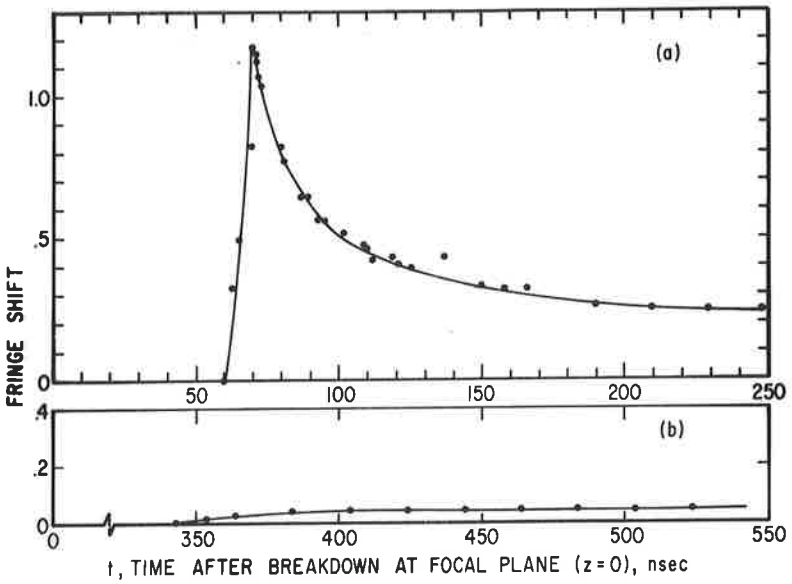

Fig. 2. Fringe shift versus time at $z = -1.25$ cm (a) without the interface (b) with the interface. H_2 at 10 torr.

In a new series of COOL experiments, a quasi-steady magnetic field of up to 270 kG, provided by a pulsed solenoid, 5-cm bore, 20-cm long, energized by a 250 kJ capacitor bank, was used to reduce the lateral expansion of the plasma. For a given initial gas pressure and at a fixed time after breakdown, the measured plasma diameter D as a function of B is characterized by three regimes, Fig. 3: (1) D is nearly constant as B is increased from zero in the regime $\beta \equiv 8\pi nkT/B^2 >> 1$, (2) D rapidly decreases as B is raised further in the regime $\beta \sim 1$, and (3) D slowly decreases and asymptotically approaches a limiting minimum value when B is still further increased, in the regime $\beta << 1$.

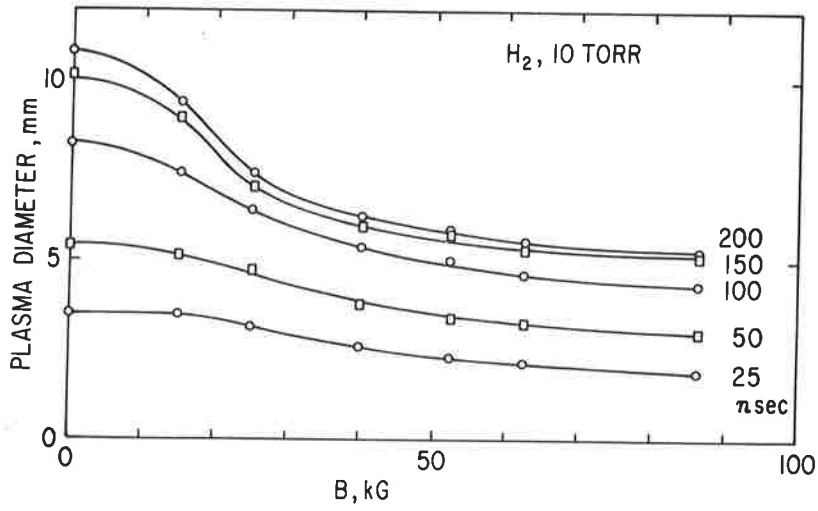

Fig. 3. Plasma diameter versus magnetic field strength at various times subsequent to breakdown (t = 0).

A side-on Mach-Zehnder interferometer, using a short-pulse ruby laser, has now been developed. This interferometer enables us to measure electron density integrated over the line of sight in a single shot (~3 nsec time resolution) for the entire r,z plane limited only by the aperture of the optics. Upon inversion, density distributions are obtained. A typical fringe shift pattern for a 250 kG magnetic field is shown in Fig. 4. The observed trapezoidal fringe shift pattern, upon inversion, yields an on-axis density minimum profile.

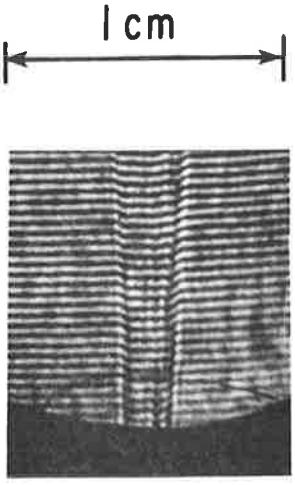

753123

Fig. 4. Interferogram showing fringe shift of ruby laser light (λ = 694 nm). Helium gas at 50 torr, B = 250 kG, t = 260 nsec. One fringe shift equals 3.2×10^{17} electrons/cm^2. CO_2 laser is incident from the left. The exit of the free-expansion jet is located 7 mm to the left of the left edge of the interferogram.

Having now successfully produced plasmas with the on-axis density minimum required for beam self focusing, having eliminated the beam-shielding backward-propagating detonation wave, and having shown inhibition of lateral expansion by an externally applied magnetic field, the next phase of the COOL experimental investigation will focus on the scaling law of propagation of the longitudinal heating wave. The knowledge of this scaling law is essential for the formation of a plasma column of large length/diameter aspect ratio.

IVB 1. Experiment on Interaction of CO_2 -Laser With Weakly Underdense Plasmas-Measurement of Beam-Self Focusing*, by L. C. Johnson and T. K. Chu

Space-and time-resolved interferometric measurements of electron density in a CO_2 -laser-produced plasma in helium show the development and evolution of radial profiles with on-axis minima, resulting in self-focusing of the laser beam.

---

* *Fourth Annual Conference On Anomalous Absorption* (Lawrence Livermore Laboratory, Livermore, Calif., 1973) Paper B.9.

IVB 2. Measurement of Electron Density and Laser Beam Self-Focusing of a CO_2 Laser-Induced Plasma in a Strong Magnetic Field.* L. C. Johnson and T. K. Chu

Measurements have been made on the plasma produced in helium or hydrogen at the focal spot of a 50 J TEA CO_2 laser and confined in a strong magnetic field of up to 250 kG. With initial gas pressure of 10 to 50 torr, the plasma was roughly cylindrical, with a radius of ~ 3 cm, and a density 1 to 5 × $10^{18}cm^{-3}$. A He-Ne laser-illuminated Mach-Zehnder interferometer was used for shot-to-shot scanning to deduce density profiles with spatial resolution of ~ 3 nsec. In addition, ruby-laser holographic interferograms (temporal resolution ~ 20 nsec) were made at specific times on individual shots. Beam self-focusing was observed by monitoring the refracted laser beam. Results show that (1) the on-axis density minimum necessary for beam self-focusing and (2) the accompanying beam self-focusing are preserved in the presence of the magnetic field.

---

* *Bull of Am. Phys. Soc.* 19, 931 (1973).

IVB 3. Elimination of Backward-Propagating Laser-Supported Detonation Wave in Weakly Underdense Plasmas,* by T. K. Chu and L. C. Johnson

Space- and time-resolved interferometric measurements of electron density in CO_2-laser produced plasmas in helium and hydrogen show shock waves propagating in both directions along the beam. The shock wave propagating toward the focusing lens effectively shields the interior plasma from the incident beam, because the lower plasma temperature and higher plasma density in the shock allow strong absorption of the incident beam energy. By arranging the laser radiation-plasma interaction to begin at a plasma-vacuum interface, the beam-shielding shock wave and its propagation are simultaneously eliminated, thus permitting efficient energy deposition in the plasma interior.

---

* *Bull. Am. Phys. Soc.* 19, 642 (1974); also *Fourth Annual Conf. on Anomalous Absorption* (Lawrence Livermore Laboratory, Livermore, Calif., 1974) Paper B.10

IVB 4. Axially Propagating Laser-Driven Shock Wave, its Beam Shielding Effect and Method of Elimination, and Plasma End Loss in a Magnetically-Confined, Laser-Produced Plasma*, by J. Fitzwilliam, T. K. Chu, and L. C. Johnson

Laser-induced breakdown of a homogeneous gas is accompanied by laser supported detonation waves which propagate in both directions along the beam. The high-density, low-temperature, backward propagating shock wave absorbs beam energy and thus reduces the energy of the beam transmitted through the shock, adversely shielding the plasma interior from the beam. Since a shock wave cannot propagate into a vacuum, the backward propagating detonation wave can be eliminated by initiating the laser-plasma interaction at a plasma-vacuum interface produced with a free-expansion jet. Measurements on CO_2 laser-induced breakdown plasmas in H_2 and He, show that the backward propagating shock wave is not present in the free-expansion jet experiment. For a magnetically confined plasma in the case with plasma-vacuum interface, the end-loss time, as determined from the plasma free-expansion rate into the vacuum, is in agreement with the observed lifetimes.

---

* *Bull. Am. Phys. Soc.* 19, 931 (1974).

IVB 5. Effects of Magnetic Field on the Lateral Expansion of a Laser-Induced Plasma*, by T. K. Chu and L. C. Johnson

The plasma produced at the focal spot of a CO_2 laser and confined radially in a strong magnetic field expands laterally against the field. The effect of a magnetic field on this lateral expansion was determined by monitoring the time-of-arrival of the leading edge of the radially expanding shock wave. For a given initial gas pressure and at a fixed time after breakdown, the measured plasma diameter D as a function of B is characterized by three regimes: (1) D is nearly constant as B increases from zero, in the regime $\beta \equiv nkT/(B^2/8\pi) \gg 1$, (2) D rapidly decreases as B increases further, in the regime $\beta \sim 1$, and (3) D slowly decreases and asymptotically approaches a limiting minimum value when B still further increases, in the regime $\beta \ll 1$. Regime (2) demonstrates the reduction of plasma expansion due to the magnetic pressure, and regime (3) is consistent with expectations by considering diffusion.

---

* *Bull. Am. Phys. Soc.* 19, 932 (1974).

C. H-1

The current H-1 program examines the physics and engineering problems associated with plasma heating near the lower hybrid frequency, and the main effort during the past year has been directed toward the forthcoming 800-MHz 200-kW lower-hybrid heating experiment on the ATC Tokamak. This preparation has taken place along two parallel paths, 1) the construction of the 200-kW radiofrequency source, and 2) experiments on the H-1 test device with a special emphasis on developing waveguide coupling structures.

The 200-kW rf system has been designed and constructed by PPL's Power Electronics Section and the power supply by the Power Engineering Section. The original estimated date for completion of this device was April 1975 and construction is on schedule. The system consists of four 50-kW modules operating at a frequency of 800 MHz with a pulse length capability of 20 msec. A more detailed description of this generator appears in the Engineering Section of this Annual Report.

The recent experiments on the H-1 test device have been related to the development of waveguide coupling systems. Today's toroidal devices are of such dimension that the free space wavelength corresponding to the lower hybrid frequency is comparable with the minor diameter of the plasma. Thus the possibility arises that one may couple the rf energy to the plasma by means of open-ended waveguide apertures in the vacuum-vessel wall rather than an internal coil structure, which is characteristic of lower frequency regimes. From an engineering viewpoint the basic problem is to match the impedance of the waveguide coupling structure to the desired plasma-wave mode. This matching problem is related but not identical to the problem of slow wave penetration to the hybrid resonance layer. For the mode in question, the wave electric field is parallel to the toroidal magnetic field in the tenuous $\omega < \omega_{pe}$ layer but at higher densities the main rf electric field component is aligned in the direction of the plasma minor radius. Consequently the proper waveguide orientation is such that the E-field in the guide is parallel to the tokamak toroidal field, driving the waveguide in a TE or TM mode to couple to the $\tilde{E}_z$ or $\tilde{E}_r$ (respectively) components of the plasma mode. In the experiments shown below only TE excitation has been used but TM excitation studies are underway on the H-1 device.

It was first shown by Stix that rf penetration to the resonance layer requires an index of refraction in the z-direction, n_z, somewhat greater than unity. A possible way to obtain waves with suitable values of n_z is to work with an array of adjacently-positioned properly-phased waveguides. Such a system is being suggested for use on the Joint European Tokamak and a similar system is planned for the forthcoming ATC experiment. The experimental set-up shown in Fig. 1 was used to study the plasma coupling and penetration using an elementary phased waveguide array. The two guides are driven in the TE_{10} mode at 3.4 GHz, that is, with a free-space wavelength approximately equal to the plasma diameter — as will be the case in the ATC device. Also for this work, as in the ATC experiments, the $\omega \simeq \omega_{pe}$ layer lies essentially at (or perhaps within!) the waveguide opening. In the H-1 experiment, the relative phase at the waveguide opening, $\Delta\phi$, is controlled by the line stretcher shown in Fig. 1 When the waveguides are driven in phase ($\Delta\phi = 0$), the Fourier-spectrum of the E_z field at the opening peaks at $n_{\parallel} = 0$ as for a single waveguide. Although this case would give efficient radiation in free space, it should not lead to rf penetration of dense plasma. When $\Delta\phi = 180^{\circ}$ the Fourier spectrum peaks at $n_{\parallel} = 2.2$ and has a null at $n_{\parallel} = 0$. This arrangement should produce little radiation into free space but much more efficient plasma penetration. A quantitative theory for the waveguide-plasma impedance mismatch and the corresponding waveguide reflection coefficients is being developed by Dr. M. Brambilla of C.E.N. in Grenoble.

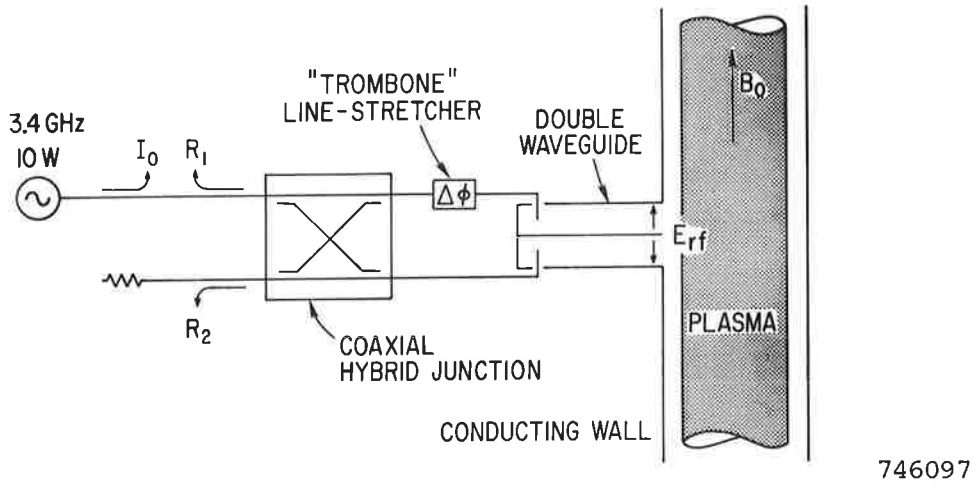

Fig. 1. Circuit of microwave excitation of double-waveguide antenna. Transmitted and reflected signals are monitored couplers I_o, R_1, and R_2.

The H-1 experiments are the first to test these wave coupling concepts. Figure 2 shows the measured time-averaged reflection coefficients of the antenna as a function of relative aperture phase for different plasma densities. In the absence of a plasma the reflection coefficient is about 3% when the apertures are driven in phase ($\Delta\phi = 0$) and reaches a maximum of 54% when $\Delta\phi = 180^{o}$, in agreement with the qualitative conclusions drawn in the preceding paragraph. For the case where the peak plasma density is 20 times the $\omega = \omega_{pe}$ critical density the reflection coefficient at 180° decreases to around 4% and an excellent impedance match is achieved. Single waveguide excitation under similar conditions shows reflection coefficients at least ten times higher.

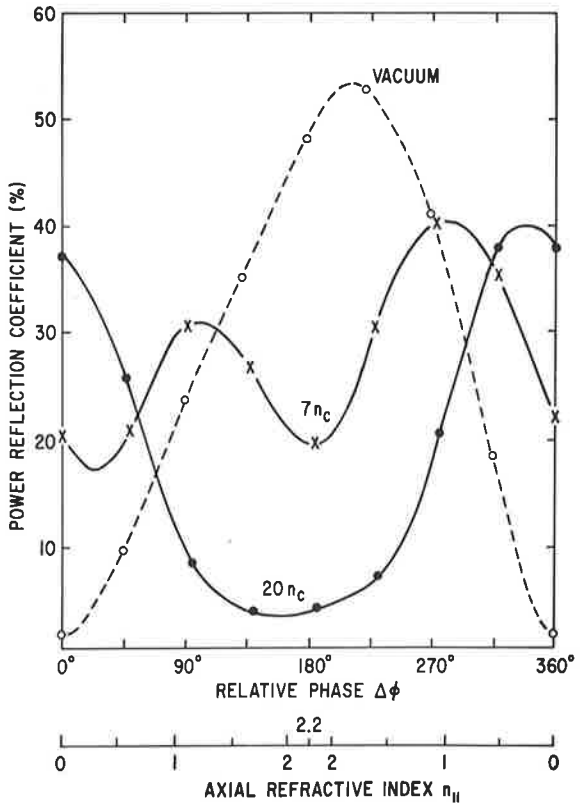

746096

Fig. 2. Measured power reflection coefficient as a function of relative aperture phase. The parameter is the peak electron density normalized to the critical density for the operating frequency, $n_c = \varepsilon_o m_e \omega^2/e^2$. The lower abscissa scale shows the peak values of the $n_{\parallel}$ Fourier spectrum calculated from the nominal aperture fields.

To obtain information on the structure of the waves in the plasma interior, electrostatic probes were used to map the wave fields, Fig. 3. With $\Delta\phi = 180^{o}$, the measured $n_{\parallel}$ in the interior of the plasma was 2.1, in close agreement with the calculated peak of the Fourier spectrum. The central portion, Fig. 3b, shows the wave amplitude at various distances down the column axis from the waveguide. The dashed lines at the bottom, Fig. 3c, show the computed ray trajectories for various $n_{\parallel}$ and the solid line marked "E" is the trajectory of the peak wave amplitude, clearly consistent with the ray computations for $n_{\parallel} = 2.1$. Wave normals, constructed from the experimental phase data, are found to be inclined at an angle of 85^{o} with respect to the group velocity, while the computed results for the slow mode with $n_{\parallel} = 2.1$ would predict an angle of 80^{o}. Analysis of the phase data also shows that the total refractive index is in the range of 5-7, again in good agreement with theory. Variation of the double-waveguide phase difference, $\Delta\phi$, affected the amplitude of the probe signal in rough agreement with the measured antenna reflection coefficients. It is apparent from these measurements internal to the plasma that the waveguide system is coupling to the slow mode which is the one desired for lower hybrid heating.

These preliminary results on the H-1 test device are not conclusive for tokamak operating conditions, but give a very positive indication that the phased array of waveguides appears to provide effective coupling to the desired mode for lower-hybrid heating.

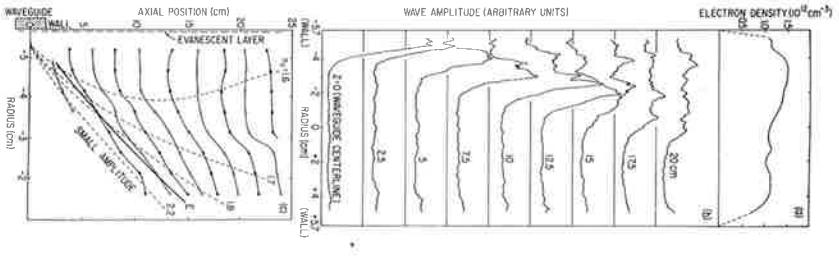

753277

Fig. 3(a). Electron density as a function of radius, $n_{max} = 10\ n_c$.

Fig. 3(b). Observed wave magnitude as function of radius in successive planes downstream from the antenna ($z = 0$);

Fig. 3(c). Experimental points defining contours of constant phase (phase difference between contours is 180^{o}). Heavy solid curve E: locus of observed maximum wave amplitude. Dashed curves: ray trajectories computed from WKB theory for various $n_{\parallel}$ values. Note the change in radial scale from (b).

IVC 1. An Overdense Radio Frequency Plasma Source*, by S. Bernabei, D. L. Jassby, W. M. Hooke, and R. W. Motley

We have developed an rf (155 MHz) plasma source for the study of wave heating at frequencies comparable to and greater than the lower hybrid resonance frequency. Ion densities of almost $10^{13}cm^{-3}$ may be attained in an 8 liter column with a power input less than 1 kW/liter. Elevated ion temperatures, comparable to and sometimes greater than the electron temperature (1-10 eV) have been measured with a Fabry Perot interferometer. Information on the wave coupling, the electron and ion heating efficiencies, and the secondary waves generated by nonlinear interaction of the pump wave will be discussed.

---

* *Second Topical Conference on RF Plasma Heating* (Lubbock, Texas, June 1974).

IVC 2. Ion Heating in Nonresonant RF Discharges*, by E. L. Tolnas, R. W. Motley, D. L. Jassby, S. Bernabei, and W. M. Hooke

Magnetically confined discharges are produced in argon and xenon by capacitively coupled rf energy with frequency (155 MHz) 3 to 10 times the maximum ion plasma frequency. Electrostatic probe and Fabry Perot measurements reveal transverse ion temperature up to 16 eV at $n_i = 0.3\text{-}2 \times 10^{12}cm^{-3}$, in the presence of self-generated dc radial electric fields (5-50 V/cm). If the electric fields are shorted out, the maximum T_i is 5 eV at rf power of 3 kW, with heating rates of 5-20 eV/msec. In most cases, $T_\perp > T_\parallel$. The observed heating when $E_r \simeq 0$, appears to be due to low-frequency turbulence.

---

* *Washington D.C. Meeting of the American Physical Society*, (April 1974).

IVC 3. Plasma Penetration and Coupling with Waveguide Excitation*, by S. Bernabei, PPL, P. L. Colestock and W. D. Getty, U. of Michigan, and M. A. Heald, Swarthmore College

In lower-hybrid heating experiments for ATC it is planned to use waveguide excitation. In order to study wave accessibility and linear mode conversion with waveguide excitation an experiment has been performed in which transverse plasma and waveguide dimensions are scaled down from those of ATC. Excitation frequency relative to the lower-hybrid frequency could not be scaled; conditions are $\omega_{LH} << \omega < \omega_{pe} < \omega_{ce}$. Microwave coupling to the 5-cm radius plasma column and the resultant plasma wave excitation were measured with moveable probes using interferometric and correlation techniques. An open-ended waveguide in the TE10 mode excited the ordinary wave ($E_{RF} \| B_o$), which was strongly reflected at the critical layer where $\omega \simeq \omega_{pe}(r)$. Density fluctuations due to drift waves at $f \simeq 6$ KHz caused large variations in the reflection coefficient and inhibited matching by external tuners. Plasma waves were observed along the column with microwave probes. Alternative excitation modes such as the TE10 with $E_{RF\perp} B_o$ and dual phased waveguides were also studied.

---

* *Sixteenth Annual Plasma Physics Meeting of the Am. Phys. Soc.* (Albuquerque, N. M., October 1974).

D. Wave Propagation and Nonlinear Effects in RF Plasma Heating Experiments (L-3)

The L-3 rf plasma heating program has centered on the following problems: 1) effects of plasma inhomogeneities upon parametric instabilities and plasma heating, 2) parametric backscatter instabilities, and 3) wave launching and wave propagation near the lower-hybrid frequency. Each of these experiments is expected to yield information valuable to the PPL large-scale tokamak rf-heating program.

Experiments on the effects of density gradients upon parametric instabilities constitute a continuation of L-3 work from the previous year. A number of theories predict that in inhomogeneous plasmas the threshold for parametric instabilities is determined by convective losses and mismatch due to gradients, rather than dissipative effects. Thus, the threshold for parametric instabilities is expected to vary as $P_{thr} \propto 1/(kL)$, where P_{thr} is the threshold pump power, k is the wavenumber of the most unstable length. Experimentally we study such effects by shining X-band ($f = 10.5$ GHz, $P \lesssim 5$ kW) microwave radiation onto the plasma by a microwave horn. Evidence for parametric decay into electron plasma waves and ion acoustic waves appears in the experimental spectra and has been noted previously (Abstract IV D1). While in the previous year in a limited number of experimental runs we found agreement with theories predicting $P_{thr} \propto 1/kL$, the more extensive investigations this year show that this dependence is not always obtained. In changing plasma conditions during the X-band microwave heating, it was found in some cases that P_{thr} was independent of k. A possible explanation for the changing behaviour is the occurrence of linear mode-conversion of the incident electromagnetic wave into electrostatic waves, which could complicate interpretation of the results. Since at 10 GHz it is very difficult to detect short-wavelength converted electrostatic waves, a considerable effort was made to determine the dispersion relation of the ion acoustic decay waves. These waves were found to be localized in the radial direction to 0.5 cm while propagating mainly along the external magnetic field. Thus, mode conversion is unlikely in these experiments, since in the ordinancy (O) mode of propagation $E_o \| B$. The measured dispersion is shown in Fig. 1(a), as well as a sample of interferometer output of the ion wave. In addition, in Fig. 1(b) the electron distribution function is also shown,

giving strong evidence of plasma heating along the magnetic field, i.e., along the direction of the electric field of the incident electromagnetic wave and the decay waves. Thus, even if there were mode conversion, a significant part of the heating could be attributed to parametric decay waves. A summary of the work has been presented at the Lubbock conference (Abstract **IV** D2).

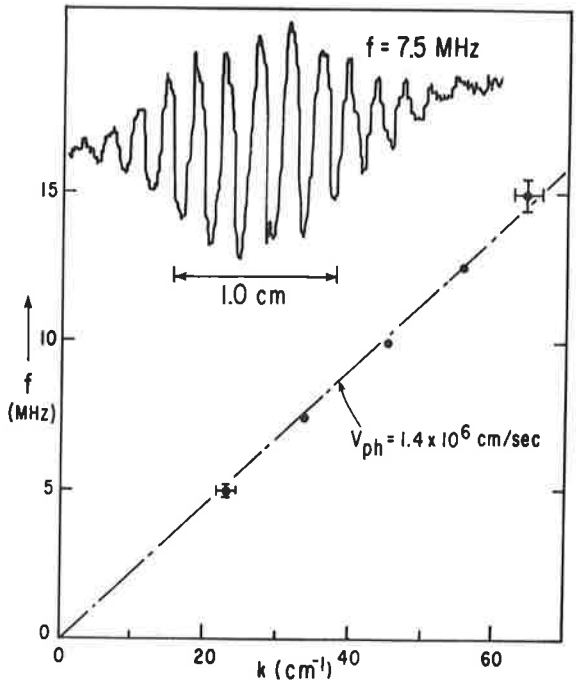

(a)

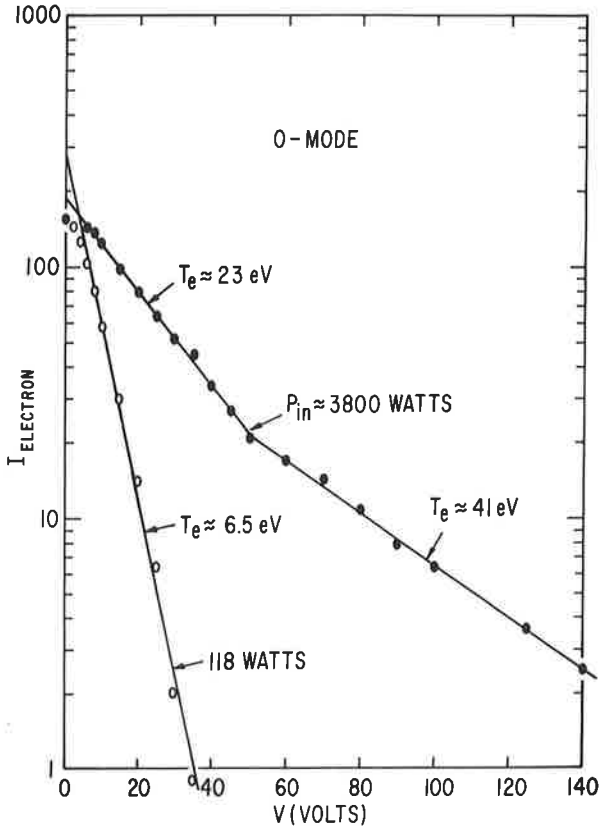

(b)

743114

Fig. 1 (a) Ion acoustic decay wave dispersion relationship during X-band heating experiments (propagation along E_o).

733538

Fig. 1 (b) Typical electron distribution function along the magnetic field (along E_o)

In the backscatter experiments a 250 kW X-band microwave beam is sent along a waveguide filled with plasma. Unfortunately, the gain is greatly limited by the short pulse length of the X-band source ($\tau < 2\mu$sec). In this time one can hope to observe a gain of less than a factor of ten. Thus far the experiment has not provided any evidence of the Brillouin backscatter instability.

A major effort in the year's program has been directed toward an understanding of lower-hybrid wave propagation. In this area of investigation, a) a theory for wave launching from a finite-size slow wave structure has been developed, including collisions and linear mode conversion (Abstract IV D3), b) using a number of different slow-wave structures with well defined k_z-spectra, the excitation and propagation of slow waves have been studied in detail (Abstracts IV D4 and IV D5), c) assembly of a CO_2 laser scattering system to detect the presence of short wavelength waves has begun (Abstract IV D6), and d) based on recent experimental observations (Abstract IV D7) a theory has been developed for parametric decay of lower-hybrid waves in uniform (Abstract IV D8) and non-uniform plasmas (Abstracts IV D9 and IV D10). In Fig. 2 is shown the geometry of the slow-wave excitation system, and Fig. 3 shows interferometer outputs of the excited waves with the predicted resonance cone clearly visible in the experimental data. Figure 4 provides a plot of the experimental verification of lower-hybrid dispersion relation. Also, in agreement with theory, it was verified that the waves were backward waves. In addition, and of particular significance, it was discovered that wavelengths shorter than $k_\parallel/k_\perp < \sqrt{m_e/m_i}$, could not be propagated. This phenomenon is not well understood, but is believed to be due to scattering of the incoming lower hybrid wave by background ion fluctuations. If valid, this interpretation would imply the absence of experimental observation of linear mode-conversion. It would also mean that low frequency fluctuations present in tokamaks may prevent mode conversion. Thus, other damping mechanisms, such as parametric decay, scattering by fluctuations, and electron Landau damping would become the primary absorption process in lower-hybrid heating experiments.

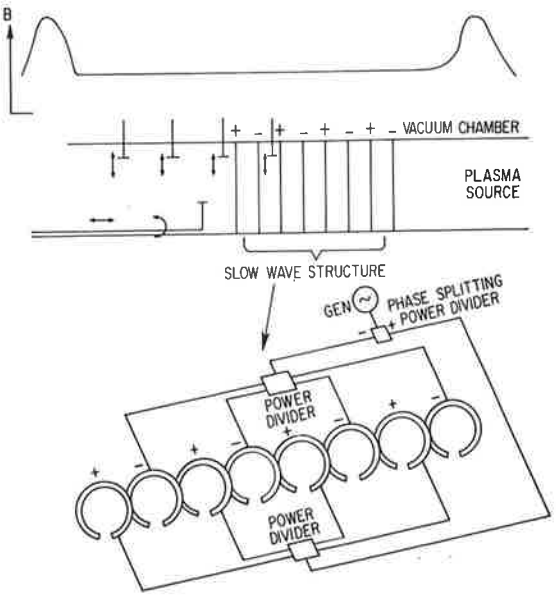

743961

Fig. 2. Experimental setup for lower-hybrid wave excitation. The eight rings driven by power dividers alternate in phase by 180°.

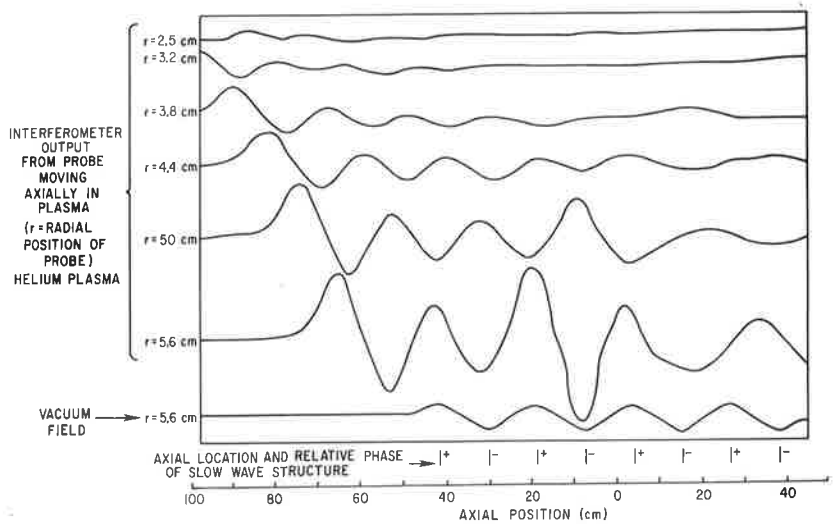

753222

Fig. 3. The bottom trace shows the vacuum field of the slow wave structure as measured by an axial probe. The other traces show a typical axial lower hybrid field excited by the slow wave structure. Note how the wave packet moves axially away from the source as the wave penetrates the plasma.

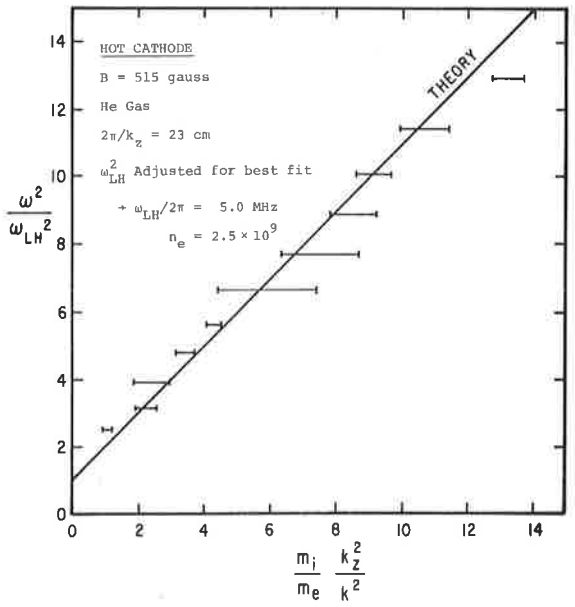

746053

Fig. 4. Verification of cold lower-hybrid wave dispersion relationship, k_x versus ω.

IVD 1. Experimental Studies of Parametric Instabilities in Inhomogeneous Plasmas*, by M. Porkolab, V. Arunasalam, N. C. Luhman, Jr. and J. Schmitt.

X-band microwave power (λ_o = 3 cm), both pulsed and CW, with powers up to 4 kW ($v_d/v_t \lesssim 0.2$) have been used to induce parametric instabilities both in the ordinary ($E \parallel B$) and extraordinary ($E \perp B$) modes of propagation in the Princeton L-3 device. The main results can be summarized as follows: (a) In the ordinary mode of propagation the density gradient dominates the growth rates, and thus the thresholds for parametric decay instabilities for $\omega \lesssim \omega_{pi}/5$. The threshold for instability behave roughly according to the inhomogeneous plasma theory of Perkins and Flick, i.e., $E_o^2 \propto 1/Lk$ where L is the density gradient scale length and k is the wave number. The wavelengths of the low frequency decay waves have been measured and the waves were identified as ion acoustic waves. (b) The heating rates due to this instability have been measured to be anomalously fast (by a factor of 20), and main body heating (by a factor of 2-3) and tail formation ($T_{tail} \sim 10$ T) occur in a few microseconds. For $P_o/P_{th} \gtrsim 10$ the anomalous heating rate (collision frequency) is independent of incident power. (c) The extraordinary mode has minimum thresholds for decay into lower-hybrid waves and Bernstein waves, nearly in agreement with uniform plasma theory. Heating rates similar to the ordinary mode have been observed.

---

* Presented at the Symposium on the Anomalous Absorption of Intense High Frequency Waves (Livermore, Calif., 1974).

IVD 2. MATT-1049 Parametric Instabilities and Enhanced Heating of Plasma in a Magnetic Field: A Review, by Miklos Porkolab

Recent developments in the theory of parametric instabilities, experimental evidence of their existence, and their relation to plasma heating is reviewed. Only modes existing in magnetically confined plasmas will be discussed, since these modes may be candidates for possible application to heat fusion plasmas with high power radio-frequency sources. Thus, particular attention is given to the regime of Trivelpiece-Gould modes, lower-hybrid frequency, ion-cyclotron frequency (fast magnetosonic wave), and upper-hybrid frequency.

IVD 3. MATT-1031, Propagation and Mode Conversion of Lower-Hybrid Waves Generated by a Finite Source, by P. M. Bellan and M. Porkolab

The propagation of electrostatic plasma waves, and their subsequent conversion into hot plasma waves at the lower hybrid frequency is calculated for realistic density profiles and finite rf souces in a slab geometry. A finite length slow wave source having a potential distribution $\phi \sim \cos k_o z$ is found to generate spatial oscillations having a well-defined wavelength. These oscillations are confined to regions bounded by conical curves originating at the ends of the source. The axial distance of rf energy propagation to the lower hybrid layer is found to be greater than the radial distance of propagation by a factor of the order $(m_i/m_e)^{1/2}$. The conversion at the lower hybrid layer of the electrostatic cold plasma waves excited by a finite source into propagating hot plasma waves is calculated. It is shown that collisional damping at the lower hybrid layer may predominate over mode conversion even for relatively low collision frequencies.

IVD 4. Experimental Investigation of Externally Launched Slow Waves Near the Lower-Hybrid Frequency* by P. Bellan and M. Porkolab

Electron plasma waves possessing several well defined perpendicular wavelengths have been excited by a multiple ring slow wave structure (4 wavelengths long, λ_z = 23 cm.) Perpendicular wavelengths from 2 cm to 4 mm have been observed. The waves follow a conical trajectory and are strongly damped before they reach the lower hybrid layer. The damping is much stronger than could be explained by Landau damping, Coulomb collisions or collisions with neutrals. In the low density region where $\omega > \omega_{LH}$ the waves satisfy the relation $k_x \propto 1/\omega$, in agreement with the $\omega=\omega_{pe}\cos\theta$ dispersion relation. The experiments have been done on the Princeton L4 plasma (B = 1.2 kg, $n_e = 10^{10}$ to 10^{11}, $T_e >> T_i$, plasma diameter = 10 cm, helium gas).

---

* *Bull. Am. Phys. Soc.*, 19, 955, (1974).

IVD 5. MATT-1090, Excitation of Lower-Hybrid Waves by a Slow-Wave Structure, by P. Bellan and M. Porkolab

We report the excitation of lower-hybrid waves by a multiple-ring slow-wave structure (four waves, λ = 23 cm) in a magnetized plasma. Wavelengths measured parallel and perpendicular to the magnetic field were in agreement with the theoretical dispersion relation. The waves propagated in a packet defined by the axial length of the slow-wave structure.

IVD 6. CO_2 Laser Scattering as a Diagnostic of Ion Temperatures and ion Waves in Tokamaks* by C. M. Surko and R. E. Slusher, Bell Labs, Murray Hill, N. J. and Miklos Porkolab

We discuss the use of CO_2 laser scattering and heterodyne detection as a diagnostic for tokamak plasmas. The CO_2 laser has the advantage that large laser powers are readily available and that plasma heating and cyclotron emission from the plasma is small at these frequencies. The spectrum of scattered light is a measure of ion and electron temperatures (T_i and T_e) and the electron drift velocity in an equilibrium plasma, and is sensitive to enhancement of the ion acoustic spectrum in non-equilibrium situations. For a plasma such as the Princeton ATC Tokamak a 300 W CW laser is sufficient for detection of scattering from non-thermal ion waves with wavelengths λ such that $5mm>\lambda>\lambda_{De}$ and frequencies up to the ion plasma frequency. Measurement of the equilibrium spectrum and T_i require either many tokamak shots or in a high-power single-mode pulsed laser.

---

* *Bull. Am. Phys. Soc.* 19, 972 (1974).

IVD 7. Parametrically Induced Nonlinear Wave-Particle Scattering and Plasma Heating Near the Lower Hybrid Frequency* by R. P. H. Chang, Bell Laboratories, Murray Hill, New Jersey and M. Porkolab

Experimental and theoretical studies of a new type of parametric instability involving the excitation of ion quasimodes (due to nonlinear wave-particle scattering) have been carried out when the "pump" frequency is near the lower hybrid frequency. Plasma heating associated with this instability has also been measured.

---

* *Phys. Rev. Lett.*, 32, 1227 (1974).

IVD 8. MATT-1028, Theory of Parametric Instability Near the Lower-Hybrid Frequency, by Miklos Porkolab

The dispersion relation for parametric instabilities near the lower-hybrid frequency is derived and analyzed. It is found that for propagation angles $\cos^2\theta(m_i/m_e) < 1$ resonant decay into ion acoustic (ion-cyclotron) waves does not occur; rather, decay into nonresonant quasi-ion modes and lower-hybrid waves occurs. The driving mechanism for this instability is shown to be analogous to nonlinear Landau damping in perturbation theory. The large amplitude dispersion relation is analyzed numerically for a number of typical experimental regimes, and growth rates and thresholds are obtained for both the purely growing mode and the newly found quasi-ion modes.

IVD 9. MATT-1069, Physical Mechanism of Parametric Instabilities Near the Lower-Hybrid Frequency in Inhomogeneous Plasma, by Miklos Porkolab

The dispersion relation for parametric instabilities near the lower-hybrid frequency is obtained from model fluid equations. The following instabilities are discussed: for rf pump frequencies $\omega_o \gtrsim 3\omega_{LH}$, $\omega_{pe} \simeq \Omega_e$, resonant decay into ion sound (ion cyclotron) modes (previously predicted) is found. In the regime of $1 \lesssim \omega_o/\omega_{LH} \lesssim 3$, $\omega_{pe} \simeq \Omega_e$, decay into ion quasi-modes is found. In strong magnetic fields decay into quasi-modes is also found for $3 \lesssim \omega_o/\omega_{LH}$. This mechanism is similar to nonlinear Landau damping in weak turbulence theory. In addition, decay into the purely growing mode and fluid quasi-modes may also occur. The results are compared with recent calculations from the Vlasov equation. The effects of plasma-inhomogeneities will also be considered, including effective thresholds due to density gradients and finite pump extent. The implications of these results to rf heating of tokamaks near the lower-hybrid frequency will be discussed.

IVD 10. Parametric Instabilities Near the Lower-Hybrid Frequency in Inhomogeneous Plasma* by Miklos Porkolab

The parametric decay of incident microwave fields in an inhomogeneous plasma as the wave approaches the lower-hybrid layer is considered. This study is motivated by future lower-hybrid rf heating experiments in tokamak plasmas. The thresholds for parametric decay into ion acoustic and/or ion cyclotron waves, ion quasi-modes, and lower-hybrid waves is obtained. The effects of finite spatial extent of the pump are included. It is found that tokamaks with $T_e \gtrsim 5$ kV, $n_e \simeq 10^{14}\text{cm}^{-3}$, $(\nabla n/n)^{-1} \gtrsim 10$ cm, are unstable to parametric decay in the underdense region (i.e., $\omega > \omega_{LH}$) for applied electric fields of $E_o \simeq 2.5$ kV/cm, and axial length of the waveguide structure $L_z \simeq 30$ cm. The E x B drift velocity at threshold for decay into quasi-mode is comparable with or less than that of decay into acoustic (cyclotron) waves.

---

* *Bull. Am. Phys. Soc.*, 19, 883 (1974)

E. Isothermal Parametric Ion Acoustic Decay Instability: Identification, Ion Heating and Saturation (Q-1)

Recently, in connection with plasma heating and ionospheric modification, there has been strong interest in the ion acoustic decay instability in isothermal plasmas ($T_e = T_i$) driven by an EM wave near ω_{pe} with $E \| B$. Identification of this instability, characterized by severely ion Landau damped acoustic waves, was achieved primarily by measurements of wavelength and frequency, and its threshold and acoustic frequency dependence on density. Ion heating due to the instability is intense and was explained on the basis of a stochastic theory. The unstable steady-state shows amplitude saturation, $\langle E_{inst} \rangle^2 \propto E_o^2$, occurring without significant changes in instability spectra and wavelength (no cascading).

Figs. 1(a) and 1(b). A theoretical model that includes parametric action of large-amplitude decay waves back on the pump (in addition to the linear parametric instability equations) agrees with observations of the saturated state. (Abstracts IV E1 and IV E2)

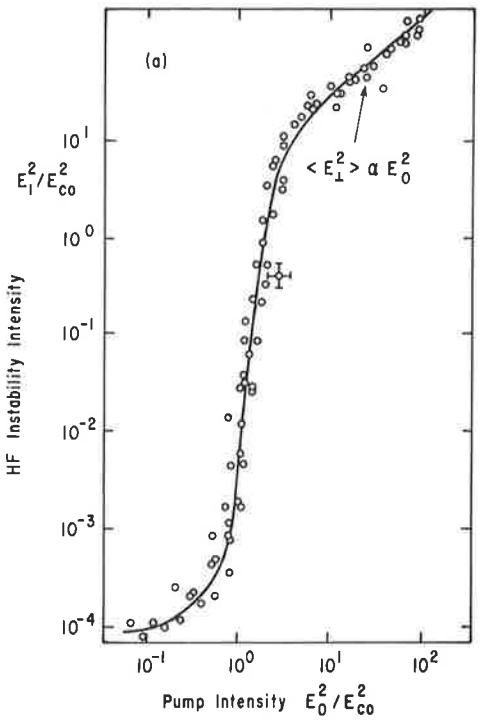

746026

Fig. 1 (a) Steady-state HF instability vs. pump intensity. $f_{LF} = 2.6$ MHz, $\omega/\omega_{pe} = 0.8$, $n = 8 \times 10^9$ cm^{-3}, $B = 2$ kG. E_{co} is the amplitude of the pump field for onset of the decay instability.

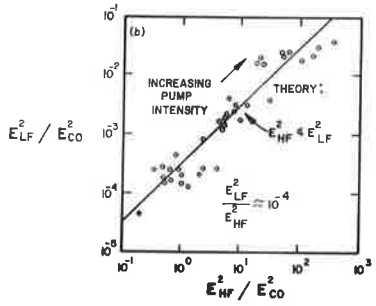

743340

Fig. 1 (b) Steady-state LF and HF instability intensities. $f_{LF} \simeq 700$ KHz, $\omega/\omega_{pe} = 0.3$, $n = 10^{10}$ cm^{-3}, $B = 3$ kG, $T_e \simeq T_i \simeq 0.2$ eV.

IVE 1. MATT-1053 Saturation of the Parametric Ion-Acoustic Decay Instability in Isothermal Plasmas, by J. T. Flick and H. W. Hendel

We report saturation measurements on the isothermal parametric ion acoustic decay instability driven by a coherent pump field, $\omega_o \simeq \omega_{pe}$. At saturation $E^2_{Inst} \simeq 10E^2_o$, and no significant changes in instability spectra and wavelengths occur (no cascading), in agreement with a theory that includes the effect of large instability fields acting parametrically back on the pump field.

---

*Also presented at the *Proceedings of Conference on RF Plasma Heating* (Lubbock, Texas, 1974).

IVE 2. MATT-1106 Identification and Saturation of the Isothermal Parametric Ion Acoustic Decay Instability by J. T. Flick and H. W. Hendel

Experimental and theoretical results on the isothermal ion acoustic decay instability, excited by an intense rf field near the electron plasma frequency, are reported. This instability, which is characterized by severely ion Landau damped acoustic waves, is identified primarily by measurements of wavelength and frequency, and of threshold and acoustic frequency dependence upon density. The unstable steady-state shows amplitude saturation, $\langle E^2_{inst} \rangle \propto E^2_o$, occurring without significant changes in instability spectra and wavelengths (no cascading). A theoretical saturation model that includes parametric action of large-amplitude decay waves back on the pump (in addition to the linear parametric instability equations) agrees with observations of the saturated state.

F. Current-Driven Instabilities in Isothermal Plasmas and Anomalous Plasma Properties (Q-1)

Successive destabilization of four different instabilities with increasing current ($u/v_{the} \simeq 0 - 1/3$ is observed in isothermal inhomogeneous plasmas, together with "anomalous" plasma properties caused by instability-particle interactions. Isothermal plasma ($T_e \simeq T_i$) are of interest because a) ion sound is damped and cannot contribute to anomalous resistivity and ion heating, and b) tokamaks and the ionosphere may be considered isothermal. Onset drift velocities and anomalous properties of the instabilities are in general agreement with expectations. Effects from four successive instability regimes are seen as u/v_{the} is increased: 1) onset of current-driven low frequency (~2kHz, $u = 5\text{-}10\ v_{thi}$) Δn drift waves leads to anomalous radial diffusion; 2) onset of the discrete spectrum resonantly driven ion cyclotron drift wave ($f = 1.15\ \omega_{ci}$, $u = 1/10\ v_{the}$) produces slight anomalous resistivity and ion heating; 3) onset of the continuous spectrum (Δn, ∇T_e) nonresonant ion cyclotron drift wave generates strong anomalous resistivity and ion heating; 4) onset of a fourth, not yet fully identified instability ($f = 5\text{-}100\ f_{pi}$, $u = 1/3\ v_{the}$) causes, or helps cause, relaxation of the radial electron temperature gradient. The third and fourth instabilities had not been observed before and the third has been described by us in detail. In the presence of the latter of three instabilities resistivity and temperatures of both particle species are mainly determined by wave-particle interactions. The third instability, the continuous ion cyclotron drift wave (ICDW), is of special interest since it shows most of the effects of ion sound but can exist in plasmas where ion sound is ion Landau damped. Finally, the instabilities observed are determined largely by the radial inhomogeneities of the plasma column. The main results are shown in Figs. 1 - 4 and Table 1. (Abstracts IV F1 and IV F2).

TABLE I

Instability	Threshold El. Current	Frequency Spectrum 10^3 10^4 10^5 10^6 10^7 10^8 (Hz)	Wavelength	Propagation	Anomalous Effects on Plasma
L. F. D. W.	$\frac{u}{v_{the}} \approx 0.03$	ν_{ii} ν_{ei} $\omega \ll \omega_{ci}$	$k_y\rho_i<1$ $k_y>>k_z \sim \frac{\pi}{L}$	Azimuthal $\frac{\omega}{k_y} \simeq v_e^*$	Anom. Diffusion
I. C. D. W.	$\frac{u}{v_{the}} = 0.15$	$\omega \approx n\omega_{ci}$	$(k_y\rho_i \sim 1)$ $\frac{\omega}{k_z} > \frac{u}{2}$	Azimuthal	Ion Heating Anom. Resistivity (~30%)
H. F. D. W.	$\frac{u}{v_{the}} = 0.20$	$\omega_{ci} \leq \omega < \omega_{pi}$	$k_y\rho_i>>1$ $\frac{\omega}{k_z} > v_{the}$	Azimuthal $\frac{\omega}{k_y} \simeq v_i^*$	Anom. Resistivity (10x) (Current Inhibition) Strong Ion Heating Electron Heating
H. F. El. W.	$\frac{u}{v_{the}} = 0.3$	$\omega_{Bu} < \omega < \omega_{pe}$			Anom. Electron Viscosity $\left(\frac{du}{dr} \neq 0 \quad \frac{dT_a}{dr} \neq 0\right)$

10^3 10^4 10^5 10^6 10^7 10^8 (Hz)

746094

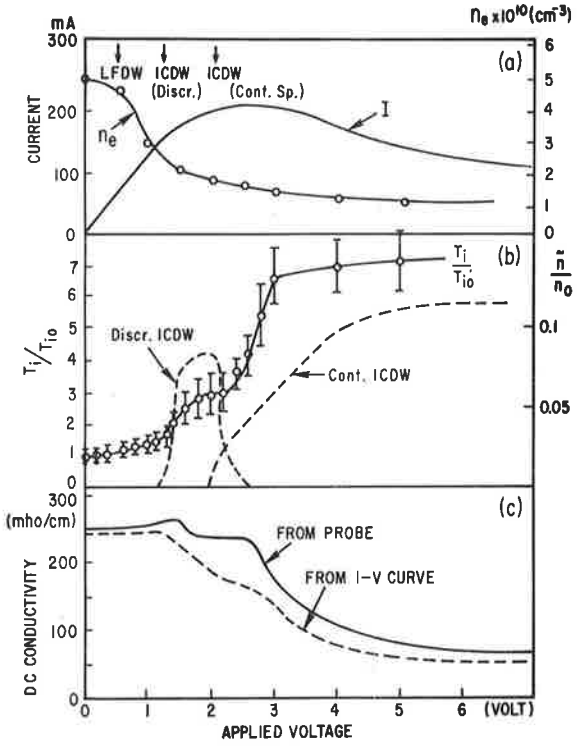

743983

Fig. 1. Evolution of plasma parameters vs applied voltage. (a) Current and density; arrows indicate onsets. (b) Normalized T_i and amplitude of ICDW. (c) Conductivity; solid line: conductivity probe; broken line: I-V curve. B = 6 kG, T_{eo} = 0.25 eV, T_{io} = 0.4 eV.

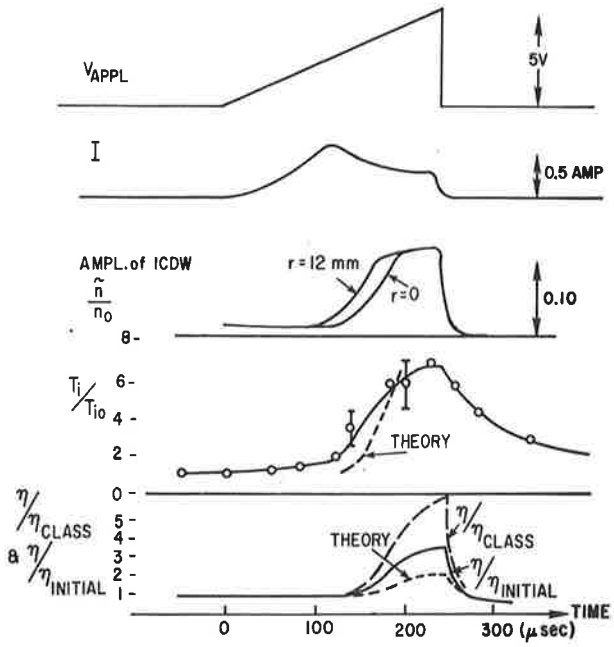

743984

Fig. 2. Time evolution of plasma parameters in pulsed operation. In η-plot, solid line is $\eta_{\parallel}$ from I-V curve. η/η_{class} is normalized to classical resistivity. $\eta_{initial} = 5 \times 10^{-3}$ ohm · m = Spitzer-Härm value. B = 2kG, $n_o = 1.1 \times 10^{11}$ cm^{-3}.

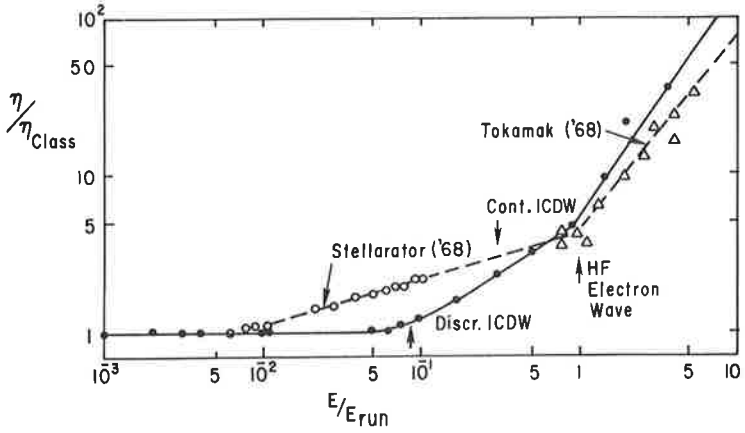

743979

Fig. 3. Normalized resistivity vs E/E_{run}. Present experiment: B = 6 kG, $n_o = 6.10^{10}$ cm^{-3}.

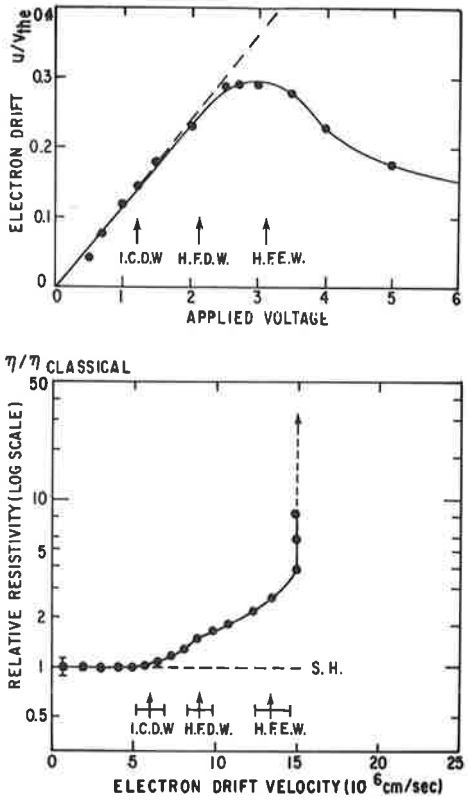

746095

Fig. 4 (a) Electron drift velocity vs v_{appl}. Decrease of u/v_{the} is due to increase of electron temperature. (b) Resistivity vs drift velocity. Plasma parameters as in Fig. 1. S.H. = Spitzer-Härm value.

IVF 1. Identification of Ion Cyclotron Drift Instability With Discrete and Continuous Spectra* by H. W. Hendel and M. Yamada

Ion cyclotron drift waves with discrete and continuous spectra are identified by measurements of ω and k and explained by a theory which includes parallel electron current. This instability has a spectrum and effects on the plasma similar to those of ion sound, and can exist in plasmas which are ion sound stable.

---

* *Phys. Rev. Lett.* 33, 1076 (1974).

IVF 2. MATT-1105 Evolution of Current-Driven Instabilities and Anomalous Properties in Isothermal Inhomogeneous Plasmas, by H. W. Hendel and M. Yamada

Successive destabilization of four different instabilities with increasing current (u/v_{the} = 0-1/3) is observed in isothermal plasmas, together with anomalous plasma properties caused by instability-particle interactions. Instabilities and their effects are largely determined by the radial inhomogeneities of the plasma, in agreement with predictions.

G. Particle-Surface Interactions

An apparatus has been constructed to investigate the interactions of energetic (300 eV-5 keV) hydrogenic ions with surfaces. This energy range is relevant to CTR research since it is characteristic of wall bombardment by charge-exchange neutrals, - one of the dominant mechanisms responsible for impurtity influx into tokamaks.

The apparatus is shown schematically in Fig. 1 . A proton or deuteron beam of appropriate energy is formed in an ion gun and directed through a Wien Filter and cryopump into the ultra-high vacuum target chamber. In the target chamber are an Auger Electron Spectrometer (AES) and a Quadrupole Mass Filter (QMF), which are used to detect sputtered ions and neutrals. The three-grid retarding potential analyzer can be placed in front of the QMF for energy analysis of the sputtered ions.

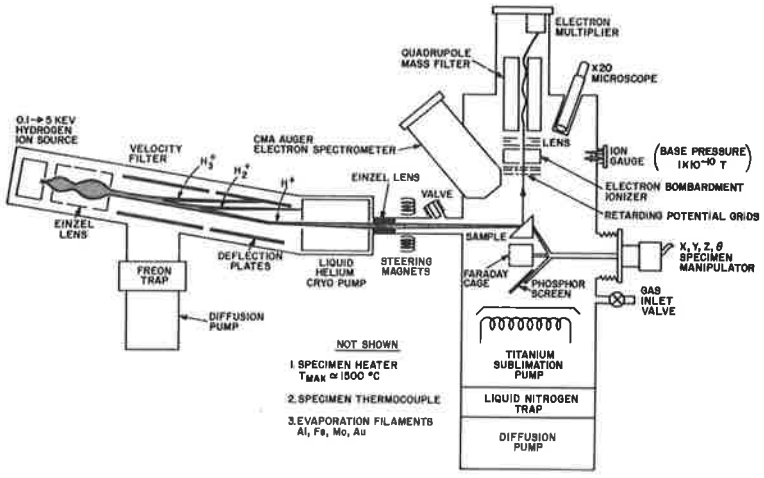

743919

Fig. 1. Apparatus used to investigate particle-surface interactions.

In the past year four experiments have been performed in this apparatus.

(1) The energy dependence of the yield of Cr^+ and Fe^+ sputtered from vacuum annealed 304 stainless steel by 350 eV and 5 keV protons has been measured. At 5 keV the sputtering yield of Cr^+ is approximately 3×10^{-6} Cr^+/H^+ . For CTR applications the interesting quantity is the sputtering yield of neutrals. With some confidence we can assume that the neutral yield parallels the ion yield data in Fig. 2 , normalized to the absolute sputtering yield of Oetjen for 5 keV H^+ on stainless steel. These data show that at low energy the sputtering yield decrease proportional to E^2. Ihe implications favor a cold, opaque plasma edge.

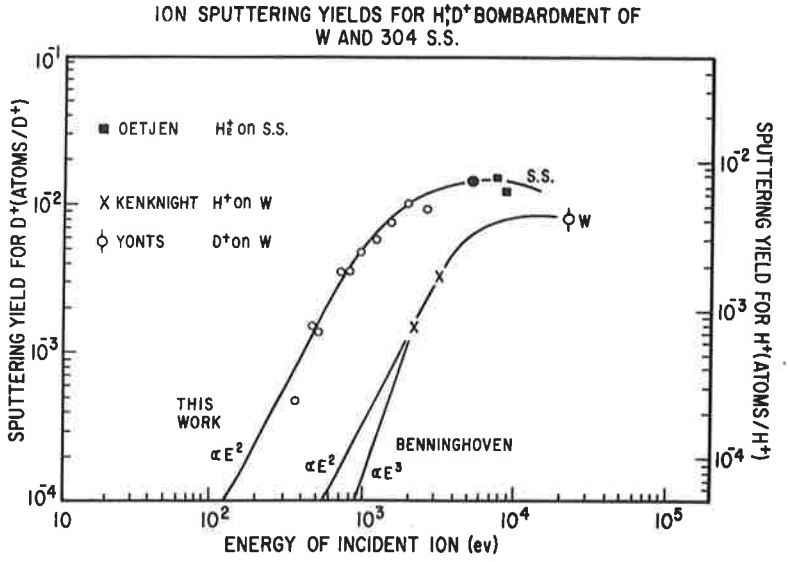

743887

Fig. 2. Ion yield data.

(2) Energy distributions of ions sputtered by 1-5 keV protons and deuterons have been measured. Results for 5 keV bombardment are shown in Fig. 3. The general shape and location of the peaks do not substantialy change when the beam energy is lowered to 1 keV. These data set an upper limit on the energy distibutions of sputtered neutrals, and hence can be used in a worst-case estimate to calculate sputtered neutral penetration of the scrape-off region in PDX or PLT. These results indicate a minimum $\int n\, dl$ in the divertor scrape-off of 1×10^{13} for a 90% efficiency in ionizing sputtered particles.

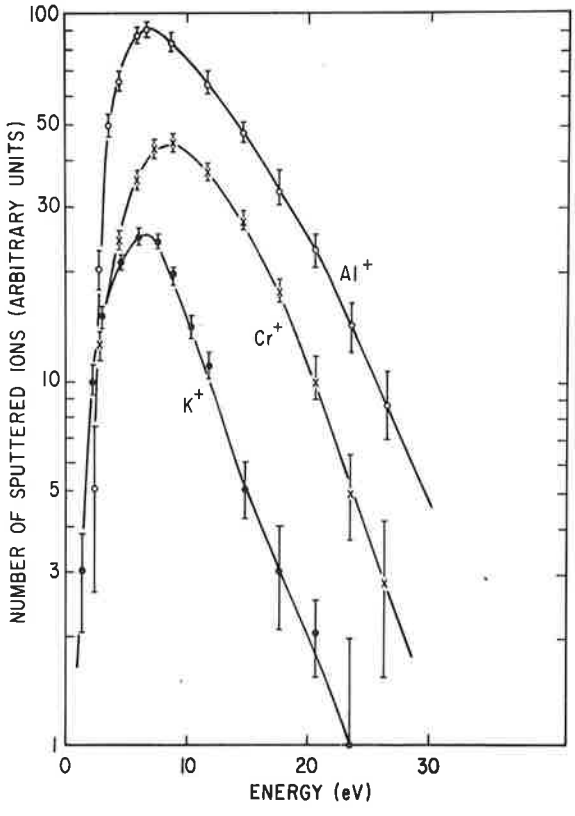

753556

Fig. 3. Energy distibution of ions sputtered by 5 keV bombardment.

(3) Absolute sputtering yields have been measured for H^+ bombardment of graphite fibers and monolayer-thick aluminum films. The sputtering yields for graphite and Al, 2.5 keV H^+ bombardment, are .014 and .007 respectively. The absolute yields for graphite were obtained by high-dose bombardment and subsequent sample examination with a scanning electron microscope to determine diameter changes. The Al results were obtained by the thin film technique. Surface monitoring during sputtering was accomplished with SIMS and AES. The relatively low sputtering yields represent additional favorable reasons for using low-Z elements as first-wall materials.

(4) Experiments to investigate blistering of stainless steel under bombardment by deuterons with a large energy spread (1000 → 5000 eV) were performed. Annealed, polished and chemically etched stainless steel samples were subjected to consecutive doses of 6×10^{18} D^+/cm^2 at the energies 1.3, 2.5 and 5.0 keV. The surface showed no evidence of blistering, but much evidence of sputtering. It has been conjectured for many years that blisters would not form under such conditions - the above fluxes closely present the burden PLT walls will experience each week - however, these experiments represent the first direct proof.

V. ENGINEERING AND DEVELOPMENT

A. Introduction

Progress on major projects during 1974 included continued fabrication of the PLT machine and accessories plus conceptual and some detailed design of PDX and its appurtenances.

Engineering liason was conducted with the Westinghouse Electric Corporation in regard to the PPPL - Westinghouse Joint Conceptual Design Report for the TCT machine, the third major project.

Engineering support for operating experimental machines was also supplied to produce new and/or improved equipment and services to aid experimental programs.

Engineering accomplished on these items as well as miscellaneous activities for general laboratory support are described in the appropriate parts of this section.

B. Major Projects

1. The Princeton Large Torus (PLT)

a. Toroidal Field (TF) Coils. Most of these coils were complete or in the last stages of fabrication at the beginning of the year. Last year's annual report described TF coil fabrication in detail and can be referred to for information regarding it.

A TF coil stress analysis had been completed in 1973 using a superposition method. Early in 1974, the ANSYS[1] finite element method was used to analyze PDX coils and it became apparent that this could be applied to the PLT coils. Analysis of the PLT coils was completed in June of '74. Results from the two methods showed general agreement, except that the finite element method indicated slightly lower stresses and a slightly more flexible coil. It was not appreciated at first, but the finite element method predicted a much higher load on the center column. Because these analyses are important are important in predicting the behavior of the coils and center column, they will be continued in 1975.

[1] ANSYS (Analyses Systems) A computer engineering analysis system, Swanson Analysis Systems, Inc., Elizabeth, Pa. V A-1, V B-1.

b. Ohmic Heating (OH) and Shaping Field (SF) Coils. The inner SF and OH coil assemblies with epoxy-glass laminate structural components were fabricated and fitted up in a final shop mock-up ready for machine installation. This mock-up was completed in late '74. Figure 1 shows the lower half of this coil group during final shop operation on it. The manufacture and fit-up of the coil segments, fillers, shelves, case rings, cooling water fittings, electrical insulation, etc. which make up the inner coil group assembly represented a major shop effort during the year.

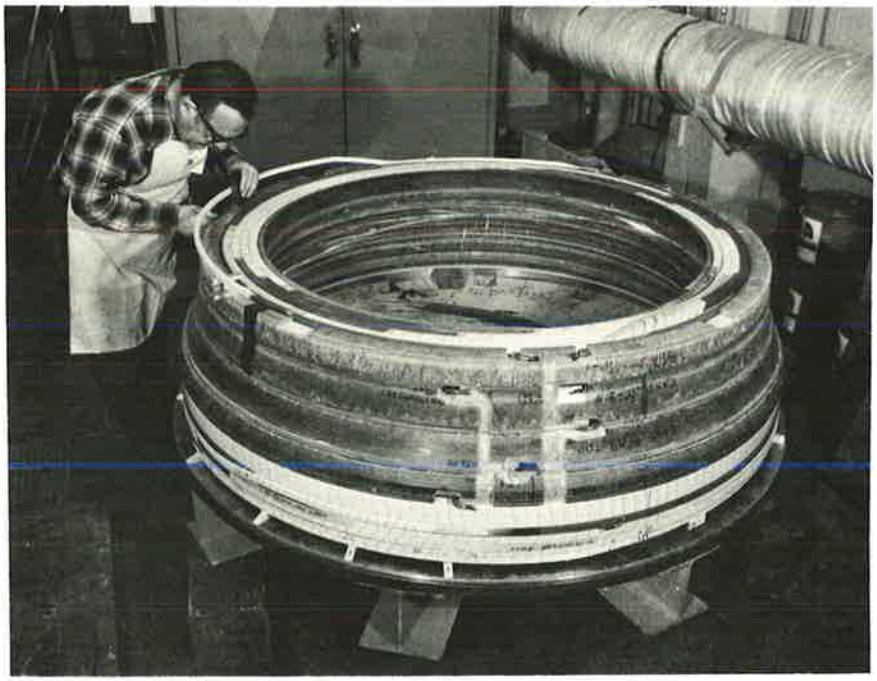

754034

Fig. 1. Lower half of the inner OH/SF coil assembly.

Fabrication and final shop mock-up of the mid and outer OH/SF coil assemblies were essentially complete and the assemblies were ready for machine installation at the year's end. Figure 2 shows one of the outer groups and the shop area used for the operations.

754035

Fig. 2. Outer OH/SF Coil assembly.

The development and tests of conductor brazing equipment to be used with these coils were completed during the year. This equipment includes induction heating work coils, holding fixtures, and a heat control system utilizing an infra-red detector. A large number of specimen braze joints were made to demonstrate the quality and reliability of the system. It was installed at the construction site and checked out shortly before the year's end. Figure 3 shows the test mock-up of a typical inner OH coil group as it will be positioned for joint braze access.

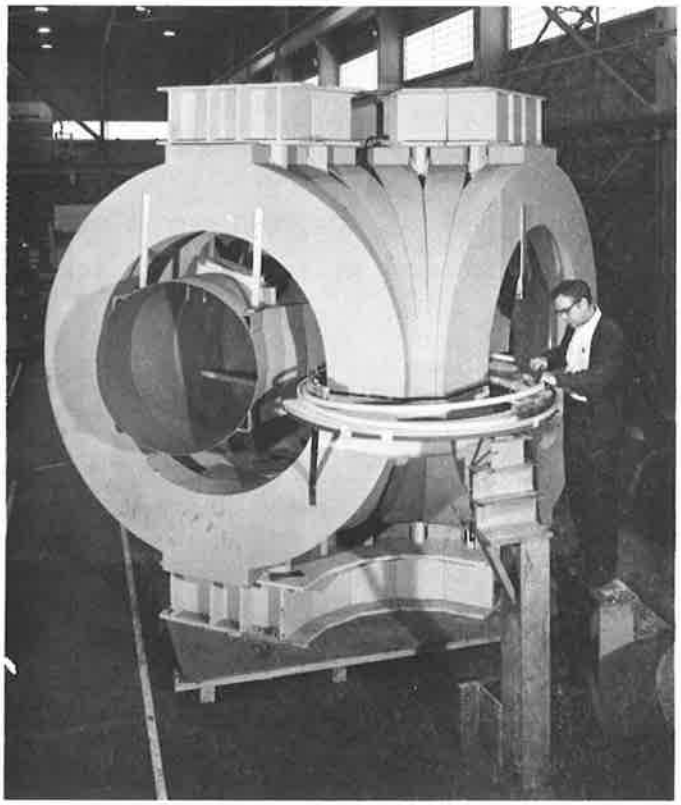

754036

Fig. 3. Test mock-up of a typical inner OH coil group positioned for joint braze access.

The vacuum vessel maneuvering trolley and track assembly were fabricated and installed in the TF coils' bore with the two vessel halves mounted thereon. This assembly permits rotation of the halves for access to the inner and mid SF/OH coil groups during assembly.

The coils' lead out bus stems, cancellation busses, the coil-to-coil connectors, electrical insulating sleeves, and support members for approximately 70% of the coils were complete prior to the end of 1974. The balance is scheduled for completion by March '75. The coils' end terminal clamp block assemblies which provide structural stability to the outer coils in the turns transitions at the terminal lead-outs were essentially completed. Half of the in-machine coil installation fixtures, temporary support hangers, handling rollers, etc. were fabricated. The remaining items are scheduled for completion in March, 1975.

c. Vacuum Vessel. The complete torus (with bellows sections replacing the ceramic sections) was assembled, pumped down and leak checked during the third quarter (see Fig. 4). A total of ten small weld leaks were found and repaired. All of these leaks were in final assembly welds of the bellows sections to the port sections. These are field welds which are difficult to make. The assembled torus were pressure cycled from 760 Torr some fifty times, leak detecting after very five cycles. No leaks developed.

A mercury pumping system having a measured speed of 100 Liters per second was used for these tests. After 72 hours of pumping, the pressure was 7×10^{-7}, corresponding to an out gassing rate of 10^{-10} Torr Liters per second per square centimeter of surface. This is considered quite good for that stage of cleaning.

The final support rings were then mounted and one complete ceramic break assembly was installed in place of an interim bellows section (see Fig. 5). Two small leaks developed in diagnostic gold seals located near a ring vessel bolt that had been installed too forcibly. In addition, complete bagging and helium soaking gave indications of a very small leak in the ceramic section. The diagnostic seal leaks were trivial, but subsequent testing in the following quarter showed a true diffusion-type leak at the ceramic-to-metal seal interface.

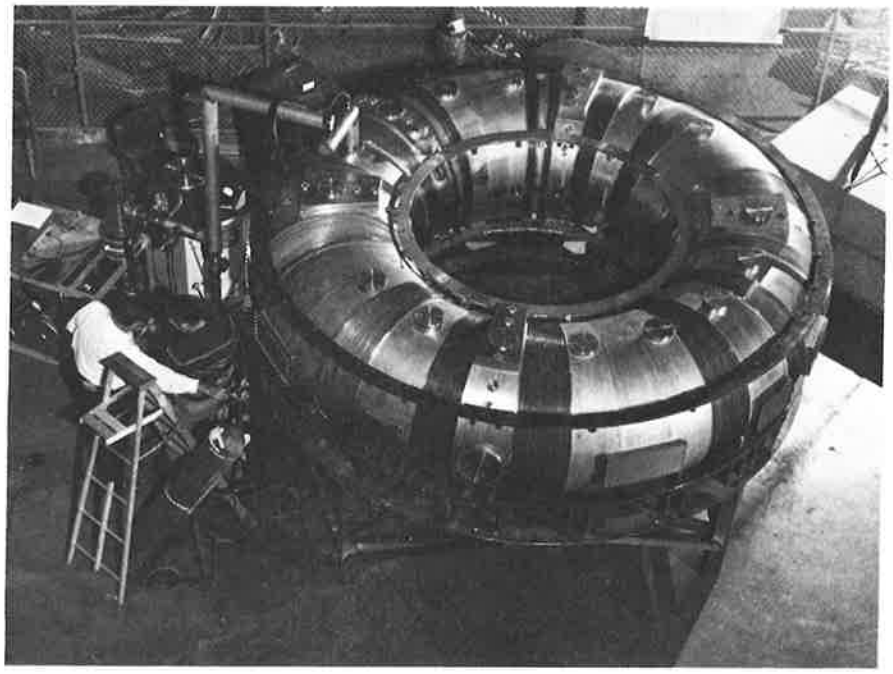

744752

Fig. 4. The PLT vacuum vessel undergoing leak checks.

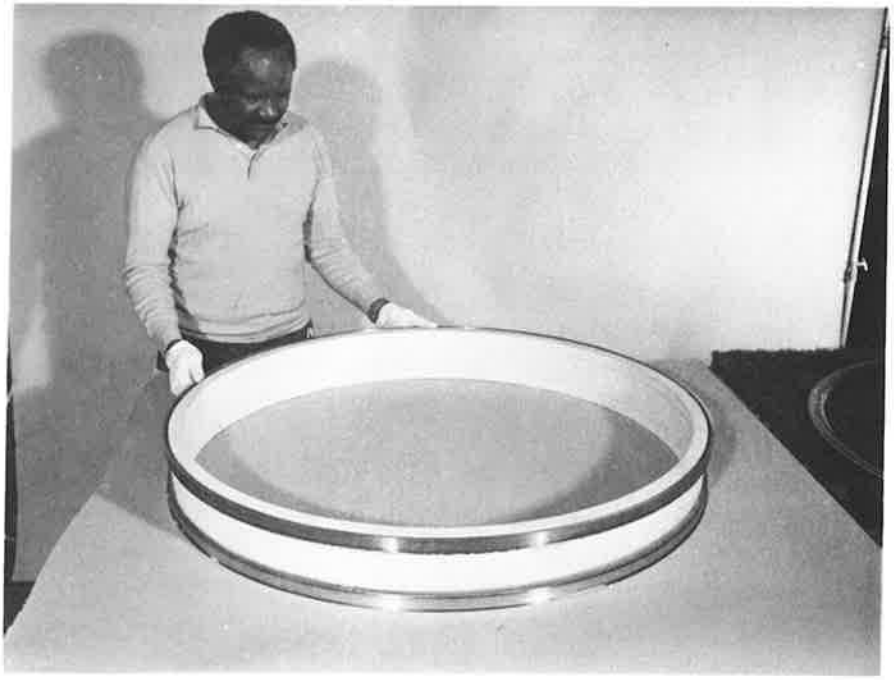

744769

Fig. 5. The PLT ceramic section with seals visible.

Since neither ceramic section (or interim sections) can be in place during installation of the inner OH and SF windings, the vacuum vessel assembly was delivered to the machine area and installed in the TF coil system on December 19 and 20, '74.

Due to the lack of a commercially available baffle meeting our requirements (high pumping speed, multi-cold wall collisions, etc.), Monte-Carlo techniques were used to design a multi-chevron baffle that was under construction at the end of the year. Tests are scheduled for the first quarter of 1975 and no problems are anticipated with the schedule.

d. Machine Structure At the beginning of 1974, ten of the thirty six wedge castings had been cast and machining had begun on two of them. Cooper Alloy Company, the foundry had delivered all castings by April 1, '74 and C-E Cast Company completed machining on all castings by mid-May.

Preliminary erection of the structure in the 1-H building had started in March. As a first step, the assembled wedge castings with adjustable shim mechanisms (Figure 6) were positioned between the torque rings, lined, reamed, and bolted in place (see Figures 7 and 8).

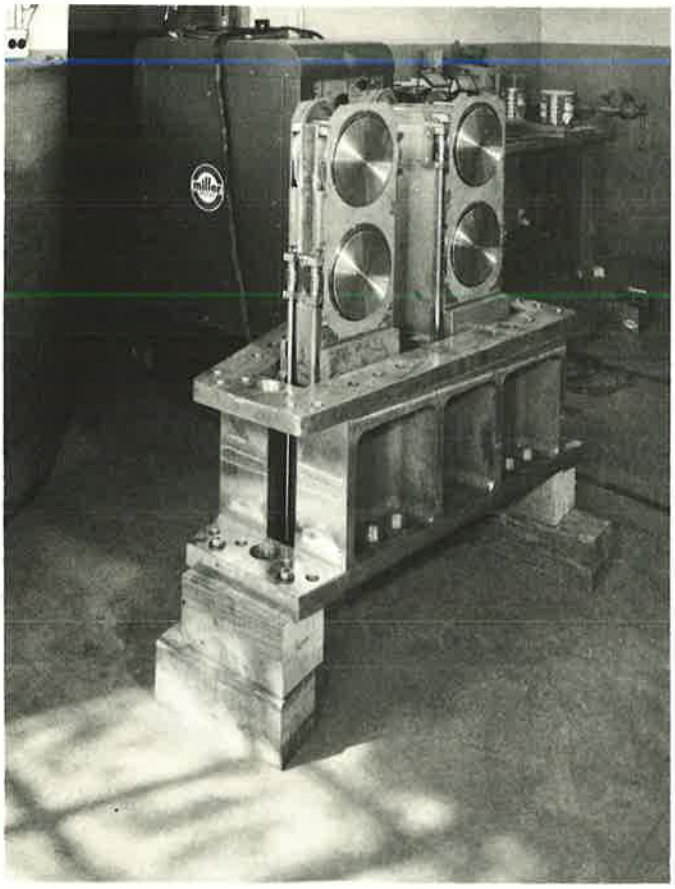

744211

Fig. 6. Assembled wedge casting with adjustable shim mechanism.

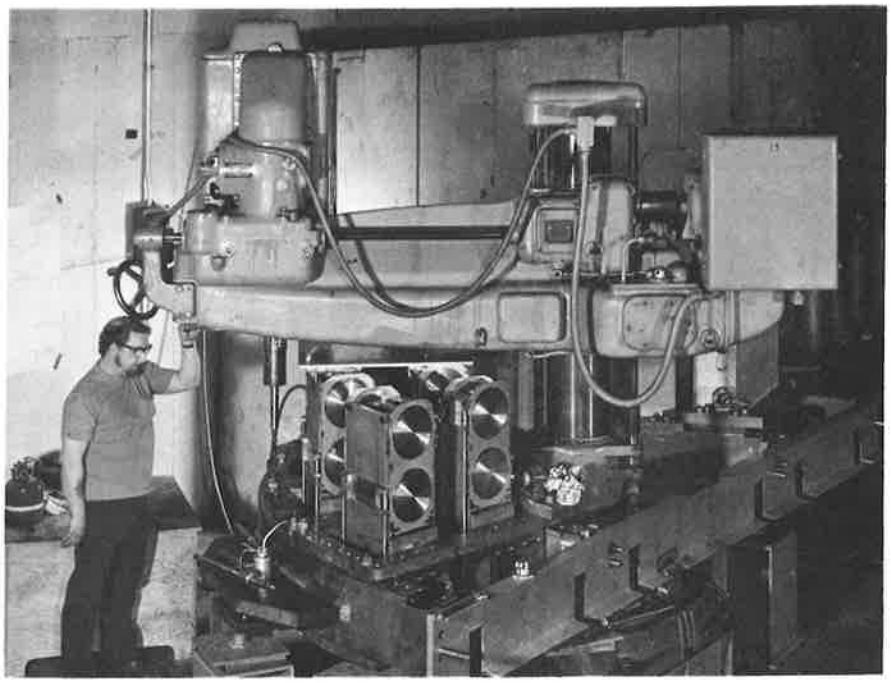

744264

Fig. 7. Positioning, lining, and reaming of PLT wedge castings.

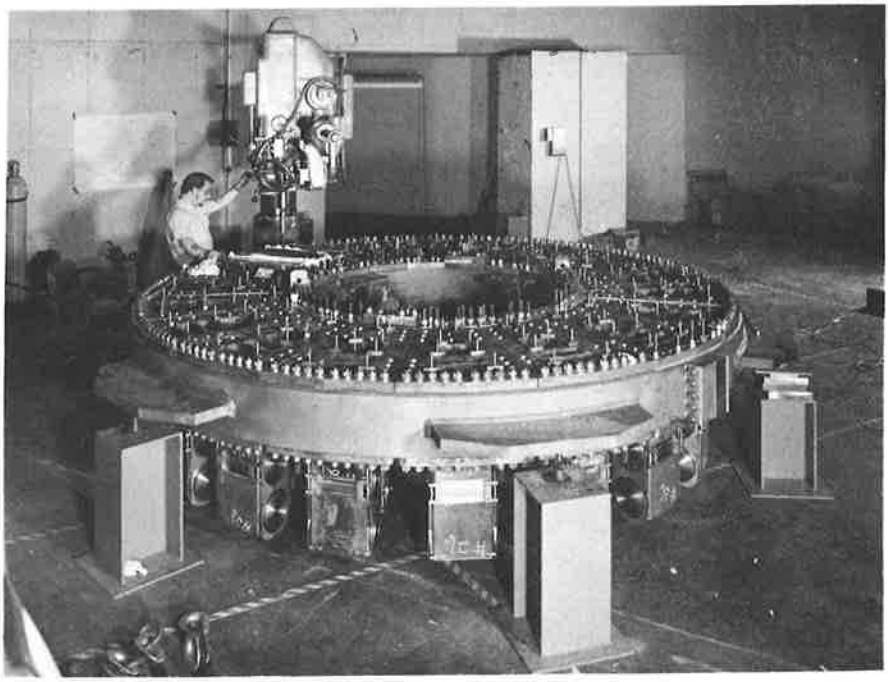

744422

Fig. 8. Completed set of PLT wedge castings positioned and bolted in place.

The first set completed became the lower shelf. Horizontal structural tubes were welded to the outer rings of this set while the second set was being reamed and assembled (Figure 9).

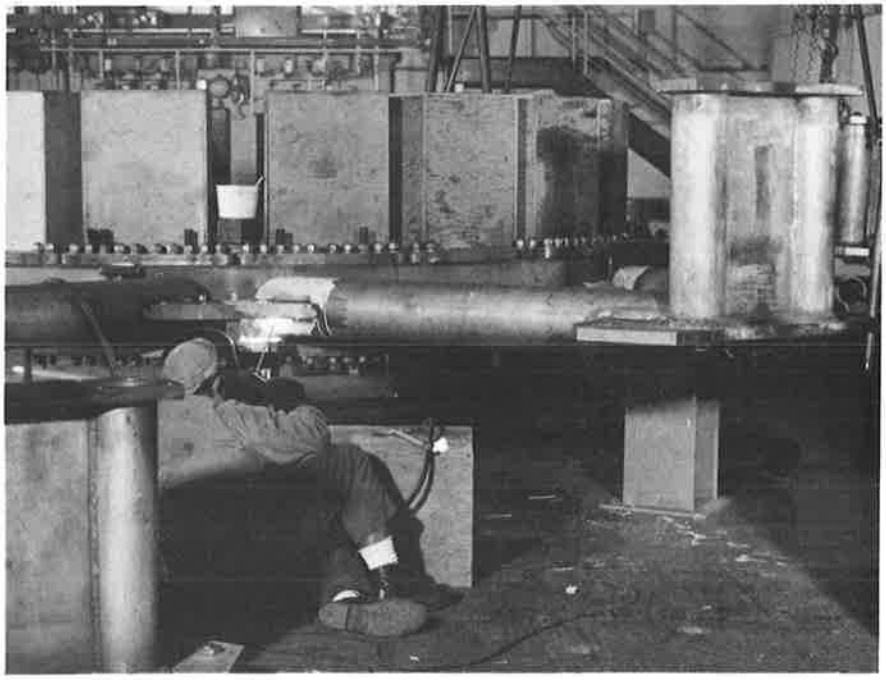

744419

Fig. 9. Welding of horizontal structured tubes to outer rings of completed set of PLT wedge castings.

When the upper shelf was completed, it was positioned above the lower shelf using a dummy center column, as the actual center column was not ready (Figure 10).

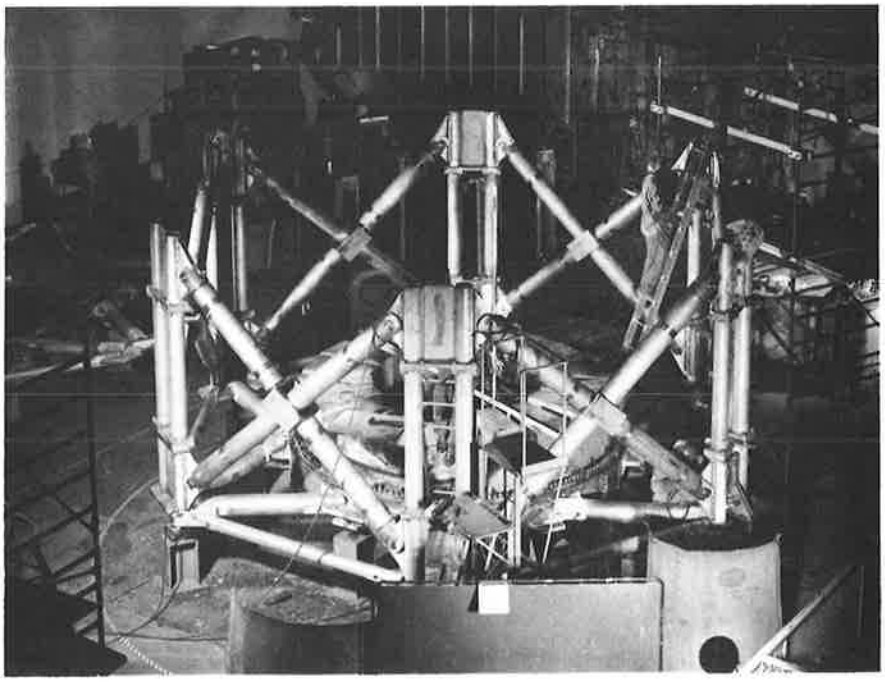

744467

Fig. 10. Completed lower shelf ready for positioning of the upper shelf.

The dummy center column is visible in Figure 11.

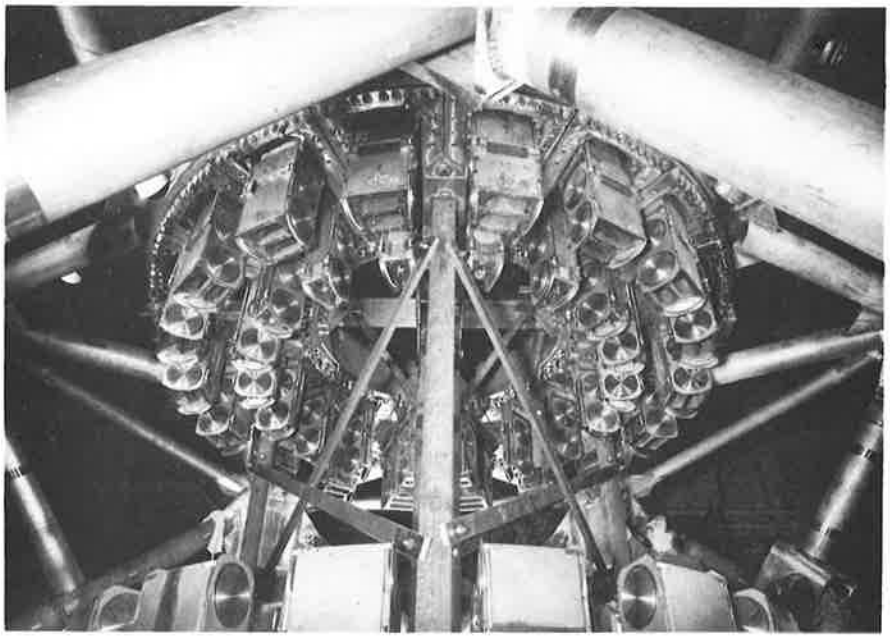

744507

Fig. 11. Upper shelf being positioned on dummy center column.

After the two shelves were properly leveled and positioned, the torque bracing was installed and the gussets for these braces were located and welded in place (Figure 12).

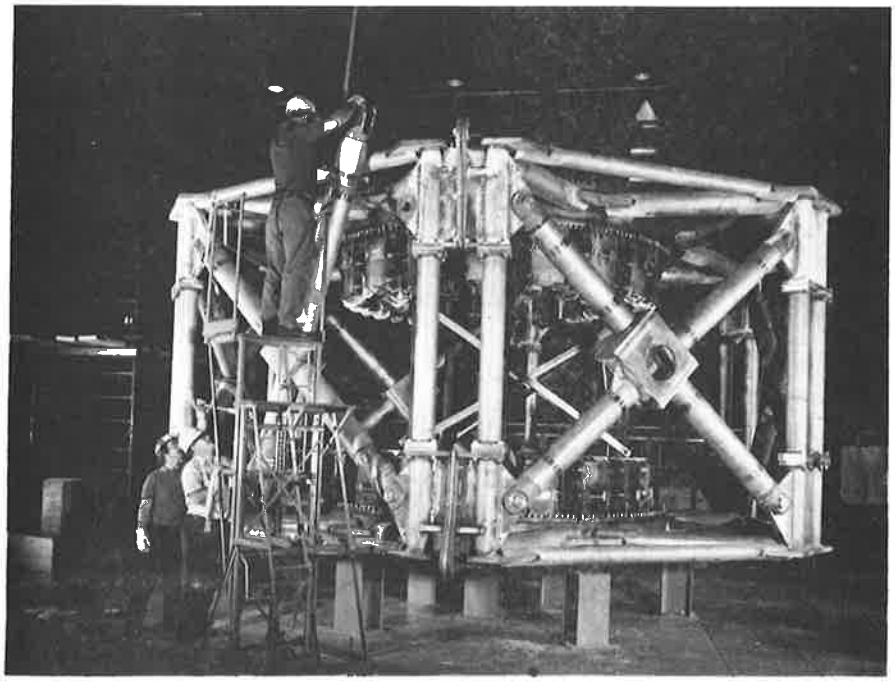

744508

Fig. 12. Installation of torque bracing and gussets.

The structure was completed, disassembled, and transported to the final assembly site in mid-August. Figure 13 shows the structure before it was disassembled.

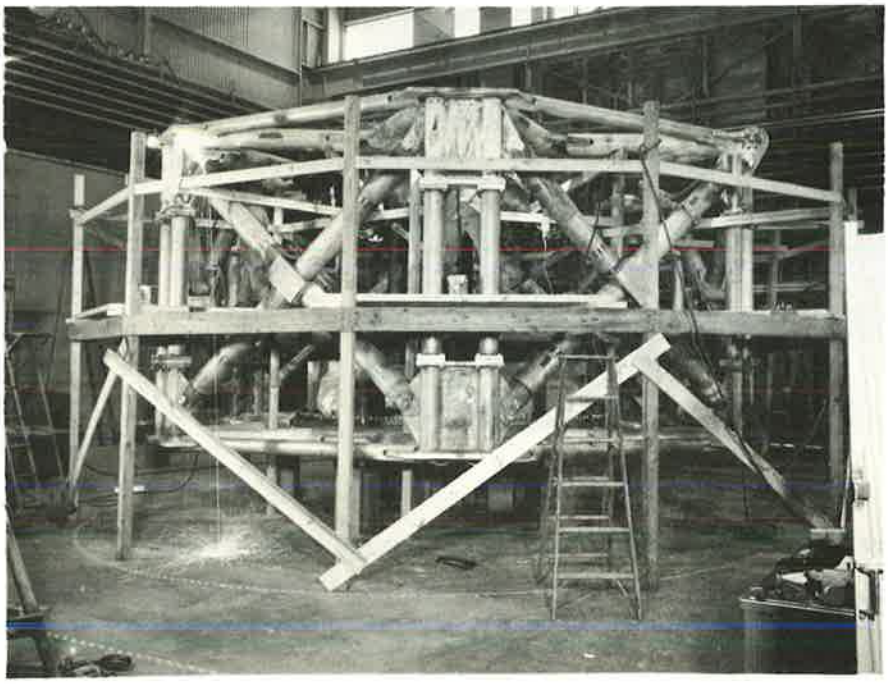

744492

Fig. 13. Torque frame prior to disassembly for removal to final assembly site.

The center column was to have been completed in time for use in the structure preliminary assembly. The column was cast in two halves and both halves were delivered in March. Cracks were first noticed in the casting during machining at Sun Shipyard and Drydock Company in Chester, Pennsylvania. Repair procedures were established with Cooper Alloy Company and PPPL with the help of consulting metallurgists from Westinghouse Research Division. Repairs were completed in August, but the castings warped during annealing and had to be returned to Cooper Alloy. They were reannealed and weighted in a manner calculated to remove the warpage. The repair seemed satisfactory,

but cracks appeared again. These cracks were repaired and again the repair seemed satisfactory. On November 5 more cracks were uncovered during machining and the decision was made not to use these castings. The castings are shown in Figs. 14 and 15.

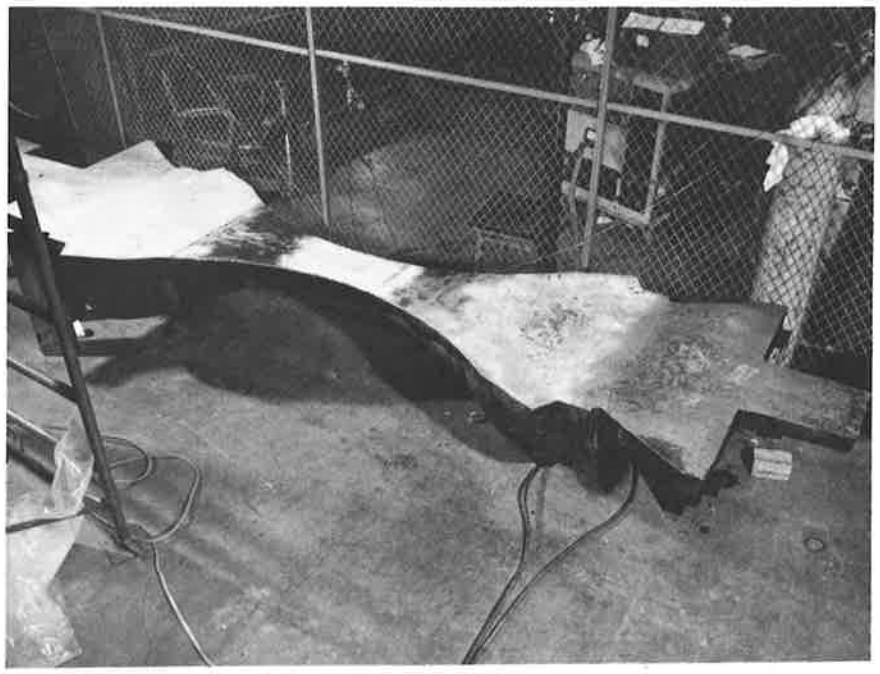

744792

Fig. 14. Casting prepared for the PLT center column

744788

Fig. 15. Casting prepared for PLT center column.

Figures 16 and 17 show the castings with the cracks outlined by dye penetrant.

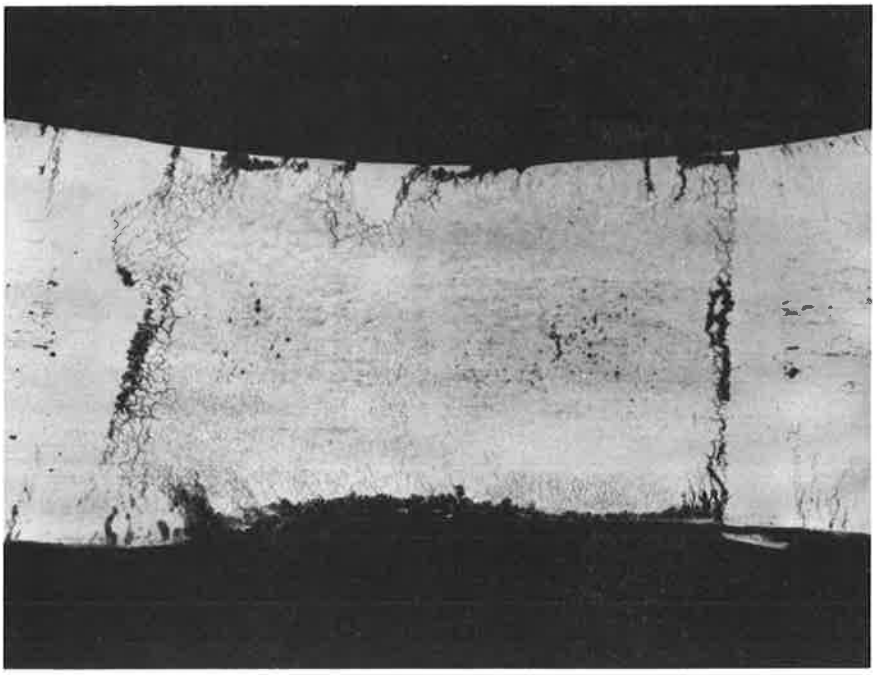

744789

Fig. 16. Center column casting with cracks outlined by dye penetrant.

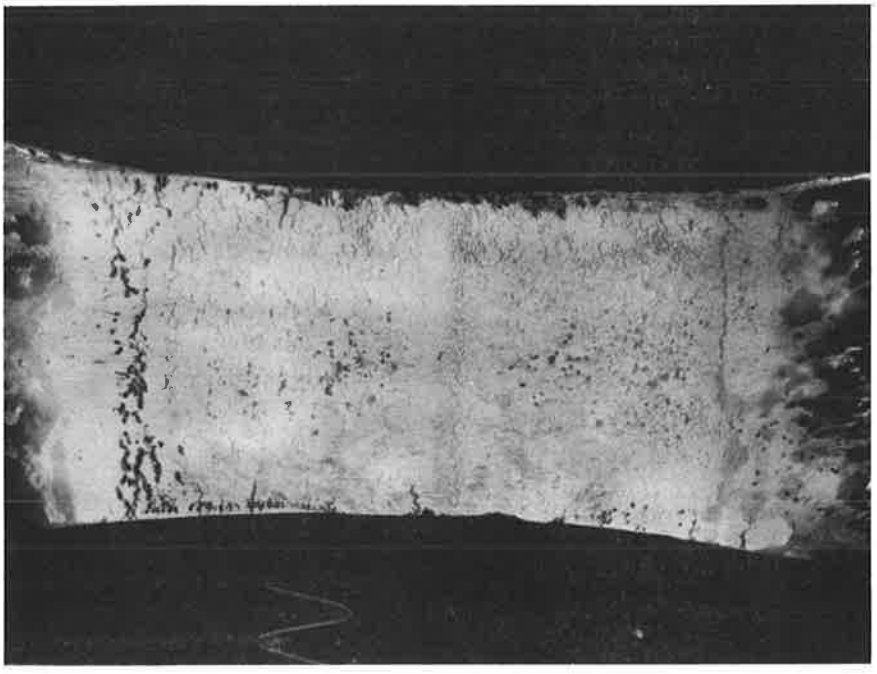

744793

Fig. 17. Center column casting with cracks outlined by dye penetrant.

The exact cause of the cracking is unknown. However, it appears that the modified HF alloy, although completely satisfactory for the wedge castings, was not suitable for a casting with the geometry and size of the center column. This alloy was selected for its high strength and low permeability.

The center column was designed to permit assembly of the structure and coils around it. A new center column will be designed to be demountable and installed after the rest of the machine is essentially complete. This column design should also benefit from the date on the elastic behavior of the toroidal field coils obtained from the power tests.

The design of the OH and SF coil supports was about complete at the beginning of 1974 and they were fabricated in this year. The inner coil group required 114 Aluminum castings and a contract was awarded in July to the Pattern Machine and Foundry Company for them. These castings were received in October and were machined in PPPL shops. Sixty-eight castings for mid and outer coil group support were supplied under contract by the Rolle Aluminum Company in September after the contract award in August. Machining was 80% complete at the end of the year. Thirty-six preload posts required for support and preloading of the inner OH solenoid were fabricated by H & L Associates and delivered in September. A weldment required for the support of the outermost coils was started in December. The fabrication of all these parts was on schedule at year's end. Figure 18 shows the castings as used to support the inner coil groups.

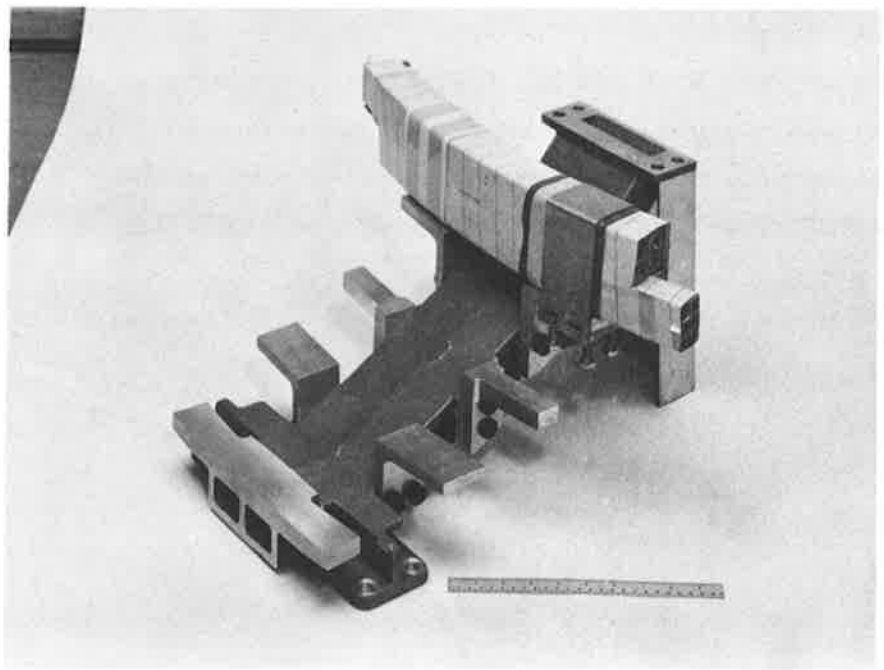

754029

Fig. 18. Casting used to support the inner OH/SF coil groups.

e. Machine Area and Assembly Operations. Area operations began in early July when the radiation shielding wall assembly was begun. Figure 19 shows a typical wall section during construction on August 7, 1974.

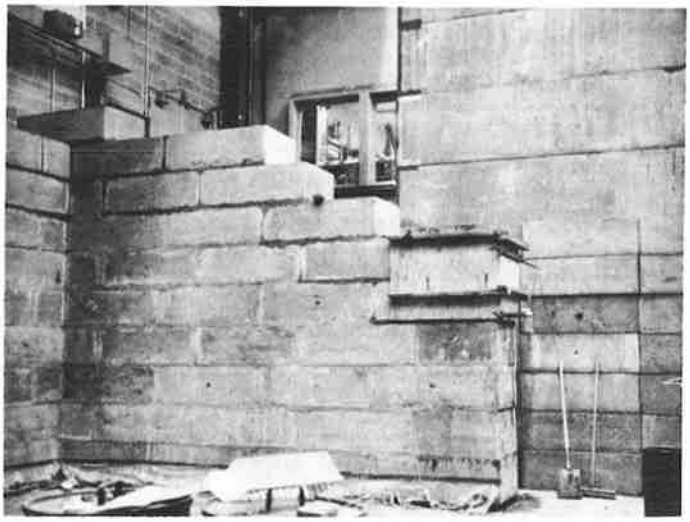

744471

Fig. 19. Southwest corner of shielding wall during construction.

Two different block sizes were used, the larger ones being salvaged shielding from the Princeton-Penn Accelerator, formerly lcoated at the Princeton University Forrestal Campus, at which site PPPL is located. The smaller sections were custom made and cemented together. A part of the South wall and most of the East wall were left unfinished to facilitate access to the assembly area.

Machine assembly was started in conjunction with that of the shielding wall. Great care was taken to insure that the machine was accurately positioned within the building, and a precision surveying device was used to aid in this task. Each base structure component was carefully leveled before more structure was built upon it. Figure 20 shows elements of the base structure during assembly on August 13, 1974.

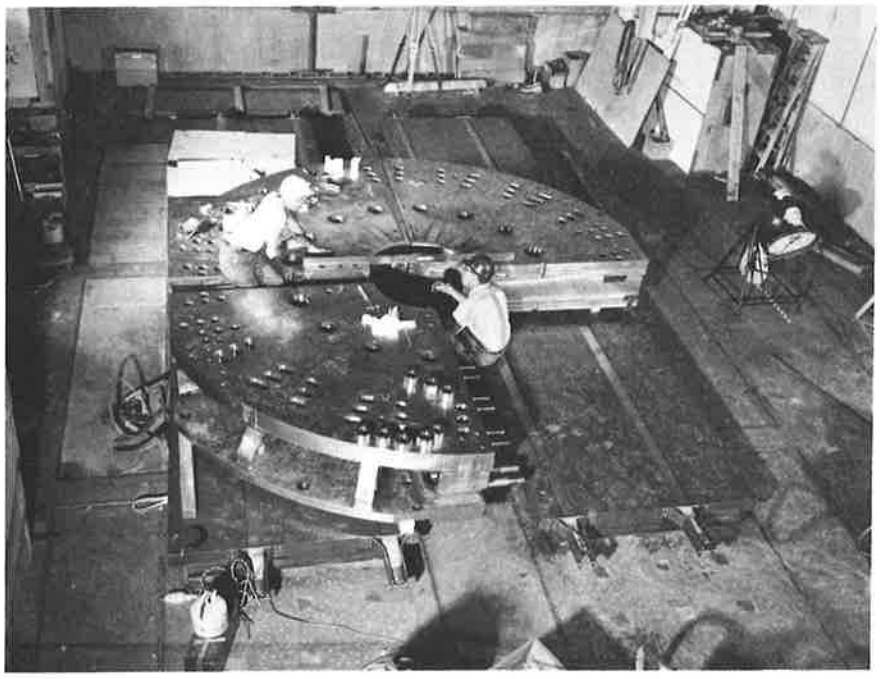

744490

Fig. 20. Base structure during assembly.

After completion of the base structure, the lower shelf and torque frame unit halves were transported from the staging area in 1-K building to the assembly area and later joined at the site. The entire lower shelf was then placed upon the ten supporting pylons which has previously been bolted to the U-coil shelves. (Figures 21 and 22) The shelf was made level and bolted hard to the pylons by August 25, 1974.

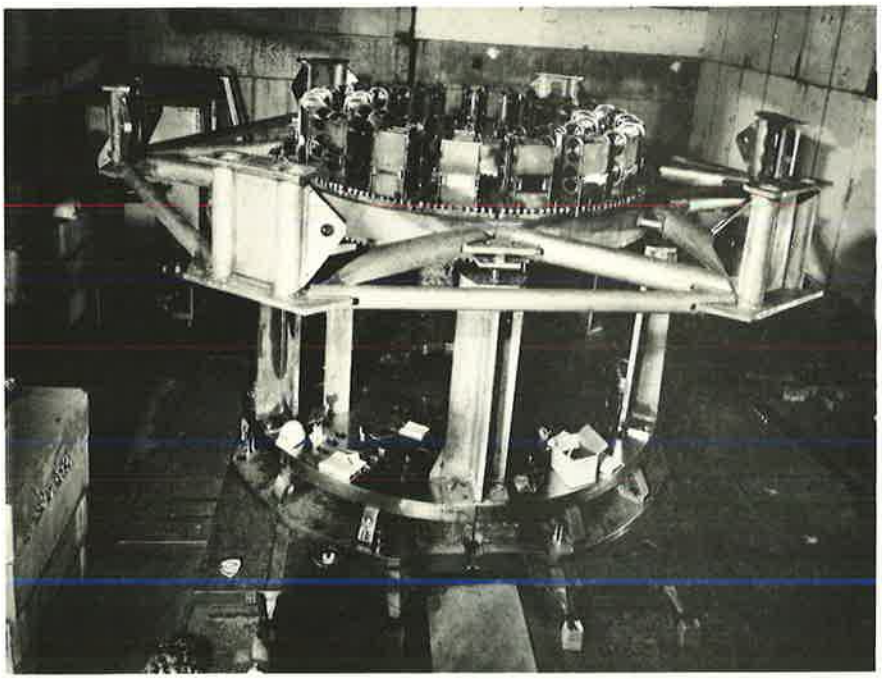

744527

Fig. 21. Completed Base Structure with Lower Shelf/Torque Frame.

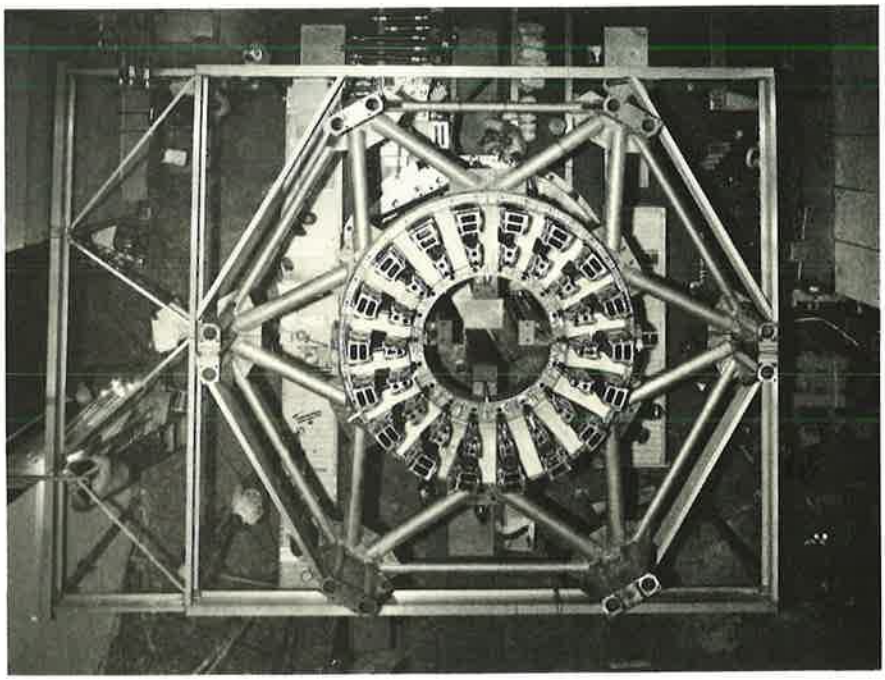

744549

Fig. 22. Top view of Lower Shelf, Torque Frame, and Platform Support.

TF coil placement began immediately after the base structure and lower shelf had been positioned. Figure 23 shows the first TF coil being lowered into place on September 13, 1974. A fixture assembly used to position each coil is visible in this photograph.

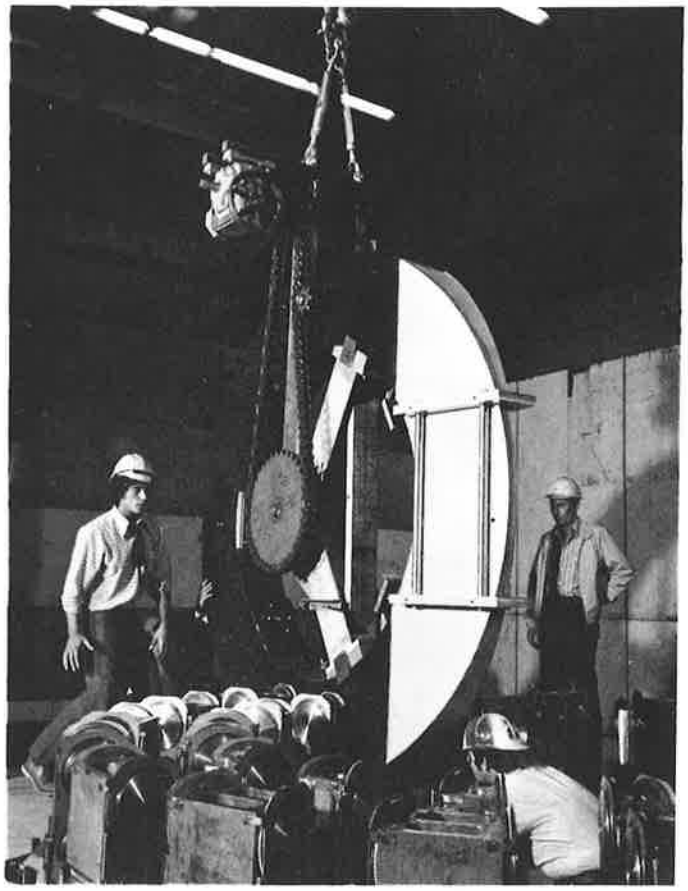

744557

Fig. 23. TF Coil being placed with aid of Lifting & Turning Fixture.

The structure at the coil base was used to turn the coil accurately through 90° from the stored position (wedge face down). The aluminum portion attached to the coil nose provided a surface perpendicular to the wedge face. This surface was employed to locate each coil radially on the lower shelf. Figure 24 shows the ninth TF coil as it was lowered into place on September 20, 1974. The last TF coil was placed on September 28, 1974.

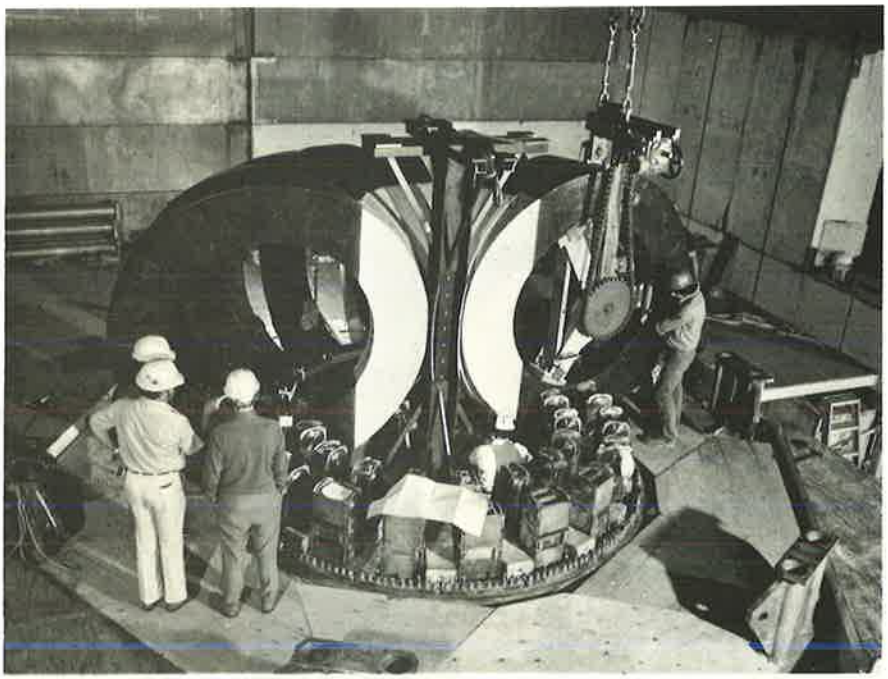

744579

Fig. 24. The ninth TF Coil being placed on the Lower Shelf.

The East and West baseplates and all but the South-East quadrant of the U-coil shelves were in place on time. Four fire-hoses employed to lift the North U-coil shelves off the baseplates are visible at the lower portion of the photograph. At this time, ten 2" holes were drilled completely through the 14" concrete floor into the basement. These holes are to line up with similar holes in the baseplate, U-coil shelf, and vacuum vessel to allow passage of very highly collimated laser beams to be used in making vertical transits of the plasma.

The upper shelf was transported from the staging area in 1-K and pre-assembled at C-Site in the same fashion as the lower shelf. Figure 25 shows the upper shelf being lowered into position on the structure with all TF coils in place on October 8, '74. Final precision leveling of the upper shelf could not be accomplished at that time. The make-shift center column did not provide stiff enough support at the center of the upper shelf for leveling. The subsequent center column will provide this support.

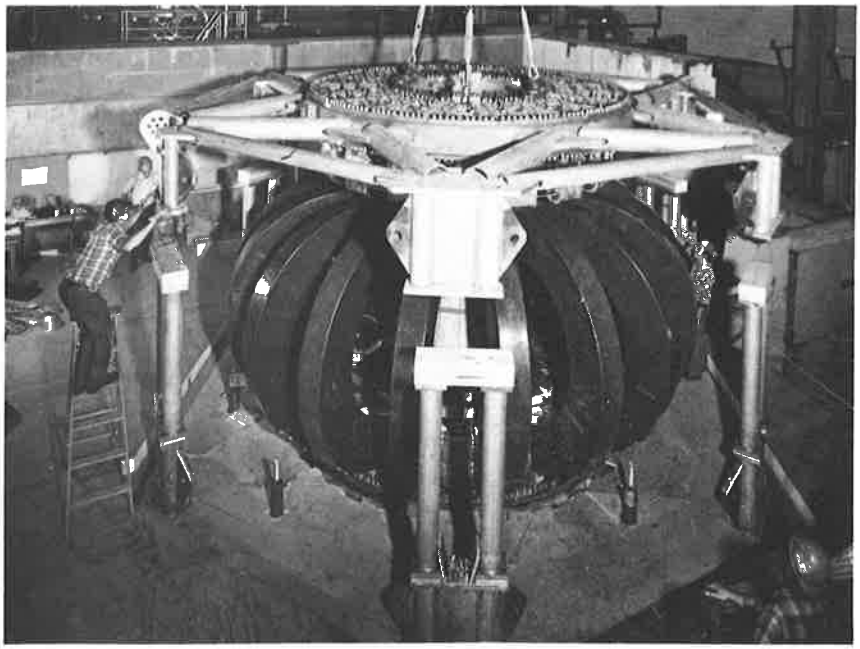

744612

Fig. 25. Placement of Upper Shelf and Torque Frame Assembly.

Assembly of the main machine structure was completed by early October. As TF coil power testing was anticipated in late October, efforts were directed to the assembly of coil tooling and bus connections.

Initial TF coil power testing began on October 23 and ended late in November. The coils were pulsed at various current levels up to 30 kA (35 kG) corresponding to approximately one-half centering force. Coil bore linear deflections were somewhat greater than expected and it was decided that more data would be required in this area. Difficulty was also experienced in attempting to make the coils "nest" in a satisfactory manner. A one inch thick epoxy annulus was finally molded to the inner nose of each coil to prohibit relative motion radially. Employment of this annulus was successful, giving definite proof that the coils' notions could be controlled. First phase power tests were terminated at that time in order to begin insertion of the vacuum vessel.

Vacuum vessel installation began with the separation of the mechanical structure on December 11 (Figure 26).

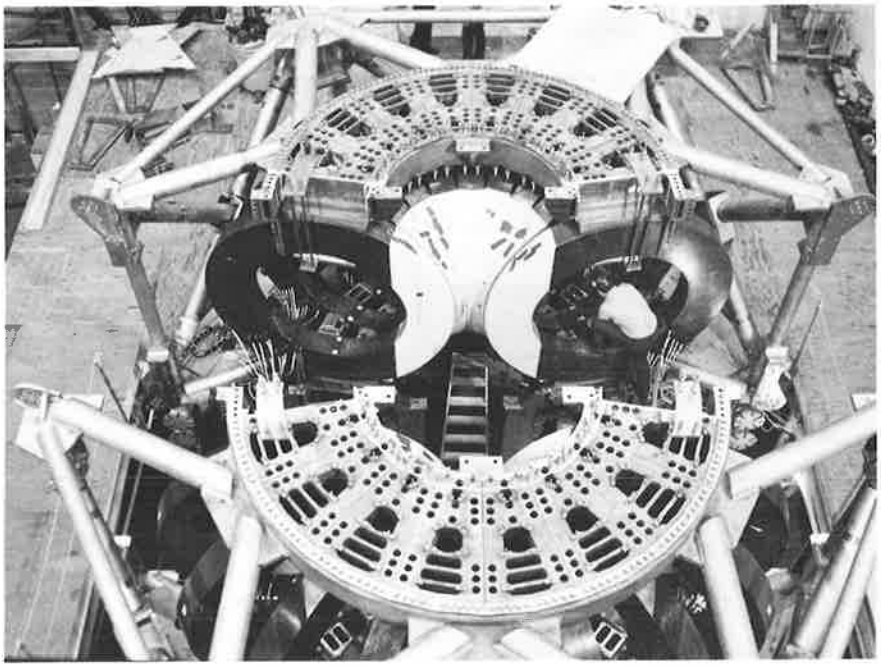

744772

Fig. 26. Top View of Machine after separation of North-South Halves.

The North half of the machine was unbolted from the lower structure and lifted (on roller bearings) 1/8 inch. The raised half was then moved North 8 feet, creating a gap which allowed the vessel to be turned into each machine half (Figure 27). The machine was then closed mechanically just prior to the end of the year.

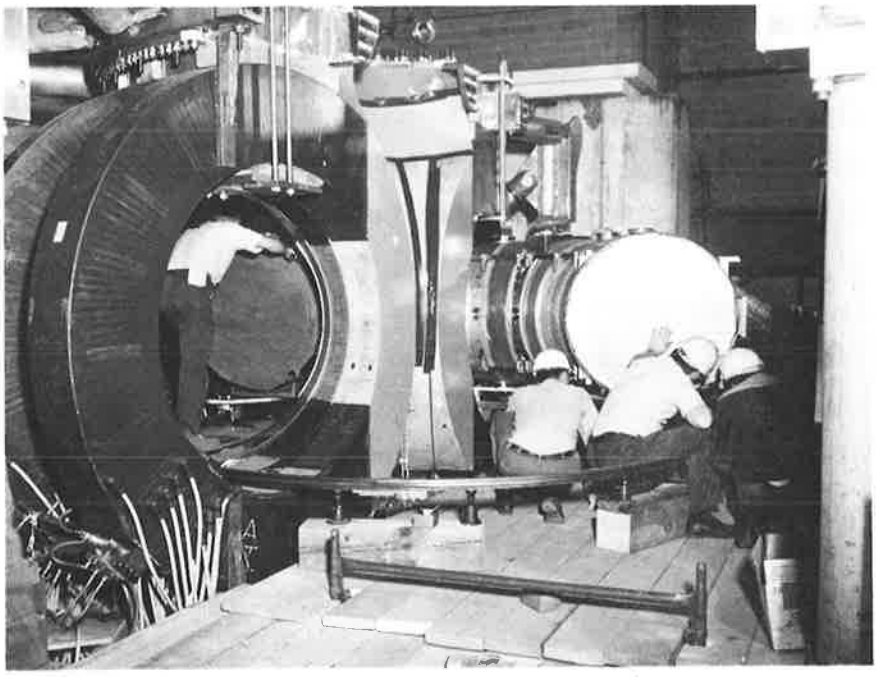

744806

Fig. 27. Insertion of Vacuum Vessel Half into Separated Machine.

f. OH and SF Power Supplies. Construction and installation of these supplies involved a major portion of total electrical engineering activity for 1974. Figures 28, 29, and 30 are photographs showing typical sections of them.

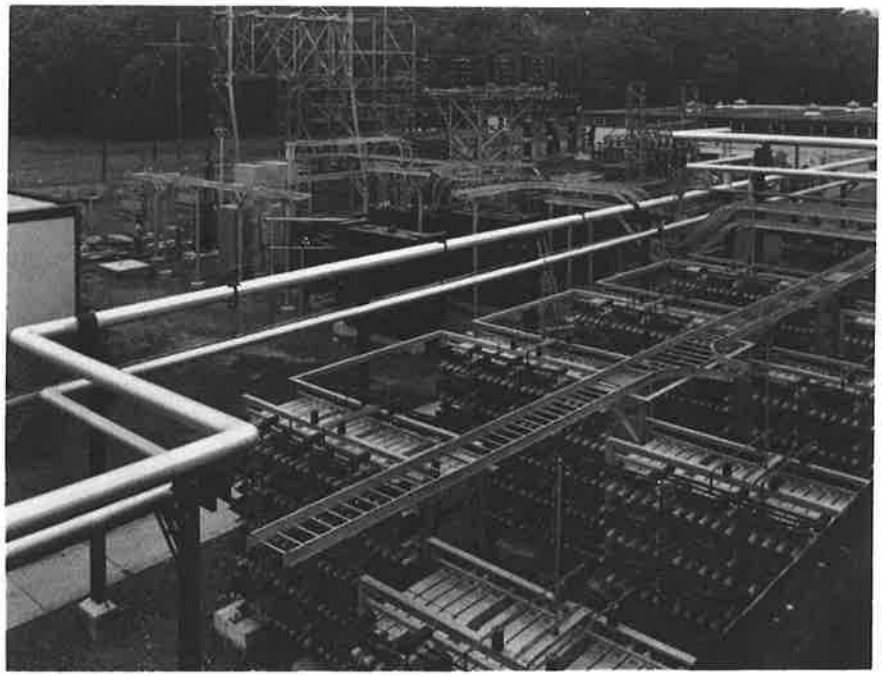

744429

Fig. 28. PLT OH/SF Power Equipment (Series Capacitors upper-left, 2.5 Megajoule Switching Capacitors in foreground.

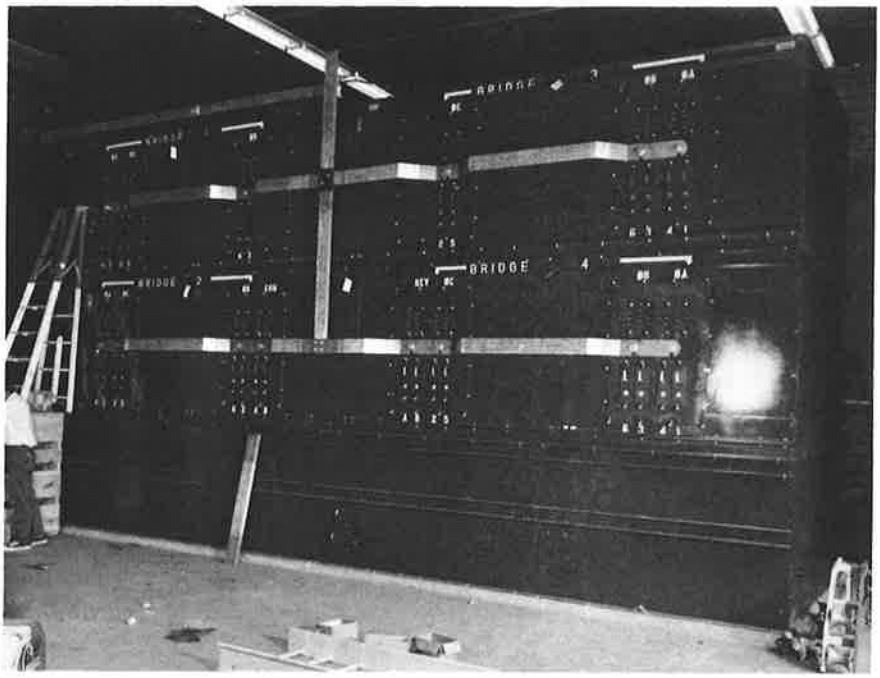

744438

Fig. 29. PLT OH Rectifier/Breaker

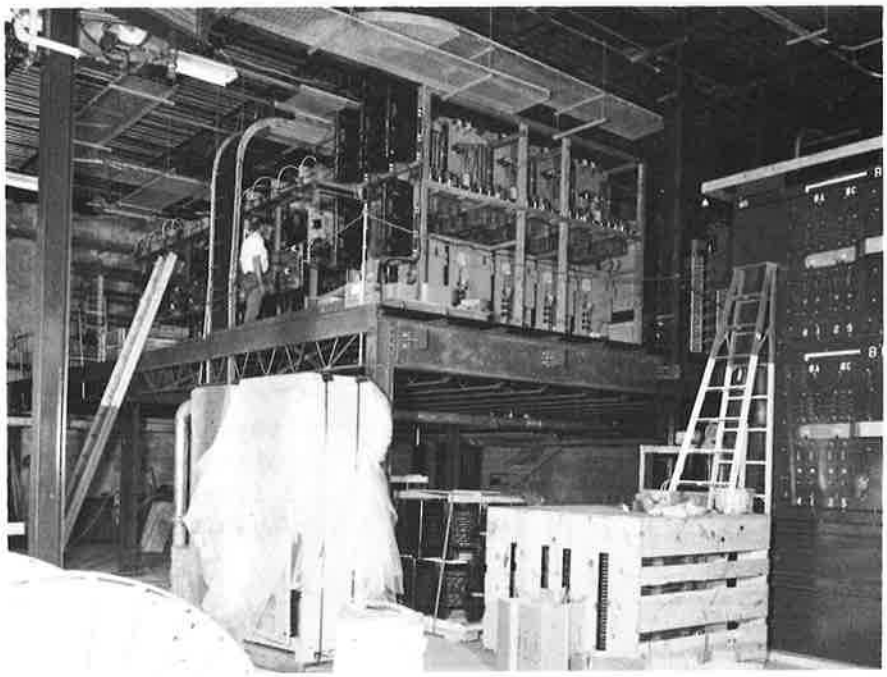

744436

Fig. 30. PLT OH Forward and Reverse Ignitron Switch Assemblies.

The ac system providing power for the rectifier transformers was energized in October and the OH Rectifier/Breaker was successfully operated into a dummy load in December. Initial operation of the SF Rectifier was also successfully accomplished. At the end of 1974 the testing levels were approaching the upper limits anticipated for machine operation.

PPPL Annual Report for 1973 summarized in some detail the OH Power Supply operation. The SF system is described elsewhere in this report as planned for the PDX EF Supply. Design improvements made for both these systems during the year are reported in Abstract VB 1. The results of the ignitron testing program completed in 1974 are reported in Abstract VB 2.

g. PLT Electronic Timer. The 124 channel PLT timer was completed shortly before the end of the year. The complete assembly is housed in a standard 19" rack cabinet that is 30" deep and 76" high. This timer replaces the original "EAST" timer built by RCA for use of the Model C stellarator and used also for the Model ST Tokamak. East measurements were the same 30" depth, but 5 ft. high and 15 ft. wide, resulting in a volume of 7.5 times that of the new timer. This contrast reflects the advantage of employing present-day circuit techniques and components that are primarily the products of a rapidly advancing

solid-state technology. In addition, this technology and good engineering design were responsible for an 80% cost reduction from the $300K price of "EAST" with only 100 channels.

This timer is actually a fourth generation unit, as it was preceded by similar ones having fewer total channels and used for the FM-1, ATC, and smaller machines.

Specifications include: 1) 60 channels settable between -99.999 seconds and +99.999 seconds with respect to the t_o output (1 millisecond resolution) and 2) 60 channels settable between -99,99999 and +99.99999 seconds (10 microseconds resolution). 3) Pulse output of 175 volts into 50 ohms for each channel having 1 ms step resolution, the pulse having a 1 microsecond risetime and a half amplitude width of 10 microseconds. 4) Pulse output of 100 volts into 50 ohms with 0.5 microsecond risetime and 3 microsecond width for each channel with 10 microsecond resolution. 5) All channels isolated from ground and each other for 1 kV.

Figure 31 is a photograph of the new timer.

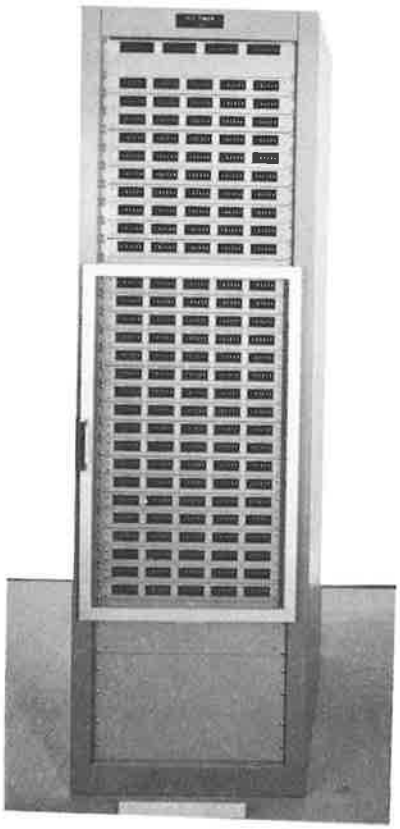

754081

Fig. 31. Front view of 124 Channel PLT Timer

h. Computerized Data Acquisition Services During 1974 a PDP 11 computer system was procured for data acquisition. Design was done for analog and digital transient recorder systems. Planning was done for interfacing schemes to the acquisition system, and design, procurement and planning were accomplished for several PLT diagnostics including Plasma TV, 8 channel microwave interferometer, and 4 channel X-Ray spectrometer.

Planning for the PLT Data Acquisition System is reported in Abstract VB 3.

2. The Poloidal Divertor Experiment (PDX)

a. Cost and Schedule The period from January to June of 1974 was spent in conceptual design of the machine. This design is particularly complex due to the involved poloidal field design required to achieve the magnetic limiting and diverting functions.

Transition from conceptual to preliminary design took place in June, coincident with project authorization. The project was broken down into nine subsystems with a total of 60 jobs. These jobs were PERTed by the engineer-in charge and linked to each other to form a project schedule.

The PERT chronological critical path for PDX is shown below.

1. TF Coil Design and Fabrication
2. Machine Structure Assembly with TF Coils
3. TF Coils Power Test
4. Disassemble Machine to Install Vacuum Vessel-Divertor Assembly
5. Reassemble Machine and Outer Section of TF Coils
6. Power Tests of All Systems
7. Combined Systems Power Tests
8. Experimental Operation

By December of '74 it became obvious that the estimated completion date of May, 1977 could not be met. The basic reasons for this were: 1) competition for mechanical engineering manpower because of difficulties with the center column for PLT, 2) difficulty in recruiting qualified coil design engineers and, 3) unanticipated problems and delays in completing the poloidal coil magnetic design.

At year end the PERT was in process of review.

The job estimate (JOBEST) produced in June of '74 showed a total cost of $13,860K, excluding the contingency. Of this total, budgeted costs were 59% with non-budgeted costs of 41%. The labor total was estimated to be 2,329 man-months, including all skills.

At the end of 1974 slightly less than 20% of the estimated money was costed or committed.

b. Planning and Supervision From June 1 to December 31 the primary effort was in expediting material acquisition, conducting machine and equipment studies, and making production preparations. All of these activities were directed toward long lead-time purchased items and hard-to-get materials. Although detailed design of the machine was not available, the general requirements gave sufficient information for substantial preparations.

In particular, acquisition and installation of a large boring mill and milling machine had been partially completed. Handling facilities for the large plates to be used in the vacuum vessel were at hand, and arrangements had been made with vendors for supply of large plates used in the main machine structure.

These preparations had given the project a strong start in areas that can often be quite troublesome.

c. Area Preparation and Assembly The major effort in 1974 was the preparation of area layout drawings as well as the conceptual design of the radiation shield blocks.

High density reinforced concrete containing an aggregate of Ilmenite will be used to maintain a minimum platform area of 2200 $ft.^2$ as well as provide the necessary shielding. The use of this material, a non-magnetic ore containing oxides of Iron and Titanium, will result in attenuation of 10 Mev X-Rays by a factor of twenty.

d. Mechanical Structure At the end of the year the mechanical design of PDX was in the preliminary stage. A number of main component layout drawings had been prepared together with drawings showing the inter-relationship of these components for various alternative arrangements under consideration. An overall and consistent mechanical design had been hampered by the lack of a reliable conceptual design for supporting the inner leg of the TF coils. One result of that fact was a delay in center column design and the interface of it with the upper and lower shelves. Several solutions were being considered, including additional support of the TF coil inner legs at

the mid-plane.

One of the original basic design concepts of PDX was to insure that the TF coils could be separated for assembly. In view of this, a major effort was directed to TF coil support structure design and that of the joint clamp. Although the coil joint development was continuing at the end of the year, the design and layout of the clamp main components had been completed. Figure 32 shows a full scale wooden model of the clamp assembly.

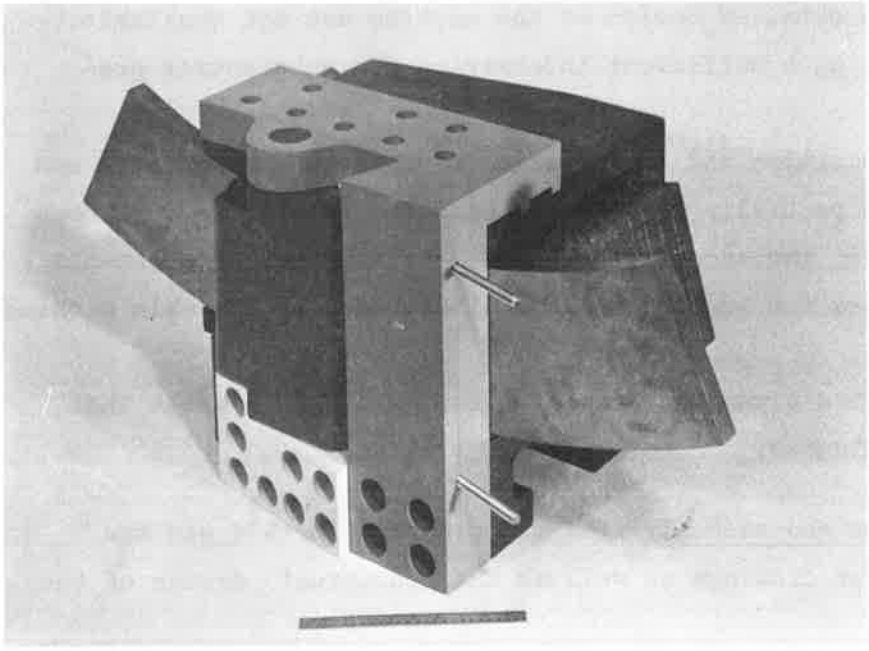

754056

Fig. 32. Full Scale Wooden Model of TF Coil Clamp.

An overall structural concept of the machine was virtually complete at the end of 1974. Layout drawings had been made and were being continually updated to reflect changes in the interacting sub-systems. Engineering of the machine sub-structure was complete and detailed drawings had been started. A stress analysis had been completed for the vacuum vessel except for the effects of the poloidal coil supports. An initial TF coil stress analysis also was complete.

The poloidal coil support design remained in the preliminary design stage awaiting information concerning coil locations, sizes, and forces. The concept to deliver a complete vacuum vessel-poloidal field subassembly to the machine area remained intact. This concept will allow parallel assembly operations, reducing the lead time.

e. Toroidal Field (TF) Coils The three major developments during 1974 were: 1) There was a dramatic change in availability and price of the required copper material, 2) Actual tests were conducted of several approaches

in the most important manufacturing processes, and 3) Discussions were conducted with a number of companies which conceivably might qualify to be prime contractors.

Early in April, '74 the price of copper rose to a record high (about $1.50/lb.) and no vendor seemed interested in the special development work required for PDX. During the summer the price began a sharp slide and interest in our problem on the part of suppliers began to pick up. A purchase order with both Anaconda and Phelps Dodge was written and trial bars were delivered in November. The quality of these bars and accuracy of the central hole should result in an easier and less time-consuming manufacturing process than that which was anticipated originally.

Both press forming and stretch bending were considered for conductor forming. Trials of the former technique demonstrated feasibility, but at a very low production rate. Initial trials of stretch forming indicated both feasibility and a very high production rate. Work was continuing to develop this process at the end of the year.

By December, eight vendors had expressed interest in considering bids on the job. Laboratory engineers had conducted on-site inspections of facilities and discussions with five of these vendors.

f. Poloidal Field Coils Progress during the last six months of 1974 was slower than originally envisioned due to delays in firming up the poloidal field design. However, the design produced by this extended effort resulted in several very significant improvements in both magnetic and physical characteristics of all poloidal coil systems. The magnetic forces are considerably lower than in previous designs; the peak voltages on the "canned" coils in the vacuum chamber are reduced significantly; and the increased space for the coils within the separatrix regions permits greater design flexibility.

The number of these "canned" coils was reduced to ten assemblies, leaving more room for coil supports, greater ease in coil fabrication, and far simpler final assembly in the machine.

The modified conceptual design utilizes a poloidal field solenoid located between the vacuum vessel and the TF coils. This solenoid is to contain portions of the ohmic heating field, equilibrium field, divertor field, centering field, and nulling field coil windings. It will be a rigid self-supporting unit, reinforced with epoxy-glass. This one unit replaces several discrete

coils that, in the previous conceptual design, were placed inside the vessel. The coils inside the vacuum vessel now will be divertor field coils, one pair of equilibrium field coils (so located to improve the coupling), and one pair of centering field coils. The remaining coils are scattered outside the vacuum vessel. Electrical insulation will be provided by mylar, while epoxy-impregnated glass over-wrap will serve to bond the turns.

Vendor contacts have resulted in a practical technique to build the "cans" required for the coils, and early delivery of the stainless steel required to manufacture them. Earlier vendor contacts regarding the extruded Copper conductor material indicated that this procurement will present no difficulty.

g. Poloidal Field Design Several attempts were made to achieve a satisfactory poloidal field design during the second half of 1974. Each of these designs yielded valuable information which allowed the final one of December to meet the design criteria originally set up. These criteria are listed below.

A. Hexapole null for initial striking of plasma
B. Linearity of plasma current vs. area during startup
C. Equilibrium and stability of plasma from null to full current
D. Separatrix clearance (of coils, vacuum vessel, etc.) from startup through full plasma current
E. Ability to operate in four modes: 1. Standard tokamak mode with circular cross section, 2. Square cross section with magnetic divertor. 3. "Inside D" with magnetic divertor, and 4. "Outside D" with magnetic divertor.
F. Minimized coil ampere-turns
G. Minimized eddy current effects through placement of most coils outside of vacuum vessel

Based on these criteria, the poloidal field coil systems in the design can be described as follows:

OH - The Ohmic Heating coils energize the plasma.
EF - The Equilibrium Field coils aid in (B) and provide (C) and the plasma cross sections, (E).
DF - The Divertor Field coils provide (E2) through (E4) and (D).
CF - The Compression Field coils aid in (B), (C), and (F).

NF - The Null Field coils provide for (A) and (D).

Positions of the DF/CF/NF coil systems are shown in the flux plots of the square and inside of operating modes in Figures 33 and 34.

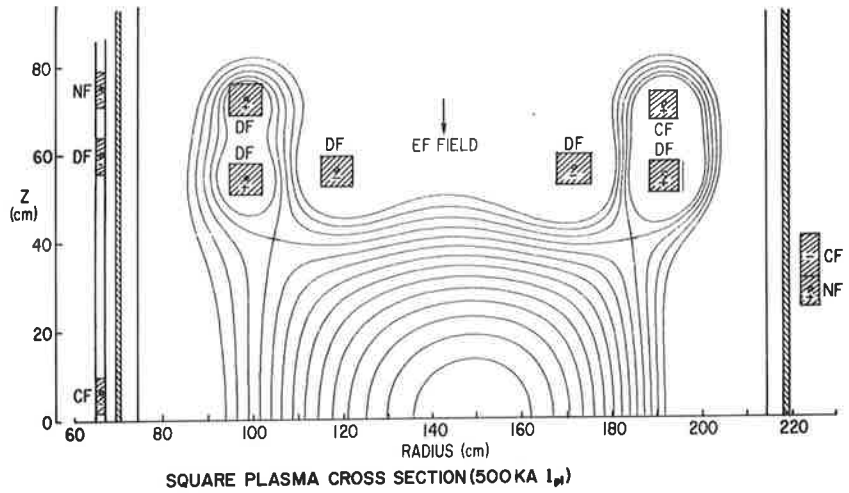

753265

Fig. 33. Flux Plot for "Square" Operating Mode.

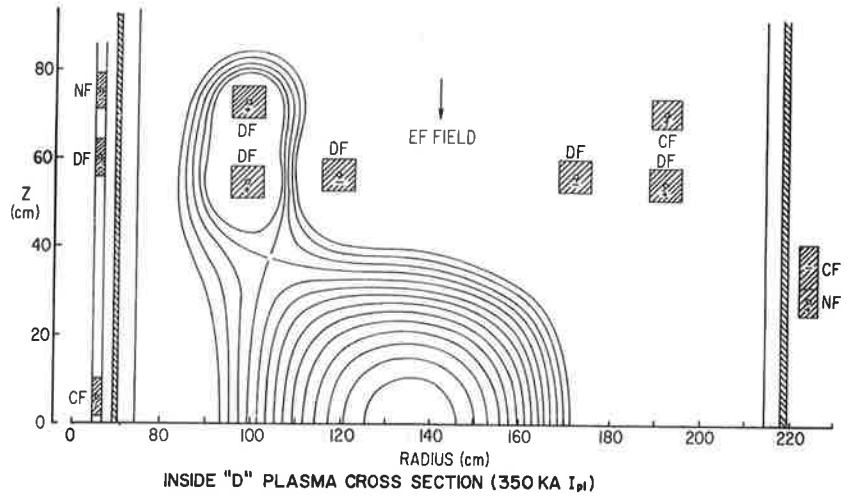

753264

Fig. 34. Flux Plot for "Inside D" Operating Mode.

The OH field design was revamped several times in order to accommodate changing design criteria in structural supports and diagnostic ports. These criteria were met and, with a current of 15,000 Amperes, there is a resultant magnetic flux of 1.1 Webers passing through the center of the machine. The new design will allow a higher safety margin in obtaining the desired plasma current of 500 kA for a duration of 1/2 second.

The EF coil system must provide the proper field index for the standard circular tokamak mode and it must also operate in conjunction with the divertor coils to provide the required equilibrium field for the various diverted plasma configurations. The final design has only two coil cans within the vacuum vessel and provides a suitable index for a 50 cm radius circular plasma centered at 145 cm as well as the diverted plasma configurations.

The unsatisfactory initial design attempts called for the use of two (-+-) coil triplets to magnetically divert the plasma and satisfy some of the other design goals. Several drawbacks were discovered in this approach, including large coil forces and currents, poor separatrix clearance during plasma buildup, etc. It was determined that the triplet design produced the problems and a doubled (+-) divertor was developed (see flux plot diagram). The new divertor with a revamped EF and pulsed CF and NF coils effectively meet the design criteria.

h. OH and EF Power Supplies and Controls Preliminary engineering had been completed for the OH and EF supplies and controls. These systems will use respectively, the OH and SF supplies of the PLT installation. Operation of the OH supply was described in the PPPL 1973 Annual Report.

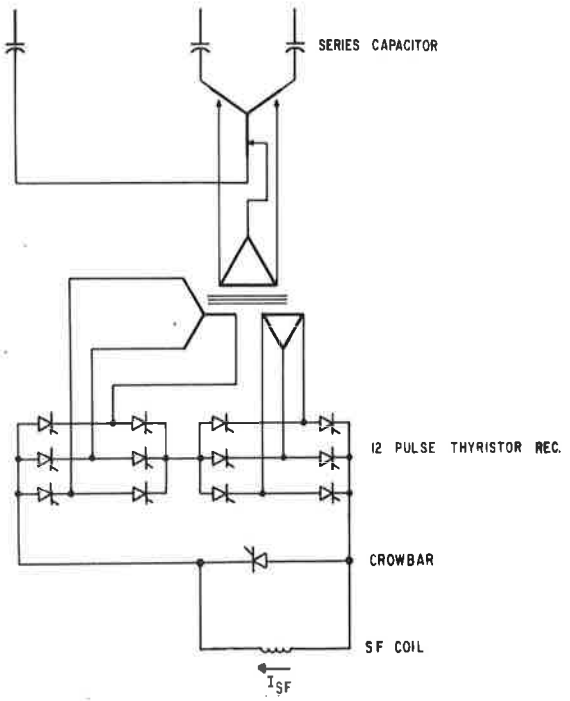

744120
Fig. 35. PDX EF Circuit Elementary.

The EF power supply is a twelve pulse silicon-controlled rectifier rated at 7.2 kA and 2 kV and is shown schematically in Figure 35. A unidirectional variable current output is controlled by changing the firing angle of the SCRS. A filter in the output reduces the ripple to a low value and the option to switch the filter in or out is provided.

i. DF/CF/NF Supply During the second half of 1974 the circuit design of this supply went through several changes corresponding to the changes previously described in the field and coil designs. At the end of the year design engineering was starting on the supply based upon the final optimum magnetic design parameters.

j. TF Power Supplies At the end of the year control simulation studies for these power supplies had been started. Some revisions in job control language required to operate existing programs had to be made due to recent changes from LASP to HASP on the 360/91 computer. TF coil data was being put into the generator control simulation computer program to determine optimum damping parameters and the system response.

k. Process Controller Process controller IBM 1800 computer will be used for all systems' operating controls. Control systems block diagrams were being developed so the necessary program logic could be extended for input and output addresses prerequisite to assembling the basic system.

l. Vacuum Vessel The order for the top and bottom of the vacuum vessel had not yet been placed at the end of the year. The only bidder (Torngren/Spincraft) was proceeding with the tooling on a limited contract basis pending an AEC audit of their proposal. The 305 stainless steel plate for the manufacture of the vessel was scheduled for delivery early in January, '75. Carlson Steel, the vendor reduced the delivery time from 32 weeks to 16 weeks as a direct result of a public relations program that PPPL had instituted with the steel manufacturers.

The design of the ports, flanges, and remainder of the vessel was continuing.

In theory, this job was on schedule, but it was felt that continued delay in placing an order with Torngren/Spincraft could ultimately cause a late job completion.

m. Poloidal Coils Fabricating Equipment During 1974 work was initiated in preparing building 1K fabrication facility to manufacture the PDX Poloidal

coils. Most of the remaining PLT TF coils tooling was dismantled and removed. A building layout was prepared and detailing of the various pieces of fabrication equipment was begun. Orders were placed for the two largest items required, a coil winder identical to the one purchased for PLT and a large epoxy curing oven. Delivery of both items is expected in May of '75. Purchase of smaller items and raw materials for in-house fabricated items was also started.

As additional crane facilities would be required for fabrication of these coils, a 5 ton crane was arranged for under contract. The crane will be installed in the 1-K building coil shop to augment the 40 ton crane in that area. Handling will be improved substantially with it because of the higher speed operation and the dual lift feature. Installation will be complete by June 30, 1975.

3. The Two Component Torus (TCT)

Westinghouse Electric Corporation was engaged to prepare a cost estimate and time schedule for a two component torus with Q=1 and to submit a report by June 29, '74. The report was submitted (Joint Conceptual Design Study for TCT) and reviewed in August, after which Westinghouse was authorized to continue refining the conceptual design and estimates. At the end of December, Addendum I to the original report, containing a description of a refined conceptual design and a more detailed cost estimate and schedule was submitted.

PPPL engineering personnel, when required, participated in these activities in conjunction with laboratory theoretical and experimental divisions' personnel.

VB 1. MATT-1056 Series Capacitor Engineering on PLT OH and SF Circuits by John G. Murray, George Bronner and Richard A. Newman

This report explains why capacitors were applied to the PLT OH and SF pulsed power circuits and the advantages of series capacitors as opposed to shunt capacitors. It outlines the technical problems that must be considered when installing series capacitors to prevent over-voltages, excessive fault currents, and resonant oscillations.

The advantages of the saturating series transformer circuit are given and the engineering procedures for selecting component sizes are provided.

VB 2. MATT-1104 Ignitron Long Pulse Testing by G. Bronner, J. G. Murray, and S. P. Duritt

The PLT and other future research machines will require fast turn-on switching devices capable of high current operation at dc pulse durations of several seconds. High voltage standoff and low voltage drop during conduction are additional requirements.

The ignitron is apparently the best commercially available component for use in such service. However, ignitron manufacturers' data are not published for ratings under the proposed applications' electrical-time environments.

This report describes tests made with the specific object of selecting one or more ignitron types suitable for use in the PLT ohmic heating system. Completion of the detailed design of this system was possible as a result of the subject testing.

Tests were performed on three types of ignitrons at current levels of from 2500 to 5000 Amperes and conduction periods of up to 5 seconds. Both mechanical deterioration and changes in certain electrical static characteristics were observed and used as criteria for test terminations.

Significant results were the selection of a moderately priced tube type for the PLT ohmic heating system and the choice of a conductor connection arrangement which extends tube life.

VB 3. MATT-1032 Data Acquisition Services at PPPL, by P. A. Thompson, S. G. Slusky, F. K. Bennett, and A. J. Greenberger

The current status of DAS-1800, the data acquisition system built around an IBM-1800 computer, is reported; hardware and software developments allowing the concurrent servicing of ST, FM-1, and ATC are described; and details are given of the changes in usage of DAS-1800 during the same three and a half years of its existence. Finally, plans are discussed for providing similar data acquisition services for PLT when it starts operation in less than 2 years.

VB 4. TM-276 Calibration Procedure for PLT Pilot Controllers, by Ronald E. Wintress

The pilot indicating controller IC07N is simply an air amplifier. A very small input pressure is amplified to a variable 0 to 20 psi output, varying with the input pressure. The "standard" output is 9 psi when the set pointer (red pointer) is lined up with the black indicating pointer. Supply is 20 psi of clean, dry, and regulated air pressure. The output will vary with the differential pressure, Δp, in a linear manner (up to 20 psi output). The input Δp is a maximum reading of the dial, 0" to 20" of water pressure, or 0" to 50" of water pressure, etc. This Δp is applied to the differential bellows assembly on the back of the pilot controller.

C. Engineering for Other Experiments

1. Symmetric Tokamak (ST)

Listed below are the engineering services and products provided for this machine prior to shutdown in May of 1974.

a. Sapphire Window - Movable Mirror Assembly Figure 1 shows this unit which consisted of a Sapphire-to-metal sealed window unit, a sliding valve type shield, and a mirror located inboard of the window/shield. It was used to observe the ST limiters or the plasma located away from the limiter location. A bellows-sealed mechanism provided linear and rotary motions to move the shield and mirror. When not in use, the window was completely covered by the shield to minimize coating from the plasma.

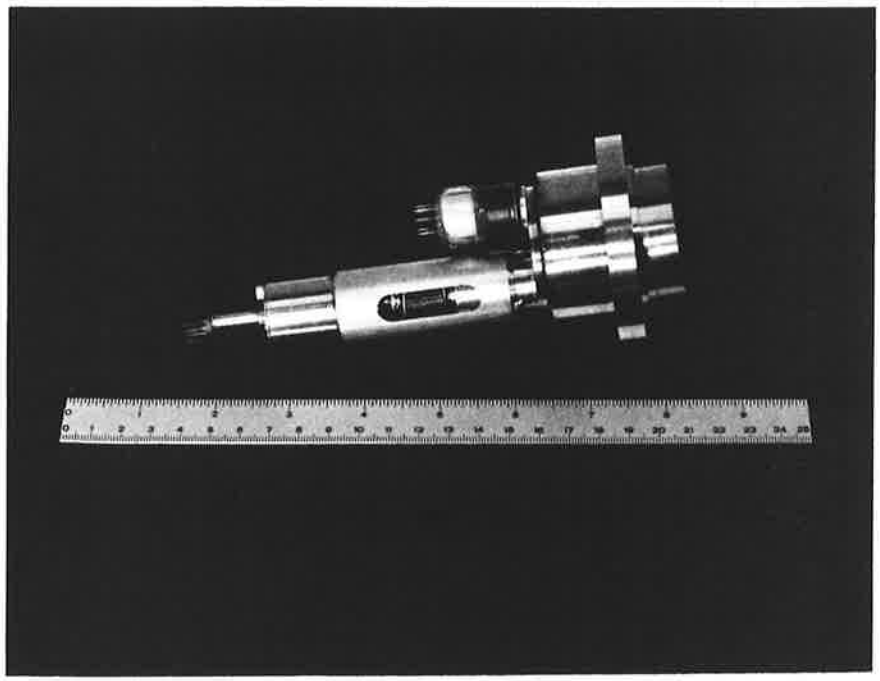

744085

Fig. 1. Sapphire Window/Movable Mirror Assembly for Model ST.

b. Soft X-Radiation Detector This assembly housed a linear diode array and a rotating disc containing filters placed in the line of sight to the array through focusing slits. A miniature vacuum feed-through (designed at this

laboratory) was used to transmit drive to the disc. A glass to metal feed-through was employed to bring out the signal leads. Figures 2 and 3 are views of this assembly.

744086

Fig. 2. View of Soft X-Radiation Monitor.

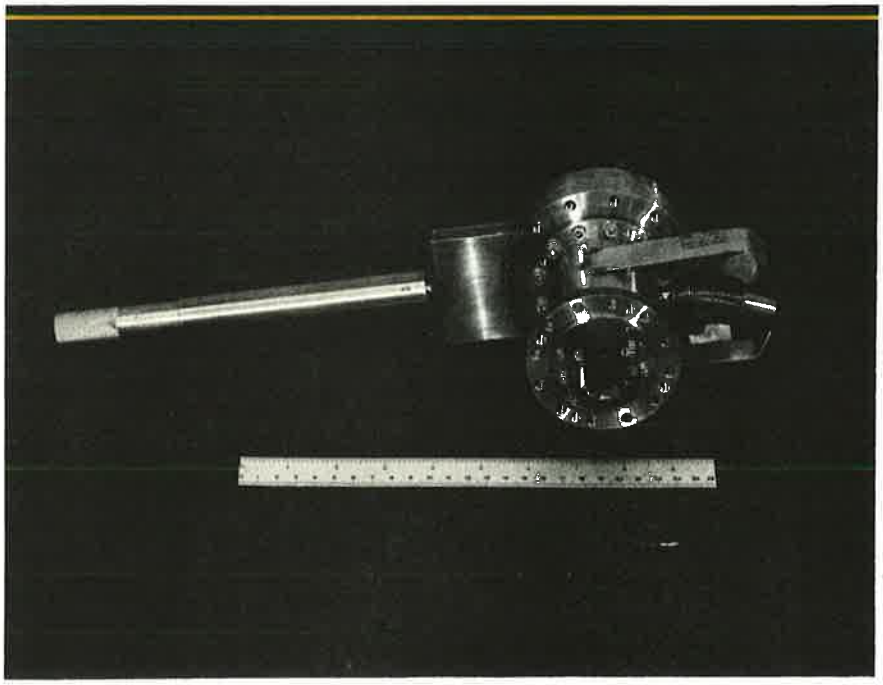

744087

Fig. 3. Opposite side view of Soft X-Radiation Monitor.

c. Phase II ICRH Coupler Installation was completed and this equipment was operated into the machine satisfactorily in the first quarter-year. Details of the assembly were described in last year's annual report.

d. Data Acquisition Services for ST For the remaining months of ST operations, hardware and software were provided for computerization of the ICRH experiment and the x-ray crystal spectrometer for the Fe impurity charge state experiment. (See Abstract VB 3 for details.)

e. Vertical Field Hard Tube Current Generator Installation and operation of this system into the machine were accomplished during the first quarter of the year. The generator performed well in producing controlled field coil currents as preset by the experimenter. There was some interference to low level instrumentation from it which was reduced, but time did not allow a complete cure. The system is described in the PPPL 1973 Annual Report.

2. Adiabatic Toroidal Compressor (ATC)

a. Neutral Injection Power Supplies and Modulators A power system was provided for operation of new higher current sources delivered from Berkeley. Designed and fabricated for either one gun operation or simultaneous use of both, it consists of filament, arc, decelerating and accelerating voltage power supplies plus suitable hard tube modulators for the accelerating voltage supplied to the high current sources.

Each arc supply provides 3000 Amperes at 150 Volts dc for 15 milliseconds per 30 second period with a maximum regulation of 15%.

Decelerating supplies each produce up to 20 Amperes at 1200 Volts for 10 milliseconds with the same regulation and period as the arc supplies.

Each accelerating supply is capable of 60 Amperes @ 25 kV with the same regulation, duration, and period as the decelerating supply.

In order to pass the 50 Ampere current required for each new gun, a major mechanical and electrical redesign of the previously used 25 Ampere modulator would have been necessary. An alternative was to use two 25 Ampere modulators in parallel for one gun and to design and construct a new modulator with capability to operate the second gun. This approach was followed in view of the facts that succeeding guns will require higher voltages and/or currents and the modulator voltage drop must be kept as low as possible.

The new modulator/regulator uses an Eimac X2170 tetrode which is normally biased to cutoff and then driven to zero grid bias during the required pulse

interval. This tube is capable of both higher current and voltage standoff than are required in this application and can, therefore, be used with future guns.

Adjustable screen and anode supplies permit operation at various load impedances, and a full complement of load and tube fault sensors protect both ion source and the modulator. Figure 4 shows a side view of the unit, modulator tube and deck on the right, water cooling coils top-center, and isolation transformer tanks lower-left.

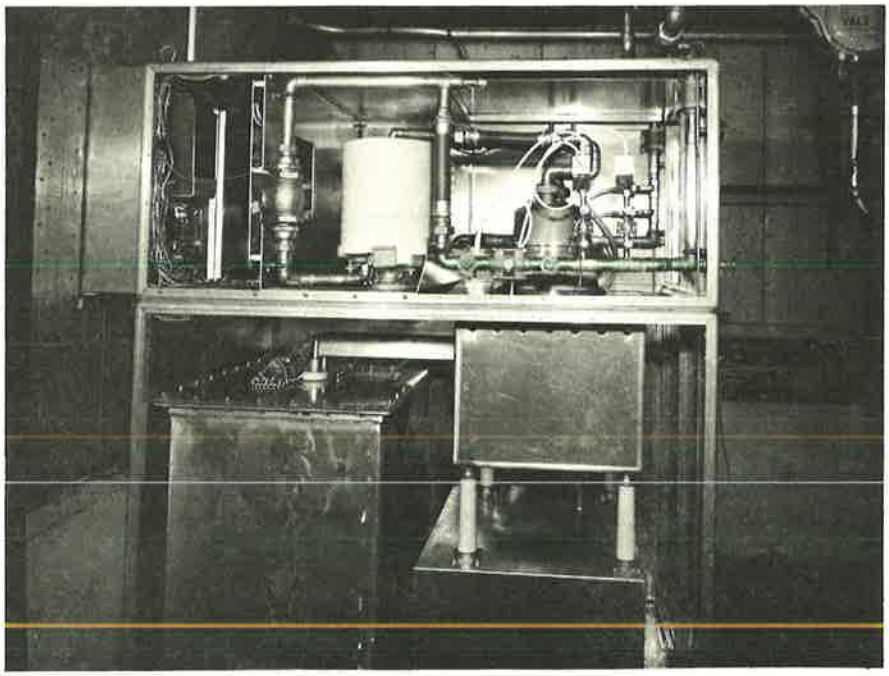

754082

Fig. 4. Side view of ATC neutral injection accelerating voltage modulator assembly.

b. Lower Hybrid Resonance (LHR) RF Heating System The design and construction of this equipment represents the major laboratory rf heating development effort of the year. At year's end the system was more than 90% complete, and it is scheduled for ATC operation in March, 1975. Four commercially available UHF TV Klystrons are used as power amplifiers to produce at least 200 kW at a frequency of 800 MHz. Pulse duration is variable between 20 microseconds and 20 milliseconds. A radar type floating deck beam modulator along with photo-optical transmitting and receiving devices were provided for pulse fidelity and general versatility. Hybrid combining techniques were used to provide two 100 kV feeds to the machine. In order to ease maintenance procedures and reduce down time in event of component failure, modular construction was emphasized in the assembly design. Figure 5 is a photograph showing one of the 55 kW amplifiers and the driver control cabinet. Figure 6

shows the floating deck modulator assembly, while Figure 7 is a close-up view through the amplifier cabinet side, showing the modulator enclosure and high voltage feed-through.

The system is described in detail as reported in Abstract VC 1.

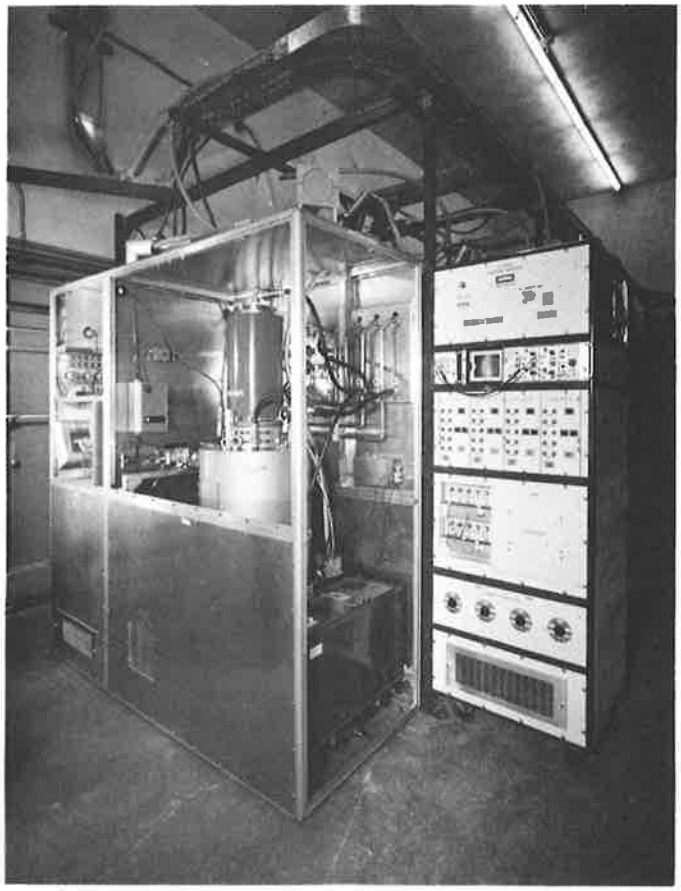

754013

Fig. 5. ATC LHR high power klystron amplifier and driver/ control cabinet.

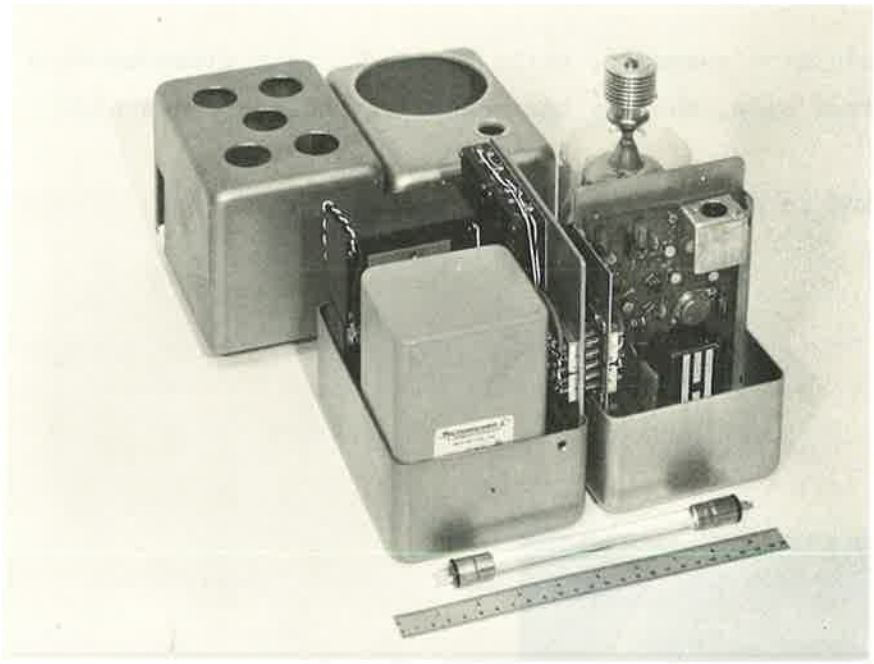

744283

Fig. 6. ATC LHR floating deck modulator assembly.

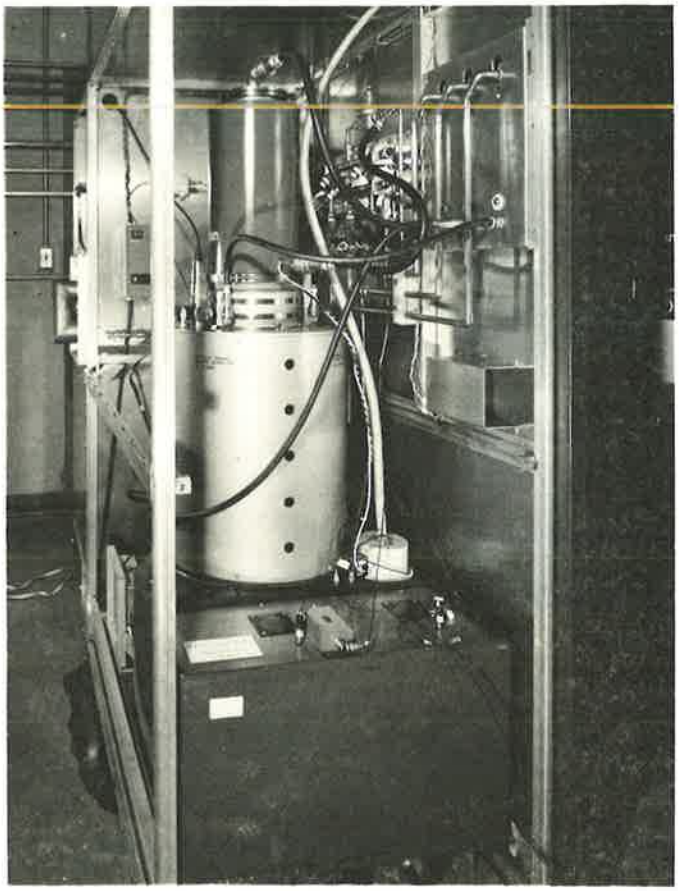

754058

Fig. 7. ATC LHR amplifier, showing modulator enclosure and high voltage feedthru.

Computerized Data Services for ATC During 1974 ATC was provided with eight channels of 50 millisecond record time, 100 kHz bandwidth electronics for a magnetic drum. Progress was made on the seven channel interferometer to be used on this machine. ATC data services are reported in Abstract VB 3.

3. Floating Multipole (FM-1)

a. New Higher Ampere-Turns Divertor Field Coil A 260 kAt divertor field coil was designed and fabricated for this machine during the last quarter of the year. This coil replaced the original 120 kAt coil and was required for a revised divertor field geometry. It is water cooled and "canned" in a stainless steel housing for operation within the vacuum vessel. A photograph of the coil is shown in Fig. 8.

754001

Fig. 8. New 260,000 ampere - turn FM-1 divertor field coil.

b. Computerized Data Services Planning and increased computerization of the data took place in 1974. (See Abstract VB 3.)

4. Miscellaneous Activities in Laboratory Support

a. General development was performed for the electronic circuits to provide isolated, noise immune, high speed analog and digital transmission systems, shorter

wavelength microwave systems, solid state conversion of microwave systems, and further radiation safety instrumentation.

b. Two ion gauge power supplies were designed and built during the year. One is used where ambient magnetic fields may exist and uses high frequency filament excitation to avoid filament fracture. The second employs dc power for the filament and is used in normal environments.

The emmission current regulation and collector measuring circuit used produce an order of stability that obviates the need for operator controlled adjustments. Specifications for models currently in use are:

Emmission Current: 100 uA or 1 mA, Selectable

Emmission Current Regulation: Better than 1% Overall

Pressure Ranges: 10^{-3} Torr - 10^{-9}Torr or 10^{-5}Torr - 10^{-11}Torr

Pressure Accuracy: Better than 2%, excluding Gauge Tube Error

Outgas: 60 Hz at 5 (Typical) Amperes

Over Pressure Trip: For over full scale reading for 3 seconds, all gauge power is turned off and a warning lamp is lit.

Recorder Output: Available from a rear panel connector

Figure 9 shows one of these supplies.

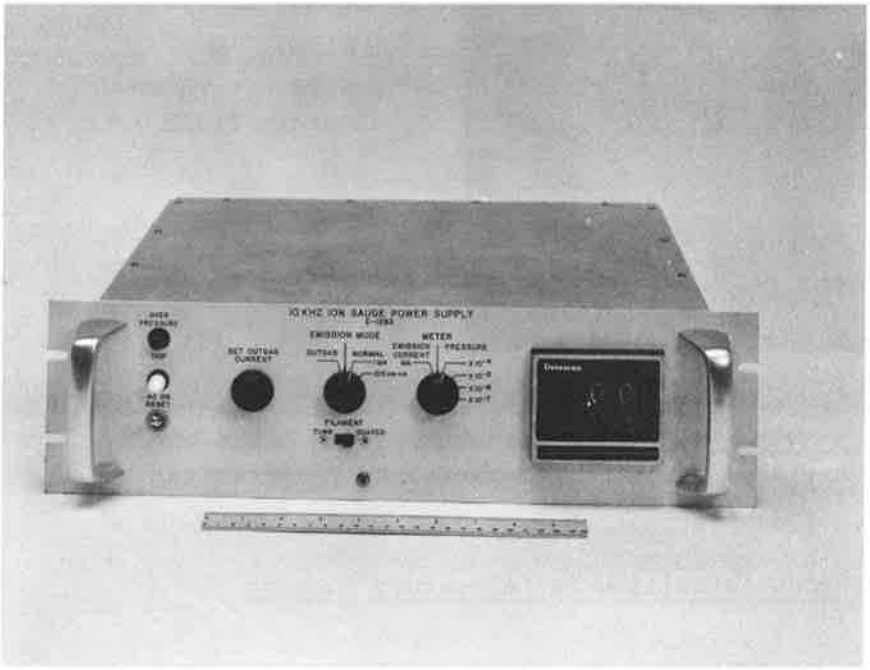

754079

Fig. 9. Typical high performance ion gauge power supply designed and fabricated during 1974.

c. During 1974 a high field solenoidal magnet was completed and operated at 250 kilogauss. Designed and fabricated for use in a CO_2 Laser heated plasma

experiment, it is believed to be the only one of its kind in existence. Figure 10 is an assembly view of the unit.

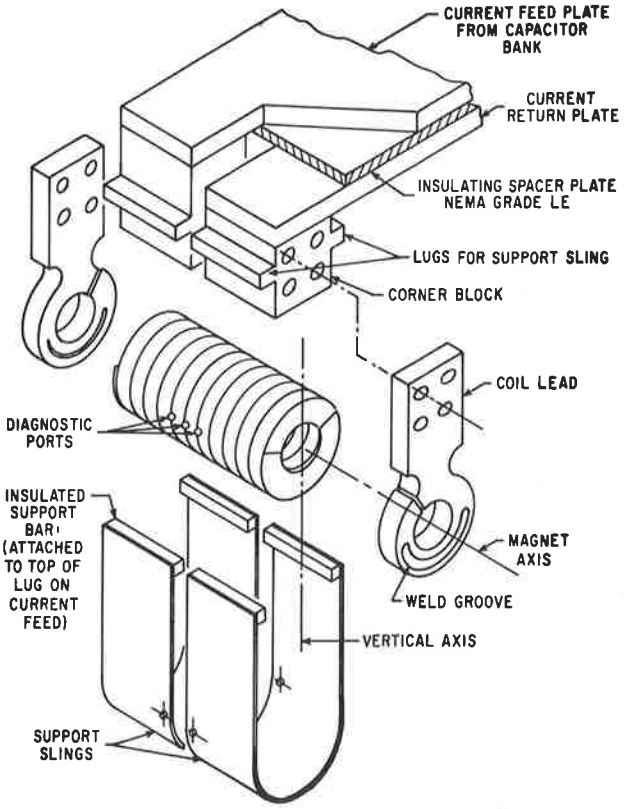

754105
Fig. 10. Detailed drawing of high field solenoidal magnet.

The solenoid is a helical coil, machined from a solid rod of Beryllium Copper (CD Alloy 172) and insulated with moldable (B-stage) glass-epoxy material. Radial diagnostic ports with a clear aperture of 0.47 cm allow viewing access near the magnet midplane. An axial prestress is provided by 7 tie rods in tension bearing on 2 Inconel compression plates. The on-axis homogeneity is within 5% over a central length of 12 cm. The table below summarizes mechanical and electro-magnetic characteristics:

Bore Diameter	5.08 cm
Outside Diameter	10.8 cm
Effective Length	23.24 cm
Maximum Field at Midplane	25 Tesla
Gauss/Ampere	0.616
Number of Turns	12
Turn Width	1.87 cm
Peak Current	406,000 Amperes
Peak Current Density	113,500 Amperes/cm^2
Coil Resistance	0.44 milliohms
Coil Inductance	2.2 microhenries
Power Supply Voltage	3 kilovolts
Insulation Thickness (Compressed)	0.124 cm

Complete design details are reported in Abstract VC 2.

VC 1. MATT-1139 A New Lower Hybrid RF Heating System, by Allan Deitz

This paper describes a high power 800 MHz LHR rf system for use on the ATC machine. With 200 kW rf output, the generator is believed to be the highest power rf device ever constructed for LHR heating experiments.

Two 100 kW feeds to the machine are provided by using hybrid combining techniques from the four Klystron final amplifiers. The final amplifiers are driven from a single crystal controlled solid state exciter capable of 10 Watts rf output.

Design details and constructional features of the system are described.

VC 2. MATT-1133 A High Field Magnet for a CO_2 Laser Heating Plasma Experiment, by Peter Bonanos

The design details and problems encountered in pursuing the production of a 250 kG solenoidal magnet for the subject use are described in this paper.

VC 3. MATT-1083 Test Results of NB_3SN Ribbons for the Princeton D Coil Test Program, by J. Kaugerts, J. File and J. W. Willard

A previously described D coil test program has been modified. Details of a smaller Nb_3Sn coil test program are described. Cusp coil tests have been made with several Nb_3Sn-NbTi hybrid field coils. Measurements of both the quench and recovery currents as a function of magnetic field component perpendicular to the wide edge of the ribbon are presented.

VC 4. MATT-1042 Proposed Superconducting Coils for the Princeton Fusion Reactor, by J. File

The Princeton Reference Design of a 2000 MW(e) Fusion Reactor has been previously described by Tenney. Among the major components of the nuclear island are the superconducting coil systems which produce the required steady fields to confine the plasma, as well as the pulsed fields which ignite, heat, control and divert the plasma. The details of the pulsed operating cycle is described in a paper by Gralnick. This paper describes a coil system including the cooling and refrigeration requirements which provides steady fields of up to 160,000 Gauss and pulsed fields of up to 30,000 Gauss.

VI. FUSION REACTOR DESIGN DIVISION

A. Introduction

The greatest single effort of the Fusion Reactor Design Division during 1974 was the completion of the preparation and publication of the 600-page document, A Fusion Power Plant.[1] Representing the work of 15 different authors, this book gives in 22 chapters and three appendices, a comprehensive description of the conceptual design study of a first generation commercial fusion power reactor that was carried out by members of the Division. A detailed drawing of the power station is shown in Fig. 1.

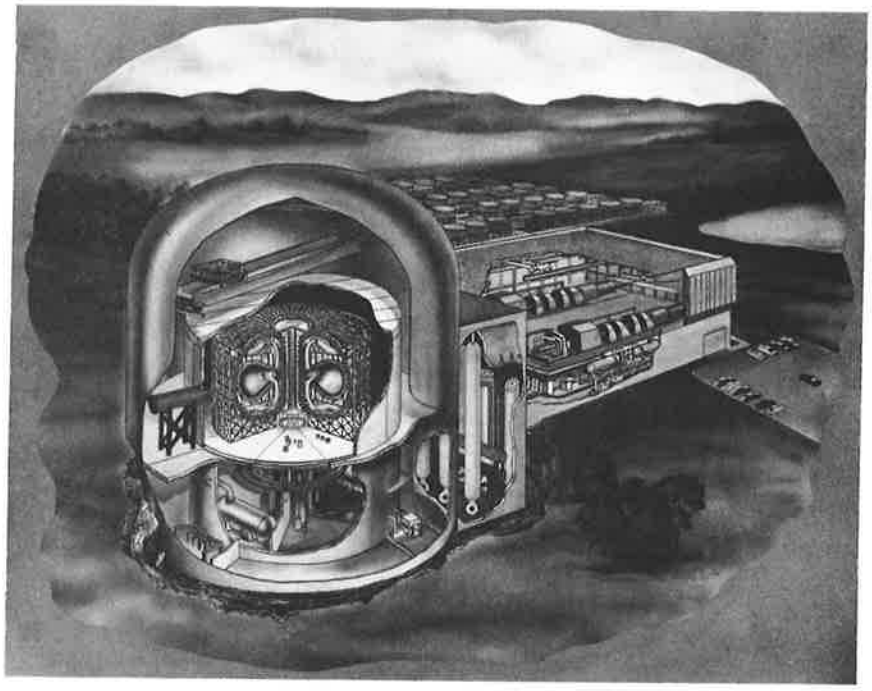

744296

Fig. 1. A first-generation fusion power plant.

The model described in the report is intended as a reference design to be used as a standard against which the value of different ideas and the effect of future developments may be measured. This publication has received wide distribution both here and abroad.

---

[1] MATT-1050, A Fusion Power Plant by R. G. Mills, ed. (1974).

Now in its fourth year, the industrial fellow program had in residence during the past year four members of manufacturing and architect engineering firms.

The cooperative effort with the Aerospace Systems Laboratory of the Department of Aerospace and Mechanical Sciences, begun late in 1973, continued in 1974. This program provides systems analysis for fusion reactors. Work accomplished included definition of nominal parameters for materials supply, materials disposal, fusion reactor, reactor auxiliary and fuel handling systems; development of a FORTRAN code to model the combinations of potential reactor, electric power generation and/or thermal power utilizations, and waste heat disposal concepts (studies continuing); formulation of an approach to investigation of fusion related national/global power demands; initial evaluation of environmental and siting constraints; review of the literature; and definitization of subcontractor support.

B. Neutronics

Studies of the tritium breeding potential of the Reference Design blanket when subjected to variations of composition were carried on during the year.[2] Results will be utilized to allow direct modification of the blanket design to achieve some specific goals (e.g., tritium breeding, maximum power production, fuel production, or actinide burning at the expense of other properties).

An investigation of neutron wall load distributions in circular cross-section tokamaks was completed and the results submitted for publication. The study was carried out using a numerical ray tracing process to solve the integral neutron transport equation and analyzed three different plasma source distributions. Normalized plasma source strength as a function of position in the circular plasma cross section for these distributions is given in Fig. 1. The data, some of which are shown in Fig. 2. indicated that significant "hot spots" may occur on the first wall affecting its design and also that of the blanket. Also the variations in the angular flux distribution were found to affect the tritium breeding in a typical blanket. A more sophisticated study is underway employing non-circular cross sections and in particular the wall shape of the Princeton Reference Design.

---

[2] E. Greenspan and W. G. Price, Jr., "Tritium Breeding Potential of the Princeton Reference Fusion Power Plant, *Proceedings of the First Topical Meeting on the Technology of Controlled Nuclear Fusion* (National Technical Information Service, Springfield, Virginia, 1974) Conf.-740402-P2, pp. 145-154.

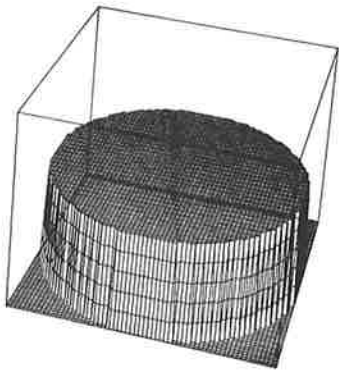

744734
Uniform Source

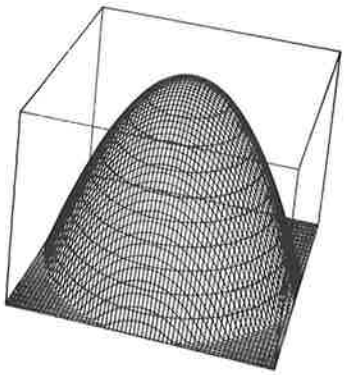

744733
Peaked Source

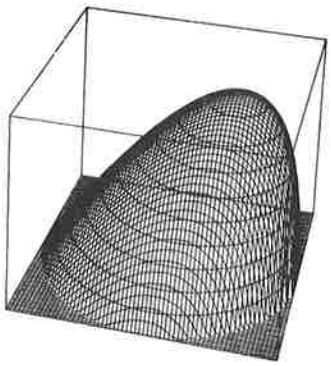

744732
Shifted Source
$\varepsilon = 0.5$

Fig. 1. Normalized plasma source strength as a function of position in the circular plasma cross section for the three source distributions.

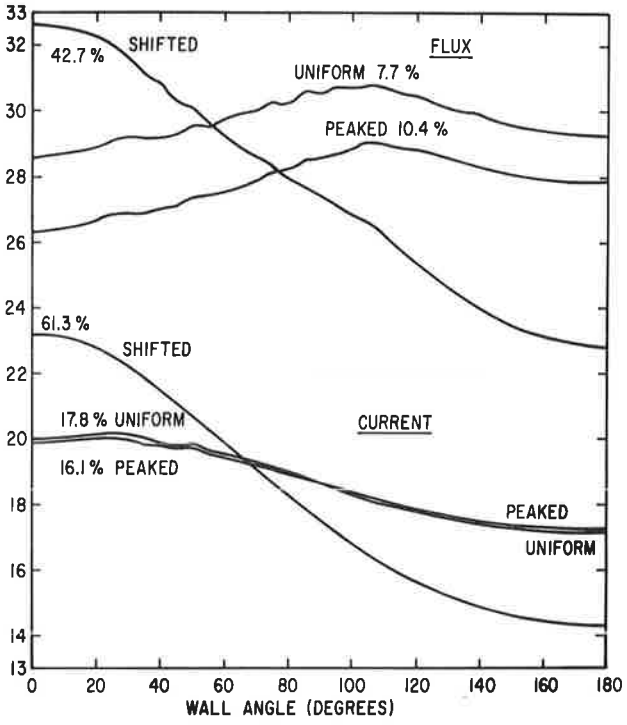

744737

Fig. 2. Scalar flux F and current J as a function of wall angle χ for the three sources. The units are arbitrary. The percent values are the difference between the minimum and maximum flux or current for each source.

Work is continuing on installation of a Monte Carlo capability for neutronics studies in three-dimensional geometry. This involves having the MORSE Monte Carlo code running for simple geometries such as sphere and slab. A cylindrical version is under investigation.

C. Tokamak Fusion Test Reactor

Division personnel have actively participated in the work of the Two-Component Torus (TCT) Conceptual Design Study team. Initial guidance and subsequent consultation on neutronics problems were provided throughout the year. Alpha orbits, as illustrated in Fig. 1., were studied,[3] and it was found that the proportion of alphas confined in TCT operating with uniform 1 MA current in a 60 cm radius current channel, but with a limiter radius of 85 cm, is about 70%. These calculations were done in full toroidal geometry. A uniform vertical field was used to provide plasma equilibrium. An alpha particle trajectory analysis report is in preparation.

Visiting members of the Division played an important role in this study, providing overall direction of the Westinghouse efforts and also coordination and interface with PPL.

During the final months of 1974, considerable time was spent in coordinating the laboratory's effort in preparing a draft Environmental Statement for the proposed tokamak fusion test reactor (TFTR) facilities. This is to be released shortly as U. S. Energy Research and Development Administration Report WASH-1544.

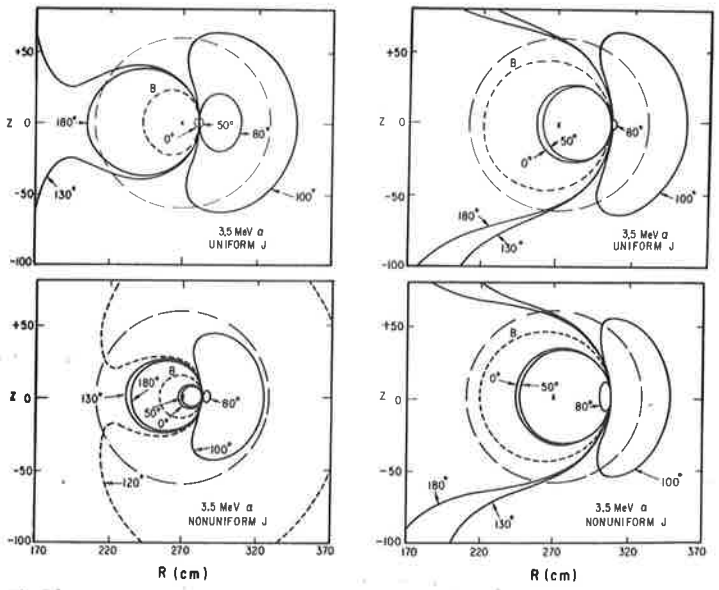

Fig. 1. TCT alpha orbits I = 1.0 MA

[3] *Bull. Am. Phys. Soc.* 19, 918 (1974)

D. Computer Codes

Substantial progress was made during the year in cooperation with personnel of the Theoretical Physics Division in replacing the current cylindrical reacting code with a full toroidal description. This involved replacement of several rather crude approximations used to date with highly accurate approximations.

This code is composed of three major blocks that solve N time dependent transport equations one dimensionally relative to the flux surfaces. The three blocks are:

a) Equilibrium Code, written by S. Jardin and R. Grimm

b) Mapping Code, B. Rosen and R. Grimm

c) Transport Code, A. M. M. Todd.

The aim of these studies is to solve multi-species plasma transport in machines with complex field geometry.

The rate of energy loss and pitch angle scattering of a suprathermal ion in a plasma of arbitrary composition has been calculated using the computer code, MOTION.[3,4] The ratio,

$$\varepsilon = \left(\frac{1}{2m\alpha E} \frac{dP_\perp^2}{dt} \right) / \left(\frac{1}{E_o} \frac{dE}{dt} \right) ,$$

is a measure of determining when pitch angle scattering can or cannot be ignored in considering the interaction of the suprathermal ion and the background plasma. Figure 1 demonstrates this effect for two cases of interest, E_o is the initial energy of the test ion (3.5 MeV alpha), and T_i is the thermal energy of the plasma ions. f is the fractional burn or the thermal ash fraction. In relatively clean plasma (TCT case) a large fraction of the test ion energy will be deposited prior to having $\varepsilon = 1$ and scattering become important. At higher Z_{eff}, however, pitch angle scattering will be important almost from the very beginning. As high Z_{eff} values may be encountered in reactors, it is important to include the effects of the pitch angle scattering in the consideration of the deposition of α particle energy in a reactor plasma.

---

[4] *Bull. Am. Phys. Soc.* 19, 832 (1974).

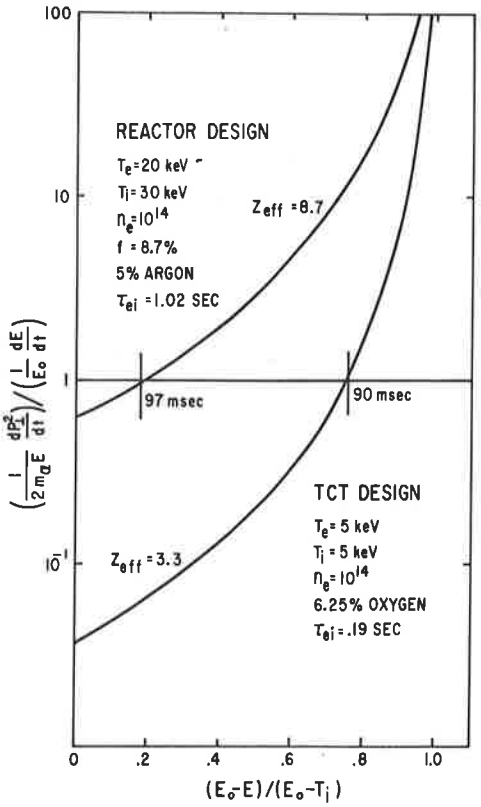

754016

Fig. 1. Ratio of scattering rate to energy transfer rate.

Studies of the thermalization of fusion alphas in toroidal burn calculations are continuing.

Other codes written during the year or adopted and put into routine operation include:

PPL-ANISN[5]	A PPL-revised version of the one dimensional discrete ordinance transport code, ANISN	W. G. Price, Jr.
AREAD[6]	A general-purpose subroutine for reading free-formal card input into fixed or variably dimensioned arrays	W. G. Price, Jr.
MANAGERY	A code to simplify the maintenance and use of partioned-data sets, e.g., libraries of card-image source or data files	W. G. Price, Jr.

---

[5] MATT-1035, (1974) Plasma Physics Laboratory

[6] MATT-1034, (1974) Plasma Physics Laboratory

PERSP	A set of subroutines that will plot a perspective view of a three-dimensional surface described by an array Z (I,J). Lines of constant contour may be superimposed on the surface.	W. G. Price, Jr.
WALLLOAD	A program to calculate the neutron wall load distribution in circular cross-section tokamaks.	D. L. Chapin
MORSE	A Monte Carlo code presently being installed and tested.	ORNL

E. Miscellaneous

Consideration of the thermal equilibrium of a reactor grade plasma for several scaling laws was undertaken based on a point model calculation.[7] Figure 1 is a summary of these results indicating that for various values of the ratio of electron to hydrogenic ion density, a spectrum of stable and unstable equilibria exists up to a maximum value of Z. Figure 2 indicates that the output power will be sensitive to this parameter and looking forward to the reactor regime this may provide a needed mechanism for controlling reactor power output. Finally, the effect of feeding a fraction, f, of the output power back into the plasma allows one to find equilibria at higher values of Z. (See Fig. 3. Higher Z implies a longer $n\tau$ value is needed, and power feedback is a mechanism of returning the system to equilibrium if insufficient $n\tau$ is available.)

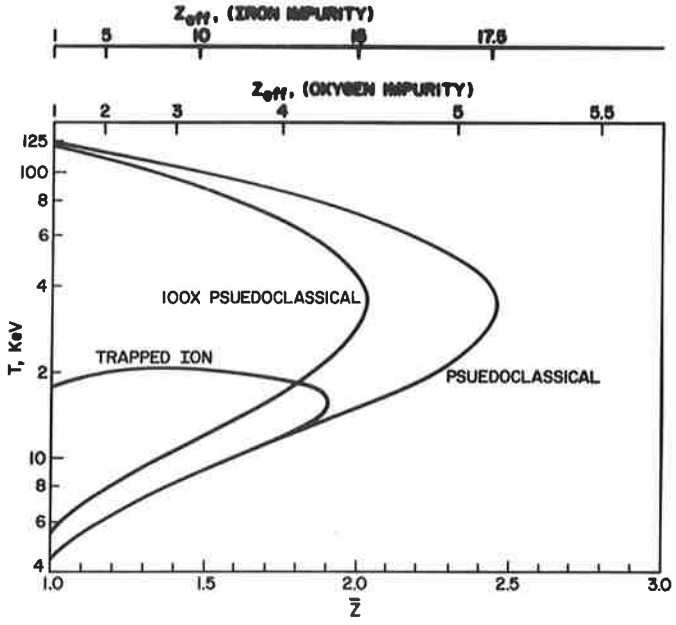

744270

Fig. 1. Equilibrium temperature versus $\bar{Z}$ for various modes of transport losses.

---

[7] *Proceedings of the First Topical Meeting on the Technology of Controlled Nuclear Fusion* (National Technical Information Service, Springfield, Virginia, 1974) Conf. 740402-P2, pp. 364-372.

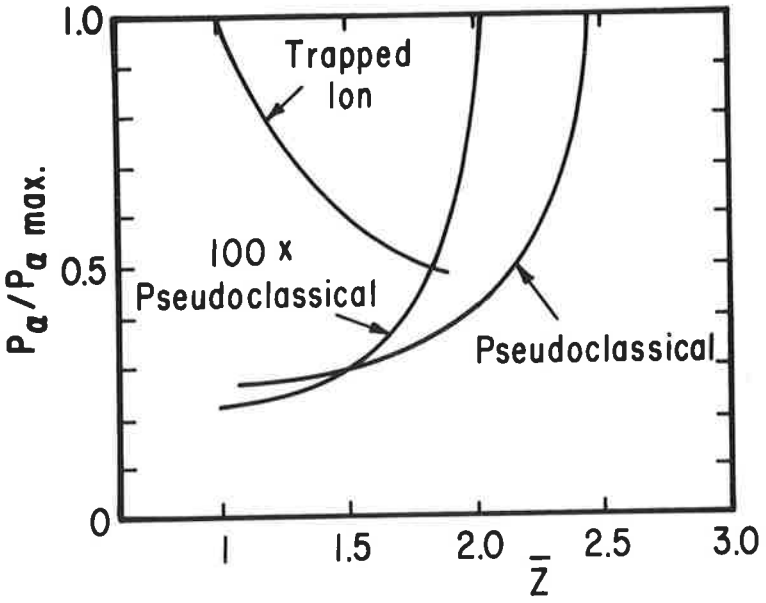

744272

Fig. 2. Ratio of alpha power density to maximum alpha power density vs. $\bar{Z}$ for various modes of transport loss.

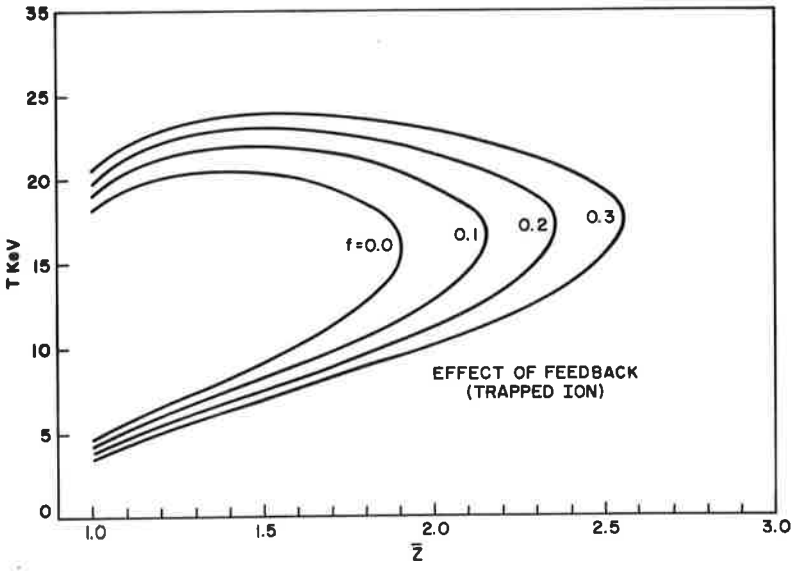

744274

Fig. 3. Effect of power feedback on equilibrium temperature vs. $\bar{Z}$ for trapped ion scaling.

Investigation of the divertor scrapeoff layer was begun with the assistance of a visiting industrial fellow.

A steady growth in the Fusion Power Library had resulted in the accumulation of 2020 documents, 398 monographs, and 358 bound journals by the end of 1974. A new, more comprehensive list of subject headings was prepared for the implementation of library services.

Throughout the year members of the Division have given a number of papers and talks, both on the fusion power plant as a whole and on specific aspects of its design including a summary of the principal features of the Princeton Reference Design prepared for the IAEA conference to Tokyo.[8] Two lectures on Low Density Closed Plasmas (Tokamaks) were presented at a CTR Workshop at the University of Arizona. The publications are described in Abstracts VI E1 - VI E15.

---

[8] MATT-1082 (1974) Plasma Physics Laboratory

VI.E 1 Economic and Environmental Aspects of a First Generation Fusion Power Plant,* by Robert G. Mills

The Reactor Studies Group at Princeton has recently completed a thorough, self-consistent conceptual design of a first generation fusion power plant. Selection of form, operating cycle, and materials has been made to avoid most known problems and to minimize the number of assumptions necessary due to lack of knowledge in plasma physics and materials damage. This plant has not been optimized in any sense, but is merely one reference design against which to test the effects of varying parameters or varying assumptions. Nevertheless it appears that even a first generation power plant will be attractive economically and environmentally acceptable. A brief description of the system is given together with cost estimates.

---

*9th Intersociety Energy Conversion Engineering Conference (American Society of Mechanical Engineers, New York, 1974) pp. 726-730.

VI.E 2 Current Expectations for Fusion Power from Toroidal Machines,* by Robert G. Mills

The rapidly increasing effort to solve the problems of the controlled release of nuclear fusion energy has been stimulated by recent maturation of the science of plasma physics, especially in one area -- the confinement of plasma in closed magnetic fields. At the same time, significant experimental progress has been achieved with magnetic mirror machines, and a large toroidal theta pinch is under construction at Los Alamos. Enthusiasm is running high in groups working on laser-ignited fusion. Perhaps all of these approaches will lead to viable power systems. It seems to be generally accepted, however, that toroidal magnetic machines have the greatest probability of being the first, if not the only, approach to succeed, and this paper restricts its attention to that category. Current theories correspond to experimental results in the laboratory, and predictions of these theories imply the possibility of successful thermonuclear reactors. At the same time increasingly more realistic studies of hypothetical fusion power stations carried out by laboratory, university, utility, and manufacturing personnel make them appear to be potentially of great economic interest. Serious problems still remain, but increasing government support leads many to expect a scientific feasibility experiment and a demonstration of thermonuclear burning of deuterium-tritium fuel before 1980.

---

*IEEE Transactions on Power Apparatus and Systems PAS-93 (1974) pp 1805-1809

VI.E.3 Problems and Promise of Controlled Fusion,* by Robert G. Mills

Rapid progress has been made in understanding magnetically confined plasma, the approach to fusion power that seems closest to realization. The way now seems clear to the fabrication of the large experimental machines that will be necessary to establish scientific feasibility and pave the way to experimental reactors. A number of important problems remain to be resolved before controlled thermonuclear fusion can become a reality, but the goal is closely matched to our need to find a way to produce large quantities of power while conserving our resources and environment. Reasons for the current optimism will be reviewed and one formulation of a complete power plant will be presented.

---

* *American Society of Mechanical Engineers* (New York 1974) Paper No. 74-WA/NE-10.

VI.E.4 Divertor Operation in the Princeton Reference Design Model Tokamak Reactor,* by F. H. Tenney

Projected operation of the poloidal field divertor is described for the Princeton Reference Design Tokamak Reactor. A relatively cold plasma blanket will form outside the separatrix and will constitute a thermal connection between the hot plasma and the exhaust chamber. The plasma blanket is expected to be a good absorber of slow neutrals. Simple one-dimensional models of the diverted plasma provide estimates of the plasma density distribution and particle flux to the walls. Recycling of particles with the divertor walls may amount to ten times the particle throughput of the reactor. The magnetic field configuration is also discussed.

---

* *J. of Nuclear Matls* 54, 43 (1974) also *Proceedings of the Conference on Surface Effects in Controlled Thermonuclear Fusion Devices and Reactors*, H. Weidersich, M. Kamnesky, K. M. Zwilsky, eds. (North-Holland Publishing Company, Amsterdam, 1974) pp 43-47.

VI. E 5 The Problems of Divertors,* by F. H. Tenney

The divertor concept was developed to solve three problems that were envisioned for a steady-state magnetically confined fusion reactor; namely, how to maintain a steady flow of material out of the confined plasma and into the vacuum pumps while maintaining a very low neutral pressure between the plasma and the walls of the vacuum vessel, how to maintain a high plasma edge temperature, and how to reduce the flow of impurities from the walls into the reacting plasma. In such a fusion reactor the plasma is to be confined in a special magnetic field which closes on itself in such a manner as to define a set of nested, closed (toroidal) magnetic surfaces that do not intersect any material walls. The divertor, by virtue of its own coils, produces a limiting magnetic

surface of the confining field, called the separatrix surface, outside of which the magnetic surfaces do intersect material walls. Plasma that passes outward across the separatrix surface, called the scrapeoff plasma, can flow easily along the diverted magnetic fieldlines to walls distant from the reacting plasma. The scrapeoff plasma constitutes the bounding medium for the plasma inside the separatrix surface.

The nature of the scrapeoff plasma will be affected by (a) the path length of the diverted magnetic field lines as measured from near the separatrix surface to where they intersect a material wall, (b) the distance between the separatrix surface and the material walls, and (c) the pumping speed of the volume into which the scrapeoff plasma flows. This (dense) scrapeoff plasmas, flowing at sonic (subsonic) speeds, are anticipated for divertor designs characterized by short (long) diverted field lines and high (low) pumping speeds. The thinner the scrapeoff plasma, the more readily a neutral impurity atom from the walls can penetrate to the separatrix surface and thence into the reacting plasma. On the other hand, the thin scrapeoff plasma will be collected from the ends of the diverted field lines before it can interact strongly with the walls en route.

The buildup of impurities within the reacting plasma is one of the major concerns for fusion reactors. Rapid collection of impurities will limit fusion reactors to a rapid, short-pulse mode of operation and will reduce the efficiency of producing power.

There has been little experience with divertors. Early experience with the divertor on the Model C Stellarator indicated a reduction in the impurity content of the discharge plasma by two orders of magnitude.

---

*_Transactions of the American Society 1974 Winter Meeting_ (American Nuclear Society, Hinsdale, Illinois, 1974) 19, p. 7.

VI.E 6 MATT-1025, Vacuum Problems Associated with the Conceptional Design of Tokamak Fusion Reactors, by G. Lewin and F. H. Tenney

The design and operation of D-T fusion reactors based on the tokamak configuration is described with special emphasis on the vacuum aspects. Particular reference is made to the reactor study of the Princeton Plasma Physics Laboratory. Vacuum requirements of two other reactor studies based on the theta pinch and the mirror configuration are briefly mentioned. Problems arising from the radioactivity of the tritium and the high, locally variant temperatures are discussed.

VI.E 7 MATT-1088, Two-Energy-Component Toroidal Fusion Devices, by H. L. Berk, H. P. Furth, D. L. Jassby, R. M. Kulsrud, C. S. Liu, M. N. Rosenbluth, P. H. Rutherford, F. H. Tenney, T. Johnson, J. Killeen, A. A. Mirin, M. E. Rensink, and C. W. Horton, Jr.

Injection of a superthermal ion component into a toroidal plasma can raise the fusion power density to levels considerably higher than those attainable in ordinary one-component plasmas. As a result, energy breakeven in D-T can be attained in bulk plasmas with $n\tau$-values as low as 10^{13} cm^{-3} sec, at temperatures of ~5 keV. The optimal energy of the superthermal ion component is in the range 100 - 200 keV; injection-energy requirements can be reduced by adiabatic compression prior to or during the reaction phase. The appropriate ratio $\bar{F}$ of fast-ion pressure to bulk-plasma pressure is about 0.5. The stability of two-component tokamak plasmas has been examined, and is found to be favorable for parameters of practical interest.

VI.E 8. Enhanced F Values for the TCT, *by E. A. Frieman and F. H. Tenney

Previous calculations[1] of the ratio F of fusion energy produced to the injected beam energy in a TCT were based on the slowing down test particle calculation of Sivukhin[2]. We here report on a more detailed numerical calculation of F based on an analytic solution of the Fokker-Planck equation for an isotropic source of beam particles. The assumption is also made that beam-beam interactions are negligible. The major new effects in the present calculations are (1) electron and ion velocity space scattering effects, (2) corrections to the drag coefficients and (3) corrections to the reaction rates resulting from the relative velocity between beam and background ions.

The results indicate that a significant enhancement of F over the previously reported values exists over a wide range of injected beam energy W_o and background plasma temperature.

---

*Bull Am. Phys. Soc. 19, 878 (1974)

VI.E 9 Finite Ion Temperature Effects in Two-Energy-Component Plasmas, * by H. Towner, G. H. Miley, Univ. of Ill.; F. H. Tenney, and D. L. Jassby

Extending previous treatments that have assumed cold target ions,[1,2] we investigate the influence of finite target-ion temperature on fusion energy multiplication Q for two-energy-component plasmas with and without energy clamping. The increase in relative velocity, on the average, between beam and bulk ions results in reduced drag on the beam ions. A more significant effect is substantial change in fusion reactivity. For D and T, with $T_i \sim T_e$, Q is substantially increased over the cold-ion case provided that injection energy $W \lesssim 130$ keV; the improvement factor increases with decreasing W and can reach 40%, for example, at W = 60 keV, $T_e = T_i = 5$ keV. For $W \gtrsim 130$ keV, Q decreases slightly. In the case of energy clamping, the cross-over $W \sim 80$ keV. These results are especially significant at the end of a clamped, low-W burn, where additional fusion energy from the thermalizing suprathermal population is obtained.

---

*Bull Am. Phys. Soc. 19, 877 (1974)

VI.E 10 Transport of Neutral Impurity Atoms Through a Plasma, *by J. G. Gilligan, U. of Mich; S. L. Gralnick and W. G. Price, Jr.

The transport of neutral atomic oxygen in a multispecies, isotropic, spatially homogeneous plasma is considered. This problem is typical of a large class of neutral transport problems which are governed by a linear Boltzmann equation and which are amenable to numerical solution by techniques developed for neutron transport studies. It is possible to use these techniques for the solution of complicated problems involving several impurity species, an inhomogeneous plasma medium and complex geometries.

The one dimensional, time-independent, discrete ordinates (S-N), code, ANISN has been adapted for solution of the following problem. A slab model is used to approximate conditions occurring in the boundary region separating a hot plasma from its surrounding physical boundaries. The analysis yields the spatial distribution of ionization sites of the atomic oxygen and examines the several energy transport mechanisms between the background plasma and the neutral species.

---

*Bull. Am. Phys. Soc. 19, 843 (1974).

VI.E 11 MATT-1102, Neutral Wall Load Distributions in a Circular Cross Section Tokamak, by W. G. Price, Jr. and D. L. Chapin

The distributions of the angular and scalar flux and current around the wall of a circular cross section tokamak are calculated by numerically solving the integral form of the neutron transport equation. The effect of the toroidal geometry is taken into account while investigating three different isotropic plasma source distributions - uniform, peaked, and shifted. The results of the calculations for a typical large scale tokamak design indicate a strong dependence of the scalar flux and the current (of DT neutrons) on the wall position, resulting in "hot spots" on the wall. The calculations also indicate a marked variation of the angular flux of DT neutrons with the wall position, which may be an important consideration in wall sputtering and tritium breeding evaluations. The angular distribution is used as a source condition for the neutron transport code ANISN, to investigate the effect on the flux and tritium breeding ratio in a fusion reactor blanket.

VI E 12 MATT-1036 LIBMAK: A Program to Manipulate ANISN-Type Binary Libraries,* by W. G. Price, Jr.

LIBMAK is a program written to manipulate ANISN-type binary libraries. Input data may be taken from old libraries or card decks in AREAD (FIDO) format. Commands are available to create, revise, combine, list, and punch material data stored in ANISN binary form.

VI E 13 TM-272 Consequences of Tritium Release to the Atomosphere, by W. G. Price, Jr.

The radiological consequences of an accidental release of tritium are estimated. First, conversion factors from atmospheric concentration to dose are computed. Second, equations for atmospheric dispersion of pollutants are reviewed. Finally, potential doses due to tritium loss from a "typical" DT-burning plasma physics experiment are estimated. Even in the worst case, these do not seem to pose a great hazard.

VI.E 14 DT Fusion Reactor Activation and Afterheat, *by W. G. Price, Jr., D. J. Dudziak, J. D. Lee, J. R. Powell, D. Steiner and W. F. Vogelsang

It is generally recognized that DT fusion provides the only near-term practical basis for fusion power systems. Since each DT reaction produces a 14 MeV neutron which must be captured in an energy-producing, tritium-breeding blanket, there is certain to be a large amount of neutron-induced transmutation of nuclides in the blanket. This paper extracts pertinent activation, afterheat, and hazard potential figures from a number of recent fusion activation studies. Fusion power will not be "clean", but its radio-isotope problems will be significantly less than those of fission systems.

---

*Transactions of the American Nuclear Soc. 1974 Winter Meeting (Amer. Nuclear Society, Hinsdale, Illinois, 1974) 19, p. 459.

VI.E 15 An Accelerated Spectral Synthesis Technique, *by W. G. Price, Jr. and J. J. Duderstadt, Univ. of Mich.

Spectral synthesis, the representation of the energy dependence of the neutron flux by a combination of overlapping trial modes, has received only limited application to the analysis of fast reactors, because the savings in computational effort achieved via synthesis have not been sufficiently dramatic to compensate for the occasional disconcerting failures of the methods. This Note develops an approximation procedure combining spectral synthesis with Wielandt's method which recovers the large savings in computation time expected with synthesis methods. Such a scheme is illustrated by applying it to calculate the flux in a fast critical assembly.

---

*Nucl. Science & Engr. 55, 98 (1974)